

Insights on local chemical structure of chalcogenide photovoltaic materials using solid state NMR spectroscopy

by

Amit Bhattacharya

A thesis submitted in partial fulfillment of the requirements for the degree of

Doctor of Philosophy

Department of Chemistry
University of Alberta

© Amit Bhattacharya, 2022

Abstract

Quaternary chalcogenides with the formula $I_2-II-IV-VI_4$ have emerged as promising candidates for photovoltaic materials, but many details about their structures remain poorly understood. This thesis describes the synthesis, structure determination, and optical properties of the sulfides Cu_2MTtS_4 ($M = Zn, Cd, Hg$; $Tt = Ge, Sn$), prepared as bulk samples by reaction of the elements. Their long- and short-range structures were elucidated by a combination of powder X-ray diffraction and multinuclear solid-state magnetic resonance spectroscopy ($^{63/65}Cu$, ^{67}Zn , ^{73}Ge , ^{113}Cd , ^{119}Sn , ^{199}Hg). Within the $Cu_2Zn_{1-x}Cd_xSnS_4$ series, ^{113}Cd NMR spectroscopy confirmed a phase transition at $x = 0.4$ and revealed the coexistence of phases with subtly different structures (space groups $I\bar{4}$ and $I\bar{4}2m$) in the intermediate region ($x = 0.3-0.4$), which were previously not apparent from XRD data alone. The ^{119}Sn NMR spectra indicated the Sn atoms are surrounded by a random distribution of Zn and Cd atoms within the second coordination sphere; these distinct local environments were resolved by their isotropic chemical shifts and quantified by their peak areas. A longstanding problem about whether disorder of Cu and Zn atoms occurs in Cu_2ZnSnS_4 was resolved by analyzing high-field (21.1 T) $^{63/65}Cu$, ^{67}Zn solid-state NMR spectra, in conjunction with DFT calculations. Similar problems plague the related compounds Cu_2HgSnS_4 and Cu_2GeSnS_4 . Evidence from ^{119}Sn and ^{199}Hg NMR spectra suggests that ordering occurs in Cu_2HgSnS_4 after annealing, a phenomenon that was not previously detected from XRD data. Within the $Cu_2ZnSn_{1-x}Ge_xS_4$ series, the influence of Ge substitution for Sn on the local structure was monitored by ^{67}Zn solid-state MAS NMR spectroscopy, which showed excellent sensitivity. For all these compounds, optical band gaps were determined experimentally from UV-visible diffuse reflectance spectra. Electronic structure calculations were performed to bear further insight into the bonding and charge distribution in these compounds.

Preface

This thesis is an original work by Amit Bhattacharya and co-workers. Prof. A. Mar and Prof. V. K. Michaelis, who acted as corresponding authors, were involved in manuscript reviewing, editing, and providing resources.

Chapter 2 was published as Bhattacharya, A.; Tkachuk, D. G.; Mar, A.; Michaelis, V. K. Mere Anarchy is Loosed: Structural Disorder in $\text{Cu}_2\text{Cd}_x\text{Zn}_{1-x}\text{SnS}_4$. *Chem. Mater.* **2021**, *33*, 4709–4722. It has been adapted and reprinted with permission from the American Chemical Society. My contribution includes synthesis, XRD, NMR, UV-visible data collection, analysis, characterization, and manuscript preparation. The solid-state NMR data at 21.1 T were collected by Dr. Victor Terskikh at the National Ultrahigh-Field NMR Facility for Solids at the University of Ottawa. GIPAW-DFT calculations were performed by Dylan G. Tkachuk. EDX data were collected with the help of Dr. Guibin Ma in the Department of Earth and Atmospheric Sciences.

Chapter 3 was published as Bhattacharya, A.; Mishra, A.; Tkachuk, D. G.; Mar, A.; Michaelis, V. K. Mercurial Possibilities: Determining Site Distributions in $\text{Cu}_2\text{HgSnS}_4$ using $^{63/65}\text{Cu}$, ^{119}Sn , and ^{199}Hg Solid-state NMR Spectroscopy. *Phys. Chem. Chem. Phys.* **2022**, *24*, 24306–24316. My contribution includes synthesis, XRD, NMR, UV-vis data collection, analysis, characterization, and manuscript preparation. The solid-state NMR data at 21.1 T were collected by Dr. Victor Terskikh. GIPAW-DFT computations were performed by Dylan Tkachuk. Electronic structure calculations were performed by Vidyanshu Mishra. EDX data were collected by Dr. Guibin Ma.

Chapter 4 is an adaptation of a current manuscript in preparation: Bhattacharya, A.; Mishra, A.; Tkachuk, D. G.; Mar, A.; Michaelis, V. K.. “Influence of Ge substitution on the Structure and Optoelectronic Properties of $\text{Cu}_2\text{ZnSn}_{1-x}\text{Ge}_x\text{S}_4$ Photovoltaic Materials using Solid-state NMR

Spectroscopy.” My contribution includes synthesis, XRD, NMR, UV-vis data collection, analysis, characterization, GIPAW-DFT computation using CASTEP program, and manuscript preparation. The solid-state NMR data at 21.1T were collected by Dr. Victor Terskikh. Electronic structure calculations were performed by Vidyanshu Mishra. EDX data were collected by Dr. Guibin Ma.

Dedicated to my parents

Acknowledgments

First, I would like to express my deepest gratitude to my supervisors, Prof. Arthur Mar and Prof. Vladimir K. Michaelis, for their guidance, motivation, and endless support throughout my Ph.D. Both of my supervisors encouraged me to think critically and pursue independent research as well. They allow me to think freely, work on my project ideas, and advise how to improve it. Dr. Mar's sense of humor made him approachable for any discussion, which made my Ph.D. journey enjoyable. Prof. Michaelis always encouraged my ideas and inspired me to aim for bigger and better during and after my Ph.D.

I would like to thank all past and present Michaelis and Mar groups members: Dr. Guy M. Bernard, Dr. Abhoy Karmakar, Dr. Michelle Ha, Madhusudan Chaudhary, Diganta Sarkar, Riley Hooper, Tony Jin, Brittney Klein, Brayden Glockzin, and Dundappa Mumbaraddi, Vidyanshu Mishra, Alex Gzyl, Dong Zhang, Mohammad Jomaa, Dmitry Vrublevsky, Ritobroto Sikdar, Fuwei Wen, Arkadii Pominov, Trinanjan Dey, Dr. Abishek Iyer, Dr. Anton Oliynyk, Dr. Yuqiao Zhou, Dr. Jan Poehls, Dr. Frank Stegemann, Dr. Lawrence Adutwum, Dr. Volodymyr Gvozdetskyi, Dr. Balaranjan Selvaratnam, Dr. Maxwell Wallace. I also like to express my heartfelt thanks to all the undergraduate students, Yu Qiu, Christopher Worsnop, Nick Friesen, Dylan Tkachuk, and Caoimhe Connaughton, who worked with me on different projects.

A special thanks to Dr. Guy M. Bernard for providing NMR training, NMR-related help, scientific discussions, data analysis, manuscript editing, and eagerness to answer any query. Also, a special thanks goes to Dr. Abhoy Karmakar for all his valuable suggestions and support in and out of graduate studies and making my lab days enjoyable.

I thank Dr. Victor Terskikh for acquiring NMR spectra at 21.1 T. at the National Ultrahigh-field NMR Facility for Solids in Ottawa. I would like to convey my thanks to all the NMR staff at

the University of Alberta — Dr. Ryan McKay, Mr. Mark Miskolzie, and Mrs. Nupur Dabral — for help with all aspects of NMR spectroscopy.

I would like to thank Prof. Eric Rivard, Prof. Jonathan G. C. Veinot, Prof. Julianne M. Gibbs, Prof. Roderick E. Wasylshen, and Prof. Yan-Yan Hu for participating during my candidacy exam or Ph.D. defence and engaging in insightful discussion. I also thank Dr. Wayne Moffat, Jennifer Jones, Anita Weiler, and Dr. Yoram Apelblat in the Department of Chemistry.

Finally, I am grateful to my parents, brother, and relatives for their love, blessing, support, and constant encouragement throughout my life. I would like to thank all my friends and housemates for making my journey enjoyable.

Table of Contents

Chapter 1: Introduction	1
1.1 Quaternary chalcogenides as next-generation photovoltaic materials	1
1.2 Effect of cation substitution on PCE and optical property in $\text{Cu}_2\text{ZnSnS}_4$	2
1.3 Structure of $\text{Cu}_2\text{ZnSnS}_4$	5
1.4 Problems in structure determination of $\text{Cu}_2\text{ZnSnS}_4$ and related compounds.....	7
1.5 Solid-state NMR spectroscopy	9
1.5.1 The Zeeman interaction	12
1.5.2 Magnetic shielding and chemical shift	14
1.5.3 Direct dipolar and indirect spin-spin coupling	17
1.5.4 Quadrupolar interaction	17
1.5.5 Magic angle spinning	21
1.5.6 Nuclear relaxation processes.....	24
1.6 References	26
Chapter 2: Mere anarchy is loosed: structural disorder in $\text{Cu}_2\text{Zn}_{1-x}\text{Cd}_x\text{SnS}_4$	35
2.1 Introduction	35
2.2 Materials and methods	38
2.2.1 Synthesis.....	38
2.2.2 X-ray diffraction and energy-dispersive X-ray analysis	38
2.2.3 Diffuse reflectance spectroscopy.....	39
2.2.4 Solid-state NMR spectroscopy	39
2.2.5 NMR data processing and analysis	41
2.2.6 Quantum chemical computations	41
2.3 Results and discussion.....	42

2.3.1 Crystal structure of $\text{Cu}_2\text{Zn}_{1-x}\text{Cd}_x\text{SnS}_4$	42
2.3.2 Local structure around Sn.....	44
2.3.3 Local structure around Cd	49
2.3.4 Local structure around Cu and Zn.....	53
2.3.5 Comparison of experimental and DFT-computed NMR parameters.....	56
2.3.6 Variation of band gaps and NMR chemical shift behaviour.	59
2.4 Conclusions	62
2.5 References	63
Chapter 3: Mercurial possibilities: determining site distributions in $\text{Cu}_2\text{HgSnS}_4$ using $^{63/65}\text{Cu}$, ^{119}Sn, and ^{199}Hg solid-state NMR spectroscopy	71
3.1 Introduction	71
3.2 Experimental	73
3.2.1 Synthesis.....	73
3.2.2 XRD and energy-dispersive X-ray (EDX) analysis.....	74
3.2.3 Diffuse reflectance spectroscopy.....	74
3.2.4 Solid-state NMR spectroscopy	75
3.2.5 Quantum chemical computations	77
3.3 Results and discussion.....	78
3.3.1 Crystal structure of Cu_2MSnS_4 ($M = \text{Zn}, \text{Cd}, \text{Hg}$).....	78
3.3.2 Local structure around Sn.....	80
3.3.3 Local structure around Cu	82
3.3.4 Local structure around Hg in $\text{Cu}_2\text{HgSnS}_4$	86
3.3.5 Effect of annealing on $\text{Cu}_2\text{HgSnS}_4$	87
3.3.6 Optical band gaps and electronic structure of Cu_2MSnS_4	89

3.4 Conclusions	91
3.5 References	91
Chapter 4: Influence of Ge substitution on the structure and optoelectronic properties of $\text{Cu}_2\text{ZnSn}_{1-x}\text{Ge}_x\text{S}_4$ photovoltaic materials.....	98
4.1 Introduction	98
4.2 Experimental	100
4.2.1 Synthesis	100
4.2.2 X-ray diffraction and energy-dispersive X-ray analysis	101
4.2.3 Diffuse reflectance spectroscopy.....	101
4.2.4 Solid-state nuclear magnetic resonance spectroscopy	102
4.2.5 Definitions of NMR parameters	103
4.2.6 Quantum chemical computations	103
4.3 Results and discussion.....	105
4.3.1 Crystal structure of $\text{Cu}_2\text{ZnSn}_{1-x}\text{Ge}_x\text{S}_4$	105
4.3.2 Local structure around Sn.....	107
4.3.3 Local structure around Ge	109
4.3.4 Local structure around Zn	111
4.3.5 Local structure around Cu	114
4.3.6 Optical band gaps and electronic structure of $\text{Cu}_2\text{ZnSn}_{1-x}\text{Ge}_x\text{S}_4$	117
4.4 Conclusions	119
4.5 References	121
Chapter 5	130
5.1 Summary	130

5.2 Outlook.....	131
5.3 References	132
Bibliography	134
Appendix 1: Supplementary data for Chapter 1	165
Appendix 2: Supplementary data for Chapter 2	166
Appendix 3: Supplementary data for Chapter 3	181
Appendix 4: Supplementary data for Chapter 4	187

List of Tables

Table 1.1. Properties of NMR active nuclei in the quaternary chalcogenides	11
Table 3.1. Experimental conditions for acquisition of NMR spectra.....	76
Table 3.2. Experimental and GIPAW DFT-computed ^{65}Cu , ^{119}Sn , and ^{199}Hg NMR parameters for Cu_2MSnS_4 ($M = \text{Zn, Cd, Hg}$).	80

List of Figures

Figure 1.1. Derivation of $\text{Cu}_2\text{ZnSnS}_4$ from ZnS through aliovalent substitutions.....	6
Figure 1.2. Different structural models for $\text{Cu}_2\text{ZnSnS}_4$	7
Figure 1.3. Energy level diagram for a spin $I = 1/2$ nucleus showing splitting due to Zeeman interaction in an applied magnetic field.....	13
Figure 1.4. Spectral simulations of solid-state ^{119}Sn ($I = 1/2$) NMR powder patterns at 9.4 T ($\nu_L = 149.2$ MHz, $\delta_{\text{iso}} = 0$ ppm, $\Omega = 200$ ppm) with different κ values. Non-spinning spectra were simulated using the WSolids program.	16
Figure 1.5. Nuclear charge distribution for spin $I = 1/2$ (spherical) and $I > 1/2$ (prolate and oblate). The arrow indicates the direction of the magnetic field.	18
Figure 1.6. Energy level diagram showing the effect of the Zeeman, first and second order quadrupolar interactions for an $I = 3/2$ nucleus.	19
Figure 1.7. Simulated solid-state NMR powder pattern of non-spinning ^{65}Cu ($I = 3/2$) at 9.4 T ($\nu_L = 113.6$ MHz, $\delta_{\text{iso}} = 0$ ppm, $\Omega = 0$) with varying C_Q while η is constant ($\eta = 0$) and varying η while C_Q is constant ($C_Q = 5$ MHz). Spectra were simulated using the WSolids program.	21
Figure 1.8. (a) Schematic diagram of a spinning rotor that is aligned at the magic angle (54.735°) relative to B_0 . (b) Simulated solid-state NMR spectra for a ^{119}Sn nucleus at 9.4 T ($\nu_L = 149.2$ MHz, $\delta_{\text{iso}} = 0$ ppm, $\Omega = 200$ ppm, $\kappa = 0$) at various spinning speeds. Spectra were simulated using the WSolids program.....	23
Figure 1.9. Comparison of non-spinning and MAS solid-state NMR spectra for ^{65}Cu ($I = 3/2$) at 9.4 T ($\nu_L = 113.6$ MHz). NMR spectra were simulated with $\delta_{\text{iso}} = 0$ ppm, $C_Q = 5.0$ MHz, $\Omega = 0$. Spectra were simulated using the WSolids program.	24
Figure 2.1. Cation site distributions as Cd substitution (x) increases in $\text{Cu}_2\text{Zn}_{1-x}\text{Cd}_x\text{SnS}_4$. For $x = 0-0.3$, Cd substitutes for Zn in the $2d$ site in the structure in space group $I\bar{4}$; for $x = 0.4-1.0$, Cd substitutes for Zn in the $2a$ site in the structure in space group $I\bar{4}2m$	36

Figure 2.2. (a) Powder XRD patterns for $\text{Cu}_2\text{Zn}_{1-x}\text{Cd}_x\text{SnS}_4$. The shaded region highlights the 220 and 204 peaks, which overlap for the lightly substituted Cd members ($x = 0-0.3$) but is visibly split for the more heavily substituted Cd members ($x = 0.4-1.0$) because the c -axis undergoes an abrupt contraction relative to the a -axis. (b) Plot of tetragonal cell parameters (a and $c/2$) and the ratio of these parameters ($\eta = c/2a$) as a function of Cd content, x	43
Figure 2.3. (a) Local coordination around Sn sites. (b) ^{119}Sn MAS NMR spectra ($B_0 = 9.4$ T) for $\text{Cu}_2\text{Zn}_{1-x}\text{Cd}_x\text{SnS}_4$. (c) Deconvolution into Gaussian-fitted peaks representing Sn sites $L^{(n)}$ with second coordination spheres $[\text{Cu}_8\text{Zn}_{4-n}\text{Cd}_n]$ in $\text{Cu}_2\text{Zn}_{0.8}\text{Cd}_{0.2}\text{SnS}_4$. (d) Dependence of isotropic ^{119}Sn chemical shift with n in $[\text{Cu}_8\text{Zn}_{4-n}\text{Cd}_n]$	45
Figure 2.4. Experimental and simulated non-spinning ^{119}Sn NMR spectra for (a) $\text{Cu}_2\text{ZnSnS}_4$ ($B_0 = 21.1$ T, $\delta_{\text{iso}} = -120.9$ ppm, $\Omega = 32 \pm 5$ ppm, $\kappa = -0.4 \pm 0.1$) and (b) $\text{Cu}_2\text{CdSnS}_4$ ($B_0 = 9.4$ T, $\delta_{\text{iso}} = -81.9$ ppm, $\Omega = 115 \pm 5$ ppm, $\kappa = 0.9 \pm 0.1$).	49
Figure 2.5. (a) Local coordination around Cd sites. (b) ^{113}Cd MAS NMR spectra ($B_0 = 9.4$ T) for $\text{Cu}_2\text{Zn}_{1-x}\text{Cd}_x\text{SnS}_4$ for $x = 0.2-1.0$. (c) ^{113}Cd MAS NMR spectra for $x = 0.3$ and 0.4 , with the two peaks assigned to separate phases adopting $I\bar{4}$ (720 ppm, red) and $I\bar{4}2m$ (680 ppm, blue) structures and their areas are used to determine their relative amounts. (d) ^{113}Cd isotropic chemical shifts, δ_{iso} , plotted as a function of Cd content, x , with linear fits applied to the peaks assigned to $I\bar{4}$ (red) and $I\bar{4}2m$ (blue) structures.	52
Figure 2.6. (a) Local coordination around Cu sites. (b) ^{63}Cu MAS NMR spectra ($B_0 = 21.1$ T) for $\text{Cu}_2\text{Zn}_{1-x}\text{Cd}_x\text{SnS}_4$. (c) ^{67}Zn NMR spectra ($B_0 = 21.1$ T) for $x = 0$ (non-spinning and MAS at 10 kHz) and $x = 0.2$ members (non-spinning).....	54
Figure 2.7. Variation of (a) average ^{119}Sn and (b) ^{113}Cd NMR isotropic chemical shifts with optical band gaps in $\text{Cu}_2\text{Zn}_{1-x}\text{Cd}_x\text{SnS}_4$	62
Figure 3.1. Structural models for $\text{Cu}_2\text{ZnSnS}_4$, $\text{Cu}_2\text{CdSnS}_4$, and $\text{Cu}_2\text{HgSnS}_4$. Two models have been proposed for $\text{Cu}_2\text{HgSnS}_4$ distinguished by the presence of two Cu sites in $I\bar{4}$ vs one site in $I\bar{4}2m$	72

Figure 3.2. Powder XRD patterns for $\text{Cu}_2\text{ZnSnS}_4$, $\text{Cu}_2\text{CdSnS}_4$, and $\text{Cu}_2\text{HgSnS}_4$	79
Figure 3.3. Experimental (black) and spectral simulation (blue) of non-spinning ^{119}Sn NMR spectra and local chemical environments around Sn atoms for $\text{Cu}_2\text{ZnSnS}_4$, $\text{Cu}_2\text{HgSnS}_4$, and $\text{Cu}_2\text{CdSnS}_4$. GIPAW DFT CSA tensors, δ_{11} , δ_{22} and δ_{33} are shown as green arrows (top). The resemblance of ^{119}Sn local chemical environment with $\text{Cu}_2\text{CdSnS}_4$ is indicated with a ✓ (green), whereas the disagreement with $\text{Cu}_2\text{ZnSnS}_4$ is indicated with an X (red). The experimental NMR simulations (blue) were performed using the Dmfit software.	82
Figure 3.4. ^{63}Cu MAS NMR spectra and local environments around Cu atoms for $\text{Cu}_2\text{ZnSnS}_4$ ($\omega_r/2\pi = 62.5$ kHz), $\text{Cu}_2\text{CdSnS}_4$ ($\omega_r/2\pi = 31.25$ kHz), and $\text{Cu}_2\text{HgSnS}_4$ ($\omega_r/2\pi = 62.5$ kHz). Central transitions are enlarged in the insets. Asterisks mark spinning sideband	83
Figure 3.5. Experimental (black) and DFT (blue) predicted (a) ^{63}Cu MAS and (b) ^{65}Cu non-spinning NMR spectra for $\text{Cu}_2\text{HgSnS}_4$. The parameters for the DFT predicted spectra are listed in Table 3.2.	84
Figure 3.6. Experimental (black) and spectral simulations (blue) for non-spinning ^{65}Cu NMR spectra at three different magnetic fields for $\text{Cu}_2\text{ZnSnS}_4$, $\text{Cu}_2\text{HgSnS}_4$ and $\text{Cu}_2\text{CdSnS}_4$. GIPAW DFT EFG tensors (V_{xx} , V_{yy} , and V_{zz}) are shown as blue arrows with merged CSA tensors (top). The resemblance of ^{65}Cu chemical environment with $\text{Cu}_2\text{CdSnS}_4$ is indicated with an ✓ (green), whereas the disagreement with $\text{Cu}_2\text{ZnSnS}_4$ is indicated with an X (red). The experimental NMR simulations (blue) were performed using the Dmfit software	85
Figure 3.7. Experimental (black) MAS (a) and non-spinning (b) ^{199}Hg NMR spectra for $\text{Cu}_2\text{HgSnS}_4$. The parameters for the simulated NMR spectrum (blue) are listed in Table 3.2, which were fit using the Dmfit software. The asterisks mark spinning sidebands.....	87
Figure 3.8. Effect of annealing $\text{Cu}_2\text{HgSnS}_4$ monitored by (a) powder XRD, (b) ^{119}Sn MAS NMR, and (c) ^{199}Hg MAS NMR spectroscopy.....	88

- Figure 3.9.** ELF plots and Bader charges for $\text{Cu}_2\text{ZnSnS}_4$, $\text{Cu}_2\text{CdSnS}_4$, and $\text{Cu}_2\text{HgSnS}_4$, projected on slices parallel to the (010) plane centred around $y = \frac{1}{2}$ 90
- Figure 4.1.** Crystal structures of $\text{Cu}_2\text{ZnSnS}_4$, $\text{Cu}_2\text{ZnSn}_{0.6}\text{Ge}_{0.4}\text{S}_4$ and $\text{Cu}_2\text{ZnGeS}_4$. Two structural models were proposed for $\text{Cu}_2\text{ZnGeS}_4$, consisting of two sets of Cu sites in $I\bar{4}$, in contrast to one set of Cu sites in $I\bar{4}2m$ 99
- Figure 4.2.** (a) Powder XRD patterns of $\text{Cu}_2\text{Zn}_{1-x}\text{Ge}_x\text{SnS}_4$, where x varies from 0 to 1. The 220 and 204 peaks overlap for lightly substituted Ge members, but become split for highly substituted Ge members. (b) Evolution of tetragonal unit cell parameters (a and $c/2$) and tetragonal distortion parameter ($c/2a$) with respect to Ge content..... 106
- Figure 4.3.** (a) ^{119}Sn MAS NMR spectra ($B_0 = 7.05$ T) for $\text{Cu}_2\text{Zn}_{1-x}\text{Ge}_x\text{SnS}_4$. (b) Coordination environments around Sn atoms for $\text{Cu}_2\text{ZnSnS}_4$ and $\text{Cu}_2\text{ZnSn}_{0.6}\text{Ge}_{0.4}\text{S}_4$ in space group $I4$. (c) ^{119}Sn and ^{73}Ge isotropic chemical shifts as a function of Ge content (x). (d) Experimental, simulated non-spinning and slow spinning ($\omega_r/2\pi = 3$ kHz) ^{119}Sn spectra for $\text{Cu}_2\text{ZnSnS}_4$ ($B_0 = 11.75$ T, $\delta_{\text{iso}} = -121$ ppm, $\Omega = 32$ ppm and $\kappa = 0.4$). The experimental NMR simulations (blue) were performed using the Dmfit software..... 108
- Figure 4.4.** (a) Local structure around Ge for $\text{Cu}_2\text{ZnSn}_{0.6}\text{Ge}_{0.4}\text{S}_4$ and $\text{Cu}_2\text{ZnGeS}_4$ in $I\bar{4}$ structure model. (b) ^{73}Ge MAS NMR spectra ($B_0 = 21.1$ T) for $\text{Cu}_2\text{Zn}_{1-x}\text{Ge}_x\text{SnS}_4$ 110
- Figure 4.5.** ^{67}Zn MAS NMR spectra ($B_0 = 21.1$ T) for $\text{Cu}_2\text{Zn}_{1-x}\text{Ge}_x\text{SnS}_4$ assigned with L(0) (blue) and L(n) (red). 112
- Figure 4.6.** Experimental (black) and simulated (blue) non-spinning ^{67}Zn spectra for $\text{Cu}_2\text{ZnSnS}_4$ ($\delta_{\text{iso}} = 361$ ppm, $\Omega = 29$ ppm, $\kappa = -0.5$, $C_Q = 0.9$ MHz, $\eta = 0$) and $\text{Cu}_2\text{ZnGeS}_4$ ($\delta_{\text{iso}} = 358$ ppm, $C_Q = 2.8$ MHz, $\eta = 0.2$) at 21.1 T. The experimental NMR simulations (blue) were performed using the Dmfit software. 113
- Figure 4.7.** (a) Local environment around Cu atoms in $\text{Cu}_2\text{ZnGeS}_4$ ($I\bar{4}$). (b) ^{63}Cu MAS (62.5 kHz) NMR spectra ($B_0 = 21.1$ T) for $\text{Cu}_2\text{ZnGeS}_4$ and $\text{Cu}_2\text{ZnSnS}_4$ with two distinct resonances associated with $2a$ and $2c$ sites in $I\bar{4}$ structure. Asterisks indicate spinning sidebands in the MAS NMR spectra. Deconvolution of non-spinning ^{65}Cu

NMR spectra for (c) $\text{Cu}_2\text{ZnGeS}_4$ and (d) $\text{Cu}_2\text{ZnSnS}_4$ at 11.75 T. The experimental NMR simulations (blue) were performed using the Dmfit software.	115
Figure 4.8. (a) ^{65}Cu non-spinning NMR spectra ($B_0 = 21\text{T}$) and (b) enlarged views of low frequency region for $\text{Cu}_2\text{Zn}_{1-x}\text{Ge}_x\text{SnS}_4$. (c) Local structure around Cu1 (2c) and Cu2 (2a) sites for $\text{Cu}_2\text{ZnGeS}_4$ in $I\bar{4}$	117
Figure 4.9. Electron localization function, projected on slices parallel to the (001) plane at $z = 0$ (top) and $1/4$ (bottom), with Bader charges shown for (a) $\text{Cu}_2\text{ZnSnS}_4$, (b) $\text{Cu}_2\text{ZnSn}_{0.5}\text{Ge}_{0.5}\text{S}_4$, and (c) $\text{Cu}_2\text{ZnGeS}_4$	119

List of symbols

a, b, c	Unit cell parameters
\AA	Angstrom
B_0	Applied static magnetic field strength
B_1	Applied oscillating magnetic field strength
$^{\circ}\text{C}$	Degrees Celsius
C_Q	Quadrupolar coupling constant
Ch	Chalcogen
δ	Chemical shift
δ_{iso}	Isotropic chemical shift
δ_{cgs}	Centre-of-gravity chemical shift
E	Energy
E_g	Band gap
η	Quadrupolar anisotropy
h	Planck constant
\hbar	Reduced Planck constant, $h/2\pi$
γ	Gyromagnetic ratio
Hz	Hertz
I	Nuclear spin
∞	Infinity
J	Indirect spin-spin coupling constant
k	Boltzmann constant
κ	Skew of the magnetic shielding tensor

λ	Wavelength
μs	Microsecond
M_0	Magnetization along the z -direction at time $t = 0$
M_z	Magnetization along the z -direction at time t ($t \neq 0$)
$M_{xy}(0)$	Magnetization in the x - y plane at time $t = 0$
$M_{xy}(t)$	Magnetization in the x - y plane at time t
ν	Frequency
ν_L	Larmor frequency
Ω	Span of the magnetic shielding tensor
Q	Quadrupolar moment
θ	Angle
t	Time
τ	Interpulse delay
T_1	Spin-lattice relaxation time constant
T_2	Spin-spin relaxation time constant
T_2^*	Effective spin-spin relaxation time constant
V	Cell volume
σ	Magnetic shielding
σ^d	Diamagnetic shielding
σ^p	Paramagnetic shielding
Tt	Tetrels (group 14 elements)
\mathcal{E}	Frequency ratio

List of abbreviations

CT	Central transition
CBM	Conduction band minima
COBI	Crystal orbital bond index
COHP	Crystal orbital Hamilton population
CSA	Chemical shift anisotropy
CASTEP	Cambridge serial total energy package
CPS	Counts per second
DFT	Density functional theory
DOS	Density of states
EFG	Electric field gradient
EDX	Energy dispersive X-ray spectroscopy
ELF	Electron localization function
et al.	And other (<i>et alia</i>)
kHz	Kilohertz
MHz	Megahertz
FWHM	Full width at half maximum
GGA	Generalized gradient approximation
ICOBI	Integrated crystal orbital bond index
GIPAW	Gauge-including projector augmented wave
MS	Magnetic shielding
MAS	Magic-angle spinning
NIR	Near-infrared spectroscopy

NMR	Nuclear magnetic resonance
PAS	Principal axis system
PAW	Projector augmented wave method
PBE	Perdew–Burke–Ernzerhof
PCE	Photoconversion efficiency
PMCA	Primitive mixed CuAu
ppm	Parts per million
R.F.	Radio frequency
SEM	Scanning electron microscopy
ST	Satellite transition
3QMAS	Triple quantum magic angle spinning
UV-Vis	Ultraviolet-visible
vs	Versus
VASP	Vienna ab initio simulation package
VBM	Valence band maxima
XPS	X-ray photoelectron spectroscopy
XRD	X-ray diffraction
ZORA	Zeroth-order regular approximation

Chapter 1

Introduction: Chalcogenide photovoltaic materials and solid-state NMR spectroscopy

1.1 Quaternary chalcogenides as next-generation photovoltaic materials

Global energy consumption is increasing dramatically because of population growth, rising living standards, and economic progress.^{1,2} Energy production relies heavily on fossil fuels, which will be in short supply in the future^{3,4} and contribute to global warming.⁵ To meet growing energy demand and to minimize pollution, solar cell technology has been touted as a sustainable energy solution.⁶ Approximately 80% of the current photovoltaic market is based on first-generation materials – crystalline Si and polycrystalline-Si wafers with photoconversion efficiency (PCE) exceeding 20%.⁷ This Si-based technology is well established, but other alternatives have been proposed as second-generation materials involving thin films and direct gap semiconductors.⁸ The most popular are hybrid metal halide perovskites, which have been developed through intense investigation by many scientists so that their PCE now exceeds 25%.^{7,9,10} Unfortunately, they have poor resistance to moisture, and the presence of Pb has precluded their widespread application.¹¹ Another important class of alternative materials are chalcogenides such as commercially available copper indium gallium diselenide ($\text{CuIn}_{1-x}\text{Ga}_x\text{Se}_2$) and cadmium telluride (CdTe), which are highly efficient (PCE of >20%) and stable compared to halide perovskites.¹²⁻¹⁴ However, they contain scarce elements (In, Te) and toxic (Cd, Te) elements. In this regard, $\text{Cu}_2\text{ZnSnS}_4$, also known by its mineral name, kesterite, has emerged as an attractive candidate because it shows a lower direct band gap (1.5 eV) as well as higher absorption coefficient (10^4 cm^{-1}), suitable for

highly efficient solar cells.¹⁵⁻¹⁹ Moreover, kesterite consists of earth-abundant elements of low toxicity.

Rapid progress has been made to improve the PCE in $\text{Cu}_2\text{ZnSnS}_4$ -based solar cells. Shin et al. first reported a maximum PCE of 8.4% for a pristine $\text{Cu}_2\text{ZnSnS}_4$ absorbing layer created using a thermal evaporation process. The record efficiency is now held by a $\text{Cu}_2\text{ZnSn}(\text{S},\text{Se})_4$ device whose absorbing active layer was fabricated by a solution-based approach, giving a PCE of 12.6%.²⁰ This is still far behind the theoretically estimated efficiency of about 30%.²¹ The main problem that limits further improvement in the performance has been identified as an open circuit voltage deficit, which has been attributed to intrinsic point defects and associated band tailing, according to experimental and theoretical studies. In a compound consisting of many elements such as $\text{Cu}_2\text{ZnSnS}_4$, there are more possibilities for antisite, interstitial, and vacancy defects. Then, like a Goldberg machine, more complex strategies are needed to improve efficiency. Among these approaches, various cation substitutions have been the most commonly proposed, such as Li or Ag for Cu; other divalent metals for Zn; or Ge for Sn.²²⁻²⁸

1.2 Effect of cation substitution on PCE and optical property in $\text{Cu}_2\text{ZnSnS}_4$

Recent studies have demonstrated that Cd, Hg, and Ge substitution in $\text{Cu}_2\text{ZnSnS}_4$ can enhance the performance of thin-film solar cells. Su et al. showed that substitution with 40% Cd through a sol-gel method increased the PCE from 5% to 9%.²⁹ They attributed the improvement to modification of the conduction band offset at the junction interface, fewer secondary phases (e.g., ZnS), and larger crystallite sizes. However, further increase in Cd concentration led to deterioration of the performance. Although band tailing remains a problem, the V_{OC} deficit is reduced by over 100 mV compared to pristine $\text{Cu}_2\text{ZnSnS}_4$.²⁹ The average grain sizes of

$\text{Cu}_2\text{Zn}_{1-x}\text{Cd}_x\text{SnS}_4$ thin films become larger as Cd substitution increases from 0 to 40%. Further Cd substitution beyond 60% resulted in a phase transition from the kesterite ($I\bar{4}$) to the stannite ($I\bar{4}2m$) structure.

Later, Yan et al. fabricated solar cells from $\text{Cu}_2\text{Zn}_{1-x}\text{Cd}_x\text{SnS}_4$ by sulfurizing chemical bath-deposited CdS on top of co-sputtered Cu/ZnS/SnS precursors, giving an active area efficiency of 11.5%.²⁴ They found that the band tailing, as assessed by the Urbach tail energy (E_{Urbach}), was reduced after Cd substitution. Another strategy for improving PCE is to replace Zn with Hg in $\text{Cu}_2\text{ZnSnS}_4$. Kukreti et al. reported a PCE of 11.6% for $\text{Cu}_2\text{HgSnS}_4$, but a maximum PCE of >17% is possible to achieve through the design and optimization of materials using 1D-solar cell simulation.³⁰ However, no report has been published regarding the effect of partial substitution of Zn with Hg on PCE.

Of course, substitution with Hg negates the very argument to advocate for $\text{Cu}_2\text{ZnSnS}_4$ in the first place. To maintain the requirement of non-toxic materials, an alternative approach is to partially substitute Ge for Sn in $\text{Cu}_2\text{ZnSnS}_4$, or in its selenium analogue $\text{Cu}_2\text{ZnSnSe}_4$. The hypothesis is that tetravalent Ge is more stable against redox processes than tetravalent Sn, which may be susceptible to transform to divalent Sn during device operation.²⁸ That is, Ge substitution in $\text{Cu}_2\text{ZnSnS}_4$ and $\text{Cu}_2\text{ZnSnSe}_4$ crystals may reduce recombination centers associated with multivalent Sn atoms, potentially improving the stability of the absorber material. Indeed, Kim et al. observed substituting Ge in $\text{Cu}_2\text{ZnSnS}_x\text{Se}_{4-x}$, with a ratio of Ge/(Sn + Se) of 0.5, increased PCE from 4.8% to 6.3%.³¹ Hages et al. demonstrated that substituting 30% Ge into $\text{Cu}_2\text{ZnSnS}_4$ solar cells increased the efficiency from 8.4% to 9.4%.³² Similarly, Giraldo et al. observed that a 4.4% nominal substitution of Sn with Ge (using 10 nm thick Ge layer) increased the efficiency from 7 to 10.1%.³³ Additional studies showed that morphology and grain size have a strong influence on

performance. Kim et al. fabricated a $\text{Cu}_2\text{Zn}(\text{Sn}_{0.78}\text{Ge}_{0.22})\text{Se}_4$ thin-film solar cell with a conversion efficiency of 12.3%.³⁴ This cell exhibits a reduced V_{OC} deficit of 0.58 V, which was attributed to the reduced tailing of the band through control of the Ge/(Sn + Se) ratio. The influence of cation substitutions on PCE in $\text{Cu}_2\text{ZnSnS}_4$ is summarized in **Table A1.1**.

Substituting Zn partially or completely with Cd or Hg reduces the band gap of $\text{Cu}_2\text{ZnSnS}_4$, which can vary from 1.5 to 1.1 eV, as determined from optical diffuse reflectance spectra and XPS measurements.^{35–37} For $\text{Cu}_2\text{ZnSnS}_4$, the valence band maximum (VBM) mainly consists of hybridization of Cu 3d and S 3p orbitals, whereas the conduction band minimum (CBM) mainly consists of Sn 5s and S 3p orbitals.^{29,35} As Zn has a negligible contribution to VBM or CBM, the expectation is that replacing Zn with Cd or Hg should not modify the band gap, in contradiction to experimental findings. The reasons for this discrepancy remain elusive. On the other hand, Ge substitution in $\text{Cu}_2\text{ZnSnS}_4$ increased the band gap from 1.5 to 1.9 eV.³⁸

The examples described above are often portrayed in the original reports as exaggerated claims of clever or rational design to improve photovoltaic efficiency, even though cation substitution is a routine and logical approach. The sad truth, as illustrated by the frequent discrepancies between theoretical predictions and experimental results, is that there is only a superficial understanding of the relationship between structure and properties. In particular, both long- and short-range structures of these compounds are surely important. However, a comprehensive study of the effect of Cd, Hg, and Ge substitutions on local environments, band structure, and chemical bonding is lacking. This thesis aspires to gain insight into the relationships among crystal and local chemical structures, band gap, and nature of chemical bonding by making use of X-ray diffraction, solid-state NMR spectroscopy, and electronic structure calculations.^{39–42}

1.3 Structure of $\text{Cu}_2\text{ZnSnS}_4$

$\text{Cu}_2\text{ZnSnS}_4$ belongs to a series of compounds with the general formula $\text{I}_2\text{-II-IV-VI}_4$, within a much larger family, sometimes called tetrahedral structures or diamond-like semiconductors (because of their resemblance to diamond in the sense of being built up from corner-sharing tetrahedra). In 1956, the mineralogist V. N. Soboleva discovered naturally occurring $\text{Cu}_2(\text{Zn,Fe})\text{S}_4$, which she named kesterite after its locale in Eastern Siberia.⁴³ The structure of $\text{Cu}_2\text{ZnSnS}_4$ can be derived from the chalcopyrite structure of CuInS_2 through aliovalent substitution of In with a mixture of Zn and Sn atoms.^{44,45} In turn, both kesterite and chalcopyrite can be derived from cubic ZnS (zincblende or sphalerite) by approximately doubling the unit cell along the c axis and replacing Zn with the corresponding cations (**Figure 1.1**). There are two fundamental cation ordering patterns found among I-III-VI_2 structures that obey the octet rule: chalcopyrite and CuAu-like structures. In a parallel fashion, the quaternary compound $\text{Cu}_2\text{ZnSnS}_4$ is generally recognized as having two possible structures: kesterite (space group $I\bar{4}$) and stannite-type (space group $I\bar{4}2m$), which are derived from chalcopyrite and CuAu-like structures, respectively. It has also been proposed that $\text{Cu}_2\text{ZnSnS}_4$ can theoretically adopt another structure with a primitive lattice derived from the CuAu structure.⁴⁶ However, this structure has never been experimentally observed, and is dismissed from further discussion. It is unfortunate that some of this mineral terminology, which is inherently imprecise, has been propagated in much of the current literature on the materials applications of the related synthetic compounds, with the result that the language used by practitioners has only served to muddle rather than to illuminate. In what follows, precise crystallographic descriptions (space group, site occupations) are provided, sometimes redundantly, so that readers are not confused by mineral names.

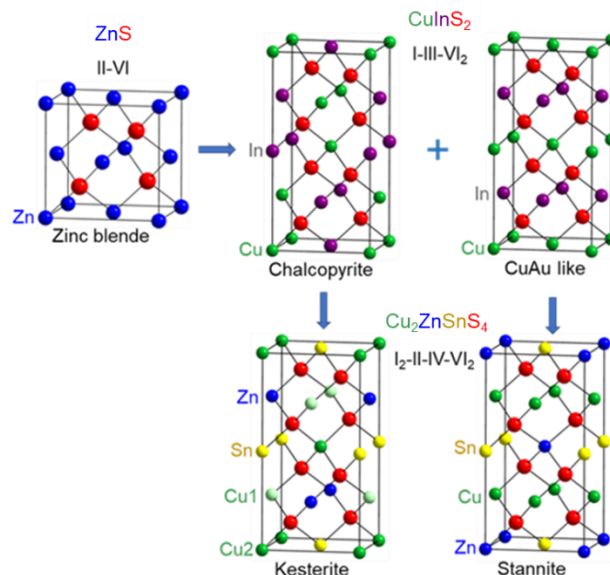


Figure 1.1. Derivation of $\text{Cu}_2\text{ZnSnS}_4$ from ZnS through aliovalent substitutions.

The distinction in the $I\bar{4}$ and $I\bar{4}2m$ structures lies in the arrangement of Cu and Zn cations, which occupy half of the tetrahedral interstices within cubic closed packed arrangements of S anions (**Figure 1.2**).^{47–49} The layers of close-packed S atoms are *not* oriented parallel to the axes of the tetragonal unit cell. One cation arrangement results in planes of Cu–Sn atoms located at $z = 0$ and $\frac{1}{2}$, and planes of Cu–Zn atoms located at $z = \frac{1}{4}$ and $\frac{3}{4}$, corresponding to space group $I\bar{4}$. This structure is often called “kesterite,” even though this mineral name is ambiguous because several possible structures have been assigned to it, as explained above. (Mineral names do not imply a one-to-one correspondence with a unique structure type.) Nevertheless, readers must be cautioned that this terminology pervades through the literature. Another cation arrangement results in planes of Zn–Sn atoms located at $z = 0$ and $\frac{1}{2}$, and planes of exclusively Cu atoms located at $z = \frac{1}{4}$ and $\frac{3}{4}$, corresponding to space group $I\bar{4}2m$. This structure is often called “stannite,” which too can be ambiguous because the name actually refers to the mineral $\text{Cu}_2\text{FeSnS}_4$. (Mineral names convey information about the chemical composition, but not necessarily their structure.). The

major difference is that the Cu atoms occupy two sets of sites ($2a$, $2c$) and lie within all planes in $I\bar{4}$, whereas they occupy one set of sites ($4d$) and lie within alternate planes in $I\bar{4}2m$. The more thermodynamically stable structure of $\text{Cu}_2\text{ZnSnS}_4$ is in the first arrangement in space group $I\bar{4}$, in agreement with most experimental observations.^{50,51} However, the difference in energy is small, and it is conceivable that the alternative structure in $I\bar{4}2m$ could be formed, or perhaps coexist with the $I\bar{4}$ structure, under non-equilibrium conditions.^{48,52} Finally, disorder of Cu and Zn atoms within the $2c$ and $2d$ sites is a very real possibility.^{53,54} This arrangement is then termed “disordered kesterite,” and to help obscure matters even further, it also occurs in space group $I\bar{4}$. The best antidote to the confusion is to be explicit when describing the structure and cation arrangements.

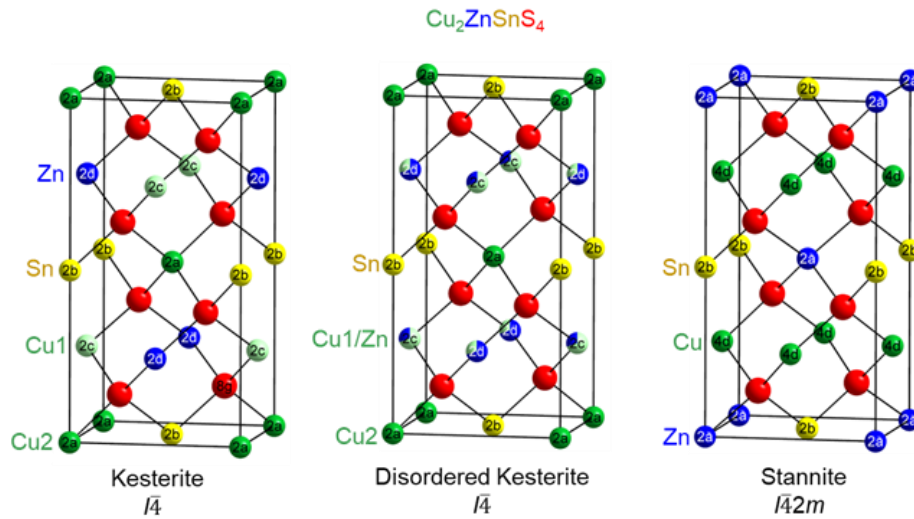


Figure 1.2. Different structural models for $\text{Cu}_2\text{ZnSnS}_4$.

1.4 Problems in structure determination of $\text{Cu}_2\text{ZnSnS}_4$ and related compounds

The lower than expected PCE of $\text{Cu}_2\text{ZnSnS}_4$ has been attributed to the occurrence of disorder of Cu and Zn atoms.^{55,56} Such a disordering is plausible because Cu and Zn have many

chemical similarities (e.g., ionic radii, coordination preferences), and they are difficult to distinguish given their nearly identical electron densities. Thus, antisite defects have often been proposed in which the Cu sites accommodate a small amount of Zn (designated as Cu_{Zn}), or conversely, the Zn sites accommodate a small amount of Cu (designated as Zn_{Cu}). To minimize the possibility of such disorder, in hopes that the PCE can be improved, it is sensible to attempt partial substitution with larger Cd cations instead of Zn. It remains uncertain whether this Cd substitution mitigates the Cu/Zn disorder or whether the disorder actually exists. The direct substitution of Cd within Zn sites has also been challenged, and instead, Hadke et al. have proposed a two-way cation redistribution pathway in which Cu atoms enter the Zn sites and Cd atoms enter the Cu sites in the partially substituted compounds $\text{Cu}_2\text{Zn}_{1-x}\text{Cd}_x\text{SnS}_4$.⁵⁷ Equivalently, the question can be rephrased as follows: Are two (Zn, Cd) or three (Cu, Zn, Cd) atoms involved in the disorder in $\text{Cu}_2\text{Zn}_{1-x}\text{Cd}_x\text{SnS}_4$? These proposals have been supported primarily by powder X-ray diffraction (XRD) measurements and first principles calculations.

X-ray diffraction has long been regarded as the *sine qua non* of structure determination. Alas, even the mighty have shortcomings. It provides information about the average long-range ordering, but not the local environment around atoms. Elements with similar scattering factors, such as Cu and Zn, may be difficult to discern (unless different X-ray wavelengths are chosen to take advantage of anomalous scattering).⁴⁹ Although neutron diffraction can distinguish Cu from Zn and has been applied to study $\text{Cu}_2\text{ZnSnS}_4$, the high neutron absorption cross-section of Cd precludes its use for Cd-substituted compounds.⁵⁷ In the Hg-containing derivative $\text{Cu}_2\text{HgSnS}_4$, the site distribution of cations might be assumed to be analogous to $\text{Cu}_2\text{CdSnS}_4$, but there have been conflicting reports. From powder XRD, Kabalov et al. suggested that the Cu atoms occupy two sets of sites ($2c$, $2d$).⁵⁸ From single-crystal XRD data, Kaplunnik et al. reported that the Cu atoms

half-occupy one set of split sites in $8h$ ($0, \frac{1}{2}, 0.2498$).⁵⁹ This splitting is so small that merging them into fully occupied unsplit sites ($4d$ at $0, \frac{1}{2}, \frac{1}{4}$) is arguably a better description, corresponding to the same structure as $\text{Cu}_2\text{CdSnS}_4$. The major difference is that in the Kabalov model, the Cu-S distances are divided into two sets (2.23 and 2.42 Å), whereas in the Kaplunnik model, they are divided into one set (2.26 Å).

The Ge-containing derivative $\text{Cu}_2\text{ZnGeS}_4$ suffers from similar ambiguities. Moodie et al. determined its structure using convergent-beam electron diffraction and lattice imaging.⁶⁰ Later, Parasyuk et al. performed a Rietveld refinement for $\text{Cu}_2\text{ZnGeS}_4$. Several publications have assumed a structural model without experimental verification.^{61–64} There are occasional reports in the literature that propagate a misunderstanding that the space group, $I\bar{4}$ vs $I\bar{4}2m$, and the detailed distribution of cations can be inferred by inspecting the degree of tetragonal distortion, as gauged by the ratio $c/2a$, from the observation of peak splitting in powder XRD patterns. For example, Khadka et al. proposed that $\text{Cu}_2\text{ZnGeS}_4$ adopts an $I\bar{4}$ structure based on this type of misguided argument.³⁸ To be sure, determining the detailed structure of a multicomponent compound such as $\text{Cu}_2\text{ZnSn}_{1-x}\text{Ge}_x\text{S}_4$, which might be susceptible to many types of cation disorder, is extremely challenging by XRD methods alone.⁶⁵ To resolve the structural ambiguities imparted by these complex cation substitutions, an experimental method is needed that can inform about the local environments around atoms.

1.5 Solid-state NMR spectroscopy

The nuclear magnetic resonance (NMR) phenomenon was first observed by Isidor I. Rabi and coworkers by applying a radio frequency field in a molecular beam of LiCl in 1937.⁶⁶ In 1945,

Felix Bloch utilized the NMR technique on solid paraffin.^{67,68} In the same year, independently, Edward Mills Purcell carried out NMR experiments on a liquid water sample.

Solid-state NMR spectroscopy provides complementary information to diffraction methods and has been used to analyze structure and dynamics of solids.⁶⁹ It has been applied to diverse materials, including porous structures, nanomaterials, organometallic compounds, and disordered solids (glasses, amorphous solids, biological samples).⁷⁰⁻⁷⁴ It reveals information about chemical environments, ion dynamics, particle sizes, crystallinity, phase segregation, kinetics, and cation distributions.⁷⁵⁻⁷⁷ In particular, it has been used to investigate cation and anion distributions in $\text{Cu}_2\text{ZnSnS}_4$, $(\text{Cu}_{1-x}\text{Li}_x)_2\text{ZnSnS}_4$, $\text{Cu}_2\text{ZnSn}(\text{S}_{1-x}\text{Se}_x)_4$, $\text{Cu}_2\text{ZnSn}_{1-x}\text{Si}_x\text{S}_4$, and $\text{Cu}_2\text{ZnGeS}_4$. Given this precedent, it is reasonable that solid state NMR spectroscopy can be similarly successful to tackle the problems discussed above in $\text{Cu}_2\text{Zn}_{1-x}\text{M}_x\text{S}_4$ ($M = \text{Zn}, \text{Cd}, \text{Hg}$) and $\text{Cu}_2\text{ZnSn}_{1-x}\text{Ge}_x\text{S}_4$.⁷⁷⁻

81

A detailed discussion of NMR theory is beyond the scope of this thesis; however, a brief overview of some relevant fundamental NMR concepts and terms is presented below.⁸²⁻⁸⁴ Properties of all NMR active nuclei for the quaternary chalcogenides studied here are given in **Table 1.1**.⁸⁵

A general Hamiltonian describing the NMR interaction is given by:

$$\hat{H}_{\text{total}} = \hat{H}_Z + \hat{H}_{\text{MS}} + \hat{H}_{\text{DD}} + \hat{H}_J + \hat{H}_Q \quad (1.1)$$

where \hat{H}_Z describes the Zeeman interaction, \hat{H}_{MS} is the magnetic shielding term, \hat{H}_{DD} is the direct dipolar interaction, \hat{H}_J is the indirect spin-spin interactions, and \hat{H}_Q represents the quadrupolar interaction.⁸⁶ The magnitude of these interactions varies from <1 Hz to 10^9 Hz. Spin interactions are classified as external interactions, which refer to the interaction of nuclear spins with external

magnetic fields (static magnetic field, B_0 and oscillating magnetic field, B_1), or internal interactions, which refer to the interactions among spins.

Table 1.1. Properties of NMR active nuclei in the quaternary chalcogenides

Isotopes	Nuclear spin (I)	Natural abundance (%)	Frequency ratio Ξ (%)	Quadrupole moment (fm^2)
^{33}S	3/2	0.76	7.7	-6.78
^{63}Cu	3/2	69.2	26.5	-22.0
^{65}Cu	3/2	30.8	28.4	-20.4
^{67}Zn	5/2	4.1	6.2	15.0
^{73}Ge	9/2	7.7	3.5	-19.6
^{113}Cd	1/2	12.2	22.2	-
^{119}Sn	1/2	8.6	37.3	-
^{199}Hg	1/2	16.9	17.9	-

The Zeeman interaction is referred to as an external interaction, and other interactions mentioned above are internal interactions. Because the internal interactions are influenced by the structure of the compounds or molecules, they provide structural information. For simulation and explanation of NMR phenomena, the high-field approximation is generally used, which assumes that Zeeman interactions are much larger than all external and internal interactions; thus, this internal interaction can be considered as perturbations on the Zeeman Hamiltonian.

1.5.1 The Zeeman interaction

The Zeeman interaction is the interaction between a magnetic moment and an applied magnetic field. In the absence of a magnetic field, nuclei have the same energy (i.e., they are degenerate), on average. In the presence of a magnetic field, the nuclear spin energies become non-degenerate (**Figure 1.3**). For a nucleus with spin I , the energies split into $(2I + 1)$ states, evenly spaced. Each energy level is related to a magnetic nuclear spin quantum number, m_I , where $m_I = +I, +I-1, +I-2, \dots, -I$.^{87,88} With an externally applied magnetic field B_0 , the Zeeman Hamiltonian can be written as:⁸⁹

$$\hat{H}_z = -\gamma\hbar B_0 \hat{I}_z \quad (1.2)$$

where γ is the gyromagnetic ratio, \hbar is the reduced Planck's constant, and \hat{I}_z is the z -component of the spin angular momentum operator of the nucleus. The external magnetic field is considered to be applied along $+z$ direction in the laboratory frame. The energy eigenvalue can be derived from the Zeeman Hamiltonian as:

$$E = -m\gamma\hbar B_0 \quad (1.2)$$

The difference between these energy levels depends on the applied magnetic field strength, which can be expressed for $I = 1/2$ as:

$$\Delta E = E_{-\frac{1}{2}} - E_{+\frac{1}{2}} = \gamma\hbar B_0 = h\nu_L \quad (1.3)$$

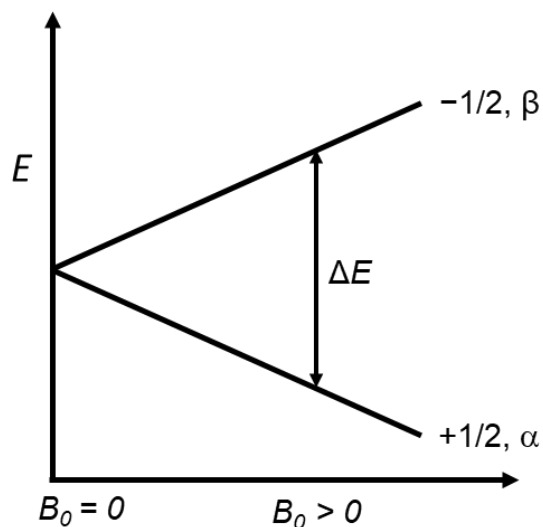


Figure 1.3. Energy level diagram for a spin $I = 1/2$ nucleus showing splitting due to Zeeman interaction in an applied magnetic field.

The Larmor frequency refers to the rate at which the magnetic moment precesses about the external magnetic field and is described by:

$$\nu_L = \frac{\gamma B_0}{2\pi} \quad (1.4)$$

The Larmor frequency, which reflects the Zeeman splitting in the applied magnetic field, is unique to each NMR-active isotope and increases with increasing magnetic field. The Larmor frequency typically falls into the radiofrequency region, i.e., on the order of MHz.

The ratio of populations in different energy states is determined by the Boltzmann distribution at thermal equilibrium, according to:⁸⁸

$$\frac{n_\beta}{n_\alpha} = e^{-\frac{\Delta E}{kT}} = e^{-\frac{\gamma \hbar B_0}{kT}} \quad (1.5)$$

where n_α and n_β are the populations of the lower and upper energy spin states. This ratio becomes greater as the energy difference between nuclear spin states becomes larger and as the temperature decreases. Thus, the signal can be enhanced by controlling the temperature and magnetic field

strength. Compared to other spectroscopic methods such as UV-visible and vibrational spectroscopy, the differences in population between spin states are small, so that NMR spectroscopy is not particularly sensitive. Nevertheless, the structural information obtained from NMR data is valuable, making it worthwhile to expend the effort to get good data.

1.5.2 Magnetic shielding and chemical shift

The magnetic field experienced by the nucleus of an atom depends on the local electronic environment, which generates a secondary field that adds to the overall magnetic field that is felt there, causing the resonance frequency of the nucleus to be altered. The magnetic shielding Hamiltonian can be described by equation 1.7, where σ is the second rank shielding tensor.⁹⁰

$$\hat{H}_{MS} = \gamma \hbar \sigma B_0 \hat{I}_z \quad (1.6)$$

This magnetic shielding (MS) tensor can be diagonalized to yield a tensor with three principal components in its principal axis system (PAS). The tensor components are ordered such that σ_{11} is the least shielded, and σ_{33} is the most shielded, i.e., $\sigma_{11} \leq \sigma_{22} \leq \sigma_{33}$.

$$\sigma = \begin{bmatrix} \sigma_{xx} & \sigma_{xy} & \sigma_{xz} \\ \sigma_{yx} & \sigma_{yy} & \sigma_{yz} \\ \sigma_{zx} & \sigma_{zy} & \sigma_{zz} \end{bmatrix} \xrightarrow{\text{diagonalization}} \sigma^{PAS} = \begin{bmatrix} \sigma_{11} & 0 & 0 \\ 0 & \sigma_{22} & 0 \\ 0 & 0 & \sigma_{33} \end{bmatrix} \quad (1.7)$$

The MS tensor is non-symmetric and non-traceless (i.e., the sum of the diagonal components is non-zero). Equation 1.6 shows that magnetic shielding anisotropy (chemical shift anisotropy, CSA) is proportional to the external magnetic field; hence, higher fields cause broadening due to CSA. The magnetic shielding is with respect to a bare nucleus and is difficult to measure experimentally. For this reason, chemical shift values are often cited instead of shielding values. The chemical shift term can then be calculated using the resonance frequencies of the sample (ν_{sample}) and a reference standard (ν_{ref}).

$$\delta_{\text{iso}} = \frac{\nu_{\text{sample}} - \nu_{\text{ref}}}{\nu_{\text{ref}}} \quad (1.8)$$

$$\delta_{\text{sample}} = \frac{\sigma_{\text{ref}} - \sigma_{\text{sample}}}{1 - \sigma_{\text{ref}}} \approx \sigma_{\text{ref}} - \sigma_{\text{sample}} \quad (1.9)$$

Chemical shifts are typically expressed in parts per million (ppm), which are independent of the frequency of the spectrometer.

For a solution sample, sharp resonances are usually observed because the rapid tumbling of molecules averages out the anisotropic effects of the MS tensor. In contrast, for a solid powdered sample, crystallites are randomly oriented within a magnetic field, each orientation having a difference resonance frequency and giving rise to a “powder pattern” in the non-spinning NMR experiment (**Figure 1.4**). The principal components of the shielding tensor, which vary in symmetry and structure, determine the shape of the CSA powder patterns. CSA interactions are reported in this thesis according to the Herzfeld-Berger convention.⁹¹ The notation is given below, where principal components are ordered such that $\delta_{11} \geq \delta_{22} \geq \delta_{33}$.

$$\delta_{\text{iso}} = \frac{\sigma_{11} + \sigma_{22} + \sigma_{33}}{3} = \frac{\delta_{11} + \delta_{22} + \delta_{33}}{3} \quad (1.10)$$

$$\Omega = \sigma_{33} - \sigma_{11} = \delta_{11} - \delta_{33} \quad (1.11)$$

$$\kappa = \frac{3(\sigma_{\text{iso}} - \sigma_{22})}{\Omega} = \frac{3(\delta_{22} - \delta_{\text{iso}})}{\Omega} \quad (1.12)$$

The isotropic chemical shift δ_{iso} represents the average chemical shift, the span Ω represents the breadth of the powder pattern, and the skew κ is a dimensionless value which describes the shape

of the powder pattern. In the case of axially symmetric tensors, $\delta_{11} = \delta_{22}$ ($\kappa = +1$) or $\delta_{22} = \delta_{33}$ ($\kappa = -1$).

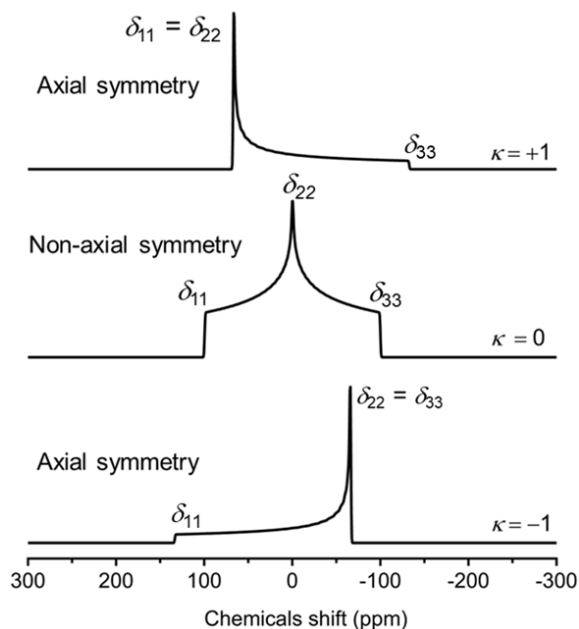


Figure 1.4. Spectral simulations of solid-state ^{119}Sn ($I = 1/2$) NMR powder patterns at 9.4 T ($\nu_L = 149.2$ MHz, $\delta_{\text{iso}} = 0$ ppm, $\Omega = 200$ ppm) with different κ values. Non-spinning spectra were simulated using the WSolids program.⁹²

According to Ramsey, magnetic shielding is the sum of diamagnetic, paramagnetic and spin orbit contributions ($\sigma_{\text{total}} = \sigma^d + \sigma^p + \sigma^{so}$).⁹³ The diamagnetic shielding part arises from the circulation of electrons near the nucleus, which generates a local magnetic field antiparallel to the external magnetic field. Paramagnetic deshielding arises from magnetic field induced mixing of the ground state and excited energy states having the proper symmetry, which typically results in a local magnetic field parallel to the applied magnetic field, thereby deshielding the nucleus.⁹⁴ The deshielding depends approximately inversely to the average excitation energy values. Hence, the smaller excitation energy leads to a larger deshielding with respect to the bare nucleus. The spin orbit term can further influence the magnetic shielding, especially for heavier metals such as

Pb and Hg. Unfortunately, the theoretical method applied in this thesis cannot account for spin orbit contributions.

1.5.3 Direct dipolar and indirect spin-spin coupling

The internal direct dipolar coupling is an interaction between the magnetic moments of the two nuclei, I and S , through space.⁹⁵ For dipolar coupling, atoms containing I and S nuclei do not need to be bonded; they just need to be within proximity. The dipolar interaction increases proportionally to the gyromagnetic ratios of the nuclei involved and is inversely proportional to the cube of the internuclear distance; however, it is independent of magnetic field strength. Therefore, if the natural abundance and gyromagnetic ratio of one of the nuclei of interest are very low (e.g., coupling with ^{33}S), NMR spectra are expected to be dominated by other interactions.

The indirect spin-spin interaction, better known as J -coupling, is the interaction between two magnetic dipole moments, I and S , mediated by the electrons in molecular orbitals that are involved in chemical bonding, as occurs in covalent or hydrogen bonding.⁹⁶ This effect dominates in liquid-state NMR, for example. In solids, J -coupling is typically overpowered by CSA and quadrupolar interactions for $I > 1/2$. The detailed discussion of dipolar and J -coupling is beyond the scope of this thesis.

1.5.4 Quadrupolar interaction

The majority of nuclei (>70%) potentially observable in NMR experiments have a nuclear spin of $I > 1/2$ and are referred to as quadrupolar nuclei.^{89,97} They have both a magnetic dipole moment and a nuclear electric quadrupole moment (eQ , where e is the elementary charge and Q is the quadrupolar moment), which results from a non-spherical charge distribution at the nucleus.

The value of eQ is constant for a given nuclear species and does not change with the chemical environment of the nucleus.⁹⁸

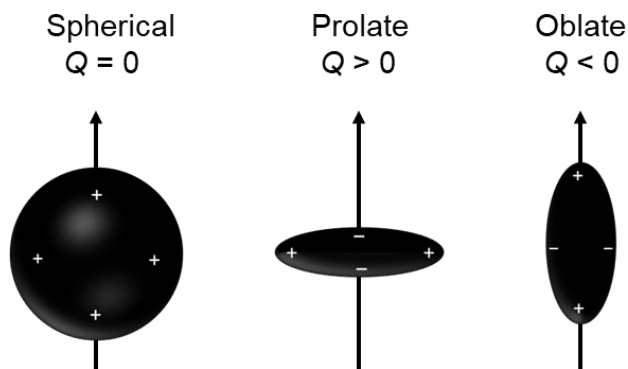


Figure 1.5. Nuclear charge distribution for spin $I = 1/2$ (spherical) and $I > 1/2$ (prolate and oblate). The arrow indicates the direction of the magnetic field.

The charge distribution can be prolate or oblate in shape, corresponding to positive or negative quadrupole moments, respectively (**Figure 1.5**). Any electric field gradients (EFG) produced by surrounding electrons will interact with the quadrupole moment. This non-magnetic interaction is known as quadrupole coupling, and its strength is determined by the magnitude of the EFG as well as the size of the quadrupole moment.

Under the high-field approximation, which assumes that the internal NMR interactions are negligible compared to the Zeeman interaction, the impact of the quadrupole coupling interaction can be described by the first two terms of the quadrupolar Hamiltonian, i.e. $H_Q = H_Q^1 + H_Q^2$, where H_Q^1 and H_Q^2 are the first and second order quadrupolar Hamiltonians, respectively.⁹⁷

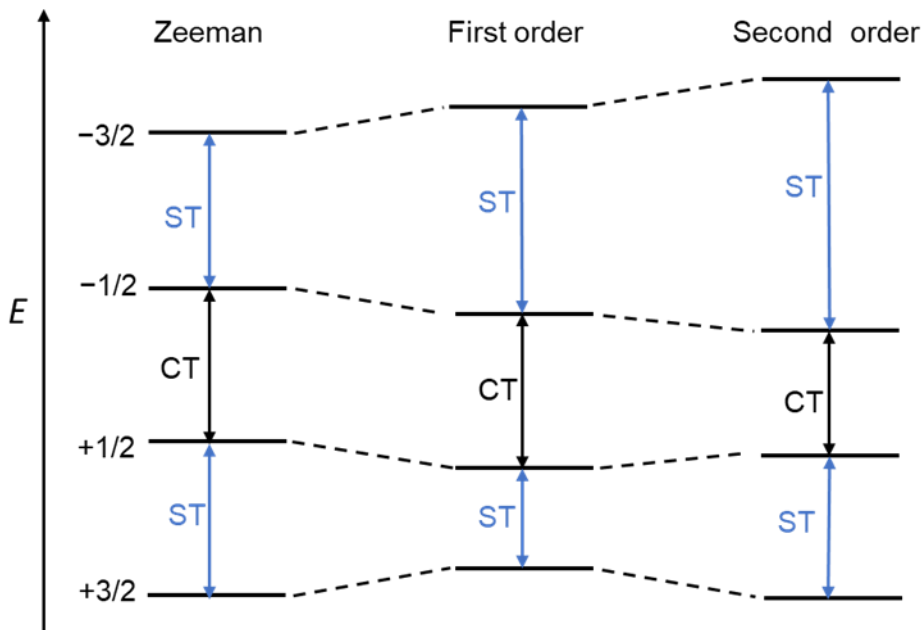


Figure 1.6. Energy level diagram showing the effect of the Zeeman, first and second order quadrupolar interactions for an $I = 3/2$ nucleus.

Using H_Q^1 , one can derive the first order perturbation to the frequency (ν_Q^1) for a transition between nuclear spin states ($m - 1$) and m expressed as:⁹⁹

$$\nu_Q^1 = \frac{\nu_Q}{4} (1 - 2m)(3 \cos^2 \theta - 1 + \eta \sin^2 \theta \cos 2\varphi) \quad (1.13)$$

where θ and φ are the polar angles relating the principal axes of the EFG tensor with respect to the direction of the applied magnetic field.

For a nucleus with $I = 3/2$, a total of $2I + 1 = 4$ energy levels and three transitions (single quantum) — a central transition (CT, $m_1 = +1/2 \leftrightarrow m_1 = -1/2$) and two satellite transitions (ST, $-1/2 \leftrightarrow -3/2$ and $1/2 \leftrightarrow 3/2$) are possible (**Figure 1.6**). From Equation 1.13, it is evident that CT is not affected by the first order quadrupolar term (H_Q^1), but the ST is perturbed.¹⁰⁰ Consequently, the satellite transitions are broadened substantially, often making them difficult to observe. In most cases, the quadrupolar interaction can be very large; a second order perturbation theory must be

used to accurately describe the observed spectrum, because a first order approximation is insufficient. The effect of H_Q^2 on CT for quadrupolar nuclei is much more complicated than H_Q^1 . It affects all energy levels and results in broadening and shift of the CT. The second order quadrupolar perturbation is inversely proportional to the Larmor frequency. Hence, with increasing magnetic field strength, the breadth of the CT decreases (assuming CSA is absent or very small). The Hamiltonian describing the quadrupolar interaction can be written as:⁹⁹

$$\hat{H}_Q = \frac{eQ}{2I(2I-1)\hbar} \hat{V} \hat{I}^2 \quad (1.14)$$

Similar to magnetic shielding interaction, V is a second rank symmetrical EFG tensor used to describe the quadrupolar interaction.

$$V^{PAS} = \begin{bmatrix} V_{xx} & 0 & 0 \\ 0 & V_{yy} & 0 \\ 0 & 0 & V_{zz} \end{bmatrix} \quad (1.15)$$

V can be diagonalized to determine the principal components of the tensors in its own PAS. The tensor components are defined such that $|V_{xx}| \leq |V_{yy}| \leq |V_{zz}|$ and is traceless such that $V_{xx} + V_{yy} + V_{zz} = 0$. The quadrupolar interaction is typically described by the nuclear quadrupolar coupling constant (C_Q) and asymmetry parameter (η), which are given in Equations 1.16 and 1.17, respectively.

$$C_Q = \frac{eQV_{zz}}{h} \quad (1.16)$$

$$\eta = \frac{V_{xx} - V_{yy}}{V_{zz}} \quad (1.17)$$

C_Q describes the magnitude of the quadrupolar interaction, and η describes the asymmetry of the quadrupolar interaction.

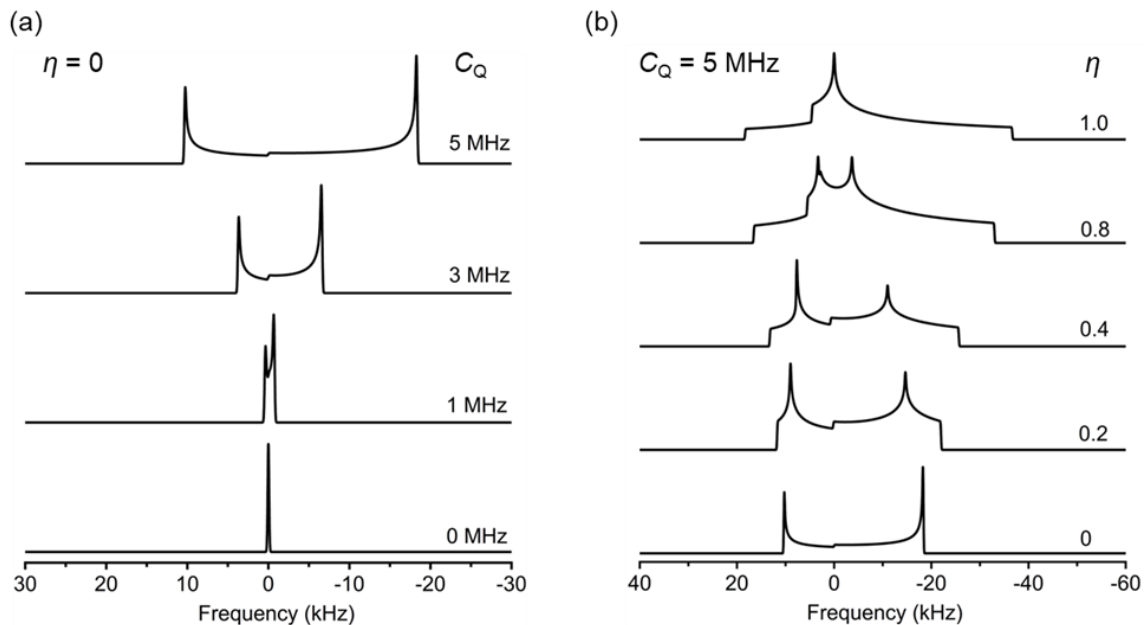


Figure 1.7. Simulated solid-state NMR powder pattern of non-spinning ^{65}Cu ($I = 3/2$) at 9.4 T ($\nu_L = 113.6$ MHz, $\delta_{\text{iso}} = 0$ ppm, $\Omega = 0$) with varying C_Q while η is constant ($\eta = 0$) and varying η while C_Q is constant ($C_Q = 5$ MHz). Spectra were simulated using the WSolids program.⁹²

All EFG tensor orientations are present in a powdered sample,¹⁰¹ similar to the case of MS tensors, which results in characteristic powder patterns as shown in **Figure 1.7**. Based on the shapes of these patterns, the EFG parameters C_Q and η can be determined. A nucleus can have a C_Q of zero if it resides in a highly symmetric environment, such as an ideal tetrahedral or octahedral environment or in highly dynamic environment. The asymmetry parameters η ($0 \leq \eta \leq 1$) define the shape of the quadrupolar powder pattern. If a nucleus has axially symmetric EFG tensors ($V_{xx} = V_{yy}$), η will be 0.

1.5.5 Magic-angle spinning

Fast molecular tumbling in solution results in an average of chemical shielding, dipolar interactions, and attenuates the first order quadrupolar interactions, leading to the observation of

sharp resonances for isotropic chemical shifts. However, molecules are not reoriented isotropically in solids. Solid-state NMR spectra are typically collected on powdered samples, which contain numerous crystallites oriented in all possible orientations with respect to the external magnetic field, resulting in broad powder patterns whose line shapes are determined by the anisotropic interactions – CSA, dipolar interactions, and quadrupolar interactions. The magic angle spinning (MAS) technique, which was developed independently by Andrew et al. and Lowe, is used to narrow the broad powder patterns.^{102,103} The sample is spun rapidly at frequencies in the kHz range, with its rotation axis aligned at 54.735° , with respect to the external magnetic field (**Figure 1.8a**). The spatial orientational dependence of a number of NMR interactions contains the common anisotropy term $(3 \cos^2 \theta - 1)$, where θ is the angle between the internuclear vector and the external magnetic field, B_0 . When $\theta = 54.735^\circ$, the term $(3 \cos^2 \theta - 1)$ vanishes; therefore, if a solid sample is spun at “infinite” speed, the spatial dependencies can average out to 0, and the isotropic peak will remain. As it is impossible to spin infinitely fast, in most cases, MAS can attenuate these anisotropic interactions but cannot eliminate them completely. However, if the spinning rate of the sample is greater than the magnitude of the anisotropic interaction, it is possible to average out the anisotropic interactions completely for nuclei with $I = 1/2$. At slower spinning speeds, lines known as spinning sidebands are produced in addition to the isotropic resonance peak (**Figure 1.8b**). These spinning sidebands have intensities that are determined by the CSA (if CSA dominates), and they are separated from the isotropic peak by integer multiples of the spinning speed, as shown in **Figure 1.8b** for 12 kHz spinning.

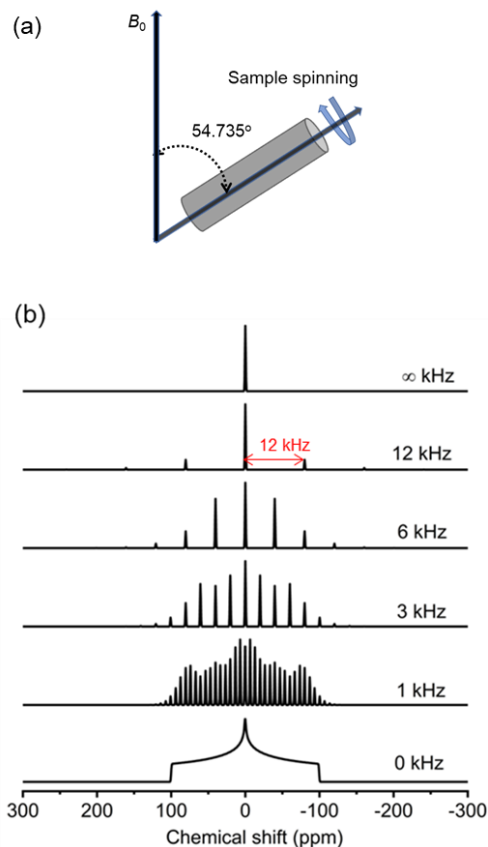


Figure 1.8. (a) Schematic diagram of a spinning rotor that is aligned at the magic angle (54.735°) relative to B_0 . (b) Simulated solid-state NMR spectra for a ^{119}Sn nucleus at 9.4 T ($\nu_L = 149.2$ MHz, $\delta_{iso} = 0$ ppm, $\Omega = 200$ ppm, $\kappa = 0$) at various spinning speeds. Spectra were simulated using the WSolids program.⁹²

The MAS technique cannot completely average out the second order quadrupolar anisotropic interaction because of its complex angular dependence. The second order quadrupolar interaction contains Legendre polynomial terms of second ($3 \cos^2 \theta - 1$) and fourth order ($35 \cos^4 \theta - 30 \cos^2 \theta + 3$).¹⁰⁴ Under MAS conditions, the second rank Legendre polynomial becomes zero, whereas the fourth rank is averaged only partially (**Figure 1.9**). Therefore, it is impossible to completely average out second order quadrupolar anisotropy through spinning at any one angle. Although MAS is not completely effective in removing second order quadrupolar broadening, it can reduce the breadth of an NMR powder pattern by approximately 60–70%.

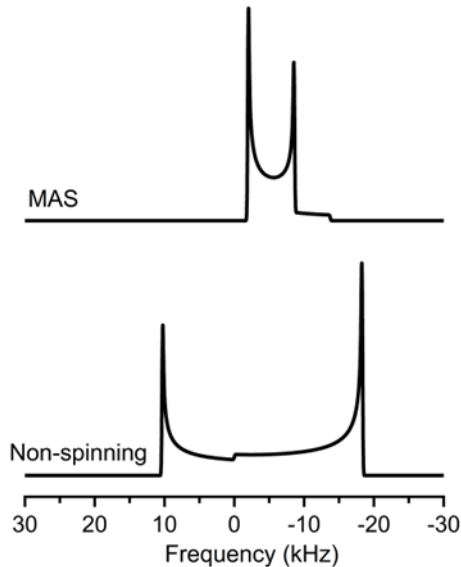


Figure 1.9. Comparison of non-spinning and MAS solid-state NMR spectra for ^{65}Cu ($I = 3/2$) at 9.4 T ($\nu_L = 113.6$ MHz). NMR spectra were simulated with $\delta_{\text{iso}} = 0$ ppm, $C_Q = 5.0$ MHz, $\Omega = 0$. Spectra were simulated using the WSolids program.⁹²

1.5.6 Nuclear relaxation processes

NMR relaxation processes can be classified into two types: longitudinal (or spin-lattice) and transverse (or spin-spin).^{105,106} A sample placed in a magnetic field will undergo changes in the nuclear spin orientation until an excess of the lower energy n_α nuclear spin state is populated. After the perturbation with the radio frequency pulse, the longitudinal relaxation time, as defined by the T_1 relaxation time constant, restores the bulk magnetization, M_z , to thermal equilibrium ($M = M_0$) along the applied field direction, i.e., z direction. In this process, the nucleus exchanges heat with the lattice. T_1 can be measured using a spin-lattice relaxation experiments such as inversion or saturation recovery and can be expressed by Equation 1.18.

$$M_z = M_0 \left(1 - e^{-\frac{t}{T_1}} \right) \quad (1.18)$$

During transverse relaxation, phase coherence or randomization of spins in the transverse direction (x - y) is lost, resulting in the loss of transverse magnetization. The free-induction decay rate is determined by spin-spin relaxation (T_2) can be expressed as:

$$M_{xy} = M_{xy(0)} e^{\frac{-t}{T_2}} \quad (1.19)$$

$M_{xy(0)}$ and M_{xy} represent the net magnetization in the x - y plane at times $t = 0$ and any other time ($t \neq 0$), respectively. In this process, energy is transferred to neighbouring nuclei. Resonances are typically heterogeneously broadened, i.e., the linewidth is determined by the distribution of local environments and associated minor variations in the interactions as described above. Also, inhomogeneous broadening can be caused by magnetic field inhomogeneities in the sample. When the linewidth is inhomogeneously broadened, the T_2 constant, is referred to as effective T_2 or T_2^* . The value of T_2^* is always equal to or shorter than T_2 .

To obtain quantitative results for NMR spectra, spectroscopists typically set the relaxation delay to $5T_1$. Note that T_1 and T_2 relaxations occur simultaneously and are caused by the fluctuating local magnetic field. These relaxation measurements can further aid in analyzing NMR data as well as provide insights into ion dynamics.

1.6 References

- (1) Annual energy outlook (2022) – U.S. energy information administration (EIA). https://www.eia.gov/outlooks/aeo/pdf/AEO2022_ReleasePresentation.pdf
- (2) Key world energy statistics 2021 – analysis. IEA. <https://www.iea.org/reports/key-world-energy-statistics-2021>.
- (3) World energy council. (2013). World energy resources 2013 survey. https://www.worldenergy.org/wp_content/uploads/2013/09/Complete_WER_2013_Survey.pdf
- (4) Muratoglu, A.; Yuce, M. World energy outlook and place of renewable resources. *Int. J. Sci. Technol. Res.* **2015**, *1*, 10–17.
- (5) IEA, World CO₂ emissions from fuel combustion by fuel, 1971-2019, IEA, Paris <https://www.iea.org/data-and-statistics/charts/world-co2-emissions-from-fuel-combustion-by-fuel-1971-2019>.
- (6) Nayak, P. K.; Mahesh, S.; Snaith, H. J.; Cahen, D. Photovoltaic solar cell technologies: analysing the state of the art. *Nat. Rev. Mater.* **2019**, *4*, 269–285.
- (7) Green, M.; Dunlop, E.; Hohl-Ebinger, J.; Yoshita, M.; Kopidakis, N.; Hao, X. Solar cell efficiency tables (version 57). *Prog. Photovolt. Res. Appl.* **2021**, *29*, 3–15.
- (8) Saha, S. A status review on Cu₂ZnSn(S,Se)₄-based thin-film solar cells. *Int. J. Photoenergy*, 2020, *2020*, 1–13.
- (9) Liu, M.; Johnston, M. B.; Snaith, H. J. Efficient planar heterojunction perovskite solar cells by vapour deposition. *Nature* **2013**, *501*, 395–398.
- (10) Kojima, A.; Teshima, K.; Shirai, Y.; Miyasaka, T. Organometal halide perovskites as visible-light sensitizers for photovoltaic cells. *J. Am. Chem. Soc.* **2009**, *131*, 6050–6051.
- (11) Xiang, W.; Liu, S; Tress, W. A review on the stability of inorganic metal halide perovskites: challenges and opportunities for stable solar cells. *Energy Environ. Sci.* **2021**, *14*, 2090–2113.
- (12) Britt, J.; Ferekides, C. Thin-film CdS/CdTe solar-cell with 15.8-percent efficiency. *Appl. Phys. Lett.* **1993**, *62*, 2851–2852

- (13) Jackson, P.; Hariskos, D.; Wuerz, R.; Kiowski, O.; Bauer, A.; Friedlmeier, T. M.; Powalla, M. Properties of Cu(In,Ga)Se₂ solar cells with new record efficiencies up to 21.7%. *Phys. Status Solidi RRL* **2015**, *9*, 28–31.
- (14) Geisthardt, R. M.; Topič, M.; Sites, J. R. Status and potential of CdTe solar-cell efficiency. *IEEE J. Photovolt.* **2015**, *5*, 1217–1221.
- (15) Siebentritt, S.; Schorr, S. Kesterites – a challenging material for solar cells. *Prog. Photovolt. Res. Appl.* **2012**, *20*, 512–519.
- (16) Sun, K.; Yan, C.; Liu, F.; Huang, J.; Zhou, F.; Stride, J. A.; Green, M.; Hao, X. Over 9% efficient kesterite Cu₂ZnSnS₄ solar cell fabricated by using Zn_{1-x}Cd_xS buffer layer. *Adv. Energy Mater.* **2016**, *6*, 1600046.
- (17) Pal, K.; Singh, P.; Bhaduri, A.; Thapa, K. B. Current challenges and future prospects for a highly efficient (>20%) kesterite CZTS solar cell: a review. *Sol. Energy Mater. Sol. Cells* **2019**, *196*, 138–156.
- (18) Shin, B.; Gunawan, O.; Zhu, Y.; Bojarczuk, N. A.; Chey, S. J.; Guha, S. Thin film solar cell with 8.4% power conversion efficiency using an earth-abundant Cu₂ZnSnS₄ absorber. *Prog. Photovolt. Res. Appl.* **2013**, *21*, 72–76.
- (19) Tanaka, K.; Moritake, N.; Uchiki, H. Preparation of Cu₂ZnSnS₄ thin films by sulfurizing sol–gel deposited precursors. *Sol. Energy Mater. Sol. Cells* **2007**, *91*, 1199–1201.
- (20) Wang, W.; Winkler, M. T.; Gunawan, O.; Gokmen, T.; Todorov, T. K.; Zhu, Y.; Mitzi, D. B. Device characteristics of CZTSSe thin-film solar cells with 12.6% efficiency. *Adv. Energy Mater.* **2014**, *4*, 1301465.
- (21) Fyfe, C. A.; Gies, H.; Kokotailo, G. T.; Pasztor, C.; Strobl, H.; Cox, D. E. Detailed investigation of the lattice structure of zeolite ZSM-11 by a combination of solid-state NMR and synchrotron X-Ray diffraction techniques. *J. Am. Chem. Soc.* **1989**, *111*, 2470–2474.
- (22) Xin, H.; Vorpahl, S. M.; Collord, A. D.; Braly, I. L.; Uhl, A. R.; Krueger, B. W.; Ginger, D. S.; Hillhouse, H. W. Lithium-doping inverts the nanoscale electric field at the grain boundaries in Cu₂ZnSn(S,Se)₄ and increases photovoltaic efficiency. *Phys. Chem. Chem. Phys.* **2015**, *17*, 23859–23866.

- (23) Gershon, T.; Sardashti, K.; Lee, Y. S.; Gunawan, O.; Singh, S.; Bishop, D.; Kummel, A. C.; Haight, R. Compositional effects in $\text{Ag}_2\text{ZnSnSe}_4$ thin films and photovoltaic devices. *Acta Mater.* **2017**, *126*, 383–388.
- (24) Yan, C.; Sun, K.; Huang, J.; Johnston, S.; Liu, F.; Veettil, B. P.; Sun, K.; Pu, A.; Zhou, F.; Stride, J. A.; Green, M. A.; Hao, X. Beyond 11% efficient sulfide kesterite $\text{Cu}_2\text{Zn}_x\text{Cd}_{1-x}\text{SnS}_4$ solar cell: effects of cadmium alloying. *ACS Energy Lett.* **2017**, *2*, 930–936.
- (25) Shin, D.; Zhu, T.; Huang, X.; Gunawan, O.; Blum, V.; Mitzi, D. B. Earth-abundant chalcogenide photovoltaic devices with over 5% efficiency based on a $\text{Cu}_2\text{BaSn}(\text{S},\text{Se})_4$ absorber. *Adv. Mater.* **2017**, *29*, 1606945.
- (26) Ghosh, A.; Chaudhary, D. K.; Biswas, A.; Thangavel, R.; Udayabhanu, G. Solution-processed Cu_2XSnS_4 ($X = \text{Fe}, \text{Co}, \text{Ni}$) photo-electrochemical and thin film solar cells on vertically grown ZnO nanorod arrays. *RSC Adv.* **2016**, *6*, 115204–115212.
- (27) Li, X.; Hou, Z.; Gao, S.; Zeng, Y.; Ao, J.; Zhou, Z.; Da, B.; Liu, W.; Sun, Y.; Zhang, Y. Efficient optimization of the performance of Mn^{2+} -doped kesterite solar cell: machine learning aided synthesis of high efficient $\text{Cu}_2(\text{Mn},\text{Zn})\text{Sn}(\text{S},\text{Se})_4$ solar cells. *Sol. RRL* **2018**, *2*, 1800198.
- (28) Collord, A. D.; Hillhouse, H. W. Germanium alloyed kesterite solar cells with low voltage deficits. *Chem. Mater.* **2016**, *28*, 2067–2073.
- (29) Su, Z.; Tan, J. M. R.; Li, X.; Zeng, X.; Batabyal, S. K.; Wong, L. H. Cation substitution of solution processed $\text{Cu}_2\text{ZnSnS}_4$ thin film solar cell with over 9% efficiency. *Adv. Energy Mater.* **2015**, *5*, 1500682.
- (30) Kukreti, S.; Gupta, G. K.; Dixit, A. Theoretical DFT studies of $\text{Cu}_2\text{HgSnS}_4$ absorber material and $\text{Al}:\text{ZnO}/\text{ZnO}/\text{CdS}/\text{Cu}_2\text{HgSnS}_4/\text{Back contact}$ heterojunction solar cell. *Sol. Energy* **2021**, *225*, 802–813.
- (31) Kim, I.; Kim, K.; Oh, Y.; Woo, K.; Cao, G.; Jeong, S.; Moon, J. Bandgap-graded $\text{Cu}_2\text{Zn}(\text{Sn}_{1-x}\text{Ge}_x)\text{S}_4$ thin-film solar cells derived from metal chalcogenide complex ligand capped nanocrystals. *Chem. Mater.* **2014**, *26*, 3957–3965.
- (32) Hages, C. J.; Levenco, S.; Miskin, C. K.; Alsmeier, J. H.; Abou-Ras, D.; Wilks, R. G.; Bär, M.; Unold, T.; Agrawal, R. Improved performance of Ge-alloyed CZTGeSSe thin-film solar cells through control of elemental losses. *Prog. Photovolt. Res. Appl.* **2015**, *23*, 376–384.

- (33) Giraldo, S.; Neuschitzer, M.; Thersleff, T.; López-Marino, S.; Sánchez, Y.; Xie, H.; Colina, M.; Placidi, M.; Pistor, P.; Izquierdo-Roca, V. Large efficiency improvement in $\text{Cu}_2\text{ZnSnSe}_4$ solar cells by introducing a superficial Ge Nanolayer. *Adv. Energy Mater.* **2015**, *5*, 1501070.
- (34) Kim, S.; Kim, K. M.; Tampo, H.; Shibata, H.; Niki, S. Improvement of voltage deficit of Ge-incorporated kesterite solar cell with 12.3% conversion efficiency. *Appl. Phys. Express* **2016**, *9*, 102301.
- (35) Zhang, Q.; Deng, H.; Chen, L.; Yu, L.; Tao, J.; Sun, L.; Yang, P.; Chu, J. Cation substitution induced structural transition, band gap engineering and grain growth of $\text{Cu}_2\text{Cd}_x\text{Zn}_{1-x}\text{SnS}_4$ thin films. *J. Alloys Compd.* **2017**, *695*, 482–488.
- (36) Xiao, Z.-Y.; Li, Y.-F.; Yao, B.; Deng, R.; Ding, Z.-H.; Wu, T.; Yang, G.; Li, C.-R.; Dong, Z.-Y.; Liu, L.; Zhang, L.-G.; Zhao, H.-F. Bandgap engineering of $\text{Cu}_2\text{Cd}_x\text{Zn}_{1-x}\text{SnS}_4$ alloy for photovoltaic applications: a complementary experimental and first-principles study. *J. Appl. Phys.* **2013**, *114*, 183506.
- (37) Vu, T. V.; Lavrentyev, A. A.; Gabrelian, B. V.; Tong, H. D.; Tkach, V. A.; Parasyuk, O. V.; Khyzhun, O. Y. A theoretical and experimental study of the valence-band electronic structure and optical constants of quaternary copper mercury tin sulfide, $\text{Cu}_2\text{HgSnS}_4$, a potential material for optoelectronics and solar cells. *Opt. Mater.* **2019**, *96*, 109296.
- (38) Khadka, D. B.; Kim, J. Band gap engineering of alloyed $\text{Cu}_2\text{ZnGe}_x\text{Sn}_{1-x}\text{Q}_4$ ($Q = \text{S, Se}$) films for solar cell. *J. Phys. Chem. C* **2015**, *119*, 1706–1713.
- (39) Tang, W.; Sanville, E.; Henkelman, G. A grid-based bader analysis algorithm without lattice bias. *J. Phys. Condens. Matter* **2009**, *21*, 084204.
- (40) Deringer, V. L.; Tchougréeff, A. L.; Dronskowski, R. Crystal orbital hamilton population (COHP) analysis as projected from plane-wave basis sets. *J. Phys. Chem. A* **2011**, *115*, 5461–5466.
- (41) Grin, Y.; Savin, A.; Silvi, B. The ELF perspective of chemical bonding. In *The Chemical Bond: Fundamental Aspects of Chemical Bonding*; Wiley, 2014.
- (42) Müller, P. C.; Ertural, C.; Hempelmann, J.; Dronskowski, R. Crystal orbital bond index: covalent bond orders in solids. *J. Phys. Chem. C* **2021**, *125*, 7959–7970.
- (43) Kesterite: mineral information, data and localities. <https://www.mindat.org/min-2189.html>.

- (44) Chen, S.; Gong, X. G.; Walsh, A.; Wei, S.-H. Electronic structure and stability of quaternary chalcogenide semiconductors derived from cation cross-substitution of II-VI and I-III-VI₂ compounds. *Phys. Rev. B* **2009**, *79*, 165211.
- (45) Chang, J.; R. Waclawik, E. Colloidal semiconductor nanocrystals: controlled synthesis and surface chemistry in organic media. *RSC Adv.* **2014**, *4*, 23505–23527.
- (46) Chen, S.; Gong, X. G.; Walsh, A.; Wei, S.-H. Crystal and electronic band structure of Cu₂ZnSnX₄ (X = S and Se) photovoltaic absorbers: first-principles insights. *Appl. Phys. Lett.* **2009**, *94*, 041903.
- (47) Hall, S. R.; Szymanski, J. T.; Stewart, J. M. Kesterite, Cu₂(Zn, Fe) SnS₄, and stannite, Cu₂(Fe,Zn) SnS₄, structurally similar but distinct minerals. *Can. Mineral.* **1978**, *16*, 131–137.
- (48) Schorr, S.; Hoebler, H.-J.; Tovar, M. A neutron diffraction study of the stannite-kesterite solid solution series. *Eur. J. Mineral.* **2007**, *19*, 65–73.
- (49) Ritscher, A.; Hoelzel, M.; Lerch, M. The order-disorder transition in Cu₂ZnSnS₄ – a neutron scattering investigation. *J. Solid State Chem.* **2016**, *238*, 68–73.
- (50) Kumar, M.; Persson, C. Cu₂ZnSnS₄ and Cu₂ZnSnSe₄ as potential earth-abundant thin-film absorber materials: a density functional theory study. *Int J Theor Appl Sci* **2013**, *5*, 1–8.
- (51) Paier, J.; Asahi, R.; Nagoya, A.; Kresse, G. Cu₂ZnSnS₄ as a potential photovoltaic material: a hybrid hartree-fock density functional theory study. *Phys. Rev. B* **2009**, *79*, 115126.
- (52) Schorr, S. Structural aspects of adamantine like multinary chalcogenides. *Thin Solid Films* **2007**, *515*, 5985–5991.
- (53) Schorr, S.; Gonzalez-Aviles, G. In-situ investigation of the structural phase transition in kesterite. *Phys. Status Solidi A* **2009**, *206*, 1054–1058.
- (54) Stahnke, U.; Brandt, A.; Graf, H. A. BENSCH experimental reports **2006**, 318.
- (55) Chen, S.; Yang, J.-H.; Gong, X. G.; Walsh, A.; Wei, S.-H. Intrinsic point defects and complexes in the quaternary kesterite semiconductor Cu₂ZnSnS₄. *Phys. Rev. B* **2010**, *81*, 245204.
- (56) Larsen, J. K.; Scragg, J. J. S.; Ross, N.; Platzer-Björkman, C. Band tails and Cu–Zn disorder in Cu₂ZnSnS₄ solar Cells. *ACS Appl. Energy Mater.* **2020**, *3*, 7520–7526.

- (57) Hadke, S.; Chen, W.; Tan, J. M. R.; Guc, M.; Izquierdo-Roca, V.; Rignanese, G.-M.; Hautier, G.; Wong, L. H. Effect of Cd on cation redistribution and order-disorder transition in $\text{Cu}_2(\text{Zn,Cd})\text{SnS}_4$. *J. Mater. Chem. A* **2019**, *7*, 26927–26933.
- (58) Yu. K. Kabalov, T. L. Evstigneeva, E. M., Spiridonov, Crystal structure of $\text{Cu}_2\text{HgSnS}_4$, a synthetic analogue of the mineral velikite. *Crystallogr. Rep.* **1998**, *43*, 16–20 (*Transl. Kristallografiya* **1998**, *43*, 21–25).
- (59) Kaplunnik, L. N.; Pobedimskaya, E. A.; Belov, N. V. Crystal structure of velikite $\text{Cu}_{3.75}\text{Hg}_{1.75}\text{Sn}_2\text{S}_8$. *Kristallografiya* **1977**, *22*, 175–177.
- (60) Moodie, A. F.; Whitfield, H. J. Determination of the structure of $\text{Cu}_2\text{ZnGeS}_4$ polymorphs by lattice imaging and convergent-beam electron diffraction. *Acta Crystallogr. B* **1986**, *42*, 236–247.
- (61) Parasyuk, O. V.; Piskach, L. V.; Romanyuk, Y. E.; Olekseyuk, I. D.; Zaremba, V. I.; Pekhnyo, V. I. Phase relations in the quasi-binary $\text{Cu}_2\text{GeS}_3\text{–ZnS}$ and quasi-ternary $\text{Cu}_2\text{S–Zn(Cd)S–GeS}_2$ systems and crystal structure of $\text{Cu}_2\text{ZnGeS}_4$. *J. Alloys Compd.* **2005**, *397*, 85–94.
- (62) Doverspike, K.; Dwight, K.; Wold, A. Preparation and characterization of copper zinc germanium sulfide selenide ($\text{Cu}_2\text{ZnGeS}_{4-y}\text{Se}_y$). *Chem. Mater.* **1990**, *2*, 194–197.
- (63) Heinrich, C. P.; Day, T. W.; Zeier, W. G.; Snyder, G. J.; Tremel, W. Effect of isovalent substitution on the thermoelectric properties of the $\text{Cu}_2\text{ZnGeSe}_{4-x}\text{S}_x$ series of solid solutions. *J. Am. Chem. Soc.* **2014**, *136*, 442–448.
- (64) Schleich, D. M.; Wold, A. Optical and electrical properties of quaternary chalcogenides. *Mater. Res. Bull.* **1977**, *12*, 111–114.
- (65) Mangelis, P.; Aziz, A.; Silva, I. da; Grau-Crespo, R.; Vaqueiro, P.; Powell, A. V. Understanding the origin of disorder in kesterite-type chalcogenides $A_2\text{ZnBQ}_4$ ($A = \text{Cu, Ag}$; $B = \text{Sn, Ge}$; $Q = \text{S, Se}$): the influence of inter-layer interactions. *Phys. Chem. Chem. Phys.* **2019**, *21*, 19311–19317.
- (66) Rabi, I. I.; Zacharias, J. R.; Millman, S.; Kusch, P. A new method of measuring nuclear magnetic moment. *Phys. Rev.* **1938**, *53*, 318–318.
- (67) Bloch, F.; Hansen, W. W.; Packard, M. Physics Nobel price 1952. *Phys Rev* **1946**, *69*, 127.
- (68) Purcell, E. M.; Torrey, H. C.; Pound, R. V. Resonance absorption by nuclear magnetic moments in a solid. *Phys. Rev.* **1946**, *69*, 37–38.

- (69) Reif, B.; Ashbrook, S. E.; Emsley, L.; Hong, M. Solid-state NMR spectroscopy. *Nat. Rev. Methods Primer* **2021**, *1*, 1–23.
- (70) Wolf, P.; Valla, M.; Núñez-Zarur, F.; Comas-Vives, A.; Rossini, A. J.; Firth, C.; Kallas, H.; Lesage, A.; Emsley, L.; Copéret, C.; Hermans, I. Correlating synthetic methods, morphology, atomic-level structure, and catalytic activity of Sn- β catalysts. *ACS Catal.* **2016**, *6*, 4047–4063.
- (71) Grykałowska, A.; Nowak, B. High-resolution solid-state ^{119}Sn and ^{195}Pt NMR studies of MPtSn semiconductors ($M = \text{Ti, Zr, Hf, Th}$). *Solid State Nucl. Magn. Reson.* **2005**, *27*, 223–227.
- (72) Eckert, H. Spying with spins on messy materials: 60 years of glass structure elucidation by NMR spectroscopy. *Int. J. Appl. Glass Sci.* **2018**, *9*, 167–187.
- (73) Bhattacharya, A.; Qiu, Y.; Bernard, G. M.; Butler, S.; Mar, A.; Michaelis, V. K. Annealing induced structural evolution in feldspar dental glass-ceramics investigated by solid-state NMR spectroscopy. *J. Solid State Chem.* **2020**, *289*, 121501.
- (74) Karmakar, A.; Bhattacharya, A.; Sarkar, D.; M. Bernard, G.; Mar, A.; K. Michaelis, V. Influence of hidden halogen mobility on local structure of $\text{CsSn}(\text{Cl}_{1-x}\text{Br}_x)_3$ mixed-halide perovskites by solid-state NMR. *Chem. Sci.* **2021**, *12*, 3253–3263.
- (75) Rosales, B. A.; Men, L.; Cady, S. D.; Hanrahan, M. P.; Rossini, A. J.; Vela, J. Persistent dopants and phase Segregation in organolead mixed-halide perovskites. *Chem. Mater.* **2016**, *28*, 6848–6859.
- (76) Kalisvaart, W. P.; Chaudhary, M.; Bhattacharya, A.; Michaelis, V. K.; Buriak, J. M. Mixing, domains, and fast Li-ion dynamics in ternary Li–Sb–Bi battery anode alloys. *J. Phys. Chem. C* **2022**, *126*, 2394–2402.
- (77) Paris, M.; Larramona, G.; Bais, P.; Bourdais, S.; Lafond, A.; Choné, C.; Guillot-Deudon, C.; Delatouche, B.; Moisan, C.; Dennler, G. ^{119}Sn MAS NMR to assess the cationic disorder and the anionic distribution in sulfoselenide $\text{Cu}_2\text{ZnSn}(\text{S}_x\text{Se}_{1-x})_4$ compounds prepared from colloidal and ceramic routes. *J. Phys. Chem. C* **2015**, *119*, 26849–26857.
- (78) Lafond, A.; Guillot-Deudon, C.; Vidal, J.; Paris, M.; La, C.; Jobic, S. Substitution of Li for Cu in $\text{Cu}_2\text{ZnSnS}_4$: toward wide band gap absorbers with low cation disorder for thin film solar cells. *Inorg. Chem.* **2017**, *56*, 2712–2721.

- (79) Bhattacharya, A.; Tkachuk, D. G.; Mar, A.; Michaelis, V. K. Mere anarchy is loosed: structural disorder in $\text{Cu}_2\text{Zn}_{1-x}\text{Cd}_x\text{SnS}_4$. *Chem. Mater.* **2021**, *33*, 4709–4722.
- (80) Zeier, W. G.; Heinrich, C. P.; Day, T.; Panithipongwut, C.; Kieslich, G.; Brunklaus, G.; Snyder, G. J.; Tremel, W. Bond strength dependent superionic phase transformation in the solid solution series $\text{Cu}_2\text{ZnGeSe}_{4-x}\text{S}_x$. *J. Mater. Chem. A* **2014**, *2*, 1790–1794.
- (81) Hamdi, M.; Benamira, M. Crystallochemical characterizations, Raman spectroscopy and studies nuclear magnetic resonance (NMR) of $\text{Cu}_2\text{Zn}(\text{Sn},\text{Si})\text{S}_4$ compounds for photovoltaic applications. *J. Mater. Sci. Chem. Eng.* **2022**, *10*, 24-40
- (82) Duer, M. J. *Introduction to Solid-state NMR Spectroscopy*; Blackwell, 2004.
- (83) Harris, R. K. *Nuclear Magnetic Resonance Spectroscopy*; Longman, 1986.
- (84) Apperley, D. C.; Harris, R. K.; Hodgkinson, P. *Solid-state NMR: Basic Principles and Practice*; Momentum Press, 2012.
- (85) Harris, R. K.; Becker, E. D.; De Menezes, S. M. C.; Goodfellow, R.; Granger, P. NMR nomenclature. Nuclear spin properties and conventions for chemical shifts (IUPAC Recommendations 2001). *Pure Appl. Chem.* **2001**, *73*, 1795–1818.
- (86) Abragam, A. *The Principles of Nuclear Magnetism*; Oxford University Press, 1961.
- (87) Levitt, M. H. *Spin Dynamics: Basics of Nuclear Magnetic Resonance*; Wiley, 2013.
- (88) Dybowski, C. Zeeman interaction in nuclear magnetic resonance. In *Encyclopedia of Analytical Chemistry*; Wiley, 2006.
- (89) Mehring, M. *Principles of High Resolution NMR in Solids*; Springer-Verlag, 1983.
- (90) Anet, F. A. L.; O’Leary, D. J. *Concepts in Magn. Reson* **1991**, *3*, 193–214.
- (91) Herzfeld, J.; Berger, A. E. Sideband intensities in NMR spectra of samples spinning at the magic angle. *J. Chem. Phys.* **1980**, *73*, 6021–6030.
- (92) Eichele, K. WSolids1 Ver. 1.21. 3; University of Tübingen, 2015.
- (93) Ramsey, N. F. Magnetic shielding of nuclei in molecules. *Phys. Rev.* **1950**, *78*, 699–703.
- (94) Yesinowski, J. P. Solid-state NMR of inorganic semiconductors. In *Solid State NMR*; Chan, J. C. C., Ed.; Springer, 2012.
- (95) Harris, R. K.; Wasylishen, R. E.; Duer, M. J., Eds.; *NMR Crystallography*; Wiley, 2009.
- (96) Grant, D. M., Harris, R. K. Ed.; *Encyclopedia of NMR.*; Wiley, 1996.
- (97) Wasylishen, R. E.; Ashbrook, S. E.; Wimperis, S. *NMR of Quadrupolar Nuclei in Solid Materials*; Wiley, 2012.

- (98) Kentgens, A. P. M. A practical guide to solid-state NMR of half-integer quadrupolar nuclei with some applications to disordered systems. *Geoderma* **1997**, *80*, 271–306.
- (99) Müller, K.; Geppi, M. *Solid-state NMR: Principles, Methods, and Applications*; Wiley, 2021.
- (100) Ashbrook, S. E. Recent advances in solid-state NMR spectroscopy of quadrupolar nuclei. *Phys. Chem. Chem. Phys.* **2009**, *11*, 6892–6905.
- (101) Bryce, D. L.; Wasylishen, R. E. Quadrupolar nuclei in solids: influence of different interactions on spectra. In *NMR of Quadrupolar Nuclei in Solid Materials*; Wiley, 2011.
- (102) Andrew, E. R.; Bradbury, A.; Eades, R. G. Nuclear magnetic resonance spectra from a crystal rotated at high speed. *Nature* **1958**, *182*, 1659–1659.
- (103) Lowe, I. J. Free induction decays of rotating solids. *Phys. Rev. Lett.* **1959**, *2*, 285–287.
- (104) Hennel, J. W.; Klinowski, J. Magic-angle spinning: a historical perspective. *Top. Curr. Chem.* **2004**, *246*, 1–14
- (105) Wasylishen, R. E. *NMR Spectroscopy Techniques*; Marcel Dekker, 1987.
- (106) Damadian, R. Tumor Detection by nuclear magnetic resonance. *Science* **1971**, *171*, 1151–1153.

Chapter 2

Mere anarchy is loosed: structural disorder in $\text{Cu}_2\text{Zn}_{1-x}\text{Cd}_x\text{SnS}_4$

2.1 Introduction

Quaternary chalcogenides $M_2M'TtCh_4$ ($M = \text{Cu}, \text{Ag}$; $M' =$ divalent metals such as Fe or Zn; $Tt = \text{Si}, \text{Ge}, \text{Sn}$; $Ch = \text{S}, \text{Se}$) have emerged as attractive candidates for photovoltaic materials fabricated from earth-abundant and inexpensive elements.^{1,2} The most well studied, $\text{Cu}_2\text{ZnSnS}_4$, exhibits a suitable band gap of 1.5 eV, a considerable absorption coefficient of 10^4 cm^{-1} , and a power conversion efficiency of about 8.4%.³ It has been proposed that disorder of similarly sized Cu and Zn atoms within the same sites (“antisite defects”) results in deleterious band-tailing effects, which limit the efficiency.^{4,5} Efforts to increase the efficiency in $\text{Cu}_2\text{ZnSnS}_4$ have focused on substitution with larger cations (e.g., Ag for Cu; Cd for Zn), on the premise that this may help to reduce the disorder.⁶ In particular, the partial substitution of Cd for Zn has meaningfully improved the efficiency to as high as 11% in $\text{Cu}_2\text{Zn}_{0.6}\text{Cd}_{0.4}\text{SnS}_4$.⁷ To be sure, the use of Cd reintroduces the vexing problem of toxicity, which should be avoided in designing new photovoltaic materials. Nevertheless, because these compounds offer such promising advances, it is worthwhile to probe the structural changes that occur upon Cd substitution, to gain insight which will provide further understanding on how to improve the photovoltaic efficiency of these and related compounds.

The chalcogenides $M_2M'TtCh_4$ generally adopt two types of tetragonal structures: $\text{Cu}_2\text{ZnSnS}_4$ -type (space group $I\bar{4}$) and $\text{Cu}_2\text{FeSnS}_4$ -type (space group $I\bar{4}2m$).⁸ These names are accepted, as also established in Pearson’s Crystal Data, to serve as unique labels for the crystal

structures in the space groups indicated.⁹ These structures are also frequently described by their mineral names: kesterite originally referred to $\text{Cu}_2\text{ZnSnS}_4$, and stannite to $\text{Cu}_2\text{FeSnS}_4$. However, $\text{Cu}_2\text{ZnSnS}_4$ itself has been modeled in both space groups $I\bar{4}$ and $I\bar{4}2m$, with varying degrees of site disorder.^{10,11} To avoid confusion, it is perhaps best to avoid the mineral names and simply express the structural models explicitly.

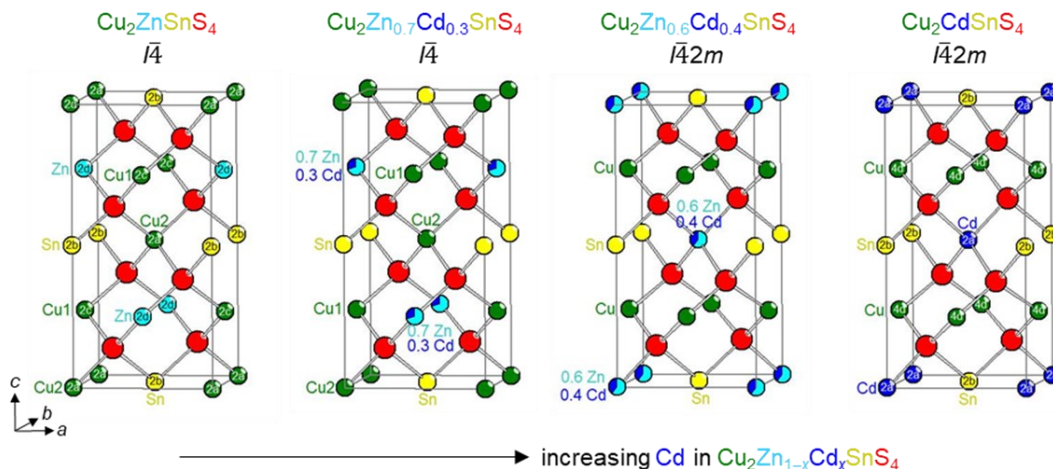


Figure 2.1. Cation site distributions as Cd substitution (x) increases in $\text{Cu}_2\text{Zn}_{1-x}\text{Cd}_x\text{SnS}_4$. For $x = 0-0.3$, Cd substitutes for Zn in the $2d$ site in the structure in space group $I\bar{4}$; for $x = 0.4-1.0$, Cd substitutes for Zn in the $2a$ site in the structure in space group $I\bar{4}2m$.

In most studies of the solid solution $\text{Cu}_2\text{Zn}_{1-x}\text{Cd}_x\text{SnS}_4$, where x represents the proportion of Cd substituted for Zn, an abrupt structural transition has been proposed to take place at around $x = 0.4$.^{7,12-18} The structure adopted by the lightly Cd-substituted members ($x = 0-0.3$) is in space group $I\bar{4}$, whereas the structure adopted by the more heavily Cd-substituted members ($x = 0.4-1.0$) is in space group $I\bar{4}2m$ (**Figure 2.1**). All cations are centered within tetrahedral sites lying on planes at $z = 0, \frac{1}{4}, \frac{1}{2}$, and $\frac{3}{4}$. The $I\bar{4}$ structure of $\text{Cu}_2\text{ZnSnS}_4$ contains planes of Cu–Sn ($z = 0$), Cu–Zn ($z = \frac{1}{4}$), Cu–Sn ($z = \frac{1}{2}$), and Cu–Zn atoms ($z = \frac{3}{4}$). The $I\bar{4}2m$ structure of $\text{Cu}_2\text{CdSnS}_4$ contains planes of Cd–Sn ($z = 0$), Cu ($z = \frac{1}{4}$), Cd–Sn ($z = \frac{1}{2}$), and Cu atoms ($z = \frac{3}{4}$). The key

difference is that the Cu atoms occupy two sets of sites ($2a$, $2c$) and lie within all planes ($z = 0$, $\frac{1}{4}$, $\frac{1}{2}$, $\frac{3}{4}$) in $\text{Cu}_2\text{ZnSnS}_4$, whereas they occupy one set of sites ($4d$) and lie within alternate planes ($z = \frac{1}{4}$, $\frac{3}{4}$) in $\text{Cu}_2\text{CdSnS}_4$. The group-subgroup relationships in $\text{Cu}_2\text{Zn}_{1-x}\text{Cd}_x\text{SnS}_4$ are presented in more detail in **Figure A2.1** in Appendix 2.

In addition to the basic models described above for $\text{Cu}_2\text{Zn}_{1-x}\text{Cd}_x\text{SnS}_4$, in which only disorder of Zn and Cd atoms occurs within the sites in the parent structures, more complex models have been proposed in which Zn and Cd atoms also disorder within the Cu sites in the $I\bar{4}$ (“partially disordered kesterite”) or $I\bar{4}2m$ structures (“disordered kesterite”).^{16,17} Further, the simple substitution of Cd within Zn sites has been challenged, and instead, a continuous transformation has been suggested to take place in which Cu enters the Zn sites, and Cd enters the Cu sites on progressing from $\text{Cu}_2\text{ZnSnS}_4$ to $\text{Cu}_2\text{CdSnS}_4$.¹⁶ In short, the central question is whether the disorder in $\text{Cu}_2\text{Zn}_{1-x}\text{Cd}_x\text{SnS}_4$ involves two (Zn, Cd) or three (Cu, Zn, Cd) atoms. Evidence for these proposals has come primarily from powder X-ray diffraction measurements and first-principles calculations.

Determining the site distributions in $\text{Cu}_2\text{Zn}_{1-x}\text{Cd}_x\text{SnS}_4$ by X-ray diffraction alone is not straightforward, especially when the disorder of up to three atoms (Cu, Zn, Cd) is invoked. In particular, Cu and Zn atoms are difficult to distinguish by X-ray diffraction because they have similar scattering factors. Although neutron diffraction has been used to examine $\text{Cu}_2\text{ZnSnS}_4$,^{10,11} it is not easily extended to $\text{Cu}_2\text{Zn}_{1-x}\text{Cd}_x\text{SnS}_4$ because Cd has very high neutron absorption cross-sections. An attractive solution is to apply solid-state nuclear magnetic resonance (NMR) spectroscopy, which can provide information about the local environment around specific elements. Multinuclear ^{65}Cu , ^{67}Zn , and ^{119}Sn NMR spectroscopy have been recently used to study the cation distribution in $\text{Cu}_2\text{ZnSnS}_4$, $\text{Cu}_2\text{ZnSn}(\text{S}_{1-x}\text{Se}_x)_4$, and $\text{Cu}_{1-x}\text{Li}_x\text{ZnSnS}_4$.^{19–24}

Given the competing proposals for the cation site distributions in $\text{Cu}_2\text{Zn}_{1-x}\text{Cd}_x\text{SnS}_4$, we present here a detailed analysis of their solid-state ^{63}Cu , ^{67}Zn , and ^{119}Sn NMR spectra, complemented by powder X-ray diffraction (XRD) measurements. To clarify the disorder of Cu and Zn atoms, the experimental ^{63}Cu and ^{67}Zn NMR spectra are compared with quantum chemical calculations. The optical band gaps, as measured by UV-visible spectroscopy, were monitored as a function of Cd substitution and correlated with the NMR chemical shifts.

2.2 Materials and methods

2.2.1 Synthesis

Starting materials were Cu powder (99.5%, Alfa-Aesar), Zn grains (99.9%, Baker), Cd powder (99.5%, Alfa-Aesar), Sn powder (99.9%, Cerac), and S flakes (99.99%, Sigma-Aldrich). Members of the solid solution $\text{Cu}_2\text{Zn}_{1-x}\text{Cd}_x\text{SnS}_4$ ($x = 0.05, 0.1, 0.2, 0.3, 0.4, 0.5, 0.6, 0.8, 1.0$) were prepared from stoichiometric mixtures of the elements, which were ground together, pressed into pellets, and loaded into carbon-coated fused silica tubes. The tubes were evacuated and sealed. They were placed in a box furnace where they were heated to 250 °C over 5 h, held there for 2 h, then heated to 800 °C over 11 h, held there for 4 d, and then cooled to room temperature over 24 h. The samples were ground, pressed into pellets, loaded into fused silica tubes, and subjected to a second heat treatment at 800 °C for 48 h, followed by cooling to room temperature over 24 h.

2.2.2 X-ray diffraction and energy-dispersive X-ray analysis

Powder X-ray diffraction patterns were collected on an Inel powder diffractometer equipped with a curved position-sensitive detector (CPS 120) and a Cu $K\alpha_1$ radiation source (1.5406 Å) operated at 40 kV and 20 mA. The patterns were analyzed using the FullProf suite of

software, with the profiles fitted by the Le Bail method.^{25,26} Samples were examined on a Zeiss Sigma 300 VP field-emission scanning electron microscope, operated at an accelerating voltage of 15 kV. Elemental compositions were obtained by energy-dispersive X-ray (EDX) analysis.

2.2.3 Diffuse reflectance spectroscopy

Optical diffuse reflectance spectra were measured from 200 nm (6.2 eV) to 2000 nm (0.6 eV) on a Cary 5000 UV-vis-NIR spectrophotometer equipped with a diffuse reflectance accessory. BaSO₄ was used as a 100% reflectance standard. The reflectance spectra were converted to optical absorption spectra using the Kubelka-Munk function, $F(R) = \alpha/S = (1-R)^2/2R$, where $F(R)$ denotes the ratio of absorption coefficient (α) and scattering coefficient (S), and R is the reflectance.^{27,28}

2.2.4 Solid-state NMR spectroscopy

NMR spectra were acquired at 9.4 T (400 MHz, ¹H) on a Bruker Avance III HD 400 NMR spectrometer equipped with a double resonance 4-mm H/X MAS Bruker probe (¹¹⁹Sn, ¹¹³Cd) or at 21.1 T (900 MHz, ¹H) on a Bruker Avance II 900 NMR spectrometer equipped with a double-resonance 4-mm H/X MAS Bruker probe (¹¹⁹Sn, ⁶³Cu, ⁶⁷Zn). Samples were ground and packed under dry nitrogen into 4 mm (¹¹⁹Sn, ¹¹³Cd, ⁶⁷Zn, ⁶³Cu non-spinning) or 2.5 mm (⁶³Cu MAS) outer diameter ZrO₂ rotors.

¹¹⁹Sn NMR. Tin-119 NMR spectra were acquired at 9.4 T under both non-spinning and MAS ($\omega_r/2\pi = 14$ kHz) conditions. For the end-members, Cu₂ZnSnS₄ and Cu₂CdSnS₄, non-spinning spectra were also collected. A rotor-synchronized Hahn-echo sequence ($\pi/2-\tau-\pi$ -ACQ) with τ of 30 μ s (non-spinning) or 71 μ s (MAS) was used. Spectra were acquired using a $\pi/2$ pulse of 4 μ s ($\gamma B_1/2\pi = 62.5$ kHz), recycle delays of 150–700 s, and 1000–2000 co-added transients. The

spectra were referenced to tetramethyltin at $\delta_{\text{iso}} = 0$ ppm by setting the chemical shift of external standard solid tetracyclohexyltin to -97.5 ppm.²⁹

Non-spinning ^{119}Sn NMR spectra for $\text{Cu}_2\text{ZnSnS}_4$ were also acquired at 21.1 T, with a solid-echo $\pi/2$ pulse of $6 \mu\text{s}$ ($\gamma B_1/2\pi = 41.6$ kHz), interpulse delay of $30 \mu\text{s}$, a recycle delay of 240 s, and 256 co-added transients. The spectra were referenced with powdered SnO_2 (-604.3 ppm) as an external standard relative to tetramethyltin ($\delta_{\text{iso}} = 0$).³⁰

^{113}Cd NMR. Cadmium-113 NMR spectra were acquired at 9.4 T, with a Hahn-echo pulse sequence ($\tau = 30 \mu\text{s}$ for non-spinning and $71 \mu\text{s}$ for MAS ($\omega_r/2\pi = 14$ kHz)), $\pi/2$ of $4 \mu\text{s}$ ($\gamma B_1/2\pi = 62.5$ kHz), a recycle delay of 120 s and 2048–4096 co-added transients. For $\text{Cu}_2\text{CdSnS}_4$, only non-spinning spectra were collected. Spectra were referenced to solid $\text{Cd}(\text{NO}_3)_2 \cdot 4\text{H}_2\text{O}$ at -100 ppm.³¹

^{63}Cu NMR. Copper-63 NMR spectra were acquired at 21.1 T using a solid-echo pulse sequence ($\pi/2-\tau-\pi/2\text{-ACQ}$), with a $\pi/2$ pulse of $1 \mu\text{s}$ (solid $\gamma B_1/2\pi = 125$ kHz), a recycle delay of 2 s, and 1000–8000 co-added transients. The samples were spun at 31.25 kHz. Non-spinning spectra were obtained using a home-built 4 mm static solenoid probe (pure Ag R.F. coil to minimize probe background from Cu metal), with a modified solid echo pulse sequence involving a recycle delay of 2 s and 512 co-added transients. Quantitative data were acquired using a short tip angle ($0.2 \mu\text{s}$) Bloch pulse experiment. Triple quantum MAS (3QMAS) NMR spectra were acquired using a three-pulse sequence with a z-filter where pulses were optimized for maximum transfer efficiency (^{63}Cu : $P1 = 3.5 \mu\text{s}$, $P2 = 1.25 \mu\text{s}$, $P3 = 7 \mu\text{s}$), a recycle delay of 0.25 s, 240–9600 scans, and 64–256 t_2 increments. All ^{63}Cu NMR spectra were referenced to solid CuCl at 0 ppm.³²

^{67}Zn NMR. Zinc-67 NMR spectra were acquired at 21.1 T using a Bloch or Hahn-echo pulse sequence with a $\pi/2$ pulse of $3 \mu\text{s}$ (liquid $\gamma B_1/2\pi = 36$ kHz), a recycle delay of 5 s, and

2000–15000 co-added transients, under both non-spinning and MAS ($\omega_r/2\pi = 10$ kHz) conditions. The ^{67}Zn spectra were referenced to 1 M $\text{Zn}(\text{NO}_3)_2$ solution at 0 ppm.³³

2.2.5 NMR data processing and analysis

NMR spectra were processed using the Bruker TOPSPIN 4.0.6 software package, with 100–400 Hz exponential apodization. The ^{119}Sn , ^{113}Cd , ^{63}Cu , and ^{67}Zn NMR spectra were fitted using WSOLIDS³⁴ to determine the NMR parameters. All data were plotted using Origin 2020, and the ^{119}Sn and ^{113}Cd NMR data were fit using Gaussian functions.

2.2.6 Quantum chemical computations

DFT computations were performed using the CASTEP software package,³⁵ which applies a gauge-including projector augmented plane wave basis set suitable for periodic structures and makes use of the Perdew-Burke-Ernzerhof functional in the generalized gradient approximation for the exchange-correlation energy.³⁶ Ultrasoft pseudopotentials and zeroth-order regular approximation relativistic effects were applied.^{37,38} Calculations were carried out with a high accuracy basis set, a maximum plane wave energy of 566 eV, and a Monkhorst-Pack grid of $4 \times 4 \times 2$ k -points from crystal structures sourced from PCD.³⁹ DFT computed shieldings were converted to chemical shifts using CdS, and $\text{Cu}_2\text{ZnSnS}_4$ as reference samples using $\delta(\text{ppm}) = \sigma_{\text{ref}}^{\text{calc}}(\text{ppm}) - \sigma_{\text{model}}^{\text{calc}}(\text{ppm})$.

2.3 Results and discussion

2.3.1 Crystal structure of $\text{Cu}_2\text{Zn}_{1-x}\text{Cd}_x\text{SnS}_4$

Bulk samples of the solid solution $\text{Cu}_2\text{Zn}_{1-x}\text{Cd}_x\text{SnS}_4$ ($x = 0.05, 0.1, 0.2, 0.3, 0.4, 0.5, 0.6, 0.8, 1.0$) were prepared by reactions of the elements at 800 °C. Energy-dispersive X-ray (EDX) spectroscopic analysis confirmed that the elemental compositions of these samples agree well with the nominal compositions (**Table A2.1** in Appendix 2). The powder XRD patterns reveal that the samples are single-phase; for the end-members $\text{Cu}_2\text{ZnSnS}_4$ ($I\bar{4}$) and $\text{Cu}_2\text{CdSnS}_4$ ($I\bar{4}2m$), they match well with the simulated patterns (**Figure 2.2(a)**). The tetragonal cell parameters (a and c) were refined from these patterns (**Table A2.2** in Appendix 2). With increasing Cd content, the cell volume increases gradually from 317.4 Å³ for $\text{Cu}_2\text{ZnSnS}_4$ to 337.4 Å³ for $\text{Cu}_2\text{CdSnS}_4$, consistent with the presence of larger Cd atoms (cf. Shannon ionic radii of 0.60 Å for Zn^{2+} and 0.78 Å for Cd^{2+} in CN4).⁴⁰ However, close inspection of the cell lengths shows that while a increases monotonically, c reaches a maximum at $x = 0.3$ and then decreases with greater Cd substitution (**Figure 2.2b**). In a hypothetical idealized structure in which all the metal-centred tetrahedra are undistorted and contain equal bond lengths, c would be exactly twice as long as a . The deviation from this idealized structure can be measured by the ratio $\eta = c/2a$, which relates to the degree of tetragonal distortion (elongation along c for $\eta > 1$ and contraction along c for $\eta < 1$).⁴¹ The set of 220 and 204 peaks (near 47° in 2θ) serves as a useful diagnostic in the XRD patterns to discern this distortion: these peaks coincide for the idealized structure ($\eta = 1$) but become

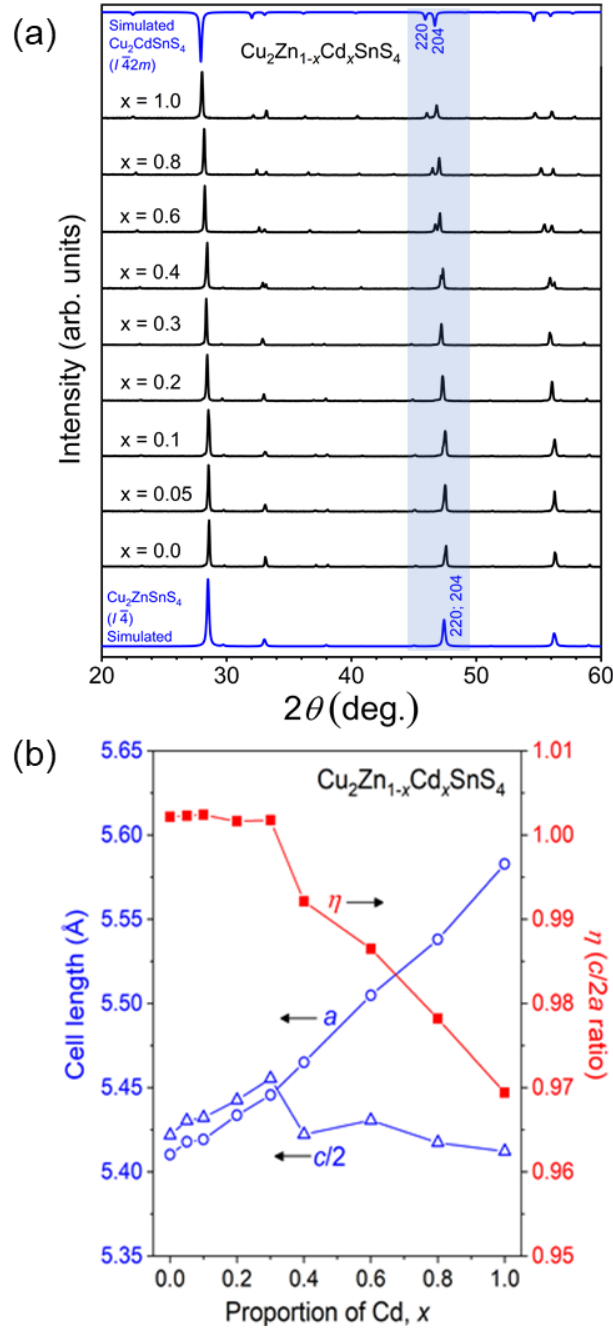


Figure 2.2. (a) Powder XRD patterns for $\text{Cu}_2\text{Zn}_{1-x}\text{Cd}_x\text{SnS}_4$. The shaded region highlights the 220 and 204 peaks, which overlap for the lightly substituted Cd members ($x = 0-0.3$) but is visibly split for the more heavily substituted Cd members ($x = 0.4-1.0$) because the c -axis undergoes an abrupt contraction relative to the a -axis. (b) Plot of tetragonal cell parameters (a and $c/2$) and the ratio of these parameters ($\eta = c/2a$) as a function of Cd content, x .

increasingly split with greater distortion. As observed, these peaks essentially overlap for the lightly substituted Cd members ($x = 0-0.3$) corresponding to a nearly undistorted structure ($\eta = 1.002$), but they are visibly split for the more heavily substituted Cd members ($x = 0.4-1.0$) as the structure contracts along c ($\eta = 0.992-0.969$) (**Figure 2.2**). The abrupt transition near $x = 0.4$ has been proposed to be related to a change in structure, from $I\bar{4}$ ($\text{Cu}_2\text{ZnSnS}_4$ to $\text{Cu}_2\text{Zn}_{0.7}\text{Cd}_{0.3}\text{SnS}_4$) to $I\bar{4}2m$ ($\text{Cu}_2\text{Zn}_{0.6}\text{Cd}_{0.4}\text{SnS}_4$ to $\text{Cu}_2\text{CdSnS}_4$).¹³⁻¹⁸ However, it is very important to appreciate that the observation of this peak splitting alone offers no direct information about the site distributions, and the assignment of space groups is merely inferred based on the structures of the end-members $\text{Cu}_2\text{ZnSnS}_4$ and $\text{Cu}_2\text{CdSnS}_4$.

2.3.2 Local structure around Sn

In the structures of the end-members $\text{Cu}_2\text{ZnSnS}_4$ ($I\bar{4}$) and $\text{Cu}_2\text{CdSnS}_4$ ($I\bar{4}2m$), the Sn atoms are fixed at one set of sites [$2b$ ($0, 0, \frac{1}{2}; \frac{1}{2}, \frac{1}{2}, 0$)], each surrounded in the first coordination sphere by 4 S atoms in tetrahedral geometry and in the second coordination sphere by 8 Cu and 4 Zn or Cd atoms in cuboctahedral geometry. This environment can be probed by ^{119}Sn NMR spectroscopy ($I = \frac{1}{2}$; 8.6% natural abundance; $\mathcal{E} = 37.29\%$),⁴² which is highly sensitive to local chemical structure and exhibits a wide range of isotropic chemical shifts of 6000 ppm for diamagnetic compounds.⁴³⁻⁴⁵ If disorder is assumed to occur only between Zn and Cd atoms in the solid solution $\text{Cu}_2\text{Zn}_{1-x}\text{Cd}_x\text{SnS}_4$, then the second coordination sphere contains $[\text{Cu}_8\text{Zn}_{4-n}\text{Cd}_n]$, where n ranges from 0 to 4 (**Figure 2.3a**), and the resonances for Sn atoms surrounded by these environments can be represented by the notation $L^{(n)}$.

The ^{119}Sn NMR spectra evolve gradually in $\text{Cu}_2\text{Zn}_{1-x}\text{Cd}_x\text{SnS}_4$ with varying degrees of resolution (**Figure 2.3b**).

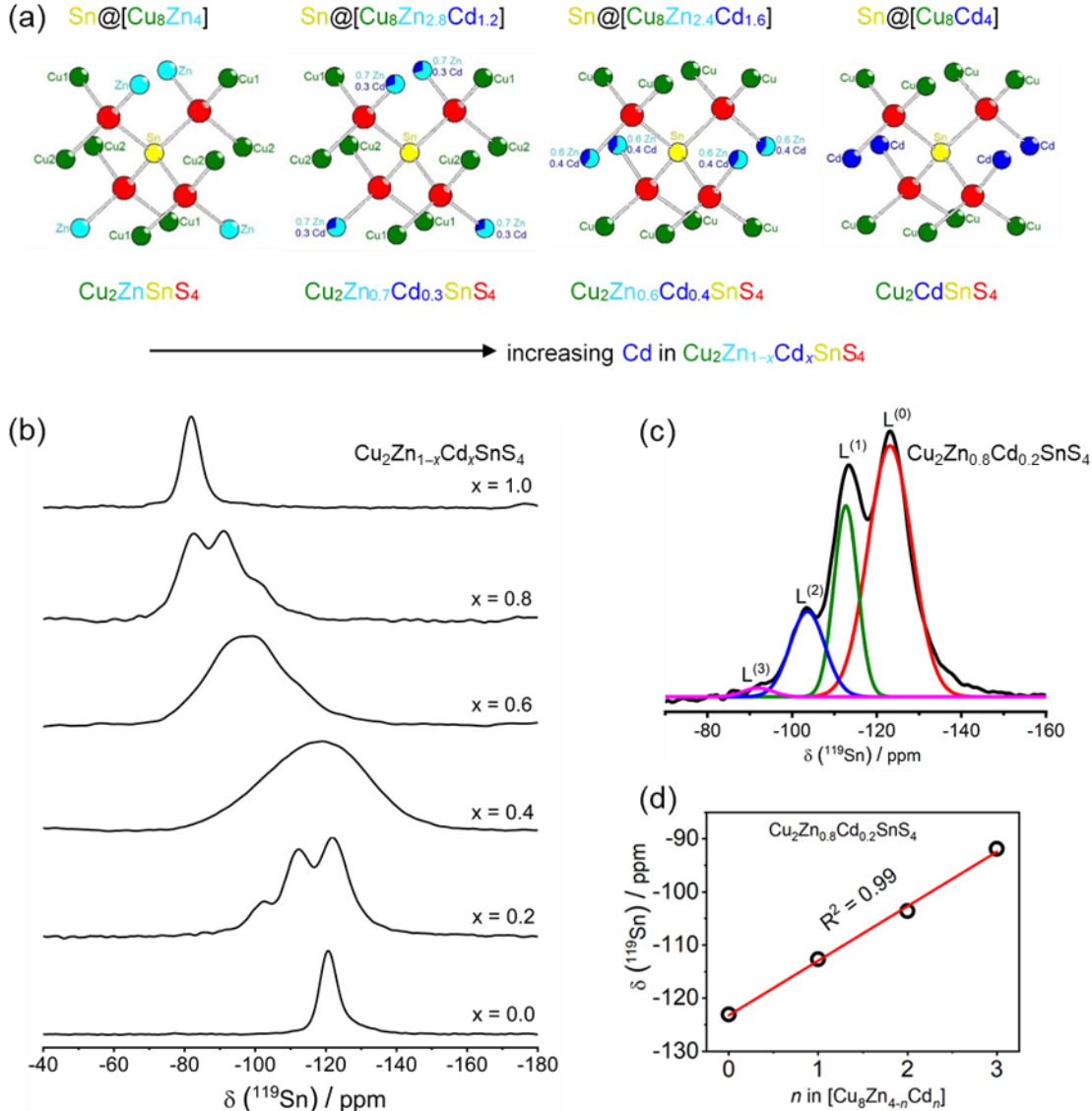


Figure 2.3. (a) Local coordination around Sn sites. (b) ^{119}Sn MAS NMR spectra ($B_0 = 9.4$ T) for $\text{Cu}_2\text{Zn}_{1-x}\text{Cd}_x\text{SnS}_4$. (c) Deconvolution into Gaussian-fitted peaks representing Sn sites $L^{(n)}$ with second coordination spheres $[Cu_8Zn_{4-n}Cd_n]$ in $\text{Cu}_2\text{Zn}_{0.8}\text{Cd}_{0.2}\text{SnS}_4$. (d) Dependence of isotropic ^{119}Sn chemical shift with n in $[Cu_8Zn_{4-n}Cd_n]$.

For the end-members, there is a single resonance located at an isotropic chemical shift of $\delta_{\text{iso}} = -121$ ppm for $\text{Cu}_2\text{ZnSnS}_4$ ($x = 0$) and -82 ppm for $\text{Cu}_2\text{CdSnS}_4$ ($x = 1$), consistent with the presence

of a single Sn site with a unique chemical environment, $[\text{Cu}_8\text{Zn}_4]$ or $[\text{Cu}_8\text{Cd}_4]$, respectively. For $\text{Cu}_2\text{Zn}_{0.8}\text{Cd}_{0.2}\text{SnS}_4$ ($x = 0.2$), four partially resolved resonances which were fitted with Gaussian profiles are observed, corresponding to Sn sites $\text{L}^{(n)}$ with environments $[\text{Cu}_8\text{Zn}_{4-n}\text{Cd}_n]$, where n ranges from 0 to 3 (**Figure 2.3c**). The missing $\text{L}^{(4)}$ resonance can be attributed to the low probability of occurrence, only about 0.2%, based on a binomial model of the environment $[\text{Cu}_8\text{Cd}_4]$. Despite the different geometrical arrangements of Cu, Zn, and Cd atoms in the second coordination sphere around the Sn atoms within the $I\bar{4}$ and $I\bar{4}2m$ structures, the isotropic ^{119}Sn chemical shifts follow a linear dependence with the number of Cd atoms n in $[\text{Cu}_8\text{Zn}_{4-n}\text{Cd}_n]$, according to the equation $\delta(^{119}\text{Sn} / \text{ppm}) = 10.3n - 123.2$ (**Figure 2.3d**). Comparison of the spectra for the lightly substituted Cd members of $\text{Cu}_2\text{Zn}_{1-x}\text{Cd}_x\text{SnS}_4$ ($x = 0.05-0.2$) confirms the expectation that these $\text{L}^{(n)}$ peaks with higher n become more intense as the Cd content increases (**Figure A2.2** in Appendix 2).

The ^{119}Sn NMR spectra for all remaining compounds $\text{Cu}_2\text{Zn}_{1-x}\text{Cd}_x\text{SnS}_4$ were analyzed in a similar way to extract the isotropic ^{119}Sn chemical shifts and linewidths of peaks $\text{L}^{(n)}$ (**Tables A2.3** and **A2.4** in Supplementary Data). Inspection of the linewidths shows that the peaks gradually broaden as the Cd content increases from $x = 0$ to $x = 0.4$, and then they become narrower from $x = 0.4$ to $x = 1.0$. The linewidths are similar for the end-members $\text{Cu}_2\text{ZnSnS}_4$ (790 Hz) and $\text{Cu}_2\text{CdSnS}_4$ (823 Hz), consistent with unique environments around the Sn sites. The peak broadening exhibited by the intermediate members arises from a more varied distribution of chemical environments with different bond distances and angles around the Sn sites as disorder of Zn and Cd atoms occurs. For the lightly substituted Cd members, such as $\text{Cu}_2\text{Zn}_{0.8}\text{Cd}_{0.2}\text{SnS}_4$, the $\text{L}^{(0)}$, $\text{L}^{(1)}$, and $\text{L}^{(2)}$ peaks are more prominent, indicating a greater proportion of Zn atoms in the second coordination sphere, whereas for the heavily substituted Cd members, such as

$\text{Cu}_2\text{Zn}_{0.2}\text{Cd}_{0.8}\text{SnS}_4$, the $L^{(2)}$, $L^{(3)}$, and $L^{(4)}$ peaks dominate, consistent with a greater proportion of Cd atoms in the second coordination sphere. For $\text{Cu}_2\text{Zn}_{0.6}\text{Cd}_{0.4}\text{SnS}_4$, the cumulative linewidth reaches a maximum of 5.1 kHz, and only a single broad Gaussian-like resonance is observed so that individual $L^{(n)}$ peaks are not resolved. Note that the structural transition in $\text{Cu}_2\text{Zn}_{1-x}\text{Cd}_x\text{SnS}_4$ (from $I\bar{4}$ to $I\bar{4}2m$) also takes place at this point ($x = 0.4$); therefore, further broadening is also attributed to the presence of both phases.

The ^{119}Sn resonances shift to higher frequency with greater Cd content in $\text{Cu}_2\text{Zn}_{1-x}\text{Cd}_x\text{SnS}_4$ (from $\delta_{\text{iso}} = -121$ ppm for $\text{Cu}_2\text{ZnSnS}_4$ to -82 ppm for $\text{Cu}_2\text{CdSnS}_4$). The change in the average chemical shifts becomes more pronounced on progressing from the lightly substituted Cd members (gradual change for $x = 0-0.4$) to the heavily substituted members (steep change for $x = 0.6-1.0$), suggesting that changes in the next-nearest neighbor chemical environment (i.e., Zn/Cd) around the Sn sites become more drastic at high Cd content.

The distribution of Cd atoms within the environment $[\text{Cu}_8\text{Zn}_{4-n}\text{Cd}_n]$ around the Sn sites can be quantified by evaluating the relative areas of the $L^{(n)}$ peaks in the ^{119}Sn NMR spectra. This analysis was carried out for the $x = 0.05, 0.1, 0.2,$ and 0.8 members for $\text{Cu}_2\text{Zn}_{1-x}\text{Cd}_x\text{SnS}_4$, for which these $L^{(n)}$ peaks are clearly resolved in the NMR spectra, and the relative areas were compared with expected values assuming a binomial distribution (**Table A2.5** in Appendix 2).⁴⁶ In general, the relative areas measured experimentally agree well with the binomial distribution for the $x = 0.05$ and 0.1 members but show deviations for the $x = 0.2$ and 0.8 members (**Figure A2.3** in Appendix 2). This observation suggests that with greater Cd substitution, the assumption of completely random mixing of Zn and Cd atoms may break down (i.e., cation clustering), resulting from the disparity in atomic sizes.

To gain further insight into structural changes upon Cd substitution in $\text{Cu}_2\text{Zn}_{1-x}\text{Cd}_x\text{SnS}_4$, the chemical shift anisotropy (CSA) was evaluated from non-spinning ^{119}Sn NMR spectra for the end members $\text{Cu}_2\text{ZnSnS}_4$ and $\text{Cu}_2\text{CdSnS}_4$ (see supporting information). In this type of analysis, three parameters are typically extracted: (i) the isotropic chemical shift, $\delta_{\text{iso}} = (\delta_{11} + \delta_{22} + \delta_{33})/3$, which is the average of the principal components of the CSA tensor, with $\delta_{11} \geq \delta_{22} \geq \delta_{33}$; (ii) the span, $\Omega = \delta_{11} - \delta_{33}$, which describes the breadth of the pattern; and (iii) the skew, $\kappa = 3(\delta_{22} - \delta_{\text{iso}})/\Omega$, which describes the shape of the powder pattern.^{47,48} For $\text{Cu}_2\text{ZnSnS}_4$, the ^{119}Sn NMR spectrum acquired at 9.4 T showed only a small CSA, so it was recollected at a higher magnetic field of 21.1 T to enhance the CSA interactions (**Figure A2.4** in Appendix 2). From the spectra, the extracted span and skew parameters are $\Omega = 32 \pm 5$ ppm and $\kappa = -0.4 \pm 0.1$ for $\text{Cu}_2\text{ZnSnS}_4$, and $\Omega = 115 \pm 5$ ppm and $\kappa = 0.9 \pm 0.1$ for $\text{Cu}_2\text{CdSnS}_4$ (**Figure 2.4**). Given that the skew is close to 1 for $\text{Cu}_2\text{CdSnS}_4$, the CSA tensor is likely nearly axially symmetric. The CSA tensor can be related to the degree of structural distortion of the Sn-centered tetrahedra.^{43,49,50} The bond angles around the Sn atoms in $\text{Cu}_2\text{ZnSnS}_4$ (109.5°) are essentially ideal,⁵¹ whereas those in $\text{Cu}_2\text{CdSnS}_4$ ($108.7\text{--}109.9^\circ$) deviate more,⁵² consistent with the tetragonal compression along the *c*-axis ($\eta = 0.969$) discussed earlier and the broader span in the ^{119}Sn NMR spectrum. To ensure that these ^{119}Sn NMR spectra have been acquired quantitatively, the longitudinal spin-lattice relaxation times (T_1) were also measured and found to be 85 ± 12 s for $\text{Cu}_2\text{ZnSnS}_4$ and 115 ± 14 s for $\text{Cu}_2\text{CdSnS}_4$.

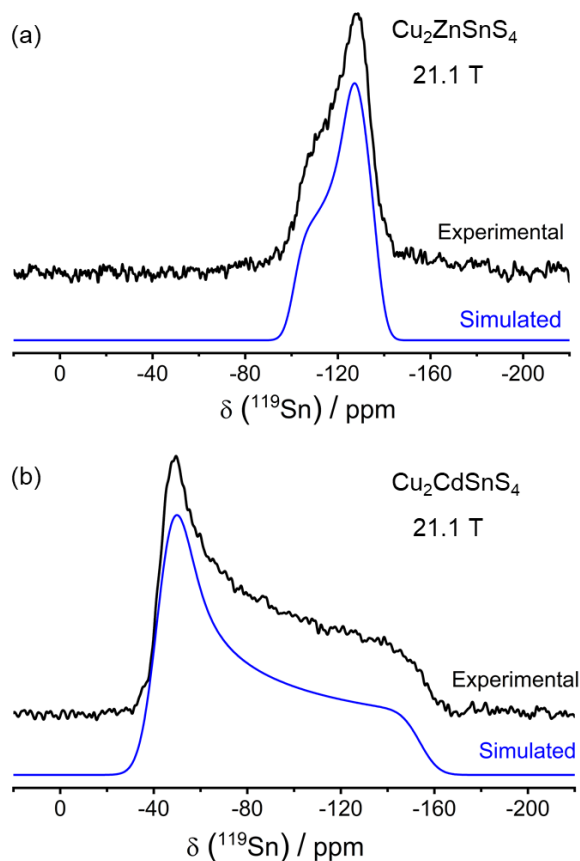


Figure 2.4. Experimental and simulated non-spinning ^{119}Sn NMR spectra for (a) $\text{Cu}_2\text{ZnSnS}_4$ ($B_0 = 21.1$ T, $\delta_{\text{iso}} = -120.9$ ppm, $\Omega = 32 \pm 5$ ppm, $\kappa = -0.4 \pm 0.1$) and (b) $\text{Cu}_2\text{CdSnS}_4$ ($B_0 = 9.4$ T, $\delta_{\text{iso}} = -81.9$ ppm, $\Omega = 115 \pm 5$ ppm, $\kappa = 0.9 \pm 0.1$).

2.3.3 Local structure around Cd

The Cd atoms are located in tetrahedral sites at either $2d$ ($0, \frac{1}{2}, \frac{3}{4}; \frac{1}{2}, 0, \frac{1}{4}$) with site symmetry $\bar{4}$.. in the $I\bar{4}$ structure expected for the lightly Cd-substituted members of $\text{Cu}_2\text{Zn}_{1-x}\text{Cd}_x\text{SnS}_4$, or $2a$ ($0, 0, 0; \frac{1}{2}, \frac{1}{2}, \frac{1}{2}$) with site symmetry $\bar{4}2m$ in the $I\bar{4}2m$ structure for the heavily substituted members. The second coordination sphere around these sites consists of 8 Cu and 4 Sn atoms in cuboctahedral geometry, but in conformity with the required site symmetries around Cd, the distribution of these atoms differs in the $I\bar{4}$ vs $I\bar{4}2m$ structures (**Figure 2.5a**). This situation offers a decisive opportunity to test the competing hypotheses of disorder occurring

between only two atoms (Zn, Cd) or among three atoms (Cu, Zn, Cd). If only Zn and Cd disorder takes place, then the chemical environment around the Cd sites remains constant (8 Cu, 4 Sn), and any effects resulting from Cd substitution will be related to different distributions of these Cu and Sn atoms and probably small changes in bond lengths to them. If a disorder of Cu, Zn, and Cd atoms occurs, then the chemical environment around the Cd sites will undergo relatively large changes (e.g., the second coordination sphere may contain a mixture of Cu and Cd atoms as well as Sn atoms). ^{113}Cd NMR spectroscopy ($I = 1/2$; 12.2% natural abundance, $\mathcal{E} = 22.2\%$)⁴² was used to probe these environments as it is sensitive to local structural variations within various solids.^{53-60.}

The ^{113}Cd NMR spectra were collected for $\text{Cu}_2\text{Zn}_{1-x}\text{Cd}_x\text{SnS}_4$ for $x = 0.2-1.0$ (**Figure 2.5b**). The most remarkable observation is that the resonances do not evolve gradually upon substitution with Cd, but rather they segregate into two disparate regions. A single resonance appears at 724 ppm for the most lightly Cd substituted member ($x = 0.2$ with $I\bar{4}$ structure), and similarly, a single resonance appears at 660 to 640 ppm for the most heavily substituted members ($x = 0.6-1.0$ with $I\bar{4}2m$ structure). However, two resonances appear within these same regions, near 720 and 670 ppm, for the $x = 0.3$ and 0.4 members (**Figure 2.5c**), where the transition between the $I\bar{4}$ vs $I\bar{4}2m$ structures has been implicated in occurring according to the evidence from XRD patterns. A reasonable interpretation is that for the samples with $x = 0.3-0.4$, two phases with the $I\bar{4}$ vs $I\bar{4}2m$ structures are present, perhaps interspersed as nanodomains with each other. If these two phases adopt similar cell parameters, then their XRD patterns may show slight differences in peak intensities (because of the different distribution of atoms), but the peaks would overlap, and it would be impossible to distinguish between them. A plot of the ^{113}Cd isotropic chemical shifts reveals the abrupt jump that correlates strongly with the structural transition (**Figure 2.5d**). The

smaller and smoother changes in chemical shifts for each of the two peaks can be related to more gradual changes in bond lengths around the Cd sites within the separate $I\bar{4}$ vs $I\bar{4}2m$ structures. The ^{113}Cd chemical shifts vary linearly with Cd content x according to the equations $\delta(^{113}\text{Cd} / \text{ppm}) = -26.0x + 728.9$ for $0 < x \leq 0.4$ ($I\bar{4}$ structure) and $\delta(^{113}\text{Cd} / \text{ppm}) = -56.7x + 696.5$ for $0.3 < x \leq 1.0$ ($I\bar{4}2m$ structure).

In addition to the isotropic chemical shifts, the linewidths and relative areas of the ^{113}Cd NMR peaks have been extracted (**Table A2.6** in Appendix 2). With increasing Cd substitution, the linewidth increases and reaches a maximum at $x = 0.4$ and decreases until the peak is sharpest for $\text{Cu}_2\text{CdSnS}_4$ ($x = 1.0$). Given that the second coordination sphere around the Cd site remains fixed at 8 Cu and 4 Sn atoms (at 4 Å away), the line broadening arises from the distribution of environments of disordered Zn and Cd atoms at slightly longer range (>5 Å). From the relative areas, the proportions of the two phases proposed to be present in the $x = 0.3$ and 0.4 samples can be estimated (70% $I\bar{4}$ and 30% $I\bar{4}2m$ for $\text{Cu}_2\text{Zn}_{0.7}\text{Cd}_{0.3}\text{SnS}_4$; 20% $I\bar{4}$ and 80% $I\bar{4}2m$ for $\text{Cu}_2\text{Zn}_{0.6}\text{Cd}_{0.4}\text{SnS}_4$).

For $\text{Cu}_2\text{CdSnS}_4$, the ^{113}Cd CSA parameters were determined from a non-spinning spectrum in a similar manner as before for the ^{119}Sn CSA parameters. The experimental and simulated spectra are shown (**Figure A2.5** in Appendix 2), and the extracted parameters are $\Omega = 54 \pm 5$ ppm and $\kappa = 0.8 \pm 0.1$.

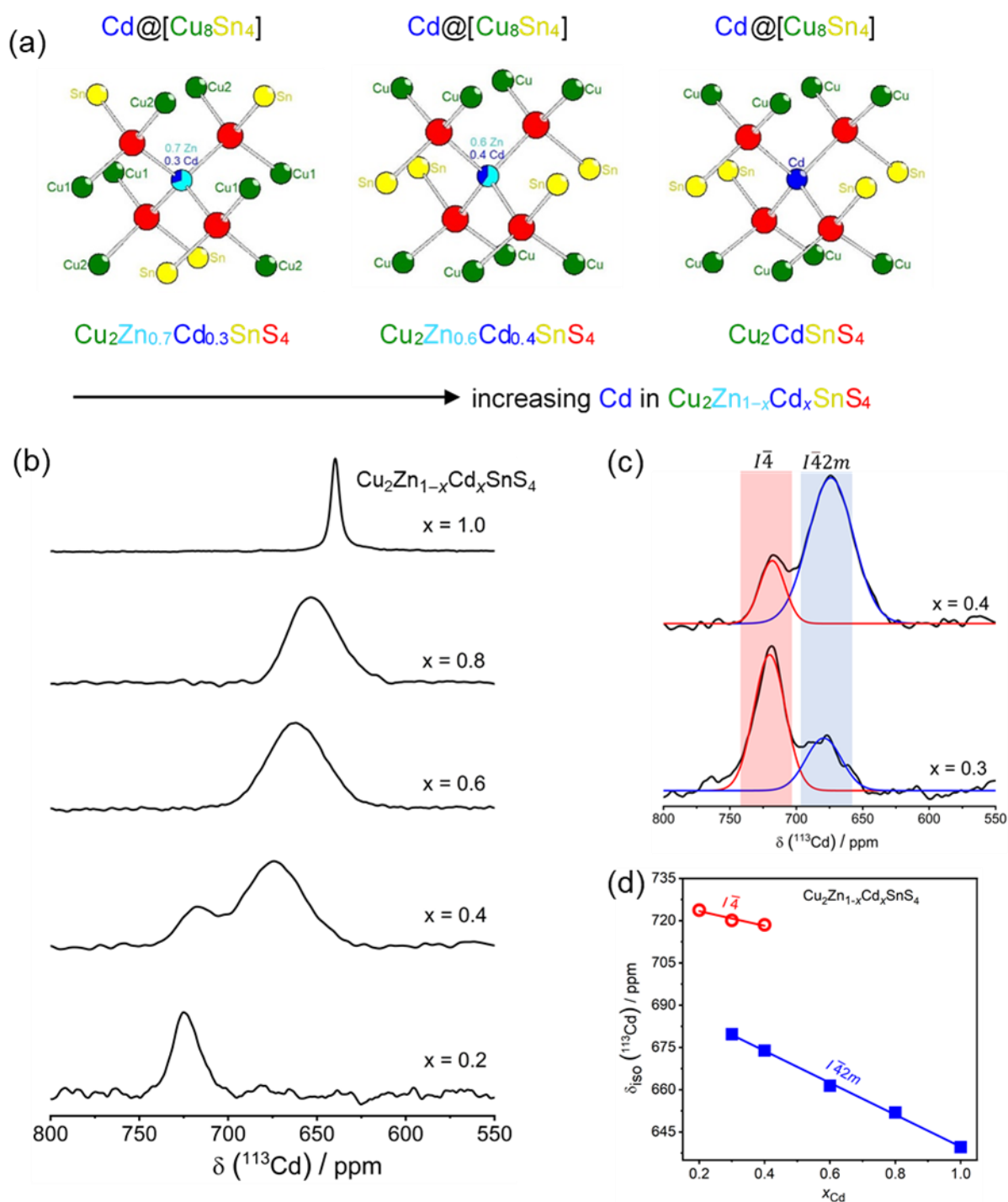


Figure 2.5. (a) Local coordination around Cd sites. (b) ^{113}Cd MAS NMR spectra ($B_0 = 9.4$ T) for $\text{Cu}_2\text{Zn}_{1-x}\text{Cd}_x\text{SnS}_4$ for $x = 0.2$ – 1.0 . (c) ^{113}Cd MAS NMR spectra for $x = 0.3$ and 0.4 , with the two peaks assigned to separate phases adopting $I\bar{4}$ (720 ppm, red) and $I\bar{4}2m$ (680 ppm, blue) structures and their areas are used to determine their relative amounts. (d) ^{113}Cd isotropic chemical shifts, δ_{iso} , plotted as a function of Cd content, x , with linear fits applied to the peaks assigned to $I\bar{4}$ (red) and $I\bar{4}2m$ (blue) structures.

2.3.4 Local structure around Cu and Zn

The Cu atoms occupy two sets of sites [$2a$ (0, 0, 0; $\frac{1}{2}$, $\frac{1}{2}$, $\frac{1}{2}$) and $2c$ (0, $\frac{1}{2}$, $\frac{1}{4}$; $\frac{1}{2}$, 0, $\frac{3}{4}$)] in the $I\bar{4}$ structure, but one set of sites [$4d$ (0, $\frac{1}{2}$, $\frac{1}{2}$; 0, $\frac{1}{2}$, $\frac{3}{4}$; $\frac{1}{2}$, 0, 0; $\frac{1}{2}$, 0, $\frac{1}{4}$)] in the $I\bar{4}2m$ structure. They experience the most complex local environments, with potentially up to four types of atoms (4 Cu, 4 Sn, and 4 Zn/Cd) in the second coordination sphere (**Figure 2.6a**), which can be probed by ^{63}Cu NMR spectroscopy ($I = 3/2$; 69.7% natural abundance, $Q = -22.0 \text{ fm}^2$, $\mathcal{E} = 26.5\%$).⁴² In particular, the interaction between the quadrupolar moment of the ^{63}Cu nuclei and the local electric field gradient (EFG) leads to NMR lineshapes that depend sensitively on any structural distortions occurring at short and medium range.^{19,32}

The ^{63}Cu NMR spectra reveal asymmetric lineshapes that are either sharp or contain features consistent with second-order quadrupole broadening for the end members, reflecting the fixed coordination environments around the Cu atoms, but they are considerably broadened for the intermediate members of $\text{Cu}_2\text{Zn}_{1-x}\text{Cd}_x\text{SnS}_4$, in agreement with the varied coordination environments caused by disorder of Zn and Cd atoms in the second coordination sphere (**Figure 2.6b**). The isotropic chemical shifts and centers of gravity for these resonances were determined (**Table A2.7** in Appendix 2). For $\text{Cu}_2\text{ZnSnS}_4$ ($x = 0$), two ^{63}Cu resonances are observed with different quadrupole coupling constants at 787 ppm ($C_Q = 6.7 \text{ MHz}$) and 807 ppm ($C_Q = 1.7 \text{ MHz}$), consistent with the presence of two inequivalent sets of Cu sites in the proposed $I\bar{4}$ structure. Based on the bond angles, the Cu atoms in the $2a$ site, labeled as Cu2, are more distorted ($106.6\text{--}110.9^\circ$) than those in the $2c$ site, labeled as Cu1 ($108.9\text{--}110.6^\circ$).⁵¹ As greater distortion leads to larger EFG (larger C_Q), the peak at 787 ppm is assigned to the $2a$ site and the peak at 807 ppm to the $2c$ site.

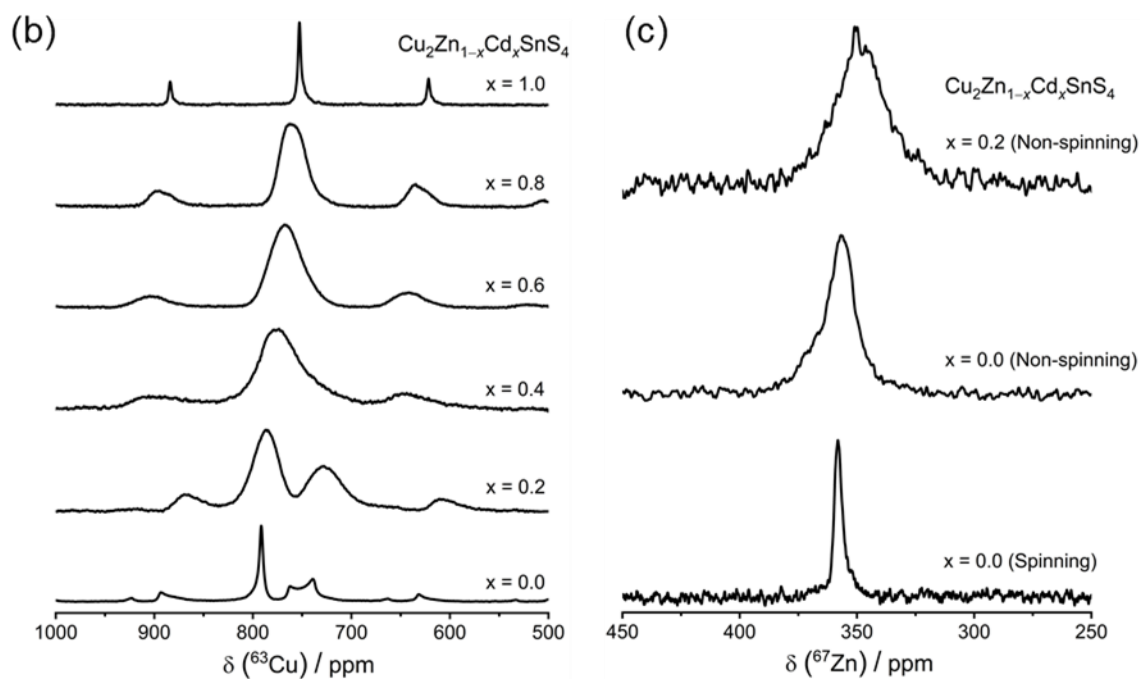
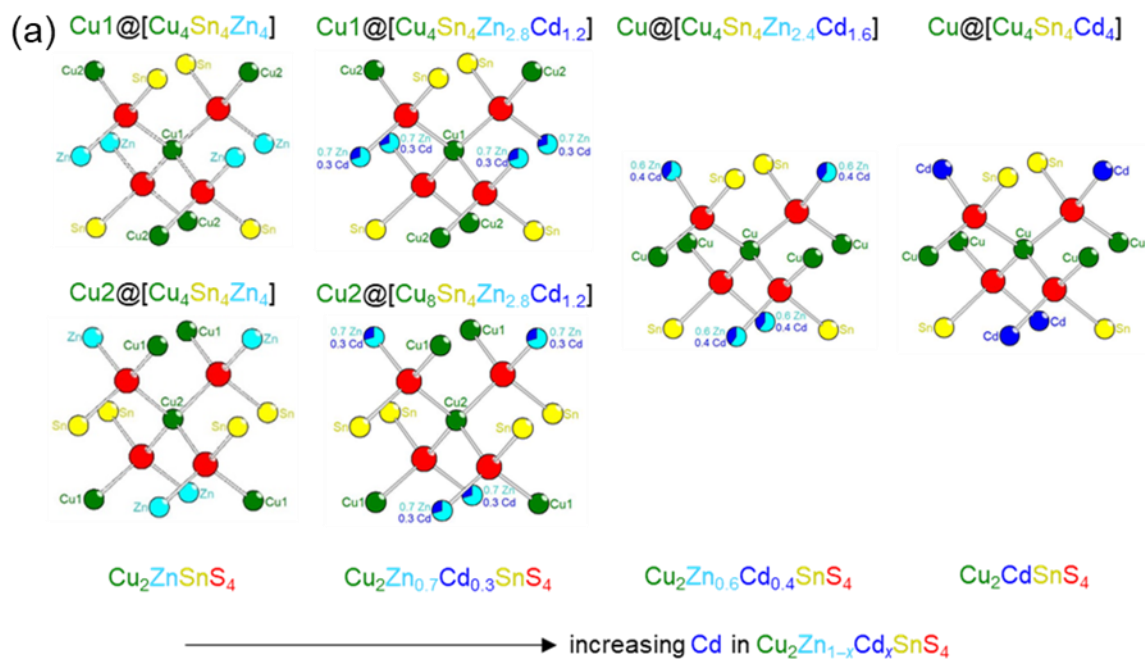


Figure 2.6. (a) Local coordination around Cu sites. (b) ^{63}Cu MAS NMR spectra ($B_0 = 21.1$ T) for $\text{Cu}_2\text{Zn}_{1-x}\text{Cd}_x\text{SnS}_4$. (c) ^{67}Zn NMR spectra ($B_0 = 21.1$ T) for $x = 0$ (non-spinning and MAS at 10 kHz) and $x = 0.2$ members (non-spinning).

The relative areas under the traces were evaluated and found to be $45\pm 5\%$ for the 787 ppm peak and $55\pm 5\%$ for the 807 ppm peak, in agreement with the equal multiplicities of the $2a$ and $2c$ sites.

For the lightly Cd substituted member $\text{Cu}_2\text{Zn}_{0.8}\text{Cd}_{0.2}\text{SnS}_4$, which retains the $I\bar{4}$ structure of $\text{Cu}_2\text{ZnSnS}_4$, the two resonances corresponding to the two Cu sites are still observed, with roughly equal relative areas of $57\pm 5\%$ for the $2a$ site and $43\pm 5\%$ for the $2c$ site. For $\text{Cu}_2\text{Zn}_{0.6}\text{Cd}_{0.4}\text{SnS}_4$ and all the remaining more heavily Cd-substituted members up to $\text{Cu}_2\text{CdSnS}_4$, which now adopt the $I\bar{4}2m$ structure, only one resonance is observed, corroborating the presence of a unique Cu site at $4d$. Close inspection reveals that the lineshape is asymmetric for $\text{Cu}_2\text{Zn}_{0.6}\text{Cd}_{0.4}\text{SnS}_4$, consistent with the presence of nanodomains with the $I\bar{4}$ structure as speculated above. The abrupt switch from two to one ^{63}Cu resonances favors the interpretation that the evolution in site distribution also changes at $x = 0.4$ (as opposed to alternative proposals for a continuous transformation involving disorder of Cu, Zn, and Cd atoms).¹⁶ This result for bulk materials is consistent with previous observations of a structural transition for $\text{Cu}_2\text{Zn}_{1-x}\text{Cd}_x\text{SnS}_4$ thin films when $x > 0.3$.¹⁸ Another report states that the transition in solution-processed $\text{Cu}_2\text{Zn}_{1-x}\text{Cd}_x\text{SnS}_4$ occurs when $x > 0.6$, but this conclusion is based on nominal compositions because the elemental analysis was not performed.¹⁴ The chemical shifts and centers of gravity of the resonances change abruptly on proceeding from $x = 0.2$ to $x = 0.4$, but then they only change gradually thereafter to $x = 1.0$. To ensure that additional Cu sites were not hidden, two-dimensional ^{63}Cu triple-quantum magic-angle spinning (3QMAS) NMR spectra were collected on $\text{Cu}_2\text{Zn}_{0.8}\text{Cd}_{0.2}\text{SnS}_4$ and $\text{Cu}_2\text{Zn}_{0.2}\text{Cd}_{0.8}\text{SnS}_4$ (**Figure A2.6** in Appendix 2). The results support the conclusions from the 1D spectra, indicating the number of Cu sites to be two ($x < 0.4$) or one ($x > 0.4$).

The ^{63}Cu CSA and quadrupolar parameters were determined from MAS and non-spinning NMR spectra ($B_0 = 21.1$ T) for $\text{Cu}_2\text{ZnSnS}_4$ and $\text{Cu}_2\text{CdSnS}_4$ (**Figure A2.7** in Appendix 2). For

$\text{Cu}_2\text{ZnSnS}_4$, the parameters were $\Omega = 271 \pm 10$ ppm, $\kappa = 1 \pm 0.1$, $C_Q = 6.7 \pm 0.2$ MHz, $\eta_Q = 0 \pm 0.1$ for $2a$ site, and $\Omega = 114 \pm 10$ ppm, $\kappa = -1 \pm 0.1$, $C_Q = 1.7 \pm 0.2$ MHz, $\eta_Q = 0 \pm 0.1$ for $2c$ site. The values of the skew κ indicate that both Cu sites ($2a$ and $2c$) are axially symmetric, although the axial tensors are aligned differently. The zero values of the quadrupolar parameter η_Q imply that the magnitudes of V_{xx} and V_{yy} are equal, within error. For $\text{Cu}_2\text{CdSnS}_4$, the parameters were $\Omega = 310 \pm 10$ ppm, $\kappa = -1 \pm 0.1$, $C_Q = 0.8 \pm 0.2$ MHz, and $\eta_Q = 0 \pm 0.1$, indicating an axially symmetric EFG tensor and higher symmetry for the Cu atoms in the $4d$ site.

The Zn atoms occupy the same sites as the Cd atoms in both $I\bar{4}$ and $I\bar{4}2m$ structures if the disorder of only these atoms is assumed to take place. Although ^{67}Zn NMR spectra ($I = 5/2$; 4.1% natural abundance, $Q = 15.0 \text{ fm}^2$, $\mathcal{E} = 6.3 \%$)⁴² are quite challenging to measure,^{33,61-63} they were obtained for $\text{Cu}_2\text{ZnSnS}_4$ and $\text{Cu}_2\text{Zn}_{0.8}\text{Cd}_{0.2}\text{SnS}_4$ (**Figure 2.6c**). For $\text{Cu}_2\text{ZnSnS}_4$, a single resonance is observed at 358 ppm with no second-order contribution and a small EFG ($C_Q < 1$ MHz), consistent with a unique Zn site (at $2d$ ($0, \frac{1}{2}, \frac{3}{4}; \frac{1}{2}, 0, \frac{1}{4}$)). The resonance shows a small CSA contribution in the non-spinning NMR spectrum and an asymmetric tail toward lower ppm in the MAS NMR spectrum. For $\text{Cu}_2\text{Zn}_{0.8}\text{Cd}_{0.2}\text{SnS}_4$, there remains a single resonance in the NMR spectrum, which rules out alternative models in which Zn atoms are found in more than one site. The lineshape is broader and Gaussian-like, suggesting chemical shifts distributions due to disordered environments.

2.3.5 Comparison of experimental and DFT-computed NMR parameters

Thus far, the NMR results appear to be most consistent with the structural model in which only Zn and Cd atoms disorder within $\text{Cu}_2\text{Zn}_{1-x}\text{Cd}_x\text{SnS}_4$. Density functional theory (DFT) computations have been carried out to theoretically calculate the ^{63}Cu , ^{113}Cd , and ^{119}Sn NMR

parameters for the end-members $\text{Cu}_2\text{ZnSnS}_4$ and $\text{Cu}_2\text{CdSnS}_4$, specifically to predict NMR features for peaks arising from atoms occupying various sites, and then to compare with the actual experimental NMR spectra (**Table A2.8** in Appendix 2). Overall, the computed NMR parameters match reasonably well with the experimental parameters. For example, the computed spans agree with the experimental values in the ^{119}Sn NMR spectra for $\text{Cu}_2\text{ZnSnS}_4$ and $\text{Cu}_2\text{CdSnS}_4$, and in the ^{113}Cd NMR spectra for $\text{Cu}_2\text{CdSnS}_4$. The computed quadrupole coupling parameters C_Q and η_Q in the ^{63}Cu NMR spectra are in good agreement with the experimental values for the Cu atoms in the $2a$ site in $\text{Cu}_2\text{CdSnS}_4$. However, C_Q is overestimated for the Cu atoms in the $2c$ site.

For the intermediate members of $\text{Cu}_2\text{Zn}_{1-x}\text{Cd}_x\text{SnS}_4$, the random distribution of atoms precludes similar DFT calculations. Nevertheless, inferences about these intermediate members can be drawn from calculations on ordered structural models of the end-members. In particular, simulating NMR spectra based on these alternative models may help ascertain if more complicated disorder involving Cu, Zn, and Cd atoms occurs in $\text{Cu}_2\text{Zn}_{1-x}\text{Cd}_x\text{SnS}_4$. Models were considered for $\text{Cu}_2\text{ZnSnS}_4$ and $\text{Cu}_2\text{CdSnS}_4$ in which the Zn or Cd atoms occupy the $2a$, $2c$, or $2d$ sites (and the Cu atoms occupy the remaining two sets of sites) in the $I\bar{4}$ structure (**Table A2.9** in Appendix 2).

As a prelude to examining the intermediate members of $\text{Cu}_2\text{Zn}_{1-x}\text{Cd}_x\text{SnS}_4$, it is of interest to see if these calculations help resolve the site distribution in the end-member $\text{Cu}_2\text{ZnSnS}_4$. In the simplest structure proposed for $\text{Cu}_2\text{ZnSnS}_4$, the Cu atoms fully occupy the $2a$ and $2c$ sites (“ordered kesterite”), but in an alternative structure sometimes proposed, the Cu atoms fully occupy the $2a$ site and mix with Zn atoms in the $2c$ and $2d$ sites (“partially disordered kesterite”). Based on a superposition of models so that Cu atoms occupy all three sites (models (1) and (2) in **Table A2.9**, the simulated ^{63}Cu NMR spectra show three resonances corresponding to these sites (**Figure A2.8a** in Appendix 2). In the experimental spectrum for $\text{Cu}_2\text{ZnSnS}_4$, the resonance arising

from a supposed occupation of the $2d$ site is absent. In a similar way, the ^{67}Zn NMR spectrum has been simulated for $\text{Cu}_2\text{ZnSnS}_4$, assuming that Zn atoms are disordered over two sites ($2c$, $2d$) instead of fully occupying just one ($2d$). This simulation was carried out by first computing the ^{67}Zn magnetic shielding and C_Q parameters for Zn atoms occupying only the $2d$ site in $\text{Cu}_2\text{ZnSnS}_4$ (model (1)); then, analogous parameters were estimated for Zn atoms in the $2c$ site by considering a hypothetical structure in which the occupations of Cu and Zn in $2c$ and $2d$ sites were swapped (model (2)). The experimental ^{67}Zn NMR spectrum of $\text{Cu}_2\text{ZnSnS}_4$ shows only one resonance assigned to the $2d$ site, whereas the hypothetical peak from the $2c$ site is absent (**Figure A2.8b** in Appendix 2). On balance, the comparison of computed and experimental ^{63}Cu and ^{67}Zn NMR spectra supports the simpler “ordered kesterite” structure for $\text{Cu}_2\text{ZnSnS}_4$ and the absence of Cu/Zn disorder.

Next, this computational analysis is extended to intermediate members of the $\text{Cu}_2\text{Zn}_{1-x}\text{Cd}_x\text{SnS}_4$ series and examine how simulated ^{113}Cd and ^{63}Cu NMR spectra compare with experimental spectra depending on different distributions of Cu, Zn, and Cd atoms. As Cd atoms are gradually substituted into $\text{Cu}_2\text{ZnSnS}_4$, they could potentially occupy the $2a$, $2c$, or $2d$ sites, or perhaps even some combination thereof, in the parent $I\bar{4}$ structure, as illustrated for $\text{Cu}_2\text{Zn}_{0.8}\text{Cd}_{0.2}\text{SnS}_4$ (**Table A2.10** in Appendix 2). Here, the Cd atoms could mix with Cu atoms in $2a$ (model (8)) or in $2c$ (model (9)) and the displaced Cu atoms then mix with Zn atoms in $2d$; or the Cd atoms could simply mix with Zn atoms in $2d$ (model (10)). The isotropic ^{113}Cd chemical shifts were computed by placing Cd atoms in either the $2a$, $2c$, or $2d$ states in hypothetical structures for $\text{Cu}_2\text{CdSnS}_4$ in $I\bar{4}$, or in the $2d$ sites in the observed structure for $\text{Cu}_2\text{CdSnS}_4$ in $I\bar{4}2m$ (**Figure A2.9** in Appendix 2). The key feature is that the computed isotropic ^{113}Cd chemical shifts lie at higher frequency for Cd atoms in the $2c$ or $2d$ sites, by about 50 ppm than those in the $2a$

sites. The experimental ^{113}Cd NMR spectrum for $\text{Cu}_2\text{Zn}_{0.8}\text{Cd}_{0.2}\text{SnS}_4$ shows one peak lying at about 50 ppm higher than the peak in $\text{Cu}_2\text{CdSnS}_4$ (where Cd atoms can only be located in $2a$) (**Figure 2.5b**). This comparison implies that Cd atoms enter either the $2c$ or $2d$ sites in $\text{Cu}_2\text{Zn}_{0.8}\text{Cd}_{0.2}\text{SnS}_4$. To complement this result, the isotropic ^{63}Cu chemical shifts for Cu atoms placed in $2a$, $2c$, or $2d$ sites, as computed earlier (**Table A2.9** in Appendix 2), were also examined. The experimental echo and 3QMAS ^{63}Cu NMR (**Figures A2.6** in Appendix 2) for $\text{Cu}_2\text{Zn}_{0.8}\text{Cd}_{0.2}\text{SnS}_4$ shows two resonances, ruling out the possibility of the more complex site distributions in which Cu atoms disorder within all three sites (models (8) and (9), **Figure A2.10** in Appendix 2) and supports the incorporation of Cd in Zn position (model (10)).

2.3.6 Variation of band gaps and NMR chemical shift behaviour

Because NMR chemical shifts depend on the degree of magnetic shielding experienced by a nucleus, they can also be influenced by charge carriers in a semiconductor. Thus, it is of interest to examine if there is a correlation between the band gaps in $\text{Cu}_2\text{Zn}_{1-x}\text{Cd}_x\text{SnS}_4$ and the NMR chemical shifts. The optical band gaps E_g were obtained by collecting UV-vis diffuse reflectance spectra, which were then converted to absorption spectra (plots of $(F(R) \cdot h\nu)^2$ vs the photon energy $h\nu$) from which straight lines were extrapolated from the absorption edges (**Figure A2.11a** in Appendix 2).²⁸ The optical band gaps, which are direct, decrease from 1.5 to 1.2 eV with increasing Cd content in $\text{Cu}_2\text{Zn}_{1-x}\text{Cd}_x\text{SnS}_4$ (**Figure A2.11b** in Appendix 2). These band gaps are consistent with the black colour of all samples. For $\text{Cu}_2\text{ZnSnS}_4$, previous band structure calculations indicate that the top of the valence band consists mostly of bonding Cu–S character, whereas the bottom of the conduction band consists mostly of antibonding Sn–S character.^{64,65} That is, the magnitude of the band gap is largely controlled by the Cu, Sn, and S atoms and less so by the Zn atoms, whose

orbital energies lie lower than those of Cu. However, the substitution of Cd atoms, which contain 4d orbitals lying at higher energies than Zn 3d orbitals, may raise the top of the valence band and narrow the band gap, as observed experimentally.⁷ Of course, other factors, such as unit cell expansion, structural changes, and electronegativity differences, also come into play. Accordingly, the band gap decreases rapidly from $\text{Cu}_2\text{ZnSnS}_4$ to $\text{Cu}_2\text{Zn}_{0.7}\text{Cd}_{0.3}\text{SnS}_4$, but then the decrease is less pronounced on proceeding from $\text{Cu}_2\text{Zn}_{0.6}\text{Cd}_{0.4}\text{SnS}_4$ to $\text{Cu}_2\text{CdSnS}_4$; the interruption at $x = 0.4$ signals the transition from the $I\bar{4}$ to the $I\bar{4}2m$ structure.

To a first approximation, the total magnetic shielding consists of diamagnetic and paramagnetic contributions.⁶⁶ The diamagnetic term arises from the circulation of electrons near the nucleus, which generates a local magnetic field as opposed to the external magnetic field; this term does not typically vary much for a given nucleus. The paramagnetic term arises from magnetic-field-induced mixing of occupied and unoccupied orbitals having proper symmetry; it is usually negative (i.e., deshielding) and has a much greater magnitude than the diamagnetic term, so it is primarily responsible for the observed anisotropic magnetic shielding. The total paramagnetic term is the sum of all contributions from pairs of suitable orbitals, the magnitude of each contribution being inversely proportional to the difference of orbital energies.⁶⁷ In certain cases, the deshielding depends approximately inversely with the average excitation energy (ΔE); for molecular substances, ΔE between highest occupied and lowest unoccupied molecular orbitals are the dominant contributions to paramagnetic shielding. In nanomaterials, this approximation is often invoked and generally holds true;⁶⁸⁻⁷² however, in these extended solids, it is unclear if the band gap plays an influential role. The average ^{119}Sn and ^{113}Cd chemical shifts for the microcrystalline semiconductors studied here have been plotted vs the band gaps in $\text{Cu}_2\text{Zn}_{1-x}\text{Cd}_x\text{SnS}_4$ (**Figure 2.7**). Although the ^{119}Sn chemical shift decreases with increasing

measured band gaps, in accordance with expectations noted above, the ^{113}Cd chemical shift follows the opposite behaviour. The associated band gap changes observed ($x > 0.3$, $I\bar{4}2m$ structure) are small and cannot account for the sizeable chemical shift changes experimentally observed. The ^{119}Sn chemical shift is dominated by changes to its next-nearest cation neighbor where Cd isoelectronic substitution with Zn influences the medium range structure in the 2d site. Above, it was shown that upon Cd incorporation, a series of distinct ^{119}Sn resonances appear (**Figure 2.3**), gradually shifting to a higher frequency (deshielded, ~ 9.5 ppm/Cd) as Cd replaces the four Zn next-nearest neighbors, $[\text{SnS}_4](\text{Zn}_{4-n}\text{Cd}_n)$. The ^{113}Cd chemical shift trends to a higher frequency (deshielded) as Cd is replaced with Zn ($\text{Cu}_2\text{CdSnS}_4 \rightarrow \text{Cu}_2(\text{Cd}_{0.4}\text{Zn}_{0.6})\text{SnS}_4$). A change in the chemical environment occurs as Zn replaces Cd; its smaller cationic radius causes distortions in the (Zn/Cd) S_4 tetrahedra (Zn–S, 2.37 Å vs Cd–S, 2.41 Å), influencing the s- or p-electron character of the local electronic environment. For example, Griffin and co-workers demonstrated this effect in ternary semiconducting tellurides, $\text{Cd}_{1-x}\text{Zn}_x\text{Te}$, where they observed a deshielding effect (shift to higher frequency) in the ^{113}Cd NMR resonance upon Zn substitution.^{73,74} They concluded that an inductive charge transfer occurs through the anionic Te, causing a net charge of s-type and that in some cases, the chemical shift may provide information to changes in bond length. A similar mechanism may apply to $\text{Cu}_2\text{Zn}_{1-x}\text{Cd}_x\text{SnS}_4$, where either an increase in p-character (or a decrease in s-character) occurs with Zn substitution that would be consistent with the shift to higher frequency (deshielded; increasing paramagnetic contribution) observed in the ^{113}Cd NMR results. These results illustrate that influences on chemical shift remain a complex property to explain that may not be easily ascribed to a single factor.

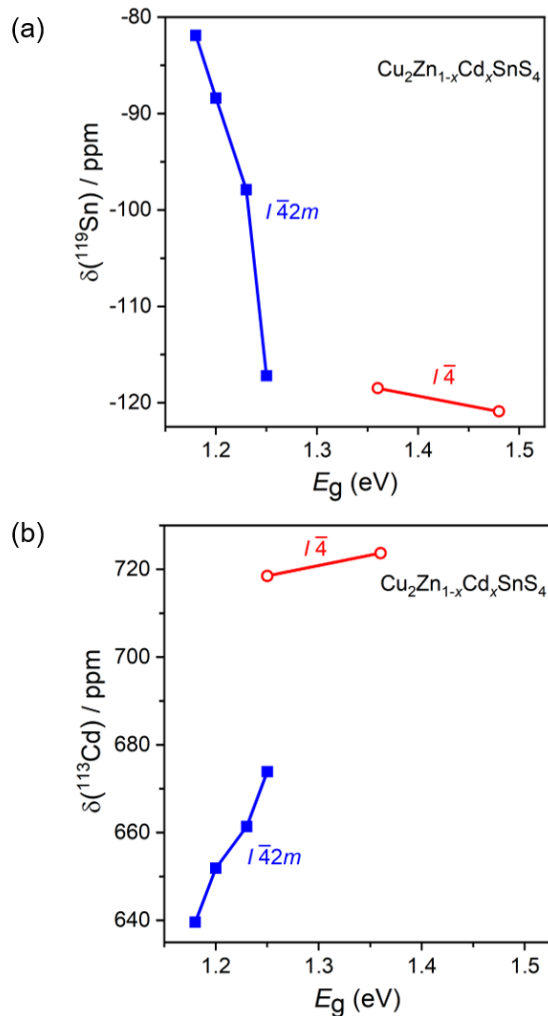


Figure 2.7. Variation of (a) average ^{119}Sn and (b) ^{113}Cd NMR isotropic chemical shifts with optical band gaps in $\text{Cu}_2\text{Zn}_{1-x}\text{Cd}_x\text{SnS}_4$.

2.4 Conclusions

The structural changes that occur in $\text{Cu}_2\text{Zn}_{1-x}\text{Cd}_x\text{SnS}_4$ at the long and short range have been examined extensively by powder XRD and solid-state NMR spectroscopy. Several key conclusions have been reached, resolving some ambiguities that had persisted in previous reports. First, and perhaps most important, the results strongly favor the simpler mechanism in which Cd substitution only entails disorder with Zn atoms, whereas more complicated mechanisms involving disorder of up to three atoms (Cu, Zn, Cd) are not likely. Although this conclusion disagrees with

some previous reports, it should be noted that the present analysis was performed on bulk samples prepared by reaction at 800 °C over 8 d, in contrast to other studies which are based on samples prepared as thin films or by ball-milling, with annealing at lower temperatures over much shorter times (600 °C, several hours), which would tend to lead to greater disorder. Second, the abrupt transition from the $I\bar{4}$ to the $I\bar{4}2m$ structure is confirmed to occur near $x = 0.4$ in $\text{Cu}_2\text{Zn}_{1-x}\text{Cd}_x\text{SnS}_4$, but in the $x = 0.3$ and 0.4 samples, phases with both structures coexist as a mixture, an insight that was gained from analysis of the ^{113}Cd NMR spectra and could not have been deduced from XRD. The ^{113}Cd isotropic chemical shifts correlate well with the Cd content, and, indeed, they could be used as a diagnostic feature to determine x for an unknown member of $\text{Cu}_2\text{Zn}_{1-x}\text{Cd}_x\text{SnS}_4$. Third, the degree of distortion around the tetrahedral sites occupied by metal atoms can be usefully related to NMR parameters such as C_Q or CSA. In this way, the two sets of Cu sites in the $I\bar{4}$ structure of $\text{Cu}_2\text{ZnSnS}_4$ (and other lightly Cd substituted members) can be assigned to separate peaks differing in C_Q . Because the relative areas of these two peaks remain unchanged upon Cd substitution, it can be assumed that Cu atoms are not involved in disorder with other atoms; this conclusion was further supported by comparison of ^{63}Cu and ^{67}Zn NMR spectra with those simulated from DFT computations. Fourth, NMR chemical shifts track closely with changes in medium range structure related to Cd/Zn substitution and the $I\bar{4}$ to the $I\bar{4}2m$ phase transition. These results demonstrate the utility of combining XRD and NMR analysis to determine structures holistically, at both long and short-range scales, which may prove useful to characterize other optical materials.

2.5 References

- (1) Siebentritt, S.; Schorr, S. Kesterites – a challenging material for solar cells. *Prog. Photovolt. Res. Appl.* **2012**, *20*, 512–519.

- (2) Fan, F.-J.; Wu, L.; Yu, S.-H. Energetic I–III–VI₂ and I₂–II–IV–VI₄ nanocrystals: synthesis, photovoltaic and thermoelectric applications. *Energy Environ. Sci.* **2014**, *7*, 190–208.
- (3) Shin, B.; Gunawan, O.; Zhu, Y.; Bojarczuk, N. A.; Chey, S. J.; Guha, S. Thin film solar cell with 8.4% power conversion efficiency using an earth-abundant Cu₂ZnSnS₄ absorber. *Prog. Photovolt. Res. Appl.* **2013**, *21*, 72–76.
- (4) Chen, S.; Yang, J.-H.; Gong, X. G.; Walsh, A.; Wei, S.-H. Intrinsic point defects and complexes in the quaternary kesterite semiconductor Cu₂ZnSnS₄. *Phys. Rev. B* **2010**, *81*, 245204.
- (5) Larsen, J. K.; Scragg, J. J. S.; Ross, N.; Platzer-Björkman, C. Band tails and Cu–Zn disorder in Cu₂ZnSnS₄ solar cells. *ACS Appl. Energy Mater.* **2020**, *3*, 7520–7526.
- (6) Li, J.; Wang, D.; Li, X.; Zeng, Y.; Zhang, Y. Cation substitution in earth-abundant kesterite photovoltaic materials. *Adv. Sci.* **2018**, *5*, 1700744.
- (7) Yan, C.; Sun, K.; Huang, J.; Johnston, S.; Liu, F.; Veettil, B. P.; Sun, K.; Pu, A.; Zhou, F.; Stride, J. A.; Green, M. A.; Hao, X. Beyond 11% efficient sulfide kesterite Cu₂Zn_xCd_{1-x}SnS₄ solar cell: effects of cadmium alloying. *ACS Energy Lett.* **2017**, *2*, 930–936.
- (8) Hall, S. R.; Szymański, J. T.; Stewart, J. M. kesterite, Cu₂(Zn,Fe)SnS₄, and stannite, Cu₂(Fe,Zn)SnS₄, structurally similar but distinct minerals. *Can. Mineral.* **1978**, *16*, 131–137.
- (9) Villars, P.; Cenzual, K. *Pearson's Crystal Data – Crystal Structure Database for Inorganic Compounds*, on DVD, release 2020/21; ASM International: Materials Park, OH, USA, 2020.
- (10) Schorr, S.; Hoebler, H.-J.; Tovar, M. A neutron diffraction study of the stannite-kesterite solid solution series. *Eur. J. Mineral.* **2007**, *19*, 65–73.
- (11) Ritscher, A.; Hoelzel, M.; Lerch, M. The order-disorder transition in Cu₂ZnSnS₄ – a neutron scattering investigation. *J. Solid State Chem.* **2016**, *238*, 68–73.
- (12) Xiao, Z.-Y.; Li, Y.-F.; Yao, B.; Deng, R.; Ding, Z.-H.; Wu, T.; Yang, G.; Li, C.-R.; Dong, Z.-Y.; Liu, L.; Zhang, L.-G.; Zhao, H.-F. Bandgap engineering of Cu₂Cd_xZn_{1-x}SnS₄ alloy for photovoltaic applications: A complementary experimental and first-principles study. *J. Appl. Phys.* **2013**, *114*, 183506.

- (13) Pilvet, M.; Kauk-Kuusik, M.; Altosaar, M.; Grossberg, M.; Danilson, M.; Timmo, K.; Mere, A.; Mikli, V. Compositionally tunable structure and optical properties of $\text{Cu}_{1.85}(\text{Cd}_x\text{Zn}_{1-x})_{1.1}\text{SnS}_{4.1}$ ($0 \leq x \leq 1$) monograin powders. *Thin solid films* **2015**, *582*, 180–183.
- (14) Su, Z.; Tan, J. M. R.; Li, X.; Zeng, X.; Batabyal, S. K.; Wong, L. H. Cation substitution of solution-processed $\text{Cu}_2\text{ZnSnS}_4$ thin film solar cell with over 9% efficiency. *Adv. Energy Mater.* **2015**, *5*, 1500682.
- (15) Ibraheem, A. S.; Al-Douri, Y.; Hashim, U.; Prakash, D.; Verma, K. D.; Ameri, M. Fabrication, analysis and characterization of $\text{Cu}_2\text{Zn}_{1-x}\text{Cd}_x\text{SnS}_4$ quinary alloy nanostructures deposited on GaN. *J. Mater. Sci.* **2016**, *51*, 6876–6885.
- (16) Hadke, S.; Chen, W.; Tan, J. M. R.; Guc, M.; Izquierdo-Roca, V.; Rignanese, G.-M.; Hautier, G.; Wong, L. H. Effect of Cd on cation redistribution and order-disorder transition in $\text{Cu}_2(\text{Zn,Cd})\text{SnS}_4$. *J. Mater. Chem. A* **2019**, *7*, 26927–26933.
- (17) Heppke, E. M.; Küllmey, T.; Efthimiopoulous, I.; Acvi, F. D.; Appelt, O.; Paulus, B.; Lerch, M. Experimental and theoretical investigations on the composition-dependent structural phase transition in $\text{Cu}_2\text{Cd}_x\text{Zn}_{1-x}\text{SnS}_4$. *Mater. Res. Express* **2019**, *6*, 125525.
- (18) Zhang, Q.; Deng, H.; Chen, L.; Yu, L.; Tao, J.; Sun, L.; Yang, P.; Chu, J. Cation substitution induced structural transition, band gap engineering and grain growth of $\text{Cu}_2\text{Cd}_x\text{Zn}_{1-x}\text{SnS}_4$ thin films. *J. Alloys Compd.* **2017**, *695*, 482–488.
- (19) Choubrac, L.; Paris, M.; Lafond, A.; Guillot-Deudon, C.; Rocquefelte, X.; Jobic, S. Multinuclear (^{67}Zn , ^{119}Sn and ^{65}Cu) NMR spectroscopy – an ideal technique to probe the cationic ordering in $\text{Cu}_2\text{ZnSnS}_4$ photovoltaic materials. *Phys. Chem. Chem. Phys.* **2013**, *15*, 10722–10725.
- (20) Lafond, A.; Guillot-Deudon, C.; Vidal, J.; Paris, M.; La, C.; Jobic, S. Substitution of Li for Cu in $\text{Cu}_2\text{ZnSnS}_4$: toward wide band gap absorbers with low cation disorder for thin film solar cells. *Inorg. Chem.* **2017**, *56*, 2712–2721.
- (21) Paris, M.; Larramona, G.; Bais, P.; Bourdais, S.; Lafond, A.; Choné, C.; Guillot-Deudon, C.; Delatouche, B.; Moisan, C.; Dennler, G. ^{119}Sn MAS NMR to assess the cationic disorder and the anionic distribution in sulfoselenide $\text{Cu}_2\text{ZnSn}(\text{S}_x\text{Se}_{1-x})_4$ compounds prepared from colloidal and ceramic routes. *J. Phys. Chem. C* **2015**, *119*, 26849–26857.

- (22) Paris, M.; Choubrac, L.; Lafond, A.; Guillot-Deudon, C.; Jobic, S. Solid-state NMR and Raman spectroscopy to address the local structure of defects and the tricky issue of the Cu/Zn disorder in Cu-poor, Zn-rich CZTS materials. *Inorg. Chem.* **2014**, *53*, 8646–8653.
- (23) Choubrac, L.; Lafond, A.; Paris, M.; Guillot-Deudon, C.; Jobic, S. The stability domain of the selenide kesterite photovoltaic materials and NMR investigation of the Cu/Zn disorder in $\text{Cu}_2\text{ZnSnSe}_4$ (CZTSe). *Phys. Chem. Chem. Phys.* **2015**, *17*, 15088–15092.
- (24) Johnson, N.; Pogue, E.; Rockett, A. Multi-nuclear (^{119}Sn and ^{65}Cu) NMR and Raman spectroscopy to probe secondary phases in $\text{Cu}_2\text{ZnSnS}_4$. *2016 IEEE 43rd Photovoltaic Specialists Conference (PVSC)* **2016**, 3046–3050.
- (25) Rodríguez-Carvajal, J. Introduction to the program Fullprof: refinement of crystal and magnetic structures from powder and single crystal data. *Lab. Léon Brillouin CEA-CNRS Saclay Fr.* **2001**.
- (26) Le Bail, A. Whole powder pattern decomposition methods and applications: a retrospection. *Powder Diffr.* **2005**, *20*, 316–326.
- (27) Kubelka, P. Ein Beitrag Zur Optik Der Farbanstriche (Contribution to the optic of paint). *Z. Tech. Phys.* **1931**, *12*, 593–601.
- (28) Kortüm, G. *Reflectance Spectroscopy*. Springer, 1969.
- (29) Karmakar, A.; Bhattacharya, A.; Bernard, G. M.; Mar, A.; Michaelis, V. K. Revealing the local Sn and Pb arrangements in $\text{CsSn}_x\text{Pb}_{1-x}\text{Br}_3$ perovskites with solid-state NMR spectroscopy. *ACS Mater. Lett.* **2021**, *3*, 261–267.
- (30) Gunther, W. R.; Michaelis, V. K.; Caporini, M. A.; Griffin, R. G.; Román-Leshkov, Y. Dynamic nuclear polarization NMR enables the analysis of Sn-beta zeolite prepared with natural abundance ^{119}Sn precursors. *J. Am. Chem. Soc.* **2014**, *136*, 6219–6222.
- (31) Eichele, K.; Wasylishen, R. E. High-resolution ^{113}Cd MAS NMR investigation of structure and bonding in cadmium thiocyanate coordination compounds. Distance dependence of cadmium-nitrogen indirect spin-spin coupling constants. *Inorg. Chem.* **1994**, *33*, 2766–2773.
- (32) Tang, J. A.; Ellis, B. D.; Warren, T. H.; Hanna, J. V.; Macdonald, C. L. B.; Schurko, R. W. Solid-state ^{63}Cu and ^{65}Cu NMR spectroscopy of inorganic and organometallic copper(I) complexes. *J. Am. Chem. Soc.* **2007**, *129*, 13049–13065.

- (33) Hibble, S. J.; Chippindale, A. M.; Marelli, E.; Kroeker, S.; Michaelis, V. K.; Greer, B. J.; Aguiar, P. M.; Bilbé, E. J.; Barney, E. R.; Hannon, A. C. Local and average structure in zinc cyanide: toward an understanding of the atomistic origin of negative thermal expansion. *J. Am. Chem. Soc.* **2013**, *135*, 16478–16489.
- (34) Eichele, K. WSolids1 Ver. 1.21. 3; University of Tübingen, 2015.
- (35) Clark, S. J.; Segall, M. D.; Pickard, C. J.; Hasnip, P. J.; Probert, M. I. J.; Refson, K.; Payne, M. C. First principles methods using CASTEP. *Z. Kristallogr.* **2005**, *220*, 567-570.
- (36) Perdew, J. P.; Burke, K.; Ernzerhof, M. Generalized gradient approximation made simple. *Phys. Rev. Lett.* **1996**, *77*, 3865–3868.
- (37) Yates, J. R.; Pickard, C. J.; Mauri, F. Calculation of NMR chemical shifts for extended systems using ultrasoft pseudopotentials. *Phys. Rev. B* **2007**, *76*, 024401.
- (38) Pickard, C. J.; Mauri, F. All-electron magnetic response with pseudopotentials: NMR chemical shifts. *Phys. Rev. B* **2001**, *63*, 245101.
- (39) Pickard, C. J.; Mauri, F.; Profeta, M. Accurate first principles prediction of ^{17}O NMR parameters in SiO_2 : assignment of the zeolite ferrierite spectrum. *J. Am. Chem. Soc.* **2003**, *125*, 541–548.
- (40) Shannon, R. D. Revised effective ionic radii and systematic studies of interatomic distances in halides and chalcogenides. *Acta Crystallogr., Sect. A: Cryst. Phys., Diffr., Theor. Gen. Crystallogr.* **1976**, *32*, 751–767.
- (41) Phillips, J. C. Electronegativity and tetragonal distortions in $A^{\text{II}}B^{\text{IV}}C^{\text{V}}_2$ semiconductors. *J. Phys. Chem. Solids* **1974**, *35*, 1205–1209.
- (42) Harris, R. K.; Becker, E. D.; De Menezes, S. M. C.; Goodfellow, R.; Granger, P. NMR nomenclature. Nuclear spin properties and conventions for chemical shifts (IUPAC recommendations 2001). *Pure Appl. Chem.* **2001**, *73*, 1795–1818.
- (43) Ha, M.; Karmakar, A.; Bernard, G. M.; Basilio, E.; Krishnamurthy, A.; Askar, A. M.; Shankar, K.; Kroeker, S.; Michaelis, V. K. Phase evolution in methylammonium tin halide perovskites with variable temperature solid-state ^{119}Sn NMR spectroscopy. *J. Phys. Chem. C* **2020**, *124*, 15015–15027.
- (44) Kubicki, D. J.; Prochowicz, D.; Salager, E.; Rakhmatullin, A.; Grey, C. P.; Emsley, L.; Stranks, S. D. Local structure and dynamics in methylammonium, formamidinium, and

- cesium tin(II) mixed-halide perovskites from ^{119}Sn solid-state NMR. *J. Am. Chem. Soc.* **2020**, *142*, 7813–7826.
- (45) Karmakar, A.; Bhattacharya, A.; Sarkar, D.; Bernard, G. M.; Mar, A.; Michaelis, V. K. Influence of hidden halogen mobility on local structure of $\text{CsSn}(\text{Cl}_{1-x}\text{Br}_x)_3$ mixed-halide perovskites by solid-state NMR. *Chem. Sci.* **2021**, *12*, 3253–3263.
- (46) Karmakar, A.; Askar, A. M.; Bernard, G. M.; Terskikh, V. V.; Ha, M.; Patel, S.; Shankar, K.; Michaelis, V. K. Mechanochemical synthesis of methylammonium lead mixed-halide perovskites: unraveling the solid-solution behavior using solid-state NMR. *Chem. Mater.* **2018**, *30*, 2309–2321.
- (47) Mason, J. *Solid state Nucl. Magn. Reson.* **1993**, *2*, 285–288.
- (48) Herzfeld, J.; Berger, A. E. Sideband intensities in NMR spectra of samples spinning at the magic angle. *J. Chem. Phys.* **1980**, *73*, 6021–6030.
- (49) Robinson, K.; Gibbs, G. V.; Ribbe, P. H. Quadratic elongation: a quantitative measure of distortion in coordination polyhedra. *Science* **1971**, *172*, 567–570.
- (50) Michaelis, V. K.; Kroeker, S. ^{73}Ge solid-state NMR of germanium oxide materials: experimental and theoretical studies. *J Phys. Chem. C* **2010**, *114*, 21736–21744.
- (51) Choubrac, L.; Lafond, A.; Guillot-Deudon, C.; Moëlo, Y.; Jobic, S. Structure flexibility of the $\text{Cu}_2\text{ZnSnS}_4$ absorber in low-cost photovoltaic cells: from the stoichiometric to the copper-poor compounds. *Inorg. Chem.* **2012**, *51*, 3346–3348.
- (52) Rosmus, K. A.; Brant, J. A.; Wisneski, S. D.; Clark, D. J.; Kim, Y. S.; Jang, J. I.; Brunetta, C. D.; Zhang, J.-H.; Srnec, M. N.; Aitken, J. A. Optical nonlinearity in $\text{Cu}_2\text{CdSnS}_4$ and $\alpha/\beta\text{-Cu}_2\text{ZnSiS}_4$: diamond-like semiconductors with high laser-damage thresholds. *Inorg. Chem.* **2014**, *53*, 7809–7811.
- (53) Kubicki, D. J.; Prochowicz, D.; Hofstetter, A.; Walder, B. J.; Emsley, L. ^{113}Cd solid-state NMR at 21.1 T reveals the local structure and passivation mechanism of cadmium in hybrid and all-inorganic halide perovskites. *ACS Energy Lett.* **2020**, *5*, 2964–2971.
- (54) Dean, P. A. W. A ^{113}Cd nuclear magnetic resonance study of some complexes of cadmium with phosphine oxides, sulfides, and selenides. *Can. J. Chem.* **1981**, *59*, 3221–3225.
- (55) Ratcliffe, C. I.; Yu, K.; Ripmeester, J. A.; Badruz Zaman, M.; Badarau, C.; Singh, S. Solid state NMR studies of photoluminescent cadmium chalcogenide nanoparticles. *Phys. Chem. Chem. Phys.* **2006**, *8*, 3510–3519.

- (56) Kuttathayil, A. V.; Handke, M.; Bergmann, J.; Lässig, D.; Lincke, J.; Haase, J.; Bertmer, M.; Krautscheid, H. ^{113}Cd solid-state NMR for probing the coordination sphere in metal–organic frameworks. *Chem. Eur. J.* **2015**, *21*, 1118–1124.
- (57) Chen, Y.; Dorn, R. W.; Hanrahan, M. P.; Wei, L.; Blome-Fernandez, R.; Medina-Gonzalez, A. M.; Adamson, M. A. S.; Flintgruber, A. H.; Vela, J.; Rossini, A. J. Revealing the surface structure of CdSe nanocrystals by dynamic nuclear polarization-enhanced ^{77}Se and ^{113}Cd solid-state NMR spectroscopy. *J. Am. Chem. Soc.* **2021**, *143*, 8747–8760.
- (58) Hanrahan, M. P.; Stein, J. L.; Park, N.; Cossairt, B. M.; Rossini, A. J. Elucidating the location of Cd^{2+} in post-synthetically treated InP quantum dots using dynamic nuclear polarization ^{31}P and ^{113}Cd solid-state NMR spectroscopy. *J. Phys. Chem. C* **2021**, *125*, 2956–2965.
- (59) Hanrahan, M. P.; Chen, Y.; Blome-Fernández, R.; Stein, J. L.; Pach, G. F.; Adamson, M. A. S.; Neale, N. R.; Cossairt, B. M.; Vela, J.; Rossini, A. J. Probing the surface structure of semiconductor nanoparticles by DNP SENS with dielectric support materials. *J. Am. Chem. Soc.* **2019**, *141*, 15532–15546.
- (60) Piveteau, L.; Dirin, D. N.; Gordon, C. P.; Walder, B. J.; Ong, T.-C.; Emsley, L.; Copéret, C.; Kovalenko, M. V. Colloidal-ALD-grown core/shell CdSe/CdS nanoplatelets as seen by DNP enhanced PASS–PIETA NMR spectroscopy. *Nano Lett.* **2020**, *20*, 3003–3018.
- (61) Larsen, F.H.; Lipton, A.S.; Jakobsen, H.J.; Nielsen, N.C.; Ellis, P.D. ^{67}Zn QCPMG solid-state NMR studies of zinc complexes as models of metalloproteins. *J. Am. Chem. Soc.* **1999**, *121*, 3783–3784.
- (62) Huang, Y.; Sutrisno, A. Recent Advances in Solid-State ^{67}Zn NMR studies: from nanoparticles to biological systems. *Annu. Rep. NMR Spectrosc.* **2014**, *81*, 1–46.
- (63) Madsen, R. S. K.; Qiao, A.; Sen, J.; Hung, I.; Chen, K.; Gan, Z.; Sen, S.; Yue, Y. Ultrahigh-field ^{67}Zn NMR reveals short-range disorder in zeolitic imidazolate framework glasses. *Science* **2020**, *367*, 1473–1476.
- (64) Chen, S.; Gong, X. G.; Walsh, A.; Wei, S.-H. Crystal and electronic band structure of $\text{Cu}_2\text{ZnSnX}_4$ ($X = \text{S}$ and Se) photovoltaic absorbers: first-principles insights. *Appl. Phys. Lett.* **2009**, *94*, 041903.

- (65) Chen, S.; Gong, X. G.; Walsh, A. Wei, S.-H. Electronic structure and stability of quaternary chalcogenide semiconductors derived from cation cross-substitution of II-VI and I-III-VI₂ compounds. *Phys. Rev. B* **2009**, *79*, 165211.
- (66) Ramsey, N. F. Magnetic shielding of nuclei in molecules. *Phys. Rev.* **1950**, *78*, 699–703.
- (67) Yesinowski, J. P. Solid-state NMR of inorganic semiconductors. In *Solid State NMR*; Chan, J. C. C., Ed.; Springer, 2012.
- (68) Thiessen, A. N.; Ha, M.; Hooper, R. W.; Yu, H.; Oliynyk, A. O.; Veinot, J. G. C.; Michaelis, V. K. Silicon nanoparticles: are they crystalline from the core to the surface? *Chem. Mater.* **2019**, *31*, 678-688.
- (69) Cadars, S.; Smith, B. J.; Epping, J. D.; Acharya, S.; Belman, N.; Golan, Y.; Chmelka, B. F. Atomic positional versus electronic order in semiconducting ZnSe nanoparticles. *Phys. Rev. Lett.* **2009**, *103*, 136802.
- (70) Tomaselli, M.; Yarger, J. L.; Bruchez, M.; Havlin, R. H.; deGraw, D.; Pines, A.; Alivisatos, A. P. NMR study of InP quantum dots: surface structure and size effects. *J. Chem. Phys.* **1999**, *110*, 8861–8864.
- (71) Thayer, A. M.; Steigerwald, M. L.; Duncan, T. M.; Douglass, D. C. NMR study of semiconductor molecular clusters. *Phys. Rev. Lett.* **1988**, *60*, 2673–2676.
- (72) Bawendi, M. G.; Carroll, P. J.; Wilson, W. L.; Brus, L. E. Luminescence properties of CdSe quantum crystallites: resonance between interior and surface localized states. *J. Chem. Phys.* **1992**, *96*, 946–954.
- (73) Beshah, K.; Zamir, D.; Becla, P.; Wolff, P. A.; Griffin, R. G. Te and Cd nuclear-magnetic-resonance study of local structure and bonding in Cd_{1-x}Zn_xTe. *Phys. Rev. B* **1987**, *36*, 6420–6425.
- (74) Willig, A.; Sapoval, B.; Leibler, K.; Verie, C. Chemical shift of NMR in HgTe, CdTe and their alloys. *J. Phys. C: Solid State Phys.* **1976**, *9*, 1981–1989.

Chapter 3

Mercurial possibilities: determining site distributions in $\text{Cu}_2\text{HgSnS}_4$ using $^{63/65}\text{Cu}$, ^{119}Sn , and ^{199}Hg solid-state NMR spectroscopy

3.1 Introduction

Multinary chalcogenides have elicited interest for various materials applications, and among these, $\text{Cu}_2\text{ZnSnS}_4$ has stood out as a promising photovoltaic material because it has a direct band gap of appropriate magnitude (1.5 eV), a high absorption coefficient (10^4 cm^{-1}), and a composition derived from inexpensive and earth-abundant elements.¹⁻⁴ The power conversion efficiency of $\text{Cu}_2\text{ZnSnS}_4$ is relatively high (9%), but much remains to be done before it can rival conventional materials such as Si (>20%). It has become very popular to suggest new photovoltaic materials through first-principles calculations and machine learning algorithms;^{5,6} such prognostications are facile to make but hardly ever tested through experiment. Among various strategies to increase the efficiency, substitution of Zn in $\text{Cu}_2\text{ZnSnS}_4$ with Cd and Hg has been proposed,⁷⁻¹² even though this entails new risks of toxicity that will eventually need to be mitigated. Some calculations indicate that the “spectroscopically limited maximum efficiency” could reach as high as 25% for $\text{Cu}_2\text{CdSnS}_4$ and $\text{Cu}_2\text{HgSnS}_4$.^{11,12} Of course, the reliability of such predictions depends on the accuracy of the crystal structures assumed,¹³ and in my opinion, further experimental evidence would be beneficial. In an actual solar cell fabricated from a $\text{Cu}_2\text{Zn}_{0.6}\text{Cd}_{0.4}\text{SnS}_4$ absorber, the partial substitution of Zn with Cd led to small improvements in efficiency (11%).^{7,8}

$\text{Cu}_2\text{ZnSnS}_4$, $\text{Cu}_2\text{CdSnS}_4$, and $\text{Cu}_2\text{HgSnS}_4$ have long been known to adopt tetragonal structures from X-ray diffraction (XRD) studies (**Figure 3.1**).^{14,15} All metal atoms lie within tetrahedral sites located on the $z = 0, \frac{1}{4}, \frac{1}{2},$ and $\frac{3}{4}$ planes. For $\text{Cu}_2\text{ZnSnS}_4$ (space group $I\bar{4}$), there is broad consensus that the Cu atoms occupy two sets of sites ($2a, 2c$) which lie within all planes, although disorder of Cu and Zn atoms is possible depending on preparative conditions.¹⁶ For $\text{Cu}_2\text{CdSnS}_4$ (space group $I\bar{4}2m$), the Cu atoms occupy one set of sites ($4d$), which lie within alternate planes.^{17,18} For $\text{Cu}_2\text{HgSnS}_4$, two structural models have been reported having site distributions similar to that of $\text{Cu}_2\text{CdSnS}_4$, with Cu atoms lying in alternate planes but with subtle differences.

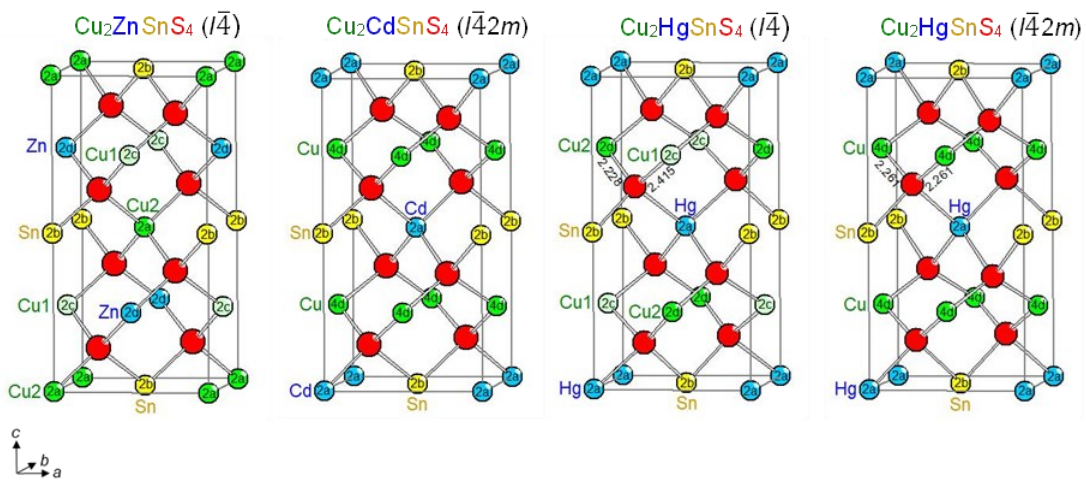


Figure 3.1. Structural models for $\text{Cu}_2\text{ZnSnS}_4$, $\text{Cu}_2\text{CdSnS}_4$, and $\text{Cu}_2\text{HgSnS}_4$. Two models have been proposed for $\text{Cu}_2\text{HgSnS}_4$ distinguished by the presence of two Cu sites in $I\bar{4}$ vs one site in $I\bar{4}2m$.

From powder XRD data, Kabalov et al. proposed that the Cu atoms occupy two sets of sites ($2c, 2d$) in $I\bar{4}$.¹⁹ From single-crystal XRD data, Kaplunnik et al. proposed that the Cu atoms half-occupy one set of split sites ($8h$ at $0, \frac{1}{2}, 0.2498$) in $I\bar{4}2m$, but the splitting is so small that merging them into fully occupied unsplit sites ($4d$ at $0, \frac{1}{2}, \frac{1}{4}$) is clearly a better description, corresponding

to the same structure as $\text{Cu}_2\text{CdSnS}_4$.²⁰ The key distinction is that the Cu–S distances fall into two sets (2.23 Å and 2.42 Å) in the Kabalov model, but one set (2.26 Å) in the Kaplunnik model.

Given that $\text{Cu}_2\text{ZnSnS}_4$, $\text{Cu}_2\text{CdSnS}_4$, and $\text{Cu}_2\text{HgSnS}_4$ exhibit different site distributions, solid solutions derived from them are likely to complex site disorder, as observed in $\text{Cu}_2\text{Zn}_{1-x}\text{Cd}_x\text{SnS}_4$, for example.^{9,21} As a complementary method to confirm the site distributions established from earlier structural determinations on the parent compounds, solid-state nuclear magnetic resonance (NMR) spectroscopy provides valuable information on the local environments around specific atoms, as has been demonstrated for $(\text{Cu}_{1-x}\text{Li}_x)_2\text{ZnSnS}_4$, $\text{Cu}_2\text{Zn}_{1-x}\text{Cd}_x\text{SnS}_4$, and $\text{Cu}_2\text{ZnSn}(\text{S}_{1-x}\text{Se}_x)_4$, among other semiconducting and catalytic compounds.^{22–27}

To clarify the site distributions, we report here an analysis of the $^{63/65}\text{Cu}$, ^{119}Sn , and ^{199}Hg NMR spectra for $\text{Cu}_2\text{HgSnS}_4$ and compare these results to our recent work on $\text{Cu}_2\text{ZnSnS}_4$ and $\text{Cu}_2\text{CdSnS}_4$.²³ Furthermore, a full analysis of the chemical shift anisotropy (CSA) and electric field gradient (EFG) tensors are presented for the first time.^{23,59} The effect of annealing in $\text{Cu}_2\text{HgSnS}_4$ was probed by XRD and NMR measurements. Optical band gap measurements and electronic structure calculations were also performed on $\text{Cu}_2\text{ZnSnS}_4$, $\text{Cu}_2\text{CdSnS}_4$, and $\text{Cu}_2\text{HgSnS}_4$.

3.2 Experimental

3.2.1 Synthesis

Starting materials were Cu powder (99.5%, Alfa-Aesar), Zn granules (99.9%, Baker), Cd powder (99.5%, Alfa-Aesar), HgS powder (99%, Alfa-Aesar), Sn powder (99.9%, Cerac), and S flakes (99.9%, Sigma-Aldrich). Stoichiometric mixtures of these substances were prepared with the loading compositions $\text{Cu}_2\text{ZnSnS}_4$, $\text{Cu}_2\text{CdSnS}_4$, and $\text{Cu}_2\text{HgSnS}_4$. The mixtures were ground together, pressed into pellets, and placed within carbon-coated fused silica tubes, which were

evacuated and sealed. For $\text{Cu}_2\text{ZnSnS}_4$ and $\text{Cu}_2\text{CdSnS}_4$, the tubes were heated to 250 °C over 5 h, held there for 2 h, heated to 800 °C over 18 h, held there for 4 d, and then cooled to room temperature over 24 h. For $\text{Cu}_2\text{HgSnS}_4$, the tubes were heated to 250 °C over 5 h, held there for 2 h, heated to 700 °C over 15 h, held there for 2 d, and then cooled to room temperature over 24 h. The slightly lower annealing temperature was used in the synthesis of $\text{Cu}_2\text{HgSnS}_4$ as a pre-emptive measure to minimize volatilization losses of HgS, which has a relatively low boiling point of 584 °C. The samples were ground, pressed into pellets, and subjected to a second heat treatment at 800 °C for 4 d (for $\text{Cu}_2\text{ZnSnS}_4$ and $\text{Cu}_2\text{CdSnS}_4$) or 700 °C for 1 d (for $\text{Cu}_2\text{HgSnS}_4$). This treatment ensures that the samples are pure phase.

3.2.2 XRD and energy-dispersive X-ray (EDX) analysis

Powder XRD patterns were collected on a Bruker D8 Advance diffractometer equipped with a $\text{Cu } K\alpha_1$ radiation source operated at 40 kV and 40 mA. Unit cell parameters were refined, and Le Bail profile fitting was applied using the FullProf suite of programs.²⁸ Samples were examined on a Zeiss Sigma 300 VP field-emission scanning electron microscope, operated with an accelerating voltage of 15 kV, and their elemental compositions were obtained by EDX analysis.

3.2.3 Diffuse reflectance spectroscopy

Optical diffuse reflectance spectra were measured from 200 nm (6.2 eV) to 2000 nm (0.6 eV) on a Cary 5000 UV-vis-NIR spectrophotometer, with a polytetrafluoroethylene disc having >98% reflectivity used as a reflectance standard. The reflectance spectra were converted to optical

absorption spectra using the Kubelka-Munk function, $F(R) = \alpha/S = (1-R)^2/2R$, where α is the Kubelka–Munk absorption coefficient, S is the scattering coefficient, and R is the reflectance.²⁹

3.2.4 Solid-state NMR spectroscopy

Solid-state $^{63/65}\text{Cu}$, ^{119}Sn , and ^{199}Hg NMR spectra were collected on Bruker Avance Neo 300 ($B_0 = 7.05$ T), Avance III HD 400 ($B_0 = 9.40$ T), Avance Neo 500 ($B_0 = 11.75$ T), or Avance II 900 ($B_0 = 21.1$ T) spectrometers equipped with double resonance H/X magic-angle-spinning (MAS) Bruker probes, with experimental details listed in **Table 3.1**. Samples were ground and packed into 4-mm outer diameter (o.d.) ZrO_2 rotors sealed with Kel-F caps, or 2.5-mm o.d. and 1.3-mm o.d. ZrO_2 rotors sealed with Vespel top and bottom caps. The non-spinning NMR spectra at 21.1 T were acquired using a home-built 4-mm solenoid probe (pure Ag R.F. coil to minimize probe background from Cu metal). The spectra were processed using the Bruker TOPSPIN 4.0.6 software package with 100–300 exponential apodizations and they were fit using the Dmfit³⁰ program to extract various NMR parameters. Reference standards were $\text{CuCl}(\text{s})$ (0 ppm for $^{63/65}\text{Cu}$ NMR), $(\text{C}_6\text{H}_{11})_4\text{Sn}(\text{s})$ (−97.5 ppm for ^{119}Sn NMR, which corresponds to 0 ppm for $(\text{CH}_3)_4\text{Sn}$), and $\text{HgF}_2(\text{s})$ (−2826 ppm for ^{199}Hg NMR).^{31–33}

Table 3.1. Experimental conditions for acquisition of NMR spectra

	⁶⁵ Cu	¹¹⁹ Sn	¹⁹⁹ Hg
spinning conditions	non-spinning	non-spinning	non-spinning
B_0 (T)	7.05, 11.75, 21.1	9.40	9.40
pulse sequence	quadrupolar echo	Hahn echo	Hahn echo
$\pi/2$ pulse (μ s)	2 or 1	4	4
$\gamma B_1/2\pi$ (kHz)	125	62.5	62.5
τ (μ s)	50	30	30
recycle delay (s)	2	50–150	3
co-added transients	2048–4096 or 256–512	1024–2048	6000–15360
	⁶³ Cu	¹¹⁹ Sn	¹⁹⁹ Hg
spinning conditions	MAS ($\omega_r/2\pi = 31.25$ and 62.5 kHz)	MAS ($\omega_r/2\pi = 14$ kHz)	MAS ($\omega_r/2\pi = 14$ kHz)
B_0 (T)	21.1	9.40	9.40
pulse sequence	rotor-synchronized quadrupolar echo	rotor-synchronized Hahn echo	rotor-synchronized Hahn echo
$\pi/2$ pulse (μ s)	1	4	4
$\gamma B_1/2\pi$ (kHz)	125	62.5	62.5
τ (μ s)	32 and 16	71.4	71.4
recycle delay (s)	2	50–150	3
co-added transients	1024	1024–2048	6000–15360

As a reminder, NMR spectra are typically characterized by features based on the chemical shift anisotropy (CSA) and quadrupolar coupling interactions, which are tensor quantities.^{34–44} The lineshape of an NMR signal is described by its isotropic chemical shift, $\delta_{\text{iso}} = (\delta_{11} + \delta_{22} + \delta_{33})/3$, its span, $\Omega = \delta_{11} - \delta_{33}$, and its skew, $\kappa = 3(\delta_{22} - \delta_{\text{iso}})/\Omega$. For nuclei having $I > 1/2$, the nuclear quadrupole coupling constant is $C_Q = eQV_{zz}/h$ (where e is the elementary charge, Q is the quadrupolar moment of the nucleus, V_{zz} is the largest principal component of the electric field

gradient (EFG), and h is Planck's constant) and the asymmetry parameter is $\eta = (V_{xx} - V_{yy})/V_{zz}$ (where $|V_{xx}| \leq |V_{yy}| \leq |V_{zz}|$).

3.2.5 Quantum chemical computations

The magnetic shielding and EFG ($I > 1/2$) tensors were calculated using the program CASTEP,⁴⁵ which applies a gauge-including projector augmented plane wave basis set suitable for periodic structures and the Perdew-Burke-Ernzerhof (PBE) functional in the generalized gradient approximation for the exchange-correlation energy.^{46–48} Ultrasoft pseudopotentials and zeroth-order regular approximation relativistic effects were applied. Calculations were carried out with an extreme accuracy basis set, a maximum plane-wave energy of 500–566 eV, and a Monkhorst-Pack grid of $4 \times 4 \times 20$ k -points for $\text{Cu}_2\text{ZnSnS}_4$ and $\text{Cu}_2\text{CdSnS}_4$ or $20 \times 20 \times 10$ k -points for $\text{Cu}_2\text{HgSnS}_4$. The computed magnetic shieldings were converted to chemical shifts, δ (ppm) = $\sigma_{\text{ref}}^{\text{calc}} - \sigma_{\text{model}}^{\text{calc}}$, using SnO for ^{119}Sn ($\sigma_{\text{ref}}^{\text{calc}} = 2802$), HgF_2 for ^{199}Hg ($\sigma_{\text{ref}}^{\text{calc}} = 6261$ ppm) and $\text{Cu}_2\text{HgSnS}_4$ for ^{65}Cu ($\sigma_{\text{ref}}^{\text{calc}} = -7$ ppm). The $^{63/65}\text{Cu}$ isotropic chemical shift was set to 815 ppm in $\text{Cu}_2\text{HgSnS}_4$ ($I\bar{4}2m$).

The electronic band structure and density of states (DOS) were calculated using the projected augmented wave method as implemented in the Vienna ab initio simulation package (VASP 5.44), with the generalized gradient approximation parameterized by PBE used to treat exchange and correlation.^{46,49–51} The recommended standard Cu, Zn, Cd, Hg, Sn_d, and S potentials were used, with the plane-wave basis cutoff energy set to 400 eV. The first Brillouin zone was sampled by a $9 \times 9 \times 5$ k -point grid. The convergence criteria were set to 10^{-6} eV for electronic optimization, and $|-2 \times 10^{-2}|$ eV for ionic relaxation. To correct for the underestimation of the PBE band gap, a hybrid HSE06 functional (PBE:Hartree-Fock = 65:35) was applied. Spin-

orbit interactions were not considered to reduce computational cost. Chemical bonding was examined by evaluating projected crystal orbital Hamilton populations ($-p\text{COHP}$), electron localization functions (ELF), and Bader charges, using the program LOBSTER (version 3.2.0).⁵²

3.3 Results and discussion

3.3.1 Crystal structure of Cu_2MSnS_4 ($M = \text{Zn, Cd, Hg}$)

Samples of $\text{Cu}_2\text{ZnSnS}_4$, $\text{Cu}_2\text{CdSnS}_4$, and $\text{Cu}_2\text{HgSnS}_4$, which were prepared at 700–800 °C, were confirmed to be single-phase from powder XRD patterns (**Figure 3.2**) and to have compositions in good agreement with expectations from EDX analyses (**Table A3.1** in Appendix 3). From Le Bail fittings of the powder XRD data (**Figure A3.1** in Appendix 3), the refined tetragonal cell parameters were found to agree well with literature values (**Table A3.2** in Appendix 3). The unit cell volume expands on proceeding from $\text{Cu}_2\text{ZnSnS}_4$ to $\text{Cu}_2\text{CdSnS}_4$, and then is little changed in $\text{Cu}_2\text{HgSnS}_4$, in accordance with trends in typical distances for Zn–S (2.3–2.5 Å), Cd–S (2.3–2.8 Å), and Hg–S bonds (2.3–2.8 Å). The $c/2a$ ratio serves as a useful measure for the degree of tetragonal distortion in these structures. For $\text{Cu}_2\text{ZnSnS}_4$, this ratio is essentially unity (0.997–0.998). For $\text{Cu}_2\text{CdSnS}_4$ and $\text{Cu}_2\text{HgSnS}_4$, this ratio is perceptibly smaller (0.97–0.98), giving rise to slight splitting of peaks in the powder XRD patterns, the most prominent being seen in the 220 and 204 peaks near 47° in 2θ . There are occasional statements made in the literature that this splitting offers direct evidence for structural assignments (i.e., site distributions and space groups), but such pronouncements are misguided.

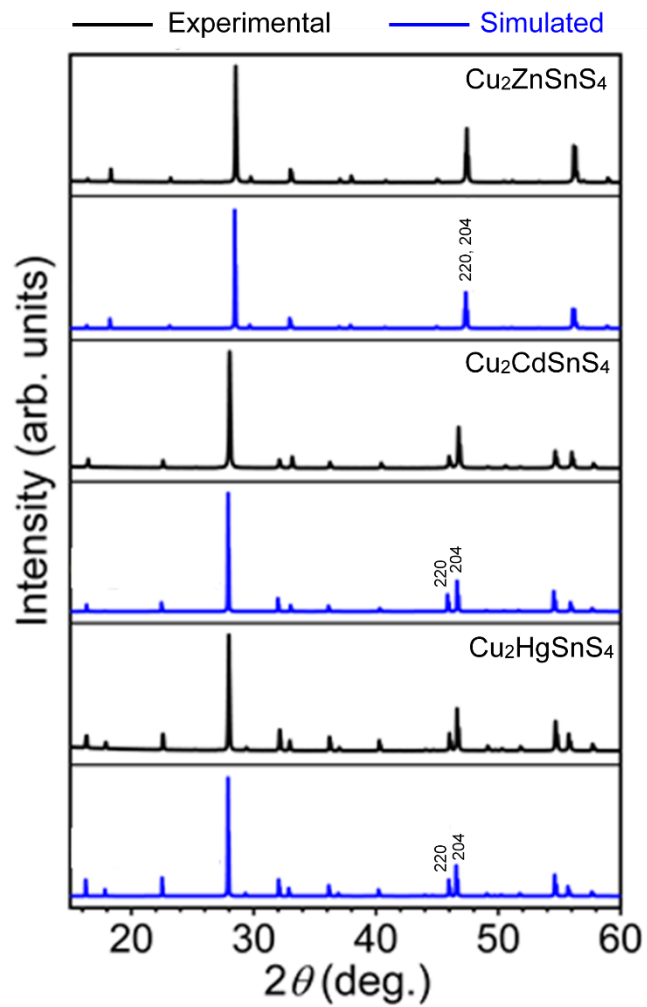


Figure 3.2. Powder XRD patterns for $\text{Cu}_2\text{ZnSnS}_4$, $\text{Cu}_2\text{CdSnS}_4$, and $\text{Cu}_2\text{HgSnS}_4$.

To examine the local environments around atoms in more detail, NMR spectra were analyzed for these compounds (NMR-fitted parameters are summarized in **Table 3.2**).

Table 3.2. Experimental and GIPAW DFT-computed ^{65}Cu , ^{119}Sn , and ^{199}Hg NMR parameters for Cu_2MSnS_4 ($M = \text{Zn, Cd, Hg}$).

	$\text{Cu}_2\text{ZnSnS}_4$		$\text{Cu}_2\text{CdSnS}_4$		$\text{Cu}_2\text{HgSnS}_4$		
	exp	DFT ($\bar{1}\bar{4}$)	exp	DFT ($\bar{1}\bar{4}2m$)	exp	DFT ($\bar{1}\bar{4}$)	DFT ($\bar{1}\bar{4}2m$)
^{119}Sn parameters ^a							
δ_{iso} (ppm, ± 0.5)	-120.9	238 ^d	-81.5	243 ^d	-89.8	211 ^d	139 ^d
Ω (ppm)	30	55	110	112	113	104	52
κ	-0.45	-1	+0.95	+1	+0.95	+1	+1
^{65}Cu parameters ^b							
δ_{iso} (ppm, ± 2)	804 (2a)	767(2a) ^d	761	802 ^d	815	594(2d) ^d	815 ^d
		786 (2c)				752(2c) ^d	
Ω (ppm, ± 5)	270 (2a)	366 (2a)	315	290	330	433 (2d)	403
		118 (2c)				295 (2c)	
κ (± 0.05)	+1 (2a)	+1 (2a)	-1	-1	-1	-1 (2d)	-1
		-1 (2c)				-1 (2c)	
C_Q (MHz, ± 0.1)	6.5 (2a)	7.2 (2a)	0.7	4.4	1.1	1.2 (2d)	5.3
		1.6 (2c)				4.7 (2c)	
η (± 0.1)	0 (2a)	0 (2a)	0	0	0.0	0 (2d)	+0.0
		0 (2c)				0 (2c)	
^{199}Hg parameters ^c							
δ_{iso} (ppm, ± 0.5)					-540.9	-667 ^d	376 ^d
Ω (ppm, ± 5)					183	152	149
κ (± 0.05)					+0.95	+1	+1

^a Non-spinning ^{119}Sn NMR ($B_0 = 9.4$ T) were used to determine the parameters (**Figure 3. 3**).

^b Non-spinning ^{65}Cu NMR acquired at 7.05, 11.75 and 21.1 T were used to determine the parameters (**Figure 3. 6**).

^c Non-spinning ^{199}Hg NMR ($B_0 = 9.4$ T) were used to determine the parameters (**Figure 3. 7**).

^d GIPAW-DFT computed isotropic chemical shift (δ_{iso} , ppm) values. Note that spin-orbit effects are unaccounted.

3.3.2 Local structure around Sn

The Sn atoms occupy one set of sites at $2b$ ($0, 0, \frac{1}{2}; \frac{1}{2}, \frac{1}{2}, 0$) in $\text{Cu}_2\text{HgSnS}_4$, similar to the Sn sites found in both $\text{Cu}_2\text{ZnSnS}_4$ and $\text{Cu}_2\text{CdSnS}_4$ compounds. They are surrounded in the first coordination sphere by four S atoms in tetrahedral geometry and in the second coordination sphere by eight Cu and four M atoms, but the arrangement of these atoms differs in $\text{Cu}_2\text{ZnSnS}_4$ vs

$\text{Cu}_2\text{CdSnS}_4$ and $\text{Cu}_2\text{HgSnS}_4$. These different environments were examined by ^{119}Sn NMR spectroscopy ($I = 1/2$; 8.6% natural abundance; $\mathcal{E} = 37.29\%$)⁵³, which is a highly sensitive technique showing a wide diamagnetic chemical shift range of up to 6000 ppm.^{54–57} The single resonance seen in the ^{119}Sn MAS NMR spectra for all three compounds is consistent with the presence of a unique Sn site, with the isotropic chemical shift (δ_{iso}) in $\text{Cu}_2\text{ZnSnS}_4$ (–120.9 ppm) found at a significantly lower frequency than in $\text{Cu}_2\text{CdSnS}_4$, $\delta_{\text{iso}} = -81.5$ ppm and $\text{Cu}_2\text{HgSnS}_4$, $\delta_{\text{iso}} = -89.8$ ppm (**Figure A3.2** in Appendix 3).

The non-spinning ^{119}Sn NMR spectra, which provide information about the CSA tensor, show that the span is narrow in $\text{Cu}_2\text{ZnSnS}_4$ (30 ppm) but wide in $\text{Cu}_2\text{CdSnS}_4$ (110 ppm) and $\text{Cu}_2\text{HgSnS}_4$ (113 ppm) indicating a less symmetric Sn environment (**Figure 3.3**). The skew is negative for $\text{Cu}_2\text{ZnSnS}_4$ (–0.45), but positive and close to unity for both $\text{Cu}_2\text{CdSnS}_4$ and $\text{Cu}_2\text{HgSnS}_4$ (+0.95), indicating axially symmetric CSA tensors with δ_{33} as the unique component. These results can be understood in terms of the tetrahedral coordination around the Sn sites by S atoms, which form nearly ideal angles in $\text{Cu}_2\text{ZnSnS}_4$ (109.5°), but show deviations in $\text{Cu}_2\text{CdSnS}_4$ ($108.7\text{--}109.8^\circ$) and $\text{Cu}_2\text{HgSnS}_4$ ($100.0\text{--}114.4^\circ$).^{18,20,58} This effect may be further influenced by the arrangement of Cu and *M* atoms in the second coordination sphere, which is closer to spherical symmetry in $\text{Cu}_2\text{ZnSnS}_4$, by virtue of the Cu atoms lying on all planes, in contrast to the axially symmetric symmetry in $\text{Cu}_2\text{CdSnS}_4$ and $\text{Cu}_2\text{HgSnS}_4$, by virtue of the Cu atoms lying on alternate planes. GIPAW DFT computed CSA tensor components bisect the SnS_4 tetrahedral angles with the δ_{11} and δ_{22} components found to be out of the plane of the page for $\text{Cu}_2\text{CdSnS}_4$ and $\text{Cu}_2\text{ZnSnS}_4$, respectively. From GIPAW DFT computations on $\text{Cu}_2\text{HgSnS}_4$, the computed span in $\text{Cu}_2\text{HgSnS}_4$ is 104 ppm (Kabalov model) or 52 ppm (Kaplunnik model), and the skew is +1, in reasonable agreement with observations.

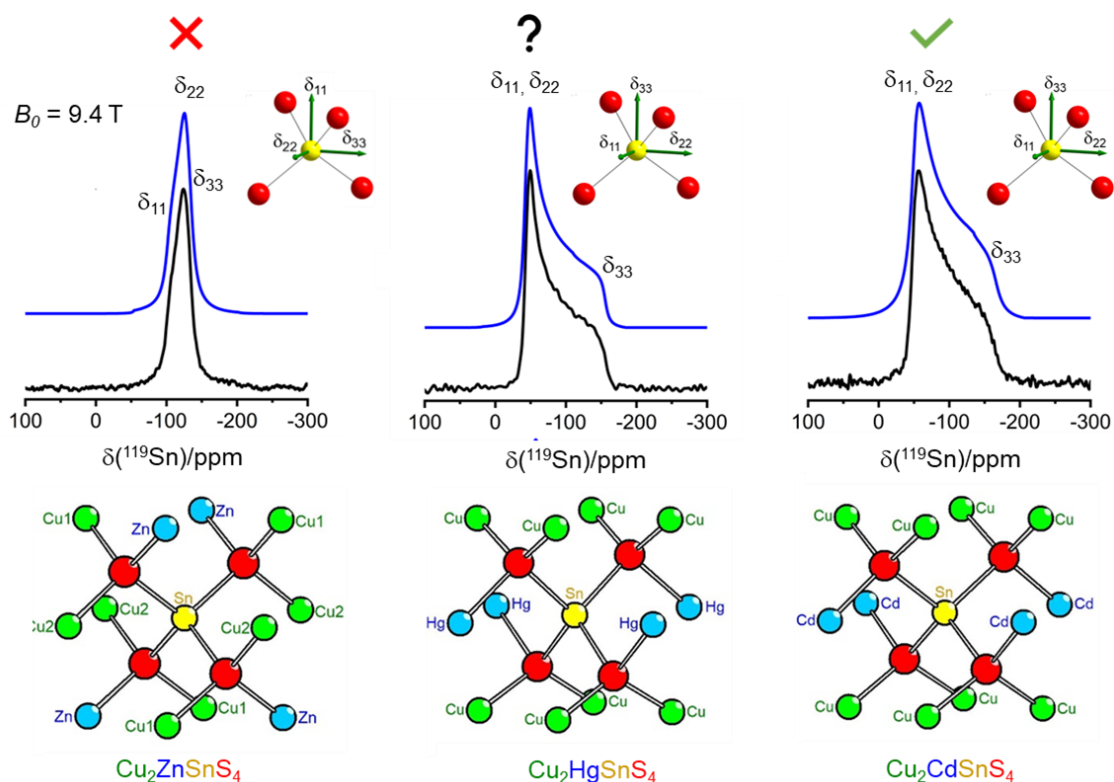


Figure 3.3. Experimental (black) and spectral simulation (blue) of non-spinning ^{119}Sn NMR spectra and local chemical environments around Sn atoms for $\text{Cu}_2\text{ZnSnS}_4$, $\text{Cu}_2\text{HgSnS}_4$, and $\text{Cu}_2\text{CdSnS}_4$. GIPAW DFT CSA tensors, δ_{11} , δ_{22} and δ_{33} are shown as green arrows (top). The resemblance of ^{119}Sn local chemical environment with $\text{Cu}_2\text{CdSnS}_4$ is indicated with a \checkmark (green), whereas the disagreement with $\text{Cu}_2\text{ZnSnS}_4$ is indicated with an X (red). The experimental NMR simulations (blue) were performed using the Dmfit software.

3.3.3 Local structure around Cu

The most definitive evidence to determine the number of crystallographically inequivalent Cu sites in Cu_2MSnS_4 ($M = \text{Zn}, \text{Cd}, \text{Hg}$) was provided by the $^{63/65}\text{Cu}$ NMR spectra. The first coordination sphere consists of four S atoms and the second coordination sphere consists of four Cu, four M, and four Sn atoms, but in different arrangements. The ^{63}Cu NMR spectra ($I = 3/2$; 69.7% natural abundance, $Q = -22.0 \text{ fm}^2$, $E = 26.5\%$)⁵³ show two resonances for $\text{Cu}_2\text{ZnSnS}_4$ with centre of gravity shifts (δ_{cgs}) of 793 and 749 ppm, but one for $\text{Cu}_2\text{CdSnS}_4$ ($\delta_{\text{cgs}} = 753 \text{ ppm}$) and

$\text{Cu}_2\text{HgSnS}_4$ ($\delta_{\text{cgs}} = 810$ ppm) (**Figure 3.4**). These observations confirm the presence of two Cu sites ($2a$, $2c$) in $\text{Cu}_2\text{ZnSnS}_4$ vs one site ($4d$) in $\text{Cu}_2\text{CdSnS}_4$. The occurrence of one resonance in $\text{Cu}_2\text{HgSnS}_4$ supports the Kaplunnik model in which Cu atoms occupy one site ($4d$), as in $\text{Cu}_2\text{CdSnS}_4$, and rules out the Kabalov model in which Cu atoms occupy two sites ($2c$, $2d$) which differ slightly in Cu–S distances.

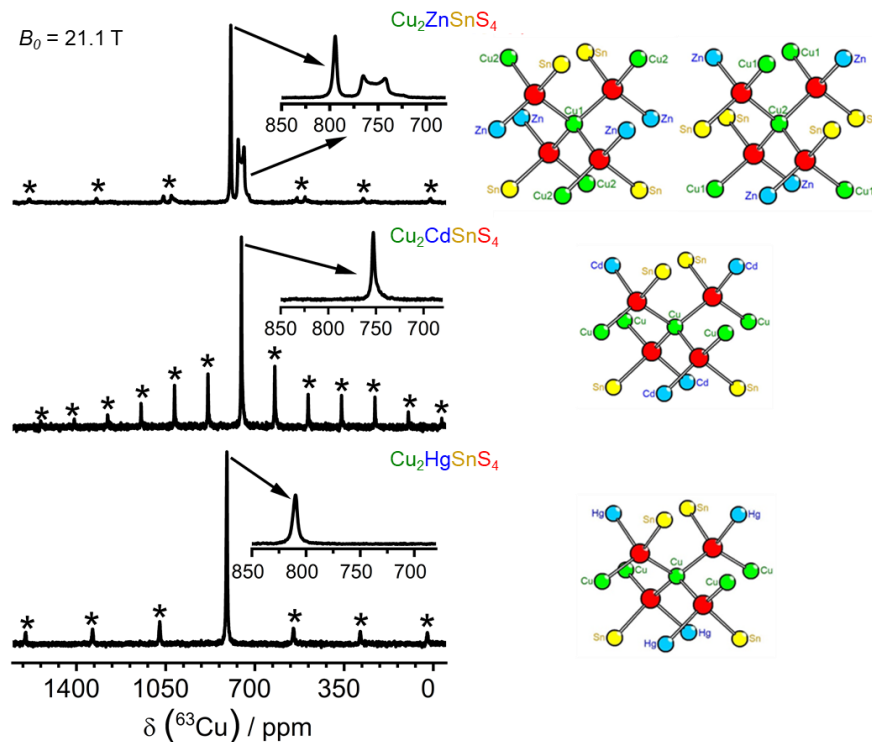


Figure 3.4. ^{63}Cu MAS NMR spectra and local environments around Cu atoms for $\text{Cu}_2\text{ZnSnS}_4$ ($\omega_r/2\pi = 62.5$ kHz), $\text{Cu}_2\text{CdSnS}_4$ ($\omega_r/2\pi = 31.25$ kHz), and $\text{Cu}_2\text{HgSnS}_4$ ($\omega_r/2\pi = 62.5$ kHz). Central transitions are enlarged in the insets. Asterisks mark spinning sideband

To discount the possibility that sizeable quadrupolar interactions or poor spectral resolution could hinder the detection of additional Cu sites, MAS ^{63}Cu and non-spinning ^{65}Cu NMR spectra were simulated from GIPAW DFT calculations for $\text{Cu}_2\text{HgSnS}_4$ with these two models (**Figure 3.5**). Under experimental conditions of 21.1 T, the resonances for the two Cu sites in the Kabalov model would be clearly resolvable, with moderate C_Q values and distinguishable isotropic

chemical shifts. Instead, these quantum chemical computations strongly favour the Kaplunnik model containing one Cu site, although they do overestimate the $^{63/65}\text{Cu}$ quadrupole coupling constant.

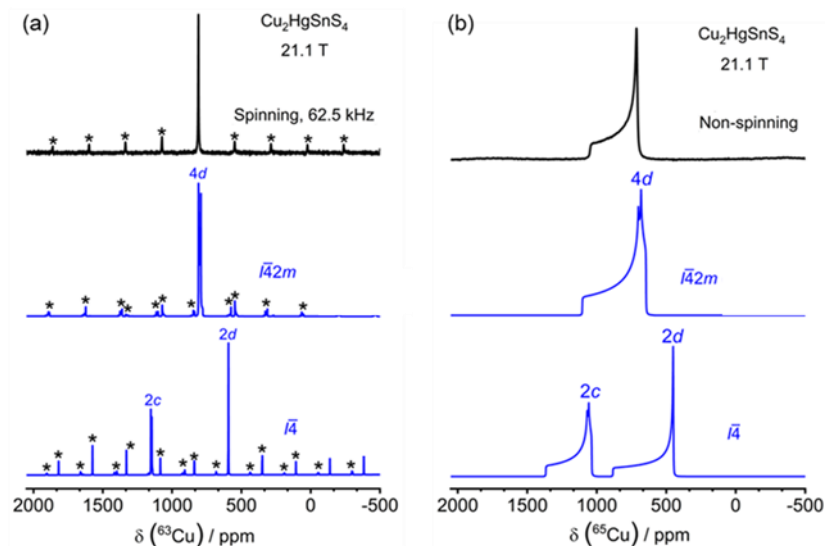


Figure 3.5. Experimental (black) and DFT (blue) predicted (a) ^{63}Cu MAS and (b) ^{65}Cu non-spinning NMR spectra for $\text{Cu}_2\text{HgSnS}_4$. The parameters for the DFT predicted spectra are listed in **Table 3.2**.

The lineshapes in the ^{65}Cu NMR spectra ($I = 3/2$; 30.8% natural abundance, $Q = -20.0 \text{ fm}^2$, $E = 28.4\%$)^{31,53} were examined in detail because they are particularly sensitive to distortions around the Cu atoms, given the strong interaction between the quadrupolar moments of ^{65}Cu nuclei with the local EFG.⁵⁹ To investigate the effect of magnetic shielding anisotropy and quadrupole coupling parameters effectively, NMR data were acquired at three magnetic field strengths, whereby the CSA interaction is more prominent at higher magnetic fields, while the second-order quadrupolar interaction is diminished. Based on fits of the ^{65}Cu NMR spectra at different magnetic fields (7.05, 11.75, and 21.1 T) at kHz (**Figure 3.6**) and ppm (**Figure A3.3** in Appendix 3) scale, the CSA and quadrupolar parameters were determined (**Table 3.2**). For $\text{Cu}_2\text{ZnSnS}_4$, two resonances at $\delta_{\text{iso}} = 804$ and 786 ppm are apparent, which correspond to the $2a$ (Cu2) and $2c$ (Cu1)

sites, respectively. From the deconvoluted spectra (**Figure A3.4** in Appendix 3), the relative areas under these peaks are roughly equal, but the $2a$ site experiences a larger C_Q (6.5 MHz) than the $2c$ site (1.5 MHz), which correlates with greater deviations from ideal tetrahedral angles ($106.6\text{--}110.9^\circ$ for $2a$, $108.9\text{--}110.6^\circ$ for $2c$).⁵⁸ The resonance for the $2a$ site narrows with the stronger magnetic field, indicating that quadrupolar interaction is the main factor affecting linewidth. In contrast, for $\text{Cu}_2\text{CdSnS}_4$ and $\text{Cu}_2\text{HgSnS}_4$, the ^{65}Cu NMR spectra show single resonances dominated by CSA as the linewidth (in kHz) of the resonances increases with increasing magnetic field.

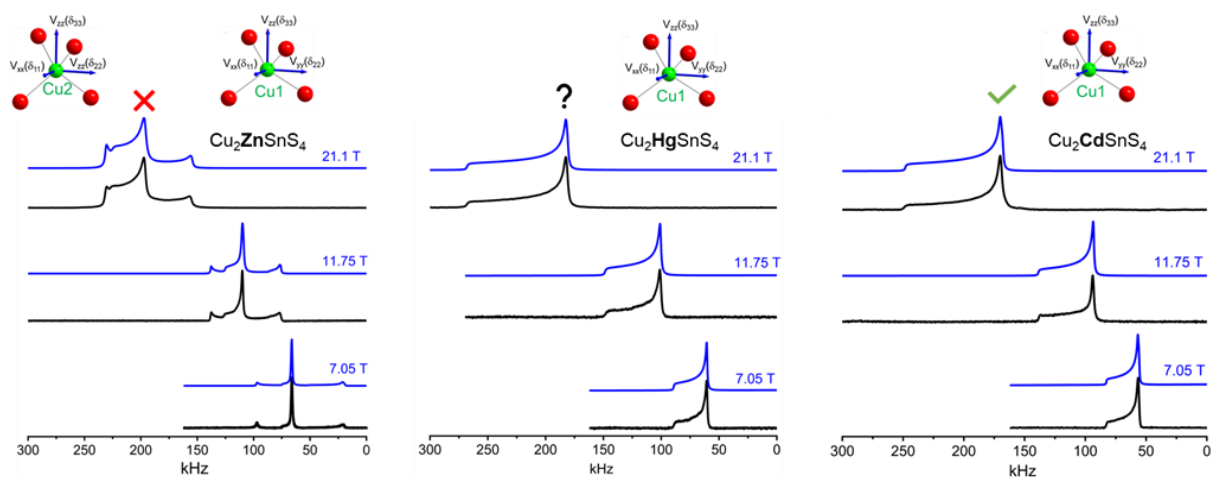


Figure 3.6. Experimental (black) and spectral simulations (blue) for non-spinning ^{65}Cu NMR spectra at three different magnetic fields for $\text{Cu}_2\text{ZnSnS}_4$, $\text{Cu}_2\text{HgSnS}_4$ and $\text{Cu}_2\text{CdSnS}_4$. GIPAW DFT EFG tensors (V_{xx} , V_{yy} , and V_{zz}) are shown as blue arrows with merged CSA tensors (top). The resemblance of ^{65}Cu chemical environment with $\text{Cu}_2\text{CdSnS}_4$ is indicated with an \checkmark (green), whereas the disagreement with $\text{Cu}_2\text{ZnSnS}_4$ is indicated with an X (red). The experimental NMR simulations (blue) were performed using the Dmfit software

Within the entire series, the maximum Ω value increases from 270 to 300 ppm on proceeding from $\text{Cu}_2\text{ZnSnS}_4$ to $\text{Cu}_2\text{HgSnS}_4$, the κ values of +1 or -1 imply that all Cu CSA tensors are axially symmetric, and the η values of 0 (or nearly so) imply that the magnitudes of V_{xx} and V_{yy} are equal, within error. CSA tensor components were coincident with the axially symmetric

EFG tensor components where δ_{11} and V_{xx} are out of the plane of the page, while the V_{zz} (δ_{33}) and V_{yy} (δ_{22}) bisect the angles within CuS_4 tetrahedra.⁶⁰

3.3.4 Local structure around Hg in $\text{Cu}_2\text{HgSnS}_4$

Although ^{199}Hg NMR spectroscopy ($I = 1/2$; 16.9% natural abundance, $\mathcal{E} = 17.1\%$)⁵³ is a sensitive method for probing short- and medium-range environments, with a sizeable chemical shift range spanning over 5000 ppm,⁶¹ it has rarely been applied to purely inorganic compounds, such as Hg-containing chalcogenides.^{62,63} The ^{199}Hg NMR spectrum for $\text{Cu}_2\text{HgSnS}_4$ shows a single resonance (**Figure 3.7**), which is consistent with the presence of a unique Hg site (*2a*), surrounded by eight Cu and four Sn atoms in the second coordination sphere, in either the Kabalov or Kaplunnik models. The isotropic chemical shift is -540.9 ppm, indicating a strongly deshielded environment around the Hg atoms in $\text{Cu}_2\text{HgSnS}_4$ compared to other previously reported inorganic compounds.^{33,64,65} The CSA parameters extracted from fitting the non-spinning NMR spectrum agree well with computed values (**Table 3.2**), with a near axially symmetric CSA tensor ($\kappa = +0.95$) and a span of $\Omega = 183 \pm 5$ ppm.

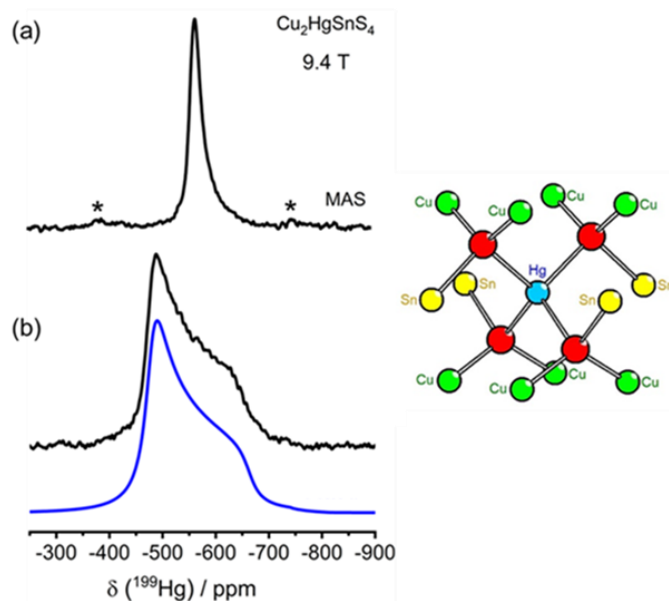


Figure 3.7. Experimental (black) MAS (a) and non-spinning (b) ^{199}Hg NMR spectra for $\text{Cu}_2\text{HgSnS}_4$. The parameters for the simulated NMR spectrum (blue) are listed in **Table 3.2**, which were fit using the Dmfit software. The asterisks mark spinning sidebands.

3.3.5 Effect of annealing on $\text{Cu}_2\text{HgSnS}_4$

$\text{Cu}_2\text{HgSnS}_4$ was synthesized through an initial heating at 700 °C for 2 d, followed by a repeated heat treatment at 700 °C for 1 d. It is interesting to evaluate if there are any changes to the long-range vs local structures after these treatments by examining powder XRD patterns as well as ^{119}Sn and ^{199}Hg MAS NMR spectra (**Figure 3.8**). The XRD patterns were not perceptibly different. However, after the second heating, the initially broad asymmetric peaks in the NMR spectra become more Gaussian-like and narrowed significantly (FWHM decreasing from 2.6 to 1.6 kHz in ^{119}Sn NMR spectrum, and 3.7 to 2.0 kHz in ^{199}Hg NMR spectrum). These observations suggest that an ordering phenomenon, of uncertain origin, takes place in a short-to-medium range that is undetected by XRD.

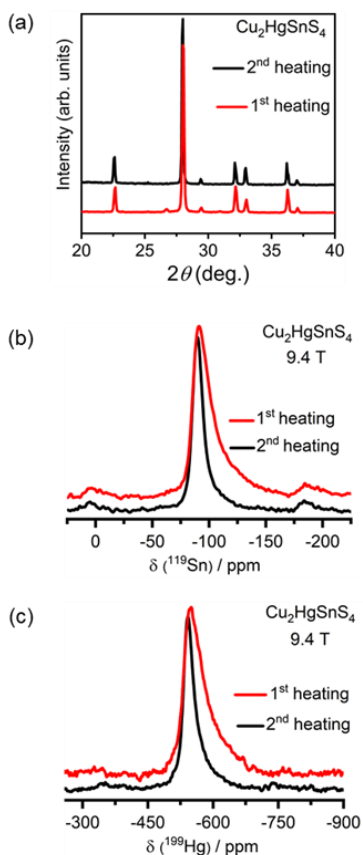


Figure 3.8. Effect of annealing $\text{Cu}_2\text{HgSnS}_4$ monitored by (a) powder XRD, (b) ^{119}Sn MAS NMR, and (c) ^{199}Hg MAS NMR spectroscopy.

For example, it can be speculated that longer annealing times improve the degree of crystallinity through further ordering of the Sn- and Hg-centred polyhedra (i.e., by reducing local distortions in bond lengths and angles); alternatively, a reduction in S vacancies could be promoted during the annealing step, which may influence the linewidths. One could further consider site mixing between Sn/Hg, creating different medium-range (i.e., second cation sphere) chemical environments for Sn and Hg, which could influence the chemical shift distributions of these nuclei. If these chemical shifts are closely spaced, they would induce peak broadening. However, significant mixing is not expected to occur due to the considerable mismatch of cation size and charge for Sn^{4+} vs Hg^{2+} , although a low level of mixing (<2%) cannot be ruled out.

3.3.6 Optical band gaps and electronic structure of Cu_2MSnS_4

Tauc plots were derived from the optical diffuse reflectance spectra (**Figure A3.5** in Supplementary Data). The extracted band gaps, based on the assumption that they are direct (as described below), follow a clearly decreasing trend of 1.5 eV for $\text{Cu}_2\text{ZnSnS}_4$, 1.2 eV for $\text{Cu}_2\text{CdSnS}_4$, and 0.9 eV for $\text{Cu}_2\text{HgSnS}_4$. These band gaps are consistent with the black colour of these samples⁶⁶ and agree well with calculated values, for which there is no shortage in the literature.^{12,67} Experimental band gaps have generally been reported to be close to 1.5 eV for $\text{Cu}_2\text{ZnSnS}_4$,^{68,69} with variations attributed to Cu/Zn disorder which introduces tailing in the optical spectra and decreases to 1.3–1.4 eV for $\text{Cu}_2\text{CdSnS}_4$.^{18,70–72} In contrast, relatively less is known about $\text{Cu}_2\text{HgSnS}_4$, for which an experimental band gap of 1.3 eV was estimated from valence band XPS spectra.¹⁰

The band structure, DOS, and $-\text{pCOHP}$ curves for these compounds were determined from DFT calculations using the hybrid HSE06 functional, which gives better estimates of band gaps (**Figure A3.6** in Appendix 3). The valence band is dominated by Cu 3d and S 3p states, and splits into lower and higher energy regions caused by the tetrahedral crystal field around Cu atoms, corresponding to Cu–S bonding and antibonding interactions, as verified by the $-\text{pCOHP}$ curves. The bottom of the conduction band is dominated by Sn 5s and S 3p states involved in Sn–S antibonding interactions. The valence and conduction band extrema are located at the Brillouin zone centre, indicating direct band gaps, which decrease on proceeding from $\text{Cu}_2\text{ZnSnS}_4$ to $\text{Cu}_2\text{HgSnS}_4$ because the bottom of the conduction band is lowered in energy. In agreement with the experimental values (as well as previous calculations on these compounds),^{12,67} the calculated direct band gaps are 1.48 eV for $\text{Cu}_2\text{ZnSnS}_4$, 1.24 eV for $\text{Cu}_2\text{CdSnS}_4$, and 0.86 eV for $\text{Cu}_2\text{HgSnS}_4$.

The bonding character in these Cu_2MSnS_4 ($M = \text{Zn, Cd, Hg}$) compounds was examined through ELF plots and Bader charges (**Figure 3.9**). The ELF plots suggest significant polar character in the bonding, with electron density strongly shifted toward the S atoms. In comparison to the charges assigned in a fully ionic formulation, $(\text{Cu}^{1+})_2\text{M}^{2+}\text{Sn}^{4+}(\text{S}^{2-})_4$, the Bader charges are not as extreme, but their relative values are in good agreement: 0.4+ to 0.6+ for Cu, 0.7+ to 1.0+ for M , 1.4+ to 1.6+ for Sn, and 0.8– to 1.0– for S atoms. Given the high electronegativity of Hg, the smallest electronegativity differences and the least extreme charges are found in $\text{Cu}_2\text{HgSnS}_4$; this leads to greater covalent character, as seen in the enhanced overlap of electron density in the Hg–S bonds.

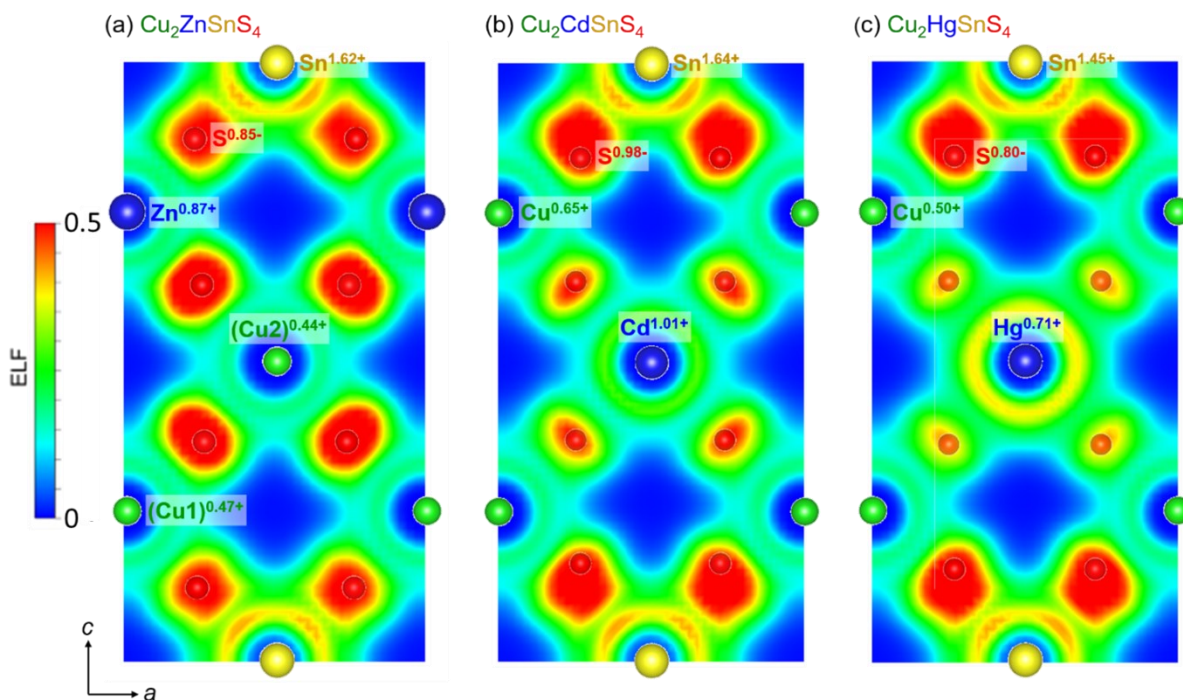


Figure 3.9. ELF plots and Bader charges for $\text{Cu}_2\text{ZnSnS}_4$, $\text{Cu}_2\text{CdSnS}_4$, and $\text{Cu}_2\text{HgSnS}_4$, projected on slices parallel to the (010) plane centred around $y = \frac{1}{2}$.

3.4 Conclusions

Comparison of the experimental and simulated $^{63/65}\text{Cu}$ NMR spectra revealed one Cu site in $\text{Cu}_2\text{HgSnS}_4$ with similar local structural parameters to $\text{Cu}_2\text{CdSnS}_4$, whereas two Cu sites are present in $\text{Cu}_2\text{ZnSnS}_4$. The CSA and C_Q NMR parameters are reliably determined using multiple magnetic fields, previously lacking in the literature. These parameters agree reasonably well with the GIPAW-DFT computations, although the magnitude of the $^{63/65}\text{Cu}$ quadrupole coupling constant remains overestimated. Moreover, it was found that these NMR parameters correlated with small changes in the local environment and the degree of distortion around metal atoms in these compounds. The results support the structural assignments previously made from XRD methods; in particular, $\text{Cu}_2\text{HgSnS}_4$ was confirmed to be isotypic to $\text{Cu}_2\text{CdSnS}_4$, adopting the so-called stannite-type structure in space group $I\bar{4}2m$ (i.e., Kaplunnik model). The ^{199}Hg NMR spectra suggest that annealing treatments of $\text{Cu}_2\text{HgSnS}_4$ help promote ordering, on a local level that is undetectable by XRD methods. An important implication of this observation is that these small structural changes need to be considered when physical properties are evaluated for compounds prepared by different synthetic methods. The band gap follows a clearly decreasing trend from 1.5 eV for $\text{Cu}_2\text{ZnSnS}_4$ to 0.9 eV for $\text{Cu}_2\text{HgSnS}_4$, a reflection of the greater covalent character imparted by the decreased electronegativity difference in Hg–S bonds.

3.5 References

- (1) Siebentritt, S.; Schorr, S. Kesterites – a challenging material for solar cells. *Prog. Photovoltaics* **2012**, *20*, 512-519.
- (2) Sun, K.; Yan, C.; Liu, F.; Huang, J.; Zhou, F.; Stride, J. A., Green, M.; Hao, X. Over 9% efficient kesterite $\text{Cu}_2\text{ZnSnS}_4$ solar cell fabricated by using $\text{Zn}_{1-x}\text{Cd}_x\text{S}$ buffer layer. *Adv. Energy Mater.*, **2016**, *6*, 1600046.

- (3) Pal, K.; Singh, P.; Bhaduri A.; Thapa, K. B. Current challenges and future prospects for a highly efficient ($> 20\%$) kesterite CZTS solar cell: a review. *Sol. Energy Mater. Sol. Cells*, **2019**, *196*, 138–156.
- (4) Shin, B.; Gunawan, O.; Zhu, Y.; Bojarczuk, N. A.; Chey, S. J.; Guha, S. Thin film solar cell with 8.4% power conversion efficiency using an earth-abundant $\text{Cu}_2\text{ZnSnS}_4$ absorber. *Prog. Photovoltaics* **2013**, *21*, 72–76.
- (5) Hasan, S.; Baral, K.; Li, N.; Ching, W.-Y. Structural and physical properties of 99 complex bulk chalcogenides crystals using first-principles calculations. *Sci. Rep.* **2021**, *11*, 9921.
- (6) Matyszczyk, G.; Zborecki, K. Application of artificial neural network and global optimization techniques for high throughput modeling of the crystal structure of stannites and kesterites. *J. Comput. Chem.* **2021**, *42*, 740–745.
- (7) Su, Z.; Tan, J. M. R.; Li, X.; Zeng, X.; Batabyal, S. K.; Wong, L. H. Cation substitution of solution-processed $\text{Cu}_2\text{ZnSnS}_4$ thin film solar cell with over 9% efficiency. *Adv. Energy Mater.* **2015**, *5*, 1500682.
- (8) Yan, C.; Sun, K.; Huang, J.; Johnston, S.; Liu, F.; Veetil, B. P.; Sun, K.; Pu, A.; Zhou, F.; Stride, J. A.; Green, M. A.; Hao, X. Beyond 11% efficient sulfide kesterite. $\text{Cu}_2\text{Zn}_x\text{Cd}_{1-x}\text{SnS}_4$ solar cell: effects of cadmium alloying. *ACS Energy Lett.* **2017**, *2*, 930–936.
- (9) Hadke, S.; Chen, W.; Tan, J. M. R.; Guc, M.; Izquierdo-Roca, V.; Rignanese, G.-M.; Hautier, G.; Wong, L. H. Effect of Cd on cation redistribution and order-disorder transition in $\text{Cu}_2(\text{Zn,Cd})\text{SnS}_4$. *J. Mater. Chem. A* **2019**, *7*, 26927–26933.
- (10) Vu, T. V.; Lavrentyev, A. A.; Gabrelian, B. V.; Tong, H. D.; Tkach, V. A.; Parasyuk, O. V.; Khyzhun, O. Y. A theoretical and experimental study of the valence-band electronic structure and optical constants of quaternary copper mercury tin sulfide, $\text{Cu}_2\text{HgSnS}_4$, a potential material for optoelectronics and solar cells. *Opt. Mater.* **2019**, *96*, 109296.
- (11) Sarmadian, N.; Saniz, R.; Partoens, B.; Lamoen, D. First-principles study of the optoelectronic properties and photovoltaic absorber layer efficiency of Cu-based chalcogenides. *J. Appl. Phys.* **2016**, *120*, 085707.
- (12) Kukreti, S.; Gupta, G. K.; Dixit, A. Theoretical DFT studies of $\text{Cu}_2\text{HgSnS}_4$ absorber material and Al:ZnO/ZnO/CdS/ $\text{Cu}_2\text{HgSnS}_4$ / back contact heterojunction solar cell. *Sol. Energy* **2021**, *225*, 802–813.

- (13) Yu, K.; Carter, E. A. Elucidating structural disorder and the effects of Cu vacancies on the electronic properties of $\text{Cu}_2\text{ZnSnS}_4$. *Chem. Mater.* **2016**, *28*, 864–869.
- (14) Hahn, H.; Schulze, H. Über Ternäre Selenide Des Bariums. *Naturwissenschaften* **1965**, *52*, 426–426.
- (15) Schäfer, W.; Nitsche, R. Tetrahedral quaternary chalcogenides of the type $\text{Cu}_2\text{-II-IV-S}_4(\text{Se}_4)$. *Mater. Res. Bull.* **1974**, *9*, 645–654.
- (16) Schorr, S. The crystal structure of kesterite type compounds: a neutron and X-ray diffraction study. *Sol. Energy Mater. Sol. Cells* **2011**, *95*, 1482–1488.
- (17) Szymański, J. T. The crystal structure of černýite, $\text{Cu}_2\text{CdSnS}_4$, a cadmium analogue of stannite. *Can. Mineral.* **1978**, *16*, 147–151.
- (18) Rosmus, K. A.; Brant, J. A.; Wisneski, S. D.; Clark, D. J.; Kim, Y. S.; Jang, J. I.; Brunetta, C. D.; Zhang, J.-H.; Srnec, M. N.; Aitken, J. A. Optical nonlinearity in $\text{Cu}_2\text{CdSnS}_4$ and $\alpha/\beta\text{-Cu}_2\text{ZnSiS}_4$: diamond-like semiconductors with high laser-damage thresholds. *Inorg. Chem.* **2014**, *53*, 7809–7811.
- (19) Kabalov, Yu. K.; Evstigneeva, T. L.; Spiridonov, E. M.; Crystal structure of $\text{Cu}_2\text{HgSnS}_4$, a synthetic analogue of the mineral velikite. *Crystallogr. Rep.* **1998**, *43*, 16–20 (*Transl. Kristallografiya* **1998**, *43*, 21–25).
- (20) Kaplunnik, L. N.; Pobedimskaya, E. A.; Belov, N. V. Crystal structure of velikite $\text{Cu}_{3.75}\text{Hg}_{1.75}\text{Sn}_2\text{S}_8$. *Kristallografiya* **1977**, *22*, 175–177.
- (21) Heppke, E. M.; Küllmey, T.; Efthimiopoulos, I.; Avci, F. D.; Appelt, O.; Paulus, B.; Lerch, M. Experimental and theoretical investigations on the composition-dependent structural phase transition in $\text{Cu}_2\text{Cd}_x\text{Zn}_{1-x}\text{SnS}_4$ thin films. *Mater. Res. Express* **2019**, *6*, 125525.
- (22) Lafond, A.; Guillot-Deudon, C.; Vidal, J.; Paris, M.; La, C.; Jobic, S. Substitution of Li for Cu in $\text{Cu}_2\text{ZnSnS}_4$: toward wide band gap absorbers with low cation disorder for thin film solar cells. *Inorg. Chem.* **2017**, *56*, 2712–2721.
- (23) Bhattacharya, A.; Tkachuk, D. G.; Mar, A.; Michaelis, V. K. Mere anarchy is loosed: structural disorder in $\text{Cu}_2\text{Cd}_x\text{Zn}_{1-x}\text{SnS}_4$. *Chem. Mater.* **2021**, *33*, 4709–4722.
- (24) Paris, M.; Larramona, G.; Bais, P.; Bourdais, S.; Lafond, A.; Choné, C.; Guillon-Deudon, C.; Delatouche, B.; Moisan, C.; Dennler, G. ^{119}Sn MAS NMR to assess the cationic disorder and the anionic distribution in sulfoselenide $\text{Cu}_2\text{ZnSn}(\text{S}_x\text{Se}_{1-x})_4$ compounds prepared from colloidal and ceramic routes. *J. Phys. Chem. C* **2015**, *119*, 26849–26857.

- (25) Shi, C.; Xi, X.; Hou, Z.; Liu, E.; Wang, W.; Chen, J.; Wu, G. Copper dynamics and structural transformation in noble metal chalcogenides CuAgS probed by ^{63}Cu NMR. *Solid State Ion.* **2017**, *300*, 182–186.
- (26) Hu, S.; Reimer, J. A.; Bell, A. T. ^{65}Cu NMR Spectroscopy of Cu-exchanged ZSM-5 catalysts. *J. Phys. Chem. B* **1997**, *101*, 1869–1871.
- (27) Reiser, S.; Brunklaus, G.; Hong, J. H.; Chan, J. C. C.; Eckert, H.; Pfitzner, A. $(\text{CuI})_3\text{P}_4\text{S}_4$: preparation, structural, and NMR spectroscopic characterization of a copper(I) halide adduct with $\beta\text{-P}_4\text{S}_4$. *Chem. Eur. J.* **2002**, *8*, 4228–4233.
- (28) Rodríguez-Carvajal, J. Introduction to the program Fullprof: refinement of crystal and magnetic structures from powder and single crystal data. Laboratoire Léon Brillouin (CEA-CNRS), Saclay, France, 2001
- (29) Kortüm, G. *Reflectance Spectroscopy*; Springer, 1969.
- (30) Massiot, D.; Fayon, F.; Capron, M.; King, I.; Le Calve, S.; Alonso, B.; Durand, O.; Bujoli, B.; Gan Z.; Hoatson G. Modeling one- and two- dimensional solid-state NMR spectra. *Magn. Reson. Chem.* **2002**, *40*, 70–76.
- (31) Tang, J. A.; Ellis, B. D.; Warren, T. H.; Hanna, J. V.; Macdonald, C. L. B.; Schurko, R. W. Solid-state ^{63}Cu and ^{65}Cu NMR spectroscopy of inorganic and organometallic copper(I) complexes. *J. Am. Chem. Soc.* **2007**, *129*, 13049-13065.
- (32) Gunther, W. R.; Michaelis, V. K.; Caporini, M. A.; Griffin, R. G.; Román-Leshkov, Y. Dynamic nuclear polarization NMR enables the analysis of Sn-beta zeolite prepared with natural abundance ^{119}Sn precursors. *J. Am. Chem. Soc.* **2014**, *136*, 6219–6222.
- (33) Taylor, R. E.; Bai, S.; Dybowski, C. A solid-state ^{199}Hg NMR study of mercury halides. *J. Mol. Strut.* **2011**, *987*, 193–198.
- (34) Mason, J. *Solid State Nucl. Magn. Res.* **1993**, *2*, 285–288.
- (35) Herzfeld, J.; Berger, A. E. Sideband intensities in NMR spectra of samples spinning at the magic angle. *J. Chem. Phys.* **1980**, *73*, 6021–6030.
- (36) Slichter, C. P. *Principles of Magnetic Resonance*; Springer, 1996.
- (37) Wasylishen, R. E.; Ashbrook, S. E.; Wimperis, S. *NMR of Quadrupolar Nuclei in Solid Materials*; Wiley, 2012.

- (38) Lucier, B. E. G.; Tang, J. A.; Schurko, R. W.; Bowmaker, G. A.; Healy, P. C.; Hanna, J. V. Solid-state ^{65}Cu and ^{31}P NMR spectroscopy of bis(triphenylphosphine) copper species. *J. Phys. Chem. C* **2010**, *114*, 7949–7962.
- (39) Marchetti, P. S.; Honkonen, R. S.; Ellis, P. D. Assignment of symmetry-related cadmium shielding tensors to lattice positions in cadmium acetate dihydrate. *J. Magn. Reson.* **1987**, *71*, 294–302.
- (40) Jiao, J.; Lee, M.-Y.; Barnes, C. E.; Hagaman, E. W. ^{119}Sn NMR Chemical shift tensors in anhydrous and hydrated $\text{Si}_8\text{O}_{20}(\text{SnMe}_3)_8$ crystals. *Magn. Reson. Chem.* **2008**, *46*, 690–692.
- (41) Sola, J.; Gonzalez-Duarte, P.; Sanz, J.; Casals, I.; Alsina, T.; Sobrados, I.; Alvarez-Larena, A.; Piniella, J. F.; Solans, X. Solid-state ^{113}Cd NMR studies of several cadmium-sulfur complexes. shielding tensor-structure correlations. *J. Am. Chem. Soc.* **1993**, *115*, 10018–10028.
- (42) Saitô, H.; Ando, I.; Ramamoorthy, A. Chemical shift tensor – the heart of NMR: insights into biological aspects of proteins. *Prog. Nucl. Magn. Reson. Spectrosc.* **2010**, *57*, 181–228.
- (43) Autschbach, J.; Zheng, S.; Schurko, R. W. Analysis of electric field gradient tensors at quadrupolar nuclei in common structural motifs. *Concepts Magn. Reson. Part A* **2010**, *36A*, 84–126.
- (44) NMRRamblingsKlausEichele. <http://anorganik.uni-tuebingen.de/klaus/nmr/index.php?p=conventions/csa/>
- (45) Clark, S. J.; Segall, M. D.; Pickard, C. J.; Hasnip, P. J.; Probert, M. I. J.; Refson, K.; Payne, M. C. First principles methods using CASTEP. *Z. Kristallgr.* **2005**, *220*, 567–570.
- (46) Perdew, J. P.; Burke K.; and Ernzerhof, M. Generalized gradient approximation made simple. *Phys. Rev. Lett.* **1996**, *77*, 3865–3868.
- (47) Pickard, C. J.; Mauri, F. All-electron magnetic response with pseudopotentials: NMR chemical shifts. *Phys. Rev. B* **2001**, *63*, 245101.
- (48) Yates, J. R.; Pickard, C. J.; Mauri, F. Calculation of NMR chemical shifts for extended systems using ultrasoft pseudopotentials. *Phys. Rev. B* **2007**, *76*, 024401.
- (49) Kresse, G.; Furthmüller, J. Efficient iterative schemes for ab initio total-energy calculations using a plane-wave basis set. *Phys. Rev. B* **1996**, *54*, 11169–11186

- (50) Kresse, G.; Joubert, D. From ultrasoft pseudopotentials to the projector augmented-wave method. *Phys. Rev. B* **1999**, *59*, 1758.
- (51) Blöchl, P. E. Projector augmented-wave method. *Phys. Rev. B* **1994**, *50*, 17953–17979.
- (52) Maintz, S.; Deringer, V. L.; Tchougréeff, A. L.; Dronskowski, R. LOBSTER: a tool to extract chemical bonding from plane-wave based DFT. *J. Comput. Chem.* **2016**, *37*, 1030–1035
- (53) Harris, R. K.; Becker, E. D.; de Menezes, S. M. C.; Goodfellow, R.; Granger, P. NMR nomenclature: Nuclear spin properties and conventions for chemical shifts (IUPAC recommendations 2001). *Pure Appl. Chem.* **2001**, *73*, 1795–1818.
- (54) Kubicki, D. J.; Prochowicz, D.; Salager, E.; Rakhmatullin, A.; Grey, C. P.; Emsley, L.; Stranks, S. D. Local structure and dynamics in methylammonium, formamidinium, and cesium tin(II) mixed-halide perovskites from ^{119}Sn solid-state NMR. *J. Am. Chem. Soc.* **2020**, *142*, 7813–7826.
- (55) Ha, M.; Karmakar, A.; Bernard, G. M.; Basilio, E.; Krishnamurthy, A.; Askar, A. M.; Shankar, K.; Kroeker, S.; Michaelis, V. K. Phase evolution in methylammonium tin halide perovskites with variable temperature solid-state ^{119}Sn NMR spectroscopy. *J. Phys. Chem. C* **2020**, *124*, 15015–15027.
- (56) Karmakar, A.; Bhattacharya, A.; Sarkar, D.; M. Bernard, G.; Mar, A.; Michaelis, V. K. Influence of hidden halogen mobility on local structure of $\text{CsSn}(\text{Cl}_{1-x}\text{Br}_x)_3$ mixed-halide perovskites by solid-state NMR. *Chem. Sci.* **2021**, *12*, 3253–3263.
- (57) Karmakar, A.; Bhattacharya, A.; Bernard, G. M.; Mar, A.; Michaelis, V. K. Revealing the local Sn and Pb arrangements in $\text{CsSn}_x\text{Pb}_{1-x}\text{Br}_3$ perovskites with solid-state NMR spectroscopy. *ACS Mater. Lett.* **2021**, *3*, 261–267.
- (58) Choubrac, L.; Lafond, A.; Guillot-Deudon, C.; Moëlo, Y.; Jobic, S. Structure flexibility of the $\text{Cu}_2\text{ZnSnS}_4$ absorber in low-cost photovoltaic cells: from the stoichiometric to the copper-poor compounds. *Inorg. Chem.* **2012**, *51*, 3346–3348.
- (59) Choubrac, L.; Paris, M.; Lafond, A.; Guillot-Deudon, C.; Rocquefelt, X.; Jobic, S. Multinuclear (^{67}Zn , ^{119}Sn and ^{65}Cu) NMR spectroscopy – an ideal technique to probe the cation ordering in $\text{Cu}_2\text{ZnSnS}_4$ photovoltaic materials. *Phys. Chem. Chem. Phys.* **2013**, *15*, 10722–10725.

- (60) Lipton, A. S.; Heck, R. W.; de Jong, W. A.; Gao, A. R.; Wu, X.; Roehrich, A.; Harbison, G. S.; Ellis, P. D. Low temperature ^{65}Cu NMR spectroscopy of the Cu^+ site in azurin. *J. Am. Chem. Soc.* **2009**, *131*, 13992–13999.
- (61) Wrackmeyer, B.; Contreras, R. ^{199}Hg NMR parameters. *Ann. Rep. NMR Spectrosc.* **1992**, *24*, 267–329.
- (62) Hung, I.; Rossini, A. J.; Schurko, R. W. Application of the Carr–Purcell Meiboom–Gill pulse sequence for the acquisition of solid-state NMR spectra of spin-1/2 nuclei. *J. Phys. Chem. A* **2004**, *108*, 7112–7120.
- (63) Gippius, A. A.; Antipov, E. V.; Hoffmann, W.; Lüders, K.; Buntkowsky, G. Low-frequency spin dynamics as probed by ^{63}Cu and ^{199}Hg NMR in $\text{HgBa}_2\text{CuO}_{4+\delta}$ superconductors with different oxygen content, *Phys. Rev. B*, **1999**, *59*, 654–660.
- (64) Peringer, Q P. ^{199}Hg Nuclear magnetic resonance studies of the mercury(II) halides. *Inorg. Chim. Acta* **1980**, *39*, 67–70.
- (65) Wu, G.; Wasylshen, R. E. Observation of ^{201}Hg NMR spectra for solid $\text{K}_2\text{Hg}(\text{CN})_4$. *Magn. Reson. Chem.* **1993**, *31*, 537–539.
- (66) Himmrich, M.; Haeuseler, H. Far infrared studies on stannite and wurtzstannite type compounds. *Spectrochim. Acta* **1991**, *47A*, 933–942.
- (67) Paier, J.; Asahi, R.; Nagoya A.; Kresse, G. $\text{Cu}_2\text{ZnSnS}_4$ as a potential photovoltaic material: A hybrid Hartree-Fock density functional theory study. *Phys. Rev. B* **2009**, *79*, 155126.
- (68) Seol, J.-S.; Lee, S.-Y.; Lee, J.-C.; Nam, H.-D.; Kim, K.-H. Electrical and optical properties of $\text{Cu}_2\text{ZnSnS}_4$ thin films prepared by rf magnetron sputtering process. *Sol. Energy Mater. Sol. Cells* **2003**, *75*, 155–162.
- (69) Scragg, J. J. S.; Larsen, J.K.; Kumar, M.; Persson, C.; Sandler, J.; Siebentritt, S.; Björkman, C. P. Cu–Zn Disorder and band gap fluctuations in $\text{Cu}_2\text{ZnSn}(\text{S},\text{Se})_4$: theoretical and experimental investigations. *Phys. Status Solidi B* **2016**, *253*, 247–254.
- (70) Matsushita, H.; Ichikawa, T.; Katsui, A. Structural, thermodynamical and optical properties of $\text{Cu}_2\text{-II-IV-VI}_4$ quaternary compounds. *J. Mater. Sci.* **2005**, *40*, 2003–2005.
- (71) Cui, Y.; Wang, G.; Pan, D. Synthesis and photoresponse of novel $\text{Cu}_2\text{CdSnS}_4$ semiconductor nanorods. *J. Mater. Chem.* **2012**, *22*, 12471–12473.
- (72) Guan, H.; Shi, Y.; Hou, H.; Wang, X.; Yu, F. Quaternary $\text{Cu}_2\text{CdSnS}_4$ nanoparticles synthesised by microwave irradiation method. *Micro Nano Lett.* **2014**, *9*, 251–252.

Chapter 4

Influence of Ge substitution on the structure and optoelectronic properties of $\text{Cu}_2\text{ZnSn}_{1-x}\text{Ge}_x\text{S}_4$ photovoltaic materials

4.1 Introduction

Among alternatives to silicon as commercial-grade photovoltaic materials, various materials such as gallium arsenide (GaAs), copper indium gallium selenide ($\text{CuIn}_{1-x}\text{Ga}_x\text{Se}_2$), hybrid metal halide perovskites, and others have been studied.¹⁻⁴ Unfortunately, many hurdles such as cost, stability, and long-term environmental impact of some leading candidate materials have precluded their widespread application.^{1,5,6} On this premise, $\text{Cu}_2\text{ZnSnS}_4$, often referred to by its mineral name kesterite, has emerged as a promising photovoltaic material due to its direct band gap (1.5 eV), a high absorption coefficient (10^4 cm^{-1}), and composition derived from inexpensive and earth-abundant elements.⁷⁻¹⁰ The power conversion efficiency reached for $\text{Cu}_2\text{ZnSnS}_4$ is around 9%, which still lags far behind that for Si, $\text{CuIn}_{1-x}\text{Ga}_x\text{Se}_2$, and perovskites.^{11,12} To improve the solar cell efficiency, the usual approach has been to substitute other cations in $\text{Cu}_2\text{ZnSnS}_4$: monovalent elements (Li, Ag) for Cu, divalent elements (Cd, Ba, Fe, Co, Ni, Mn) for Zn, or Ge for Sn.¹³⁻¹⁹ In particular, partial substitution of Ge for Sn reduces open-circuit voltage (V_{oc}) deficit and increases photovoltaic efficiency.¹⁹⁻²² For example, Kim et al. reported significant improvements in photoconversion efficiency by substituting 22% of Sn by the smaller congener Ge within the series $\text{Cu}_2\text{ZnSn}_{1-x}\text{Ge}_x\text{S}_4$.²³ Because structure and physical properties are correlated, it is imperative to conduct a thorough structural evaluation on $\text{Cu}_2\text{ZnSn}_{1-x}\text{Ge}_x\text{S}_4$ to gain insight into how to improve the photovoltaic efficiency of these compounds.

Based on convergent-beam electron diffraction and lattice imaging, Moodie et al. proposed that $\text{Cu}_2\text{ZnGeS}_4$ adopts a structure in space group $I\bar{4}2m$, in which planes of Zn–Ge atoms are located at $z = 0$ and $\frac{1}{2}$, and planes of Cu atoms are located at $z = \frac{1}{4}$ and $\frac{3}{4}$.²⁴ This structural model has been assumed in several publications without further verification.^{25–28} On the other hand, based on observation of tetragonal distortion of the cell parameters refined from X-ray diffraction, Khadka et al. proposed that $\text{Cu}_2\text{ZnGeS}_4$ adopts a structure in space group $I\bar{4}$, in which planes of Cu–Sn atoms are located at $z = 0$ and $\frac{1}{2}$, and planes of Cu–Zn atoms are located at $z = \frac{1}{4}$ and $\frac{3}{4}$.²⁹ The main difference is that Cu atoms occupy two sets of sites ($2a$ and $2c$) in the $I\bar{4}$ model, whereas they occupy a single set of sites ($4d$) in the $I\bar{4}2m$ model (**Figure 4.1**). Because Cu^+ , Zn^{2+} , and Ge^{4+} are isoelectronic and have similar X-ray scattering factors, it is difficult to determine the cation distribution unequivocally.³⁰

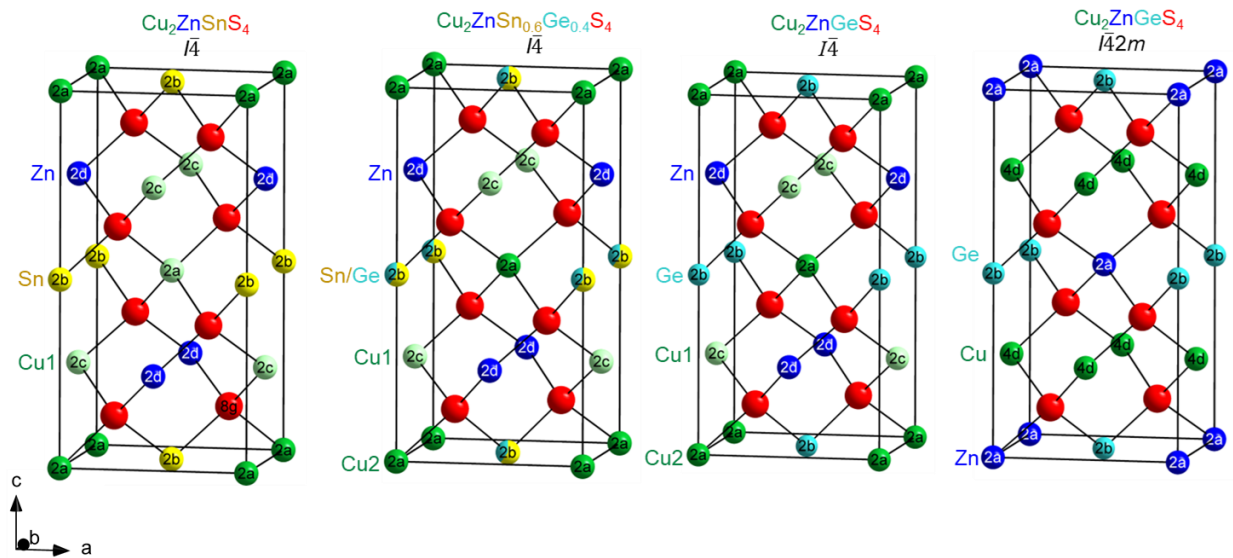


Figure 4.1. Crystal structures of $\text{Cu}_2\text{ZnSnS}_4$, $\text{Cu}_2\text{ZnSn}_{0.6}\text{Ge}_{0.4}\text{S}_4$ and $\text{Cu}_2\text{ZnGeS}_4$. Two structural models were proposed for $\text{Cu}_2\text{ZnGeS}_4$, consisting of two sets of Cu sites in $I\bar{4}$, in contrast to one set of Cu sites in $I\bar{4}2m$.

Solid-state nuclear magnetic resonance (NMR) spectroscopy provides element-specific information about local environments around atoms, allowing the effects of chemical substitution, cation disorder, and phase segregation of nanodomains to be probed. For example, ^{119}Sn , $^{63/65}\text{Cu}$, and ^{67}Zn NMR spectroscopy have been used to confirm the crystal structure of $\text{Cu}_2\text{ZnSnS}_4$ and to investigate the cation and anion distributions in $(\text{Cu}_{1-x}\text{Li}_x)_2\text{ZnSnS}_4$, $\text{Cu}_2\text{Zn}_{1-x}\text{Cd}_x\text{SnS}_4$, $\text{Cu}_2\text{ZnSn}(\text{S}_{1-x}\text{Se}_x)_4$, $\text{Cu}_2\text{ZnSn}_{1-x}\text{Si}_x\text{S}_4$, and $\text{Cu}_2\text{ZnGeS}_4$.^{31–35} A similar approach of applying solid-state NMR spectroscopy can be proposed to clarify the site distributions in $\text{Cu}_2\text{ZnSn}_{1-x}\text{Ge}_x\text{S}_4$.

This study reports a detailed analysis of $^{63/65}\text{Cu}$, ^{67}Zn , ^{73}Ge , and ^{119}Sn NMR and X-ray diffraction measurements to resolve the competing proposals for the site distributions in $\text{Cu}_2\text{ZnGeS}_4$ and to reveal how they change as Ge and Sn are mixed in the solid solution series $\text{Cu}_2\text{ZnSn}_{1-x}\text{Ge}_x\text{S}_4$. $^{63/65}\text{Cu}$ NMR measurements and GIPAW-DFT calculations were applied to assign the structure of $\text{Cu}_2\text{ZnGeSe}_4$ unambiguously. Moreover, because ^{67}Zn NMR spectroscopy shows excellent sensitivity to local environment effects, it was used to provide insight into the cation distribution. Optical band gaps were measured by UV-visible spectroscopy. The electronic structure calculations were performed to understand the band structure and chemical bonding.

4.2 Experimental

4.2.1 Synthesis

Cu powder (99.5 %, Alfa-Aesar), Zn grains (99.9%, Baker Analyzed), Sn powder (99.9 %, Cerac), Ge powder (99.9%, Alfa-Aesar), and S flakes (99.9 %, Sigma-Aldrich) were used as starting materials to synthesize $\text{Cu}_2\text{ZnMSnS}_4$ ($M = \text{Sn, Ge}$) compounds. Stoichiometric mixtures of Cu, Zn, Sn, Ge, and S were cold-pressed into pellets and placed in carbon-coated fused silica tubes, which were evacuated and sealed. The tubes were heated in a box furnace to 250 °C at a

rate of 50 °C/h, held there for 2 h, heated to 700–750 °C at a rate of 30 °C/h, held there for 4 days, and then cooled to room temperature over 24 h. The samples were ground, reloaded in fused silica tubes, and subjected to a second heat treatment at 700–750 °C for 4 d.

4.2.2 X-ray diffraction and energy-dispersive X-ray analysis

Powder X-ray diffraction (XRD) patterns for the samples were collected on a Bruker D8 Advance diffractometer equipped with an SSD160 detector and Cu K α radiation source operated at 40 kV and 40 mA. The cell parameters were determined using the FullProf software suite, with the profiles fitted by the Le Bail method for all compounds. Rietveld refinement was performed on the patterns for Cu₂ZnSnS₄ and Cu₂ZnGeS₄.³⁶ The elemental compositions were determined by energy-dispersive X-ray (EDX) analyses, performed using a Zeiss Sigma 300 VP-FESEM scanning electron microscope, operated with an accelerating voltage of 15 kV.

4.2.3 Diffuse reflectance spectroscopy

Optical diffuse reflectance spectra for all compounds were collected from 200 nm (6.2 eV) to 1600 nm (0.8 eV) on a Cary 5000 UV-Vis-NIR spectrophotometer, which was calibrated using an optical polytetrafluoroethylene disc (>98% reflectivity) as a standard. The reflectance spectra were converted to optical absorption spectra using the Kubelka-Munk function:

$$F(R) = \frac{\alpha}{S} = \frac{(1-R)^2}{2R}$$

where α is the Kubelka–Munk absorption coefficient, S is the scattering coefficient, and R is the reflectance.³⁷

4.2.4 Solid-state nuclear magnetic resonance spectroscopy

Solid-state NMR spectra were collected on Bruker Avance Neo 300 ($B_0 = 7.05$ T), Avance Neo 500 ($B_0 = 11.75$ T), and Avance II 900 ($B_0 = 21.1$ T) spectrometers using double resonance (H/X) MAS Bruker probes. The details of acquisition parameters are listed in **Table A4.1** in Appendix. Additional ^{119}Sn slow-spinning MAS NMR data were collected for $\text{Cu}_2\text{ZnSnS}_4$ and $\text{Cu}_2\text{ZnSn}_{0.4}\text{Ge}_{0.4}\text{S}_4$. Samples were ground into fine powders using an agate mortar and pestle, and then packed into 4-mm outer diameter (o.d.) ZrO_2 rotors, which were sealed with Kel-F caps or 1.3-mm o.d. ZrO_2 rotors with Vespel top and bottom caps. Non-spinning ^{65}Cu NMR data were collected using a home-built 4 mm static solenoid probe (pure Ag R.F. coil to minimize probe background from Cu metal). NMR spectra were referenced using $(\text{C}_6\text{H}_{11})_4\text{Sn}(\text{s})$ (-97.5 ppm for ^{119}Sn NMR), 1 M $\text{Zn}(\text{NO}_3)_2$ (aq) (0 ppm for ^{67}Zn NMR), GeCl_4 ($+30.9$ ppm for ^{73}Ge) or $\text{CuCl}(\text{s})$ (0 ppm for $^{63/65}\text{Cu}$ NMR).^{38–41} The NMR spectra were processed using the Bruker TOPSPIN 4.0.6 software suite with 50–200 Hz exponential apodization and plotted using Origin 2020. The Dmfit program⁴² was used to fit the $^{63/65}\text{Cu}$, ^{67}Zn , ^{73}Ge , and ^{119}Sn NMR data to extract the unique NMR parameters for each compound.

4.2.5 Definitions of NMR parameters

NMR spectra of solids are typically discussed using chemical shift anisotropy (CSA) and quadrupolar interactions.^{43–49}

a. CSA

- (i) Isotropic chemical shift, $\delta_{\text{iso}} = \frac{(\delta_{11} + \delta_{22} + \delta_{33})}{3}$, where $\delta_{11} \geq \delta_{22} \geq \delta_{33}$
- (ii) Span, $\Omega = \delta_{11} - \delta_{33}$, which describes the breadth of the pattern.
- (iii) Skew, $\kappa = \frac{3(\delta_{22} - \delta_{\text{iso}})}{\Omega}$, which describes the shape of the powder pattern.

b. Quadrupolar interactions ($I > 1/2$)

- (i) Nuclear quadrupole coupling constant, $C_Q = \frac{eQV_{zz}}{h}$, where e is the elementary charge, Q is the quadrupolar moment of the nucleus, V_{zz} is the largest principal component of electric field gradient (EFG), and h is Planck's constant. C_Q describes the strength of the quadrupolar interaction between the nucleus and the surrounding EFG.
- (ii) Asymmetry parameter, $\eta = (V_{xx} - V_{yy})/V_{zz}$, where $|V_{xx}| \leq |V_{yy}| \leq |V_{zz}|$. η describes quadrupolar NMR line shape.

4.2.6 Quantum chemical computations

Calculations of chemical shift tensors and electric field gradients ($I > 1/2$) were performed using CASTEP,⁵⁰ which uses a gauge-including projector augmented plane wave (GIPAW) basis set suitable for periodic structures. The Perdew-Burke-Ernzerhof (PBE) functional was used in the generalized gradient approximation (GGA) for the exchange-correlation energy and ultrasoft pseudopotentials.^{51–53} All calculations were performed with an extreme accuracy basis set precision, maximum plane-wave energy of 600 eV, zeroth-order regular approximation for

relativistic effects, and a Monkhorst-Pack grid of $12 \times 12 \times 6$ k points for Cu_2ZnMS_4 ($M = \text{Sn}, \text{Ge}$). To simulate the DFT predicted spectra, calculated magnetic shieldings were set to experimental shielding.

Electronic structure calculations were performed using the projected augmented wave method as implemented in the Vienna ab initio simulation package (VASP Version 5.4.4).^{53–55} The GGA parameterized by PBE was used to treat exchange and correlation.^{51,56,57} The recommended standard PAW potentials (Cu, Zn, S, Sn_d, and Ge_d) were used with the plane-wave basis cutoff energy set to 400 eV. A $9 \times 9 \times 5$ gamma-centred k -point grid was used to sample the first Brillouin zone. The relaxation of the electronic degrees of freedom was set to be stopped if the changes in total energy and band structure energy between two steps were smaller than 10^{-6} eV. The break condition for the ionic relaxation loop was set if the norms of all the forces became smaller than $| -2 \times 10^{-2} |$.

The HSE06 functional (PBE:Hartree-Fock (65:35)) was used to correct the significant underestimation of the PBE band gap. To reduce computational cost, spin-orbit interactions were not considered. Chemical bonding was examined by evaluating electron localization functions (ELF), Bader charges, projected crystal orbital Hamilton populations ($-p\text{COHP}$), and crystal orbital bond index (COBI) using the program LOBSTER (version 4.1.0).^{58–62}

4.3 Results and discussion

4.3.1 Crystal structure of $\text{Cu}_2\text{ZnSn}_{1-x}\text{Ge}_x\text{S}_4$

A series of bulk samples $\text{Cu}_2\text{ZnSn}_{1-x}\text{Ge}_x\text{S}_4$ were prepared by reaction of elements between 700 and 750 °C. EDX analysis confirmed that the elemental compositions of these samples agree well with the nominal compositions (**Table A4.2** in Appendix 4). The powder XRD patterns indicate that all samples are phase-pure (**Figure 4.2a**). For the parent compounds $\text{Cu}_2\text{ZnSnS}_4$ and $\text{Cu}_2\text{ZnGeS}_4$, the experimental XRD patterns match with those simulated with the structure assignment in space group $I\bar{4}$. The tetragonal cell parameters (a , c , V) were refined from these XRD data (**Table A4.3** in Appendix 4). The unit cell contracts as Sn is substituted by Ge, and the refined cell parameters decrease linearly on proceeding from $\text{Cu}_2\text{ZnSnS}_4$ to $\text{Cu}_2\text{ZnGeS}_4$, consistent with the relative sizes of the ions (0.55 Å for Sn^{4+} vs 0.39 Å for Ge^{4+} for CN4) and implying a random mixing of Sn and Ge atoms. The $c/2a$ ratio serves as a useful measure of the degree of tetragonal distortion (**Table A4.3** in Appendix 4). For $\text{Cu}_2\text{ZnSnS}_4$, the ratio is 0.997, which is close to 1, implying all the metal-centred tetrahedra are nearly undistorted (**Figure 4.2b**). This ratio deviates increasingly from 1 with greater Ge substitution, reaching 0.983 for $\text{Cu}_2\text{ZnGeS}_4$ where the tetragonal distortion is most pronounced, as evidenced by the clear splitting of 220 and 240 peaks nearly 47° in 2θ in the powder XRD pattern. Sometimes this splitting is misinterpreted as a means to infer the space group and site distribution, but a proper structure determination requires a detailed analysis of both the XRD and solid-state NMR data.

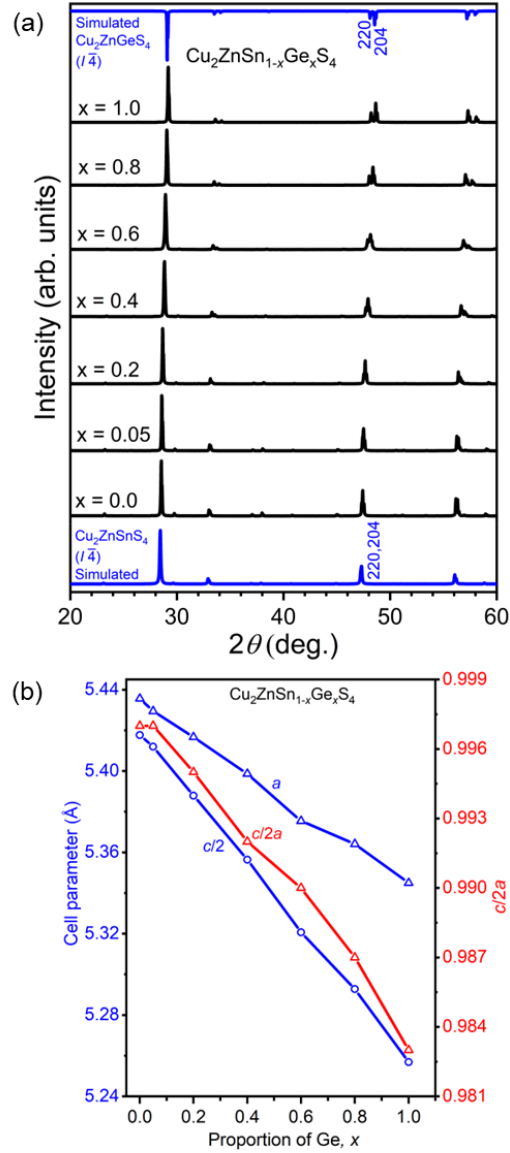


Figure 4.2. (a) Powder XRD patterns of $\text{Cu}_2\text{ZnSn}_{1-x}\text{Ge}_x\text{S}_4$, where x varies from 0 to 1. The 220 and 204 peaks overlap for lightly substituted Ge members, but become split for highly substituted Ge members. (b) Evolution of tetragonal unit cell parameters (a and $c/2$) and tetragonal distortion parameter ($c/2a$) with respect to Ge content.

4.3.2 Local structure around Sn

For $\text{Cu}_2\text{ZnSnS}_4$, the Sn atoms occupy one set of sites at $2b$ $(0, 0, \frac{1}{2}; \frac{1}{2}, \frac{1}{2}, 0)$ with site symmetry $\bar{4}$. in space group $I\bar{4}$. Each Sn atom is surrounded by four S atoms in the first coordination sphere, and by eight Cu and four Zn atoms in the second coordination sphere (**Figure 4.3b**). Because ^{119}Sn NMR spectroscopy ($I = 1/2$; 8.6% natural abundance; $\mathcal{E} = 37.3\%$)⁶³ is highly sensitive to the chemical environment about Sn, with a chemical shift range of $\sim 6,000$ ppm in diamagnetic solids, it is an ideal method to probe the intermediate-range structural variation within the $\text{Cu}_2\text{ZnSn}_{1-x}\text{Ge}_x\text{S}_4$ series.⁶⁴⁻⁶⁷ The ^{119}Sn magic-angle spinning (MAS) NMR spectra (**Figure 4.3a**) exhibit a single resonance with an isotropic chemical shift (δ_{iso}) of -121 ppm, consistent with a unique Sn chemical environment. As Ge is substituted for Sn, the ^{119}Sn isotropic chemical shift moves toward higher frequency in a nearly linear fashion up to $x = 0.4$, remains constant at $x = 0.6$, and increases further at $x = 0.8$ (**Figure 4.3c**). The full width at half maximum (FWHM) of the peaks for intermediate compositions (**Table A4.4** in Appendix 4) is greater than for the parent compound $\text{Cu}_2\text{ZnSnS}_4$ (FWHM = 795 Hz), which can be attributed to the more varied distribution of chemical environments having different bond distances and angles around the Sn sites as disorder of Sn and Ge atoms occurs in the medium range.

In previous studies on $\text{Cu}_2\text{Zn}_{1-x}\text{Cd}_x\text{SnS}_4$, partially resolved ^{119}Sn resonances were observed.³² However, for the present series $\text{Cu}_2\text{Zn}_{1-x}\text{Ge}_x\text{SnS}_4$, all ^{119}Sn resonances (for $x > 0$) are found to be spectrally unresolved, with only an associated shift to lower frequency as Ge replaces Sn. Additional non-spinning and slow spinning (3 kHz) NMR spectra were collected at 11.75 T to probe the chemical shift anisotropy (**Figure 4.3d**). The extracted span and skew parameters are $\Omega = 32 \pm 5$ ppm and $\kappa = -0.45 \pm 0.05$ for $\text{Cu}_2\text{ZnSnS}_4$, which are in good agreement with previous results and theoretical calculations (**Table A4.5** in Appendix 4).³²

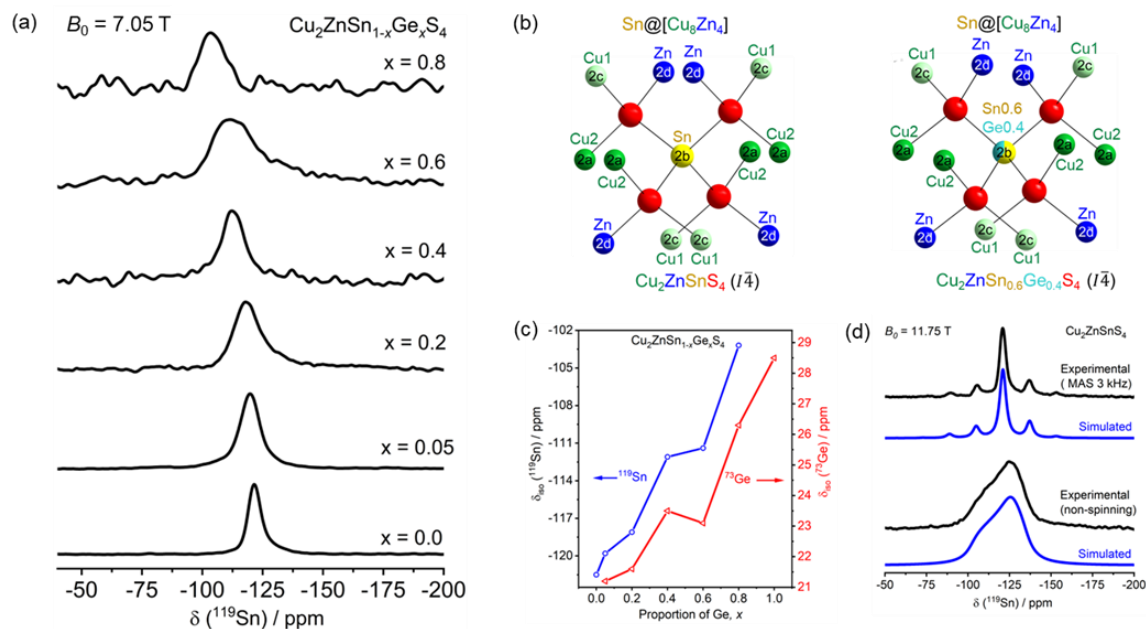


Figure 4.3. (a) ^{119}Sn MAS NMR spectra ($B_0 = 7.05$ T) for $\text{Cu}_2\text{ZnSn}_{1-x}\text{Ge}_x\text{S}_4$. (b) Coordination environments around Sn atoms for $\text{Cu}_2\text{ZnSnS}_4$ and $\text{Cu}_2\text{ZnSn}_{0.6}\text{Ge}_{0.4}\text{S}_4$ in space group $I\bar{4}$. (c) ^{119}Sn and ^{73}Ge isotropic chemical shifts as a function of Ge content (x). (d) Experimental, simulated non-spinning and slow spinning ($\omega_r/2\pi = 3$ kHz) ^{119}Sn spectra for $\text{Cu}_2\text{ZnSnS}_4$ ($B_0 = 11.75$ T, $\delta_{\text{iso}} = -121$ ppm, $\Omega = 32$ ppm and $\kappa = 0.4$). The experimental NMR simulations (blue) were performed using the Dmfit software.

A comparison of slow spinning $\text{Cu}_2\text{ZnSnS}_4$ and $\text{Cu}_2\text{ZnSn}_{0.4}\text{Ge}_{0.6}$ data shows that the linewidth of spinning sidebands increases whereas the total number remains the same, implying that the Ge substitution leads to multiple spatial configurations, but has a negligible effect on span (**Figure A4.1** in Appendix 4).

4.3.3 Local structure around Ge

For $\text{Cu}_2\text{ZnGeS}_4$, two models have been proposed, in space group $I\bar{4}$ or $I\bar{4}2m$. In both cases, the Ge atoms located at one set of sites at $2b$ $(0, 0, \frac{1}{2}; \frac{1}{2}, \frac{1}{2}, 0)$, and each Ge atom is surrounded by eight Cu and four Zn atoms in cuboctahedral geometry in the second coordination sphere. However, the site symmetry of these Ge atoms and distribution of surrounding atoms differ in these models: site symmetry $\bar{4}$ with Cu atoms lying on all planes in space group $I\bar{4}$ vs site symmetry $\bar{4}2m$ with Cu atoms lying on alternate planes in space group $I\bar{4}2m$ (**Figure 4.4a** and **Figure A4.2** in Appendix 4). It might be expected that ^{73}Ge NMR spectroscopy would be effective in distinguishing between these different chemical environments around the Ge atoms in the two possible models. Alas, the intrinsic properties of ^{73}Ge nuclei ($I = 9/2$), which has a low natural abundance of 7.7%, a large quadrupolar moment of $Q = -19.6 \text{ fm}^2$, and a low resonance frequency of $\mathcal{E} = 3.49\%$ (relative to ^1H), make it very challenging to perform these measurements.⁶³ It is no surprise that ^{73}Ge is regarded as an exotic nucleus.⁶⁸ To date, there have been few solid-state ^{73}Ge NMR studies on inorganic oxides and halides,^{41,69–73} and they have scarcely been applied to chalcogenides.^{74–76}

The ^{73}Ge NMR spectrum for $\text{Cu}_2\text{ZnGeS}_4$ exhibits a single resonance ($\delta_{\text{cgs}} = 28.5 \text{ ppm}$), which is consistent with the presence of a unique Ge site (**Figure 4.4b**). With increasing Ge concentration, δ_{cgs} gradually decreases from 21 to 29 ppm, which mimics the ^{119}Sn NMR spectra for $\text{Cu}_2\text{ZnSnS}_4$ (**Figure 4.3c**), indicating the environments around the Ge and Sn atoms in these compounds are similar. The ^{73}Ge resonance is sharp (FWHM = 95 Hz, $\sim 3 \text{ ppm}$) and remarkably narrower for $\text{Cu}_2\text{ZnGeS}_4$ compared to the ^{119}Sn resonance for $\text{Cu}_2\text{ZnSnS}_4$ ($I = 1/2$), implying that Ge resides in a highly symmetric environment with a narrow distribution of spatial configurations or lower amount of defects.

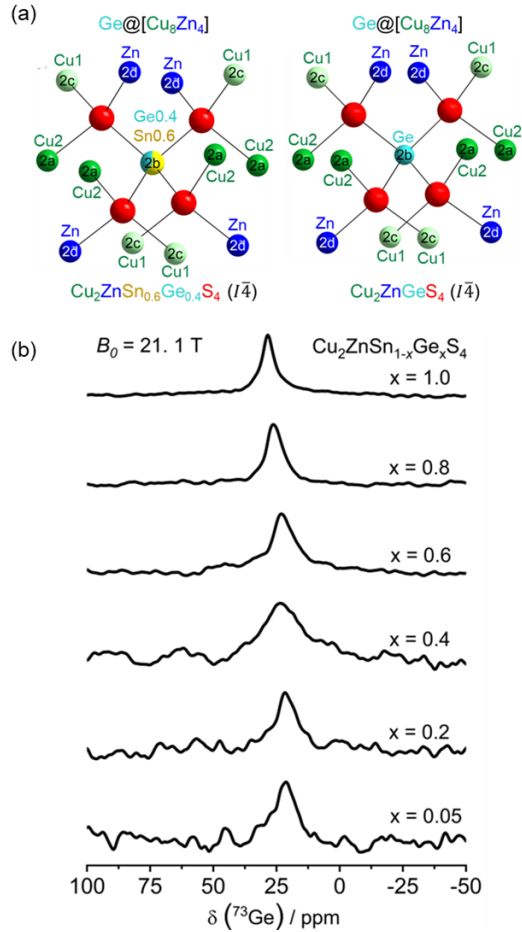


Figure 4.4. (a) Local structure around Ge for $\text{Cu}_2\text{ZnSn}_{0.6}\text{Ge}_{0.4}\text{S}_4$ and $\text{Cu}_2\text{ZnGeS}_4$ in $I\bar{4}$ structure model. (b) ^{73}Ge MAS NMR spectra ($B_0 = 21.1$ T) for $\text{Cu}_2\text{ZnSn}_{1-x}\text{Ge}_x\text{S}_4$.

Interestingly, the maximum linewidths for ^{73}Ge and ^{119}Sn NMR spectra are observed for $\text{Cu}_2\text{ZnSn}_{0.4}\text{Ge}_{0.6}\text{S}_4$ and $\text{Cu}_2\text{ZnSn}_{0.6}\text{Ge}_{0.4}\text{S}_4$, respectively, in which the concentrations of Ge and Sn are the same. However, in the case of $\text{Cu}_2\text{ZnGeS}_4$, the presence of a spinning sideband manifold (satellite transitions) indicates a non-zero C_Q (**Figure A4.3** in Appendix 4). The best fits on non-spinning and slow spinning ^{73}Ge NMR spectra of $\text{Cu}_2\text{ZnGeS}_4$ give $C_Q = 0.3$ MHz and $\eta = 0$ (**Figure A4.3**), which are in excellent agreement with computed values of $C_Q = 0.3$ MHz and $\eta = 0$ based on structure model in $I\bar{4}$ rather than $I\bar{4}2m$ (**Table A4.5** in Appendix 4) It should be noted that while the DFT calculation predicts a small CSA ($\Omega = 26$ ppm), it does not influence the fitting of

the experimental NMR data. Although ^{73}Ge NMR is usually very challenging, signals were relatively easily to detect, even for a 5% Ge concentration, because of the highly symmetrical environment around the Ge atoms in these chalcogenides. I believe that these results will motivate NMR spectroscopists to perform more ^{73}Ge measurements for related chalcogenides to extract valuable structural information.

4.3.4 Local structure around Zn

The Zn atoms in $\text{Cu}_2\text{Zn}_{1-x}\text{Ge}_x\text{SnS}_4$ occupy one set of sites at $2d$ ($0, \frac{1}{2}, \frac{3}{4}, \frac{1}{2}, 0, \frac{1}{4}$) with site symmetry $\bar{4}$ in the $I\bar{4}$ model, or at $2a$ ($0, 0, 0; \frac{1}{2}, \frac{1}{2}, \frac{1}{2}$) with site symmetry $\bar{4}2m$ in the $I\bar{4}2m$ model. In each case, the second coordination sphere consists of eight Cu and four Sn/Ge atoms. ^{67}Zn is a quadrupolar nucleus that reflects the interaction between the quadrupole moment of the nucleus and the local electric field gradient (EFG). As such, the NMR lineshape arising from this interaction strongly depends on the local and medium-range environment of the ^{67}Zn nuclei and is sensitive to any distortions that may be present.⁷⁷⁻⁸¹ To gain further insight into the environments around these atoms, ^{67}Zn NMR spectra ($I = 5/2$; 4.1% natural abundance, $Q = 15.0 \text{ fm}^2$, $\mathcal{E} = 6.3\%$)⁶³ were obtained for the complete series $\text{Cu}_2\text{ZnSn}_{1-x}\text{Ge}_x\text{S}_4$. For the parent compounds, a single resonance (δ_{iso}) is seen at 361 ppm without any second-order contribution for $\text{Cu}_2\text{ZnSnS}_4$, and at 358 ppm with a marked second-order contribution for $\text{Cu}_2\text{ZnGeS}_4$ (**Figure 4 5**). This observation implies that unique Zn sites are present in both end-members, but they vary in the degree of distortion in the local environments. For the series, the resonances arising from Zn atoms can be separated into those with environment $[\text{Cu}_8\text{Sn}_4]$, denoted as $L(0)$, and those with environments $[\text{Cu}_8\text{Sn}_{4-n}\text{Ge}_n]$, denoted as $L(n)$, where n ranges from 1 to 4. As more Ge is substituted in $\text{Cu}_2\text{ZnSn}_{1-x}\text{Ge}_x\text{S}_4$, δ_{egs} of the $L(0)$ line increases from 359 ($x = 0$) to 382 ppm ($x =$

0.4) (Table A4.7 in Appendix 4) and then starts decreasing, suggesting that longer range effects may be imparted by Ge atoms beyond the second coordination sphere.

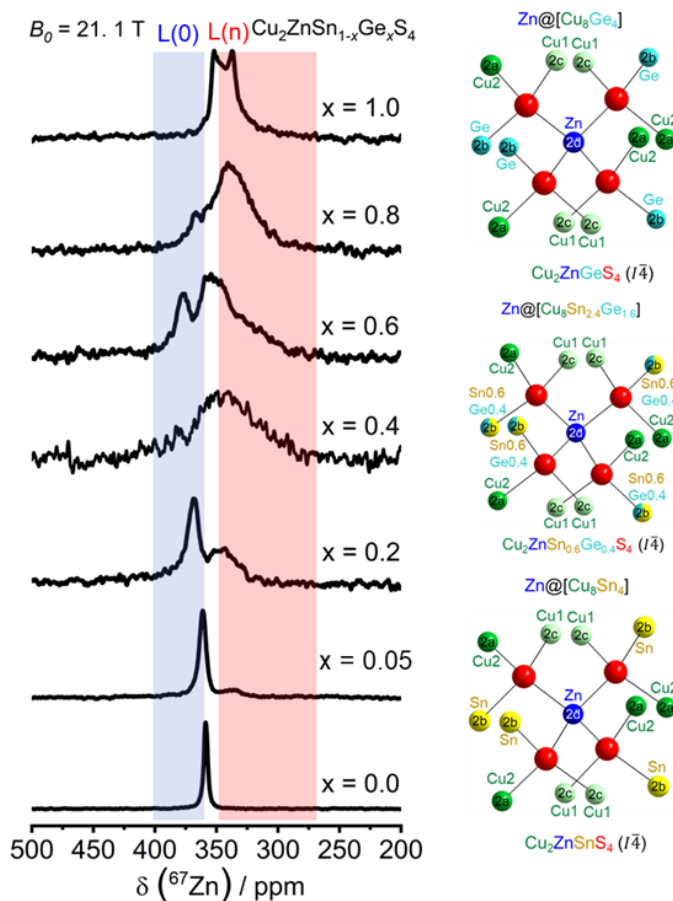


Figure 4.5. ^{67}Zn MAS NMR spectra ($B_0 = 21.1$ T) for $\text{Cu}_2\text{Zn}_{1-x}\text{Ge}_x\text{SnS}_4$ assigned with L(0) (blue) and L(n) (red).

On the other hand, the intensity of L(n) ($n = 1-4$) increases, with second-order quadrupolar lineshapes arising from greater electric field gradient due to the lowering of symmetry upon Ge substitution. The intensity of the L(0) line gradually decreases for lightly Ge-substituted compositions ($x = 0, 0.05, 0.2$), but it does not follow any trend for highly Ge-substituted compositions ($x = 0.4, 0.6$). This finding suggests that Sn/Ge mixing is not random at the atomic

length scale, but may be suggestive of cation clustering or nanodomain formation for highly Ge-substituted members. Note that it may not be possible to detect all the distinct Zn environments within $[\text{Cu}_8\text{Sn}_{4-n}\text{Ge}_n]$, because C_Q can be very high for a particular value of n , resulting in broad, undetected resonances.⁷³

Non-spinning experimental spectra ^{67}Zn NMR for $\text{Cu}_2\text{ZnSnS}_4$ ($\Omega = 29$ ppm, $\kappa = -0.5$, $C_Q = 0.9$ MHz, $\eta = 0$) and $\text{Cu}_2\text{ZnGeS}_4$ ($C_Q = 2.8$ MHz, $\eta = 0.2$) agree well with the simulated spectra (**Figure 4.6**). The higher C_Q value for $\text{Cu}_2\text{ZnGeS}_4$ can be correlated with greater tetragonal distortion ($c/2a$) as evident from the XRD analyses. This experimental value of C_Q is in better agreement with the computed value based on the $I\bar{4}$ model (5.1 MHz) than on the $I\bar{4}2m$ model (7.2 MHz).

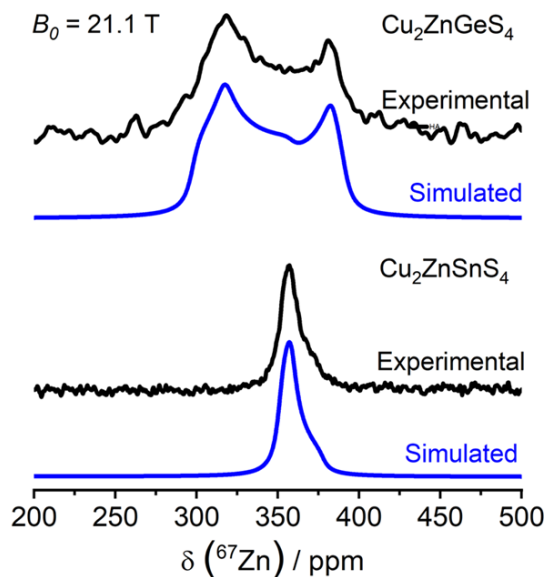


Figure 4.6. Experimental (black) and simulated (blue) non-spinning ^{67}Zn spectra for $\text{Cu}_2\text{ZnSnS}_4$ ($\delta_{\text{iso}} = 361$ ppm, $\Omega = 29$ ppm, $\kappa = -0.5$, $C_Q = 0.9$ MHz, $\eta = 0$) and $\text{Cu}_2\text{ZnGeS}_4$ ($\delta_{\text{iso}} = 358$ ppm, $C_Q = 2.8$ MHz, $\eta = 0.2$) at 21.1 T. The experimental NMR simulations (blue) were performed using the Dmfit software.

4.3.5 Local structure around Cu

We now turn to $^{63/65}\text{Cu}$ NMR spectroscopy,^{34,35,77,82,83} which should provide the missing piece of the puzzle to reliably assign the appropriate structure for $\text{Cu}_2\text{ZnGeS}_4$. The Cu atoms occupy two sets of sites at $2a$ ($0, 0, 0; \frac{1}{2}, \frac{1}{2}, \frac{1}{2}$) and $2c$ ($0, \frac{1}{2}, \frac{1}{4}; \frac{1}{2}, 0, \frac{3}{4}$) in space group $I\bar{4}$, in contrast to one set of sites at $4d$ ($0, \frac{1}{2}, \frac{1}{2}; 0, \frac{1}{2}, \frac{3}{4}; \frac{1}{2}, 0, 0; \frac{1}{2}, 0, \frac{1}{4}$) in space group $I\bar{4}2m$. The environment around Cu atoms can be generalized as $[\text{Cu}_4\text{Zn}_4\text{Sn}_{4-n}\text{Ge}_n]$ (**Figure 4.7a**). The ^{63}Cu NMR spectra ($I = 3/2$; 69.2% natural abundance, $Q = -22.0 \text{ fm}^2$, $E = 26.5\%$)⁶³ acquired at 21.1 T with fast magic-angle spinning of 62.5 kHz reveal two ^{63}Cu resonances for $\text{Cu}_2\text{ZnSnS}_4$ with δ_{cgs} of 794 and 754 ppm, and similarly for $\text{Cu}_2\text{ZnGeS}_4$ with δ_{cgs} of 797 and 561 ppm (**Figure 4.7b**). These observations confirm the presence of two distinct Cu sites ($2a$ and $2c$), consistent with the $I\bar{4}$ model. To support this structural assignment, DFT computations were performed to predict the NMR parameters and compare them with experimental spectra (**Figure A4.4** in Appendix 4). The experimental spectra of $\text{Cu}_2\text{ZnGeS}_4$ agree well with the simulated spectrum for the structure in $I\bar{4}$ instead of $I\bar{4}2m$. Note that the copper chemical shifts are sensitive to heating, caused by magic-angle spinning at 62.5 kHz, so the centre-of-gravity shift is reported here; the isotropic chemical shift at room temperature is reported based on the non-spinning pattern (*vide infra*).

Additional non-spinning ^{65}Cu NMR spectra for $\text{Cu}_2\text{ZnSnS}_4$ and $\text{Cu}_2\text{ZnGeS}_4$ were acquired (**Figure A4.5** in Appendix 4) at different magnetic fields (7.05, 11.75, and 21.1 T) to reliably determine the CSA and quadrupolar parameters (**Table A4.5** in Appendix 4). For both compounds, two distinct resonances were observed: at δ_{iso} of 785 ppm ($C_Q = 6.5 \text{ MHz}$, $2a$ site) and 804 ppm ($C_Q = 1.5 \text{ MHz}$, $2c$ site) for $\text{Cu}_2\text{ZnSnS}_4$, and at $\delta_{\text{iso}} = 705 \text{ ppm}$ ($C_Q = 15.2 \text{ MHz}$, $2a$ site) and $\delta_{\text{iso}} = 812 \text{ ppm}$ ($C_Q = 4.3$, $2c$) for $\text{Cu}_2\text{ZnGeS}_4$. The ^{65}Cu NMR spectra were deconvoluted to determine CSA and EFG parameters for $2a$ and $2c$ sites individually (**Figure 4.7c, d**). The relative areas of the two

peaks are nearly equal for both compounds, in agreement with the $I\bar{4}$ model. The resonances for the Cu $2a$ site resonances become narrower with increasing magnetic field, indicating that the quadrupolar interaction is the dominant anisotropic interaction (**Figure A4.5** in Appendix 4).

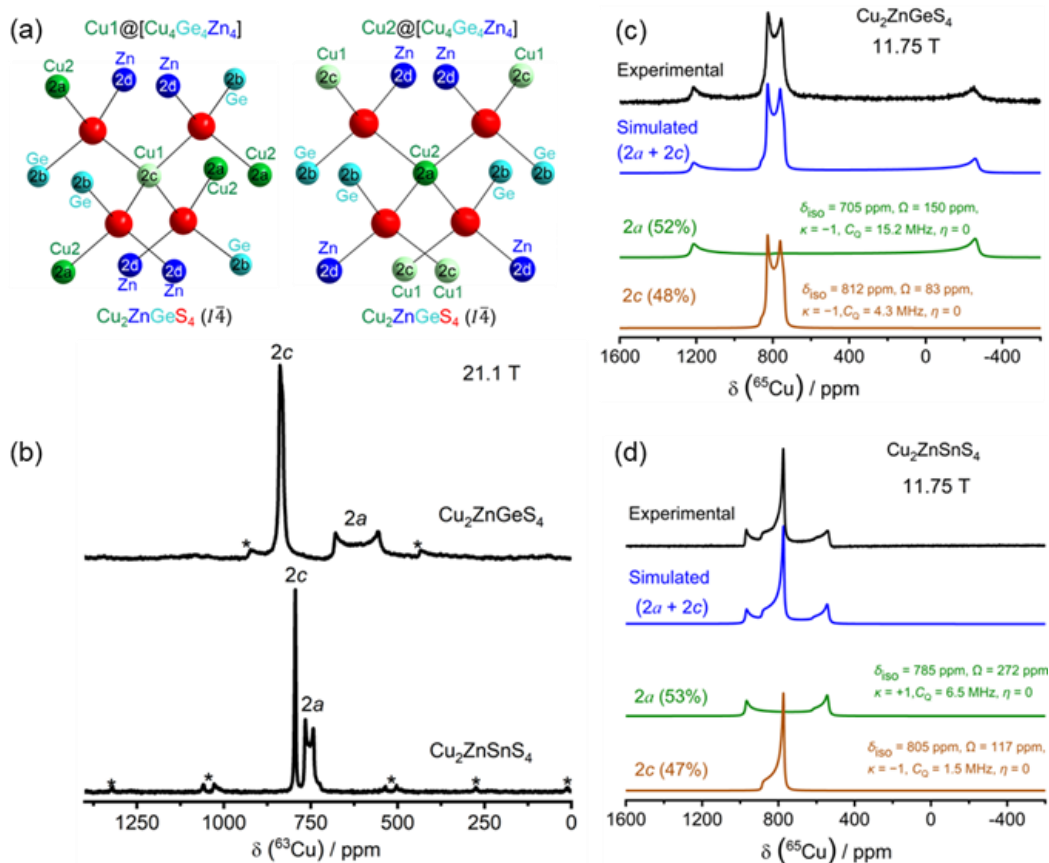


Figure 4.7. (a) Local environment around Cu atoms in $\text{Cu}_2\text{ZnGeS}_4$ ($I\bar{4}$). (b) ^{65}Cu MAS (62.5 kHz) NMR spectra ($B_0 = 21.1$ T) for $\text{Cu}_2\text{ZnGeS}_4$ and $\text{Cu}_2\text{ZnSnS}_4$ with two distinct resonances associated with $2a$ and $2c$ sites in $I\bar{4}$ structure. Asterisks indicate spinning sidebands in the MAS NMR spectra. Deconvolution of non-spinning ^{65}Cu NMR spectra for (c) $\text{Cu}_2\text{ZnGeS}_4$ and (d) $\text{Cu}_2\text{ZnSnS}_4$ at 11.75 T. The experimental NMR simulations (blue) were performed using the Dmfit software.

The difference in C_Q for the $2a$ and $2c$ sites can be correlated to the degree of structural distortion of the Cu-centered tetrahedra. The bond angles around the $2a$ site, labelled as Cu2 (108.5–109.9°), deviate more from the ideal tetrahedral angle (109.5°) than do those for the $2c$ site (109.2°) (**Table A4.6** in Appendix 4); this conclusion is further supported by quantum chemical

calculations. Similarly, the difference in C_Q for $2a$ site (108.1–112.3°) and $2c$ site (108.8 –110.8°) in $\text{Cu}_2\text{ZnGeS}_4$ can be related to the degree of structural distortion of the Cu-centered tetrahedra. In addition to the first coordination sphere, C_Q is further affected by the arrangement of Cu and Sn/Ge atoms in the second coordination sphere in both $\text{Cu}_2\text{ZnSnS}_4$ and $\text{Cu}_2\text{ZnGeS}_4$. Moreover, the increase in the C_Q values ($2a$ and $2c$) on proceeding from $\text{Cu}_2\text{ZnSnS}_4$ to $\text{Cu}_2\text{ZnGeS}_4$ can be correlated with the greater tetragonal distortion for $\text{Cu}_2\text{ZnGeS}_4$. The spans of ^{65}Cu NMR peaks decrease on going from $\text{Cu}_2\text{ZnSnS}_4$ ($\Omega = 270$ and 118 ppm) to $\text{Cu}_2\text{ZnGeS}_4$ ($\Omega = 150$ and 83 ppm); the skew values of +1 or –1 imply that all Cu CSA tensors are axially symmetric and the magnitudes of V_{xx} and V_{yy} are equal within error.

Lightly Ge substituted members ($x = 0.05$ and 0.2) exhibit two distinct resonances; however, these are broadened compared to those for the parent compounds, indicating that upon Ge substitution, both Cu sites experience a range of chemical shifts and EFGs, demonstrating their sensitivity to changes in nearby surroundings (**Figure 4.8**). For $x = 0.8$, three distinct resonances appear to be present: the resonances at 592 and 375 ppm are close to the lower frequency horn of $2c$ resonances for $\text{Cu}_2\text{ZnSnS}_4$ and $\text{Cu}_2\text{ZnGeS}_4$ respectively, while the resonances associated with 498 ppm lie between these compounds (**Figure 4.8b**). Therefore, the origin of these resonances can be ascribed to the local environments $[\text{Cu}_4\text{Zn}_4\text{Sn}_4]$, $[\text{Cu}_4\text{Zn}_4\text{Ge}_4]$, and $[\text{Cu}_4\text{Zn}_4\text{Sn}_{4-n}\text{Ge}_n]$, where $1 < n < 4$ at 592, 375, and 498 ppm respectively. For $x = 0.4$ and 0.6, the tailing toward lower frequency indicates that a range of C_Q values arises from the variation in the medium-range environment within the $[\text{Cu}_4\text{Zn}_4\text{Sn}_{4-n}\text{Ge}_n]$ network. The presence of two distinct $2a$ and $2c$ sites for all the members in $\text{Cu}_2\text{ZnSn}_{1-x}\text{Ge}_x\text{S}_4$ further confirms the $I\bar{4}$ model throughout this series. Overall, the computed NMR parameters match reasonably well with the experimental parameters (**Table A4.5** in Appendix 4).

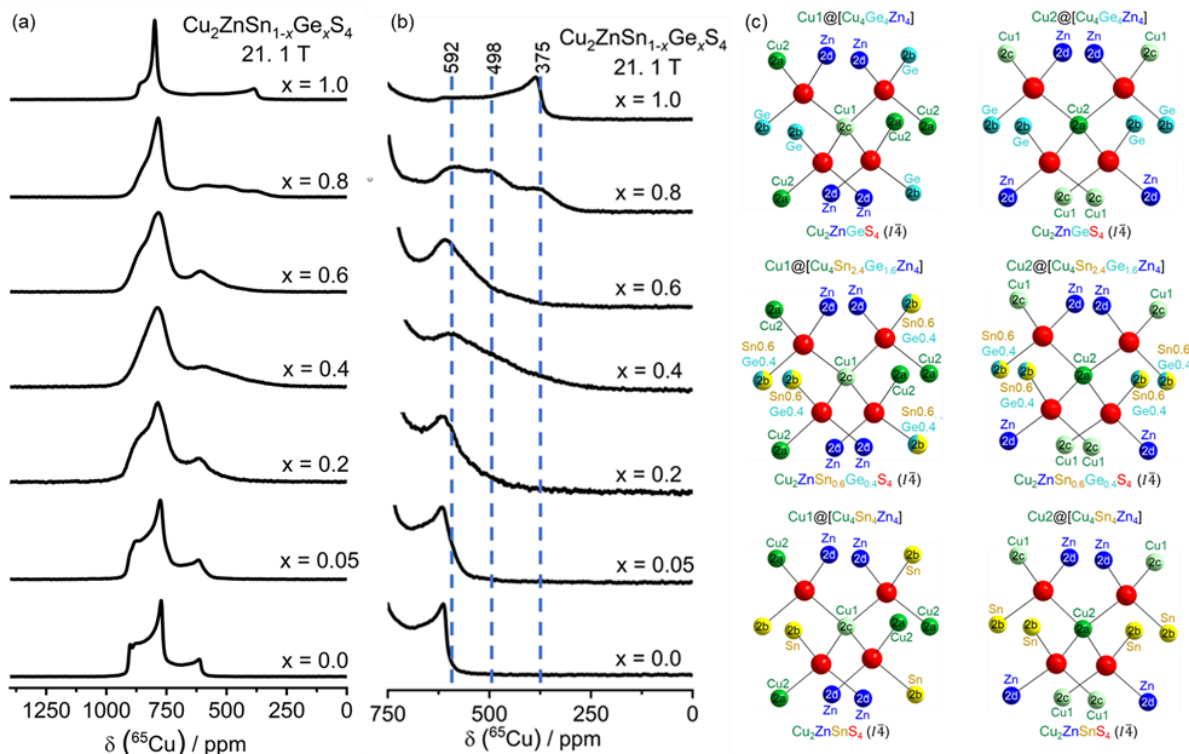


Figure 4.8. (a) ^{65}Cu non-spinning NMR spectra ($B_0 = 21.1\text{ T}$) and (b) enlarged views of low frequency region for $\text{Cu}_2\text{ZnSn}_{1-x}\text{Ge}_x\text{SnS}_4$. (c) Local structure around Cu1 ($2c$) and Cu2 ($2a$) sites for $\text{Cu}_2\text{ZnGeS}_4$ in $I\bar{4}$.

4.3.6 Optical band gaps and electronic structure of $\text{Cu}_2\text{ZnSn}_{1-x}\text{Ge}_x\text{S}_4$

Optical band gaps were measured by UV-Vis diffuse reflectance spectroscopy and determined from Tauc plots, with a direct band gap being assumed (**Figure A4.6**). The band gaps increase with greater Ge substitution, from 1.49 eV for $\text{Cu}_2\text{ZnSnS}_4$ to 1.97 eV for $\text{Cu}_2\text{ZnGeS}_4$. This increasing trend of band gaps agrees with previously reported results.^{84,85}

Electronic structure calculations implemented with the HSE functional give band gaps of 1.48 eV for $\text{Cu}_2\text{ZnSnS}_4$, 1.75 eV for $\text{Cu}_2\text{ZnSn}_{0.5}\text{Ge}_{0.5}\text{S}_4$, and 2.06 eV for $\text{Cu}_2\text{ZnGeS}_4$,^{86,87} in good agreement with the experimental values (**Table A4.3** in Appendix 4). The valence and conduction band extrema are found at the Brillouin zone centre, indicating direct band gaps (**Figure A4.7**).

The top of the valence band of these compounds is heavily dominated by the Cu 3d and S 3p states. In accordance with the tetrahedral crystal field around Cu atoms, the valence band is split into an upper (0 to about -3.0 eV) and lower parts (-3.5 to -6.5 eV). The upper region is dominated by antibonding states involving mixing of Cu 3d and S 3p states, and the lower region results from Cu–S and Sn–S bonding interactions and Zn–S antibonding interactions. The bottom of the conduction band involves Sn–S antibonding interactions (as well as Ge–S interactions in Ge-substituted compounds). The conduction band minima shift to higher energy with greater Ge substitution.

Bonding character of the metal-sulfur bonds was evaluated from COBI values.⁵⁹ The Cu–S and Zn–S bonds tend to be more ionic (ICOBI of 0.20 and 0.22, respectively), whereas the Sn–S and Ge–S bonds tend to be more covalent (ICOBI of 0.84 and 0.87, respectively). ELF plots suggest polar character in the Cu–S bonds, for which the electron density is shifted closer to the S atoms, in contrast to the more equal sharing of electron density (yellow-green colours) within the Sn–S and Ge–S bonds (**Figure 4.9**). The Bader charges are not as extreme as charges assigned in a fully ionic formulation which is $(\text{Cu}^{1+})_2\text{Zn}^{2+}(\text{M})^{4+}(\text{S}^{2-})_4$. However, their relative values are in good agreement with expectations: 0.4+ to 0.5+ for Cu, 0.9+ for Zn, 1.6+ for Sn, 1.4+ for Ge, and 0.8– to 0.9– for S.

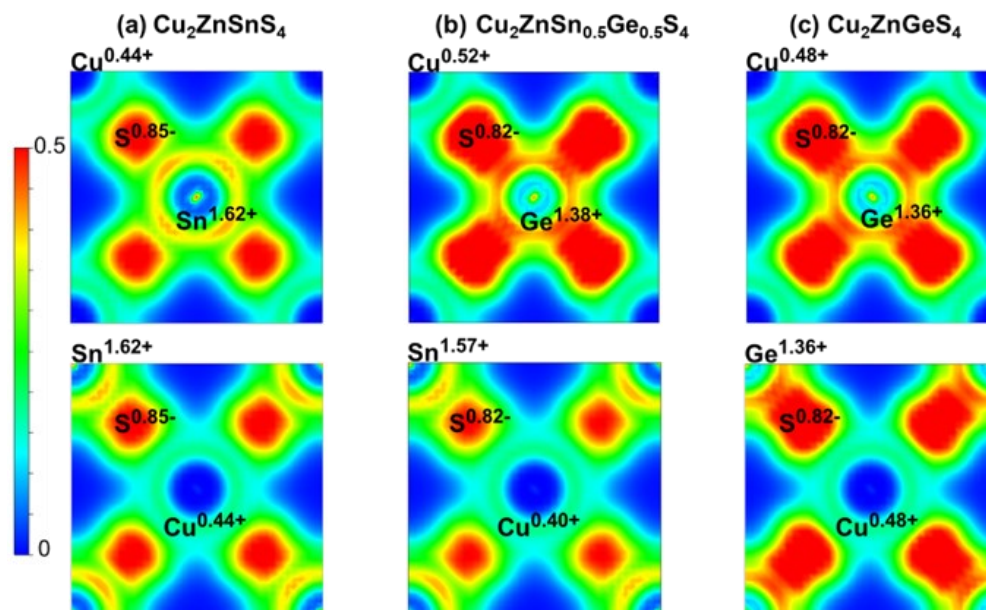


Figure 4.9. Electron localization function, projected on slices parallel to the (001) plane at $z = 0$ (top) and $1/4$ (bottom), with Bader charges shown for (a) $\text{Cu}_2\text{ZnSnS}_4$, (b) $\text{Cu}_2\text{ZnSn}_{0.5}\text{Ge}_{0.5}\text{S}_4$, and (c) $\text{Cu}_2\text{ZnGeS}_4$.

4.4 Conclusions

Within the solid solution $\text{Cu}_2\text{ZnSn}_{1-x}\text{Ge}_x\text{S}_4$, the ^{119}Sn and ^{73}Ge chemical shifts are sensitive to structural changes upon Ge substitution. Although magnetic shielding is governed by both electronic and chemical structures, the chemical shifts increase with larger band gaps. This seems counterintuitive because the chemical shift would be expected to decrease with increasing band gap, given that the paramagnetic contribution is inversely related to the average excitation energy (ΔE) corresponding to the band gap energy.^{88–90} This general argument often holds true for nanomaterials when the influence of only the diamagnetic and paramagnetic magnetic shielding contributions are considered. However, these trends can also be affected by spin-orbit contributions, which have been shown to be substantial in Sn-containing semiconductors.⁹¹

This study has resolved some earlier ambiguities about the structure of $\text{Cu}_2\text{ZnSn}_{1-x}\text{Ge}_x\text{S}_4$. The experimental spinning and non-spinning $^{63/65}\text{Cu}$ solid-state NMR, in combination with DFT

calculations, support the $I\bar{4}$ model for $\text{Cu}_2\text{ZnGeS}_4$, as seen by the occurrence of multiple local environments $[\text{Cu}_4\text{Zn}_4\text{Sn}_4]$, $[\text{Cu}_4\text{Zn}_4\text{Sn}_{4-n}\text{Ge}_n]$, and $[\text{Cu}_4\text{Zn}_4\text{Ge}_4]$. The surprisingly narrow linewidth of the ^{73}Ge NMR spectra, which are the first obtained for these chalcogenides, implies a highly symmetric chemical environment around the Ge atoms. The degree of distortion around Cu atoms was related to C_Q parameters, and variable-field ^{65}Cu NMR allowed reliable CSA and EFG parameters to be determined. The ^{67}Zn NMR suggested possible formation of domains for the highly substituted members ($x > 0.2$). Electronic structure calculations confirm that the band gap becomes wider with greater Ge substitution and help to quantify the bonding character in these compounds.

It was observed that $^{63/65}\text{Cu}$ NMR data are highly sensitive to local chemical environment, providing important structural information for several series of quaternary chalcogenides, including $\text{Cu}_2\text{ZnSnS}_4$, $\text{Cu}_2\text{CdSnS}_4$, $\text{Cu}_2\text{HgSnS}_4$, and $\text{Cu}_2\text{ZnGeS}_4$ (discussed here). Initially, $^{63/65}\text{Cu}$ NMR spectroscopy provided insight into local structural evolution upon Cd substitution in $\text{Cu}_2\text{ZnSnS}_4$. Moreover, it revealed two crystallographically inequivalent Cu sites in $\text{Cu}_2\text{ZnSnS}_4$, providing conclusive evidence in favour of the $I\bar{4}$ model. The combination $^{63/65}\text{Cu}$ NMR experiments with GIPAW–DFT computations helped to resolve the question about Cu/Zn disorder. In a similar way, the site distributions in $\text{Cu}_2\text{CdSnS}_4$ and $\text{Cu}_2\text{HgSnS}_4$ were clarified, and shown to be consistent with the $I\bar{4}2m$ model. In the present work, $\text{Cu}_2\text{ZnGeS}_4$ was shown to have an analogous structure to $\text{Cu}_2\text{ZnSnS}_4$. The $^{63/65}\text{Cu}$ C_Q correlates well with the degree of polyhedral distortion experienced by the $2a$ and $2c$ sites in $\text{Cu}_2\text{ZnSnS}_4$ and $\text{Cu}_2\text{ZnGeS}_4$. It is noteworthy that informative spectra could be obtained, without interference from Cu metal within the coil of the spectrometer.

4.5 References

- (1) Lee, T. D.; Ebong, A. U. A review of thin film solar cell technologies and challenges. *Renew. Sustain. Energy Rev.* **2017**, *70*, 1286–1297.
- (2) Kim, J. Y.; Lee, J.-W.; Jung, H. S.; Shin, H.; Park, N.-G. High-efficiency perovskite solar cells. *Chem. Rev.* **2020**, *120*, 7867–7918.
- (3) Jackson, P.; Hariskos, D.; Lotter, E.; Paetel, S.; Wuerz, R.; Menner, R.; Wischmann, W.; Powalla, M. New world record efficiency for Cu(In,Ga)Se₂ thin-film solar cells beyond 20%. *Prog. Photovolt. Res. Appl.* **2011**, *19*, 894–897.
- (4) Chirilă, A.; Reinhard, P.; Pianezzi, F.; Bloesch, P.; Uhl, A. R.; Fella, C.; Kranz, L.; Keller, D.; Gretener, C.; Hagendorfer, H.; Jaeger, D.; Erni, R.; Nishiwaki, S.; Buecheler, S.; Tiwari, A. N. Potassium-induced surface modification of Cu(In,Ga)Se₂ thin films for high-efficiency solar cells. *Nat. Mater.* **2013**, *12*, 1107–1111.
- (5) Berhe, T. A.; Su, W.-N.; Chen, C.-H.; Pan, C.-J.; Cheng, J.-H.; Chen, H.-M.; Tsai, M.-C.; Chen, L.-Y.; Aregahegn Dubale, A.; Hwang, B.-J. Organometal halide perovskite solar cells: degradation and stability. *Energy Environ. Sci.* **2016**, *9*, 323–356.
- (6) Li, J.; Cao, H.-L.; Jiao, W.-B.; Wang, Q.; Wei, M.; Cantone, I.; Lü, J.; Abate, A. Biological impact of lead from halide perovskites reveals the risk of introducing a safe threshold. *Nat. Commun.* **2020**, *11*, 310.
- (7) Sun, K.; Yan, C.; Liu, F.; Huang, J.; Zhou, F.; Stride, J. A.; Green, M.; Hao, X. Over 9% efficient kesterite Cu₂ZnSnS₄ solar cell fabricated by using Zn_{1-x}Cd_xS buffer layer. *Adv. Energy Mater.* **2016**, *6*, 1600046.
- (8) Pal, K.; Singh, P.; Bhaduri, A.; Thapa, K. B. Current challenges and future prospects for a highly efficient (>20%) kesterite CZTS solar cell: a review. *Sol. Energy Mater. Sol. Cells* **2019**, *196*, 138–156.
- (9) Shin, B.; Gunawan, O.; Zhu, Y.; Bojarczuk, N. A.; Chey, S. J.; Guha, S. Thin film solar cell with 8.4% power conversion efficiency using an earth-abundant Cu₂ZnSnS₄ absorber. *Prog. Photovolt. Res. Appl.* **2013**, *21*, 72–76.
- (10) Siebentritt, S.; Schorr, S. Kesterites – a challenging material for solar cells. *Prog. Photovolt. Res. Appl.* **2012**, *20*, 512–519.

- (11) Green, M.; Dunlop, E.; Hohl-Ebinger, J.; Yoshita, M.; Kopidakis, N.; Hao, X. Solar cell efficiency tables (version 57). *Prog. Photovolt. Res. Appl.* **2021**, *29*, 3–15.
- (12) National renewable energy laboratory (NREL). *Best research-cell efficiency chart*. <https://www.nrel.gov/pv/cell-efficiency.html>.
- (13) Xin, H.; Vorpahl, S. M.; Collord, A. D.; Braly, I. L.; Uhl, A. R.; Krueger, B. W.; Ginger, D. S.; Hillhouse, H. W. Lithium-doping inverts the nanoscale electric field at the grain boundaries in $\text{Cu}_2\text{ZnSn}(\text{S},\text{Se})_4$ and increases photovoltaic efficiency. *Phys. Chem. Chem. Phys.* **2015**, *17*, 23859–23866.
- (14) Gershon, T.; Sardashti, K.; Lee, Y. S.; Gunawan, O.; Singh, S.; Bishop, D.; Kummel, A. C.; Haight, R. Compositional effects in $\text{Ag}_2\text{ZnSnSe}_4$ thin films and photovoltaic devices. *Acta Mater.* **2017**, *126*, 383–388.
- (15) Yan, C.; Sun, K.; Huang, J.; Johnston, S.; Liu, F.; Veettil, B. P.; Sun, K.; Pu, A.; Zhou, F.; Stride, J. A.; Green, M. A.; Hao, X. Beyond 11% efficient sulfide kesterite $\text{Cu}_2\text{Zn}_x\text{Cd}_{1-x}\text{SnS}_4$ solar cell: effects of cadmium alloying. *ACS Energy Lett.* **2017**, *2*, 930–936.
- (16) Shin, D.; Zhu, T.; Huang, X.; Gunawan, O.; Blum, V.; Mitzi, D. B. Earth-abundant chalcogenide photovoltaic devices with over 5% efficiency based on a $\text{Cu}_2\text{BaSn}(\text{S},\text{Se})_4$ absorber. *Adv. Mater.* **2017**, *29*, 1606945.
- (17) Ghosh, A.; Chaudhary, D. K.; Biswas, A.; Thangavel, R.; Udayabhanu, G. Solution-processed Cu_2XSnS_4 ($X = \text{Fe}, \text{Co}, \text{Ni}$) photo-electrochemical and thin film solar cells on vertically grown ZnO nanorod arrays. *RSC Adv.* **2016**, *6*, 115204–115212.
- (18) Li, X.; Hou, Z.; Gao, S.; Zeng, Y.; Ao, J.; Zhou, Z.; Da, B.; Liu, W.; Sun, Y.; Zhang, Y. Efficient optimization of the performance of Mn^{2+} -doped kesterite solar cell: machine learning aided synthesis of high efficient $\text{Cu}_2(\text{Mn}, \text{Zn})\text{Sn}(\text{S},\text{Se})_4$ solar cells. *Sol. RRL* **2018**, *2*, 1800198.
- (19) Collord, A. D.; Hillhouse, H. W. Germanium alloyed kesterite solar cells with low voltage deficits. *Chem. Mater.* **2016**, *28*, 2067–2073.
- (20) Giraldo, S.; Neuschitzer, M.; Thersleff, T.; López-Marino, S.; Sánchez, Y.; Xie, H.; Colina, M.; Placidi, M.; Pistor, P.; Izquierdo-Roca, V. Large efficiency improvement in $\text{Cu}_2\text{ZnSnSe}_4$ solar cells by introducing a superficial Ge nanolayer. *Adv. Energy Mater.* **2015**, *5*, 1501070.

- (21) Kim, I.; Kim, K.; Oh, Y.; Woo, K.; Cao, G.; Jeong, S.; Moon, J. Bandgap-graded $\text{Cu}_2\text{Zn}(\text{Sn}_{1-x}\text{Ge}_x)\text{S}_4$ thin-film solar cells derived from metal chalcogenide complex ligand capped nanocrystals. *Chem. Mater.* **2014**, *26*, 3957–3965.
- (22) Hages, C. J.; Levencenco, S.; Miskin, C. K.; Alsmeier, J. H.; Abou-Ras, D.; Wilks, R. G.; Bär, M.; Unold, T.; Agrawal, R. Improved performance of Ge-alloyed CZTGeSSe thin-film solar cells through control of elemental losses. *Prog. Photovolt. Res. Appl.* **2015**, *23*, 376–384.
- (23) Kim, S.; Kim, K. M.; Tampo, H.; Shibata, H.; Niki, S. Improvement of voltage deficit of Ge-incorporated kesterite solar cell with 12.3% conversion efficiency. *Appl. Phys. Express* **2016**, *9*, 102301.
- (24) Moodie, A. F.; Whitfield, H. J. Determination of the structure of $\text{Cu}_2\text{ZnGeS}_4$ polymorphs by lattice imaging and convergent-beam electron diffraction. *Acta Crystallogr. B* **1986**, *42*, 236–247.
- (25) Parasyuk, O. V.; Piskach, L. V.; Romanyuk, Y. E.; Olekseyuk, I. D.; Zaremba, V. I.; Pekhnyo, V. I. Phase relations in the quasi-binary $\text{Cu}_2\text{GeS}_3\text{--ZnS}$ and quasi-ternary $\text{Cu}_2\text{S--Zn}(\text{Cd})\text{S--GeS}_2$ systems and crystal structure of $\text{Cu}_2\text{ZnGeS}_4$. *J. Alloys Compd.* **2005**, *397*, 85–94.
- (26) Doverspike, K.; Dwight, K.; Wold, A. Preparation and characterization of copper zinc germanium sulfide selenide ($\text{Cu}_2\text{ZnGeS}_{4-y}\text{Se}_y$). *Chem. Mater.* **1990**, *2*, 194–197.
- (27) Heinrich, C. P.; Day, T. W.; Zeier, W. G.; Snyder, G. J.; Tremel, W. Effect of isovalent substitution on the thermoelectric properties of the $\text{Cu}_2\text{ZnGeSe}_{4-x}\text{S}_x$ series of solid solutions. *J. Am. Chem. Soc.* **2014**, *136*, 442–448.
- (28) Schleich, D. M.; Wold, A. Optical and electrical properties of quaternary chalcogenides. *Mater. Res. Bull.* **1977**, *12*, 111–114.
- (29) Khadka, D. B.; Kim, J. Band gap engineering of alloyed $\text{Cu}_2\text{ZnGe}_x\text{Sn}_{1-x}\text{Q}_4$ ($Q = \text{S, Se}$) films for solar cell. *J. Phys. Chem. C* **2015**, *119*, 1706–1713.
- (30) Mangelis, P.; Aziz, A.; da Silva, I.; Grau-Crespo, R.; Vaqueiro, P.; Powell, A. V. Understanding the origin of disorder in kesterite-type chalcogenides $A_2\text{ZnBQ}_4$ ($A = \text{Cu, Ag}$; $B = \text{Sn, Ge}$; $Q = \text{S, Se}$): the influence of inter-layer interactions. *Phys. Chem. Chem. Phys.* **2019**, *21*, 19311–19317.

- (31) Lafond, A.; Guillot-Deudon, C.; Vidal, J.; Paris, M.; La, C.; Jobic, S. Substitution of Li for Cu in $\text{Cu}_2\text{ZnSnS}_4$: toward wide band gap absorbers with low cation disorder for thin film solar cells. *Inorg. Chem.* **2017**, *56*, 2712–2721.
- (32) Bhattacharya, A.; Tkachuk, D. G.; Mar, A.; Michaelis, V. K. Mere anarchy is loosed: structural disorder in $\text{Cu}_2\text{Zn}_{1-x}\text{Cd}_x\text{SnS}_4$. *Chem. Mater.* **2021**, *33*, 4709–4722.
- (33) Paris, M.; Larramona, G.; Bais, P.; Bourdais, S.; Lafond, A.; Choné, C.; Guillot-Deudon, C.; Delatouche, B.; Moisan, C.; Dennler, G. ^{119}Sn MAS NMR to assess the cationic disorder and the anionic distribution in sulfoselenide $\text{Cu}_2\text{ZnSn}(\text{S}_x\text{Se}_{1-x})_4$ compounds prepared from colloidal and ceramic routes. *J. Phys. Chem. C* **2015**, *119*, 26849–26857.
- (34) Shi, C.; Xi, X.; Hou, Z.; Liu, E.; Wang, W.; Chen, J.; Wu, G. Copper dynamics and structural transformation in noble metal chalcogenides CuAgS probed by ^{63}Cu NMR. *Solid State Ion.* **2017**, *300*, 182–186.
- (35) Zeier, W. G.; Heinrich, C. P.; Day, T.; Panithipongwut, C.; Kieslich, G.; Brunklaus, G.; Snyder, G. J.; Tremel, W. Bond strength dependent superionic phase transformation in the solid solution series $\text{Cu}_2\text{ZnGeSe}_{4-x}\text{S}_x$. *J. Mater. Chem. A* **2014**, *2*, 1790–1794.
- (36) Rodríguez-Carvajal, J. Introduction to the Program FULLPROF: Refinement of crystal and magnetic structures from powder and single crystal data. *Lab. Léon Brillouin CEA-CNRS Saclay Fr.* **2001**.
- (37) Kortüm, G. *Reflectance Spectroscopy*; Springer, 1969.
- (38) Rusanova, D.; Forsling, W.; Antzutkin, O. N.; Pike, K. J.; Dupree, R. Solid-State ^{31}P CP/MAS and Static ^{65}Cu NMR Characterization of polycrystalline copper(I) dialkyldithiophosphate clusters. *J. Magn. Reson.* **2006**, *179*, 140–145.
- (39) Gunther, W. R.; Michaelis, V. K.; Caporini, M. A.; Griffin, R. G.; Román-Leshkov, Y. Dynamic nuclear polarization NMR enables the analysis of Sn-beta zeolite prepared with natural abundance ^{119}Sn precursors. *J. Am. Chem. Soc.* **2014**, *136*, 6219–6222.
- (40) Wu, G. Zinc-67 nuclear magnetic resonance spectroscopy of solids. *Chem. Phys. Lett.* **1998**, *298*, 375–380.
- (41) Michaelis, V. K.; Aguiar, P.; Terskikh, V.; Kroeker, S. Germanium-73 NMR of amorphous and crystalline GeO_2 . *Chem. Commun.* **2009**, *31*, 4660–4662.

- (42) Massiot, D.; Fayon, F.; Capron, M.; King, I.; Le Calve S; Alonso B; Durand O.; Bujoli B. *Gan Z Hoatson G*. Modeling one- and two- dimensional solid-state NMR spectra, *Magn Reson Chem*, **2002**, *40*, 70–76.
- (43) Mason, J. *Solid State Nucl. Magn. Reson.* **1993**, *2*, 285–288.
- (44) Herzfeld, J.; Berger, A. E. Sideband intensities in NMR spectra of samples spinning at the magic angle. *J. Chem. Phys.* **1980**, *73*, 6021–6030.
- (45) Slichter, C. P. *Principles of Magnetic Resonance*; Springer, 1996.
- (46) Wasylishen, R. E.; Ashbrook, S. E.; Wimperis, S. *NMR of Quadrupolar Nuclei in Solid Materials*; Wiley, 2012.
- (47) Lucier, B. E. G.; Tang, J. A.; Schurko, R. W.; Bowmaker, G. A.; Healy, P. C.; Hanna, J. V. Solid-State ^{65}Cu and ^{31}P NMR spectroscopy of bis(triphenylphosphine) copper species. *J. Phys. Chem. C* **2010**, *114*, 7949–7962.
- (48) Taulelle, F. NMR of quadrupolar nuclei in the solid state. In *Multinuclear Magnetic Resonance in Liquids and Solids—Chemical Applications*; Springer, 1990.
- (49) MacKenzie, K. J. D.; Smith, M. E. *Multinuclear Solid-state NMR of Inorganic Materials*, 1st ed.; Pergamon, 2002.
- (50) Clark, S. J.; Segall, M. D.; Pickard, C. J.; Hasnip, P. J.; Probert, M. I. J.; Refson, K.; Payne, M. C. First principles methods using CASTEP. *Z. Kristallgr.* **2005**, *220*, 567–570.
- (51) Perdew, J. P.; Burke, K.; Ernzerhof, M. Generalized gradient approximation made simple. *Phys. Rev. Lett.* **1996**, *77*, 3865–3868.
- (52) Yates, J. R.; Pickard, C. J.; Mauri, F. Calculation of NMR chemical shifts for extended systems using ultrasoft pseudopotentials. *Phys. Rev. B* **2007**, *76*, 024401.
- (53) Kresse, G.; Furthmüller, J. Efficient iterative schemes for ab-Initio total-energy calculations using a plane-wave basis set. *Phys. Rev. B* **1996**, *54*, 11169–11186.
- (54) Kresse, G.; Joubert, D. From ultrasoft pseudopotentials to the projector augmented-wave method. *Phys. Rev. B* **1999**, *59*, 1758.
- (55) Blöchl, P. E. Projector augmented-wave method. *Phys. Rev. B* **1994**, *50*, 17953–17979.
- (56) Hohenberg, P.; Kohn, W. Inhomogeneous electron gas. *Phys. Rev.* **1964**, *136*, B864–B871.
- (57) Kohn, W.; Sham, L. J. Self-consistent equations including exchange and correlation effects. *Phys. Rev.* **1965**, *140*, A1133.

- (58) Tang, W.; Sanville, E.; Henkelman, G. A Grid-based bader analysis algorithm without lattice bias. *J. Phys. Condens. Matter* **2009**, *21*, 084204.
- (59) Müller, P. C.; Ertural, C.; Hempelmann, J.; Dronskowski, R. Crystal orbital bond index: covalent bond orders in solids. *J. Phys. Chem. C* **2021**, *125*, 7959–7970.
- (60) Deringer, V. L.; Tchougréeff, A. L.; Dronskowski, R. Crystal orbital hamilton population (COHP) analysis as projected from plane-wave basis sets. *J. Phys. Chem. A* **2011**, *115*, 5461–5466.
- (61) Grin, Y.; Savin, A.; Silvi, B. The ELF perspective of chemical bonding. In *The Chemical Bond: Fundamental Aspects of Chemical Bonding*; Wiley, 2014.
- (62) Maintz, S.; Deringer, V. L.; Tchougréeff, A. L.; Dronskowski, R. LOBSTER: a tool to extract chemical bonding from plane-wave based DFT. *J. Comput. Chem.* **2016**, *37*, 1030–1035.
- (63) Harris, R. K.; Becker, E. D.; De Menezes, S. M. C.; Goodfellow, R.; Granger, P. NMR nomenclature. Nuclear spin properties and conventions for chemical shifts (IUPAC recommendations 2001). *Pure Appl. Chem.* **2001**, *73*, 1795–1818.
- (64) Kubicki, D. J.; Prochowicz, D.; Salager, E.; Rakhmatullin, A.; Grey, C. P.; Emsley, L.; Stranks, S. D. Local structure and dynamics in methylammonium, formamidinium, and cesium tin(II) mixed-halide perovskites from ^{119}Sn solid-state NMR. *J. Am. Chem. Soc.* **2020**, *142*, 7813–7826.
- (65) Ha, M.; Karmakar, A.; Bernard, G. M.; Basilio, E.; Krishnamurthy, A.; Askar, A. M.; Shankar, K.; Kroeker, S.; Michaelis, V. K. Phase evolution in methylammonium tin halide perovskites with variable temperature solid-state ^{119}Sn NMR spectroscopy. *J. Phys. Chem. C* **2020**, *124*, 15015–15027.
- (66) Karmakar, A.; Bhattacharya, A.; Sarkar, D.; M. Bernard, G.; Mar, A.; K. Michaelis, V. Influence of hidden halogen mobility on local structure of $\text{CsSn}(\text{Cl}_{1-x}\text{Br}_x)_3$ mixed-halide perovskites by solid-state NMR. *Chem. Sci.* **2021**, *12*, 3253–3263.
- (67) Karmakar, A.; Bhattacharya, A.; Bernard, G. M.; Mar, A.; Michaelis, V. K. Revealing the local Sn and Pb arrangements in $\text{CsSn}_x\text{Pb}_{1-x}\text{Br}_3$ perovskites with solid-state NMR spectroscopy. *ACS Mater. Lett.* **2021**, *3*, 261–267.
- (68) Leroy, C.; Bryce, D. L. Recent advances in solid-state nuclear magnetic resonance spectroscopy of exotic nuclei. *Prog. Nucl. Magn. Reson. Spectrosc.* **2018**, *109*, 160–199.

- (69) Greer, B. J.; Michaelis, V. K.; Terskikh, V. V.; Kroeker, S. Reconnaissance of diverse structural and electronic environments in germanium halides by solid-state ^{73}Ge NMR and quantum chemical calculations. *Can. J. Chem.* **2011**, *89*, 1118–1129.
- (70) Michaelis, V. K.; Kroeker, S. ^{73}Ge Solid-State NMR of germanium oxide materials: experimental and theoretical studies. *J. Phys. Chem. C* **2010**, *114*, 21736–21744.
- (71) Hooper, R. W.; Ni, C.; Tkachuk, D. G.; He, Y.; Terskikh, V. V.; Veinot, J. G. C.; Michaelis, V. K. Exploring structural nuances in germanium halide perovskites using solid-state ^{73}Ge and ^{133}Cs NMR spectroscopy. *J. Phys. Chem. Lett.* **2022**, *13*, 1687–1696.
- (72) Kidd, R. G.; Spinney, H. G. Germanium-73 nuclear magnetic resonance spectra of germanium tetrahalides. *J. Am. Chem. Soc.* **1973**, *95*, 88–90.
- (73) Sutrisno, A.; A. Hanson, M.; A. Rupar, P.; V. Terskikh, V.; M. Baines, K.; Huang, Y. Exploring the limits of ^{73}Ge solid-state NMR spectroscopy at ultrahigh magnetic field. *Chem. Commun.* **2010**, *46*, 2817–2819.
- (74) Kaseman, D. C.; Sen, S. A review of the application of 2D isotropic-anisotropic correlation NMR spectroscopy in structural studies of chalcogenide glasses. *J. Non-Cryst. Solids* **2021**, *561*, 120500.
- (75) Sen, S.; Gan, Z. Chemical order around Ge atoms in binary germanium selenide glasses: results from ^{73}Ge solid-state NMR spectroscopy at 19.6 Tesla. *J. Non-Cryst. Solids* **2010**, *356*, 1519–1521.
- (76) Gonçalves, C.; Mereau, R.; Nazabal, V.; Boussard-Pledel, C.; Roiland, C.; Furet, E.; Deschamps, M.; Bureau, B.; Dussauze, M. Study of the $\text{Ge}_{20}\text{Te}_{80-x}\text{Se}_x$ glassy structures by combining solid state NMR, vibrational spectroscopies and DFT modelling. *J. Solid State Chem.* **2021**, *297*, 122062.
- (77) Choubrac, L.; Paris, M.; Lafond, A.; Guillot-Deudon, C.; Rocquefelte, X.; Jobic, S. Multinuclear (^{67}Zn , ^{119}Sn and ^{65}Cu) NMR spectroscopy – an ideal technique to probe the cationic ordering in $\text{Cu}_2\text{ZnSnS}_4$ photovoltaic materials. *Phys. Chem. Chem. Phys.* **2013**, *15*, 10722–10725.
- (78) Hibble, S. J.; Chippindale, A. M.; Marelli, E.; Kroeker, S.; Michaelis, V. K.; Greer, B. J.; Aguiar, P. M.; Bilbé, E. J.; Barney, E. R.; Hannon, A. C. Local and average structure in zinc cyanide: toward an understanding of the atomistic origin of negative thermal expansion. *J. Am. Chem. Soc.* **2013**, *135*, 16478–16489.

- (79) Huang, Y.; Sutrisno, A. Recent advances in solid-state ^{67}Zn NMR studies: from nanoparticles to biological systems. *Annu. Rep. NMR Spectrosc.*; Academic press, **2014**, *81*, 1–46.
- (80) Madsen, R. S. K.; Qiao, A.; Sen, J.; Hung, I.; Chen, K.; Gan, Z.; Sen, S.; Yue, Y. Ultrahigh-field ^{67}Zn NMR reveals short-range disorder in zeolitic imidazolate framework glasses. *Science* **2020**, *367*, 1473–1476.
- (81) Cadars, S.; Smith, B. J.; Epping, J. D.; Acharya, S.; Belman, N.; Golan, Y.; Chmelka, B. F. Atomic positional versus electronic order in semiconducting ZnSe nanoparticles. *Phys. Rev. Lett.* **2009**, *103*, 136802.
- (82) Tang, J. A.; Ellis, B. D.; Warren, T. H.; Hanna, J. V.; Macdonald, C. L. B.; Schurko, R. W. Solid-State ^{63}Cu and ^{65}Cu NMR spectroscopy of inorganic and organometallic copper(I) complexes. *J. Am. Chem. Soc.* **2007**, *129*, 13049–13065.
- (83) Reiser, S.; Brunklaus, G.; Hong, J. H.; Chan, J. C. C.; Eckert, H.; Pfitzner, A. $(\text{CuI})_3\text{P}_4\text{S}_4$: preparation, structural, and NMR spectroscopic characterization of a copper(I) halide adduct with $\beta\text{-P}_4\text{S}_4$. *Chem. – Eur. J.* **2002**, *8*, 4228–4233.
- (84) Hayashi, S.; Hayamizu, K. Effect of Spinning on chemical shifts in magic-angle-spinning nuclear magnetic resonance. *J. Chem. Phys.* **1990**, *92*, 2818–2827.
- (85) Garcia-Llamas, E.; Merino, J. M.; Serna, R.; Fontané, X.; Victorov, I. A.; Pérez-Rodríguez, A.; León, M.; Bodnar, I. V.; Izquierdo-Roca, V.; Caballero, R. Wide band-gap tuning $\text{Cu}_2\text{ZnSn}_{1-x}\text{Ge}_x\text{S}_4$ single crystals: optical and vibrational properties. *Sol. Energy Mater. Sol. Cells* **2016**, *158*, 147–153.
- (86) Mora-Herrera, D.; Pal, M.; Paraguay-Delgado, F. Facile solvothermal synthesis of $\text{Cu}_2\text{ZnSn}_{1-x}\text{Ge}_x\text{S}_4$ nanocrystals: effect of Ge content on optical and electrical properties. *Mater. Chem. Phys.* **2021**, *257*, 123764.
- (87) Kukreti, S.; Gupta, G. K.; Dixit, A. Theoretical DFT studies of $\text{Cu}_2\text{HgSnS}_4$ absorber material and Al:ZnO/ZnO/CdS/ $\text{Cu}_2\text{HgSnS}_4$ /back contact heterojunction solar cell. *Sol. Energy* **2021**, *225*, 802–813.
- (88) Paier, J.; Asahi, R.; Nagoya, A.; Kresse, G. $\text{Cu}_2\text{ZnSnS}_4$ as a potential photovoltaic material: a hybrid hartree-fock density functional theory study. *Phys. Rev. B* **2009**, *79*, 115126.
- (89) Müller, P. C.; Ertural, C.; Hempelmann, J.; Dronskowski, R. Crystal orbital bond index: covalent bond orders in solids. *J. Phys. Chem. C* **2021**, *125*, 7959–7970.

- (90) Ramsey, N. F. Magnetic shielding of nuclei in molecules. *Phys. Rev.* **1950**, 78, 699–703.
- (91) Yesinowski, J. P. Solid-state NMR of inorganic semiconductors. In *Solid State NMR*; Chan, J. C. C., Ed.; Springer, 2012.

Chapter 5

Conclusions

5.1 Summary

Chapter 2 described the Cd-substituted solid solutions $\text{Cu}_2\text{Zn}_{1-x}\text{Cd}_x\text{SnS}_4$ synthesized by high-temperature reactions and their detailed structural analysis. X-ray diffraction indicates a structural transition from space group $\bar{I}4$ to $\bar{I}42m$ at $x = 0.4$. From ^{113}Cd MAS NMR spectroscopy, phases with these two structures were found to coexist at this composition, which is a new insight. The Sn atoms occupy distinct sites whose chemical environments could be distinguished by ^{119}Sn NMR spectroscopy through their isotropic chemical shifts upon Cd substitution. High-field (21.1 T) ^{63}Cu NMR spectroscopy revealed two sets of Cu sites in the $\bar{I}4$ structure for the lightly Cd-substituted compositions (up to $\text{Cu}_2\text{Zn}_{0.8}\text{Cd}_{0.2}\text{SnS}_4$) and one set of Cu sites in the $\bar{I}42m$ structure for the more heavily substituted compositions. Finally, a combination of DFT calculations and high-field ^{63}Cu and ^{67}Zn NMR spectroscopy revealed details about Cu/Zn disorder and the Cd substitution pathway.

Chapter 3 described the differences in long- and short-range structure for $\text{Cu}_2\text{ZnSnS}_4$, $\text{Cu}_2\text{CdSnS}_4$, and $\text{Cu}_2\text{HgSnS}_4$. Experimental spinning and non-spinning $^{63/65}\text{Cu}$ solid-state NMR and DFT calculations confirm that $\text{Cu}_2\text{CdSnS}_4$ and $\text{Cu}_2\text{HgSnS}_4$ adopt the $\bar{I}42m$ structure. The degree of distortion around Cu or Sn atoms correlates with NMR parameters (C_Q or CSA). For example, the two sets of Cu sites for the $\bar{I}4$ structure of $\text{Cu}_2\text{ZnSnS}_4$ can be assigned to separate peaks with different C_Q values. ^{119}Sn and ^{199}Hg NMR spectroscopy reveal that local order/disorder phenomena occur upon heating, while XRD reveals that the long-range structure for these

materials does not vary significantly. The band gap decreases from 1.5 eV for $\text{Cu}_2\text{ZnSnS}_4$ to 0.9 eV for $\text{Cu}_2\text{HgSnS}_4$ as electronegativity differences become smaller, in agreement with DFT calculations.

Chapter 4 described the structural analysis of $\text{Cu}_2\text{ZnSn}_{1-x}\text{Ge}_x\text{S}_4$, which consists of nontoxic elements, through solid-state multinuclear ($^{63/65}\text{Cu}$, ^{67}Zn , ^{73}Ge , and ^{119}Sn) magnetic resonance spectroscopy and XRD measurements. The ^{73}Ge , ^{119}Sn , and ^{67}Zn NMR spectra show chemical shifts and linewidths that are sensitive to changes in the local environment up to the second coordination sphere and possibly beyond. The Zn atoms reside in sites of lower symmetry in $\text{Cu}_2\text{ZnGeS}_4$ than in $\text{Cu}_2\text{ZnSnS}_4$, as evident by the quadrupole coupling values. High-field (21.1 T) $^{63/65}\text{Cu}$ NMR spectroscopy reveals two distinct Cu sites in $\text{Cu}_2\text{ZnGeS}_4$, similar to $\text{Cu}_2\text{ZnSnS}_4$. In conjunction with DFT results, this observation supports the $\bar{I}4$ structure for $\text{Cu}_2\text{ZnGeS}_4$. The band gap increases from 1.49 eV for $\text{Cu}_2\text{ZnSnS}_4$ to 1.97 eV $\text{Cu}_2\text{ZnGeS}_4$, in agreement with DFT results.

5.2 Outlook

In Chapter 4, $\text{Cu}_2\text{ZnSn}_{0.2}\text{Ge}_{0.8}\text{S}_4$ displays three distinct ^{65}Cu resonances that correspond to the local environment $\text{Cu}@[\text{Cu}_4\text{Zn}_4\text{Sn}_{4-n}\text{Ge}_n]$. To improve the resolution, quantum magic angle spinning ^{65}Cu NMR experiments can be performed at 36 T (1.5 GHz, ^1H).^{1,2} Ultra-high fields can reduce the second order broadening significantly, but fast MAS is required because the CSA will also increase. It will be interesting to see these resonances evolve within finer increments of the solid solution $\text{Cu}_2\text{ZnSn}_{1-x}\text{Ge}_x\text{S}_4$ ($x = 0.7, 0.8, 0.9, 0.95$).

Suggested future directions include the synthesis of Cu_2MTtS_4 ($M = \text{Zn, Cd, Hg}$; $Tt = \text{Si, Sn, Ge}$) through varied approaches, such as ball milling, hydrothermal reactions, and vapour deposition methods.³⁻⁵ Samples prepared by these methods could differ in particle size, crystal

structure, and local structure, which will affect the properties in turn. There remains some discrepancy in the literature about $\text{Cu}_2\text{ZnGeS}_4$, which was reported to adopt a tetragonal structure (containing two Cu sites) for samples prepared by high-temperature reaction, but an orthorhombic structure (containing one Cu site) for nanoparticles prepared by solution methods.⁴ These two structural models, as well as degree of crystallinity or coexistence of polymorphs, could thus be distinguished by ^{65}Cu NMR spectroscopy.

Notwithstanding the heavy emphasis on photovoltaic materials, these chalcogenides do have other applications. An interesting related chalcogenide is $\text{Cu}_2\text{ZnSiS}_4$, which has been investigated as a nonlinear optical material because it adopts a noncentrosymmetric structure in space group $Pnm2_1$, based on single crystal XRD.⁵ Subsequently, a second polymorph in space group Pc was identified using high-resolution synchrotron powder XRD.⁶ The powder XRD patterns of the two polymorphs are similar, making them difficult to distinguish. It would be helpful to carry out ^{65}Cu non-spinning MAS NMR spectroscopy to analyze these compounds and distinguish between them by noting the number of resonances. Different synthetic conditions may also need to be investigated to ascertain if a mixture of two polymorphs can coexist.

Beyond the quaternary sulfides, the corresponding selenides and tellurides also form: $\text{Cu}_2\text{ZnSiSe}_4$ in space group $Pmn2_1$ and $\text{Cu}_2\text{ZnSiTe}_4$ in space group $I\bar{4}2m$.^{7,8,9} They have not been as thoroughly investigated, but ^{65}Cu , ^{77}Se , and ^{125}Te are accessible NMR nuclei. The work in this thesis can easily be extended to many other chalcogenides.

5.3 References

- (1) Chen, K. A practical review of NMR lineshapes for spin-1/2 and quadrupolar nuclei in disordered materials. *Int. J. Mol. Sci.* **2020**, *21*, 5666.

- (2) Bhattacharya, A.; Tkachuk, D. G.; Mar, A.; Michaelis, V. K. Mere anarchy is loosed: structural disorder in $\text{Cu}_2\text{Zn}_{1-x}\text{Cd}_x\text{SnS}_4$. *Chem. Mater.* **2021**, *33*, 4709–4722.
- (3) Pinto, A. H.; Shin, S. W.; Isaac, E.; Knutson, T. R.; Aydil, E. S.; Penn, R. L. Controlling $\text{Cu}_2\text{ZnSnS}_4$ (CZTS) phase in microwave solvothermal synthesis. *J. Mater. Chem. A* **2017**, *5*, 23179–23189.
- (4) Fan, C. M.; Regulacio, M. D.; Ye, C.; Lim, S. H.; Lua, S. K.; Xu, Q.-H.; Dong, Z.; Xu, A.-W.; Han, M.-Y. Colloidal nanocrystals of orthorhombic $\text{Cu}_2\text{ZnGeS}_4$: phase-controlled synthesis, formation mechanism and photocatalytic behaviour. *Nanoscale* **2015**, *7*, 3247–3253.
- (5) Rosmus, K. A.; Aitken, J. A. $\text{Cu}_2\text{ZnSiS}_4$. *Acta Crystallogr., Sect. E* **2011**, *67*, i28.
- (6) Rosmus, K. A.; Brunetta, C. D.; Srnec, M. N.; Karuppanan, B.; Aitken, J. A. Synchrotron X-ray powder diffraction and electronic band structure of α - and β - $\text{Cu}_2\text{ZnSiS}_4$. *Z. Anorg. Allg. Chem.* **2012**, *638*, 2578–2584.
- (7) Nakamura, S.; Maeda, T.; Wada, T. Phase stability and electronic structure of In free photovoltaic materials: $\text{Cu}_2\text{ZnSiSe}_4$, $\text{Cu}_2\text{ZnGeSe}_4$, and $\text{Cu}_2\text{ZnSnSe}_4$. *Jpn. J. Appl. Phys.* **2010**, *49*, 121203.
- (8) Zhang, X.; Rao, D.; Lu, R.; Deng, K.; Chen, D. First-principles study on electronic and optical properties of $\text{Cu}_2\text{ZnSiVI}_4$ (VI = S, Se, and Te) quaternary semiconductors. *AIP Adv.* **2015**, *5*, 057111.
- (9) Haeuseler, H.; Ohrendorf, F. W.; Himmrich, M. Z. Zur Kenntnis quaternärer Telluride $\text{Cu}_2\text{MM}'\text{Te}_4$ mit Tetraederstrukturen/Quaternary Tellurides $\text{Cu}_2\text{MM}'\text{Te}_4$ with Tetrahedral Structures. *Z. Naturforsch. B.* **1991**, *46*, 1049–1052.

Bibliography

Chapter 1

- (1) Annual energy outlook (2022) – U.S. energy information administration (EIA). https://www.eia.gov/outlooks/aeo/pdf/AEO2022_ReleasePresentation.pdf
- (2) Key world energy statistics 2021 – analysis. IEA. <https://www.iea.org/reports/key-world-energy-statistics-2021>.
- (3) World energy council. (2013). World energy resources 2013 survey. https://www.worldenergy.org/wp_content/uploads/2013/09/Complete_WER_2013_Survey.pdf
- (4) Muratoglu, A.; Yuce, M. World energy outlook and place of renewable resources. *Int. J. Sci. Technol. Res.* **2015**, *1*, 10–17.
- (5) IEA, World CO₂ emissions from fuel combustion by fuel, 1971-2019, IEA, Paris <https://www.iea.org/data-and-statistics/charts/world-co2-emissions-from-fuel-combustion-by-fuel-1971-2019>.
- (6) Nayak, P. K.; Mahesh, S.; Snaith, H. J.; Cahen, D. Photovoltaic solar cell technologies: analysing the state of the art. *Nat. Rev. Mater.* **2019**, *4*, 269–285.
- (7) Green, M.; Dunlop, E.; Hohl-Ebinger, J.; Yoshita, M.; Kopidakis, N.; Hao, X. Solar cell efficiency tables (version 57). *Prog. Photovolt. Res. Appl.* **2021**, *29*, 3–15.
- (8) Saha, S. A status review on Cu₂ZnSn(S,Se)₄-based thin-film solar cells. *Int. J. Photoenergy*, 2020, *2020*, 1–13
- (9) Liu, M.; Johnston, M. B.; Snaith, H. J. Efficient planar heterojunction perovskite solar cells by vapour deposition. *Nature* **2013**, *501*, 395–398.
- (10) Kojima, A.; Teshima, K.; Shirai, Y.; Miyasaka, T. Organometal halide perovskites as visible-light sensitizers for photovoltaic cells. *J. Am. Chem. Soc.* **2009**, *131*, 6050–6051.
- (11) Xiang, W.; Liu, S; Tress, W. A review on the stability of inorganic metal halide perovskites: challenges and opportunities for stable solar cells. *Energy Environ. Sci.* **2021**, *14*, 2090–2113.
- (12) Britt, J.; Ferekides, C. Thin-film CdS/CdTe solar-cell with 15.8-percent efficiency. *Appl. Phys. Lett.* **1993**, *62*, 2851–2852

- (13) Jackson, P.; Hariskos, D.; Wuerz, R.; Kiowski, O.; Bauer, A.; Friedlmeier, T. M.; Powalla, M. Properties of Cu(In,Ga)Se₂ solar cells with new record efficiencies up to 21.7%. *Phys. Status Solidi RRL* **2015**, *9*, 28–31.
- (14) Geisthardt, R. M.; Topič, M.; Sites, J. R. Status and potential of CdTe solar-cell efficiency. *IEEE J. Photovolt.* **2015**, *5*, 1217–1221.
- (15) Siebentritt, S.; Schorr, S. Kesterites – a challenging material for solar cells. *Prog. Photovolt. Res. Appl.* **2012**, *20*, 512–519.
- (16) Sun, K.; Yan, C.; Liu, F.; Huang, J.; Zhou, F.; Stride, J. A.; Green, M.; Hao, X. Over 9% efficient kesterite Cu₂ZnSnS₄ solar cell fabricated by using Zn_{1-x}Cd_xS buffer layer. *Adv. Energy Mater.* **2016**, *6*, 1600046.
- (17) Pal, K.; Singh, P.; Bhaduri, A.; Thapa, K. B. Current challenges and future prospects for a highly efficient (>20%) kesterite CZTS solar cell: a review. *Sol. Energy Mater. Sol. Cells* **2019**, *196*, 138–156.
- (18) Shin, B.; Gunawan, O.; Zhu, Y.; Bojarczuk, N. A.; Chey, S. J.; Guha, S. Thin film solar cell with 8.4% power conversion efficiency using an earth-abundant Cu₂ZnSnS₄ absorber. *Prog. Photovolt. Res. Appl.* **2013**, *21*, 72–76.
- (19) Tanaka, K.; Moritake, N.; Uchiki, H. Preparation of Cu₂ZnSnS₄ thin films by sulfurizing sol–gel deposited precursors. *Sol. Energy Mater. Sol. Cells* **2007**, *91*, 1199–1201.
- (20) Wang, W.; Winkler, M. T.; Gunawan, O.; Gokmen, T.; Todorov, T. K.; Zhu, Y.; Mitzi, D. B. Device characteristics of CZTSSe thin-film solar cells with 12.6% efficiency. *Adv. Energy Mater.* **2014**, *4*, 1301465.
- (21) Fyfe, C. A.; Gies, H.; Kokotailo, G. T.; Pasztor, C.; Strobl, H.; Cox, D. E. Detailed investigation of the lattice structure of zeolite ZSM-11 by a combination of solid-state NMR and synchrotron X-Ray diffraction techniques. *J. Am. Chem. Soc.* **1989**, *111*, 2470–2474.
- (22) Xin, H.; Vorpahl, S. M.; Collord, A. D.; Braly, I. L.; Uhl, A. R.; Krueger, B. W.; Ginger, D. S.; Hillhouse, H. W. Lithium-doping inverts the nanoscale electric field at the grain boundaries in Cu₂ZnSn(S,Se)₄ and increases photovoltaic efficiency. *Phys. Chem. Chem. Phys.* **2015**, *17*, 23859–23866.

- (23) Gershon, T.; Sardashti, K.; Lee, Y. S.; Gunawan, O.; Singh, S.; Bishop, D.; Kummel, A. C.; Haight, R. Compositional effects in $\text{Ag}_2\text{ZnSnSe}_4$ thin films and photovoltaic devices. *Acta Mater.* **2017**, *126*, 383–388.
- (24) Yan, C.; Sun, K.; Huang, J.; Johnston, S.; Liu, F.; Veetil, B. P.; Sun, K.; Pu, A.; Zhou, F.; Stride, J. A.; Green, M. A.; Hao, X. Beyond 11% efficient sulfide kesterite $\text{Cu}_2\text{Zn}_x\text{Cd}_{1-x}\text{SnS}_4$ solar cell: effects of cadmium alloying. *ACS Energy Lett.* **2017**, *2*, 930–936.
- (25) Shin, D.; Zhu, T.; Huang, X.; Gunawan, O.; Blum, V.; Mitzi, D. B. Earth-abundant chalcogenide photovoltaic devices with over 5% efficiency based on a $\text{Cu}_2\text{BaSn}(\text{S},\text{Se})_4$ absorber. *Adv. Mater.* **2017**, *29*, 1606945.
- (26) Ghosh, A.; Chaudhary, D. K.; Biswas, A.; Thangavel, R.; Udayabhanu, G. Solution-processed Cu_2XSnS_4 ($X = \text{Fe}, \text{Co}, \text{Ni}$) photo-electrochemical and thin film solar cells on vertically grown ZnO nanorod arrays. *RSC Adv.* **2016**, *6*, 115204–115212.
- (27) Li, X.; Hou, Z.; Gao, S.; Zeng, Y.; Ao, J.; Zhou, Z.; Da, B.; Liu, W.; Sun, Y.; Zhang, Y. Efficient optimization of the performance of Mn^{2+} -doped kesterite solar cell: machine learning aided synthesis of high efficient $\text{Cu}_2(\text{Mn},\text{Zn})\text{Sn}(\text{S},\text{Se})_4$ solar cells. *Sol. RRL* **2018**, *2*, 1800198.
- (28) Collord, A. D.; Hillhouse, H. W. Germanium alloyed kesterite solar cells with low voltage deficits. *Chem. Mater.* **2016**, *28*, 2067–2073.
- (29) Su, Z.; Tan, J. M. R.; Li, X.; Zeng, X.; Batabyal, S. K.; Wong, L. H. Cation substitution of solution processed $\text{Cu}_2\text{ZnSnS}_4$ thin film solar cell with over 9% efficiency. *Adv. Energy Mater.* **2015**, *5*, 1500682.
- (30) Kukreti, S.; Gupta, G. K.; Dixit, A. Theoretical DFT studies of $\text{Cu}_2\text{HgSnS}_4$ absorber material and $\text{Al}:\text{ZnO}/\text{ZnO}/\text{CdS}/\text{Cu}_2\text{HgSnS}_4/\text{Back contact}$ heterojunction solar cell. *Sol. Energy* **2021**, *225*, 802–813.
- (31) Kim, I.; Kim, K.; Oh, Y.; Woo, K.; Cao, G.; Jeong, S.; Moon, J. Bandgap-graded $\text{Cu}_2\text{Zn}(\text{Sn}_{1-x}\text{Ge}_x)\text{S}_4$ thin-film solar cells derived from metal chalcogenide complex ligand capped nanocrystals. *Chem. Mater.* **2014**, *26*, 3957–3965.
- (32) Hages, C. J.; Levenco, S.; Miskin, C. K.; Alsmeier, J. H.; Abou-Ras, D.; Wilks, R. G.; Bär, M.; Unold, T.; Agrawal, R. Improved performance of Ge-alloyed CZTGeSSe thin-film solar cells through control of elemental losses. *Prog. Photovolt. Res. Appl.* **2015**, *23*, 376–384.

- (33) Giraldo, S.; Neuschitzer, M.; Thersleff, T.; López-Marino, S.; Sánchez, Y.; Xie, H.; Colina, M.; Placidi, M.; Pistor, P.; Izquierdo-Roca, V. Large efficiency improvement in $\text{Cu}_2\text{ZnSnSe}_4$ solar cells by introducing a superficial Ge Nanolayer. *Adv. Energy Mater.* **2015**, *5*, 1501070.
- (34) Kim, S.; Kim, K. M.; Tampo, H.; Shibata, H.; Niki, S. Improvement of voltage deficit of Ge-incorporated kesterite solar cell with 12.3% conversion efficiency. *Appl. Phys. Express* **2016**, *9*, 102301.
- (35) Zhang, Q.; Deng, H.; Chen, L.; Yu, L.; Tao, J.; Sun, L.; Yang, P.; Chu, J. Cation substitution induced structural transition, band gap engineering and grain growth of $\text{Cu}_2\text{Cd}_x\text{Zn}_{1-x}\text{SnS}_4$ thin films. *J. Alloys Compd.* **2017**, *695*, 482–488.
- (36) Xiao, Z.-Y.; Li, Y.-F.; Yao, B.; Deng, R.; Ding, Z.-H.; Wu, T.; Yang, G.; Li, C.-R.; Dong, Z.-Y.; Liu, L.; Zhang, L.-G.; Zhao, H.-F. Bandgap engineering of $\text{Cu}_2\text{Cd}_x\text{Zn}_{1-x}\text{SnS}_4$ alloy for photovoltaic applications: a complementary experimental and first-principles study. *J. Appl. Phys.* **2013**, *114*, 183506.
- (37) Vu, T. V.; Lavrentyev, A. A.; Gabrelian, B. V.; Tong, H. D.; Tkach, V. A.; Parasyuk, O. V.; Khyzhun, O. Y. A theoretical and experimental study of the valence-band electronic structure and optical constants of quaternary copper mercury tin sulfide, $\text{Cu}_2\text{HgSnS}_4$, a potential material for optoelectronics and solar cells. *Opt. Mater.* **2019**, *96*, 109296.
- (38) Khadka, D. B.; Kim, J. Band gap engineering of alloyed $\text{Cu}_2\text{ZnGe}_x\text{Sn}_{1-x}\text{Q}_4$ ($Q = \text{S, Se}$) films for solar cell. *J. Phys. Chem. C* **2015**, *119*, 1706–1713.
- (39) Tang, W.; Sanville, E.; Henkelman, G. A grid-based bader analysis algorithm without lattice bias. *J. Phys. Condens. Matter* **2009**, *21*, 084204.
- (40) Deringer, V. L.; Tchougréeff, A. L.; Dronskowski, R. Crystal orbital hamilton population (COHP) analysis as projected from plane-wave basis sets. *J. Phys. Chem. A* **2011**, *115*, 5461–5466.
- (41) Grin, Y.; Savin, A.; Silvi, B. The ELF perspective of chemical bonding. In *The Chemical Bond: Fundamental Aspects of Chemical Bonding*; Wiley, 2014.
- (42) Müller, P. C.; Ertural, C.; Hempelmann, J.; Dronskowski, R. Crystal orbital bond index: covalent bond orders in solids. *J. Phys. Chem. C* **2021**, *125*, 7959–7970.
- (43) Kesterite: mineral information, data and localities. <https://www.mindat.org/min-2189.html>.

- (44) Chen, S.; Gong, X. G.; Walsh, A.; Wei, S.-H. Electronic structure and stability of quaternary chalcogenide semiconductors derived from cation cross-substitution of II-VI and I-III-VI₂ compounds. *Phys. Rev. B* **2009**, *79*, 165211.
- (45) Chang, J.; R. Waclawik, E. Colloidal semiconductor nanocrystals: controlled synthesis and surface chemistry in organic media. *RSC Adv.* **2014**, *4*, 23505–23527.
- (46) Chen, S.; Gong, X. G.; Walsh, A.; Wei, S.-H. Crystal and electronic band structure of Cu₂ZnSnX₄ (X = S and Se) photovoltaic absorbers: first-principles insights. *Appl. Phys. Lett.* **2009**, *94*, 041903.
- (47) Hall, S. R.; Szymanski, J. T.; Stewart, J. M. Kesterite, Cu₂(Zn,Fe)SnS₄, and stannite, Cu₂(Fe,Zn)SnS₄, structurally similar but distinct minerals. *Can. Mineral.* **1978**, *16*, 131–137.
- (48) Schorr, S.; Hoebler, H.-J.; Tovar, M. A neutron diffraction study of the stannite-kesterite solid solution series. *Eur. J. Mineral.* **2007**, *19*, 65–73.
- (49) Ritscher, A.; Hoelzel, M.; Lerch, M. The order-disorder transition in Cu₂ZnSnS₄ – a neutron scattering investigation. *J. Solid State Chem.* **2016**, *238*, 68–73.
- (50) Kumar, M.; Persson, C. Cu₂ZnSnS₄ and Cu₂ZnSnSe₄ as potential earth-abundant thin-film absorber materials: a density functional theory study. *Int J Theor Appl Sci* **2013**, *5*, 1–8.
- (51) Paier, J.; Asahi, R.; Nagoya, A.; Kresse, G. Cu₂ZnSnS₄ as a potential photovoltaic material: a hybrid hartree-fock density functional theory study. *Phys. Rev. B* **2009**, *79*, 115126.
- (52) Schorr, S. Structural aspects of adamantine like multinary chalcogenides. *Thin Solid Films* **2007**, *515*, 5985–5991.
- (53) Schorr, S.; Gonzalez-Aviles, G. In-situ investigation of the structural phase transition in kesterite. *Phys. Status Solidi A* **2009**, *206*, 1054–1058.
- (54) Stahnke, U.; Brandt, A.; Graf, H. A. BENSCH experimental reports **2006**, 318.
- (55) Chen, S.; Yang, J.-H.; Gong, X. G.; Walsh, A.; Wei, S.-H. Intrinsic point defects and complexes in the quaternary kesterite semiconductor Cu₂ZnSnS₄. *Phys. Rev. B* **2010**, *81*, 245204.
- (56) Larsen, J. K.; Scragg, J. J. S.; Ross, N.; Platzer-Björkman, C. Band tails and Cu–Zn disorder in Cu₂ZnSnS₄ solar Cells. *ACS Appl. Energy Mater.* **2020**, *3*, 7520–7526.

- (57) Hadke, S.; Chen, W.; Tan, J. M. R.; Guc, M.; Izquierdo-Roca, V.; Rignanese, G.-M.; Hautier, G.; Wong, L. H. Effect of Cd on cation redistribution and order-disorder transition in $\text{Cu}_2(\text{Zn,Cd})\text{SnS}_4$. *J. Mater. Chem. A* **2019**, *7*, 26927–26933.
- (58) Yu. K. Kabalov, T. L. Evstigneeva, E. M., Spiridonov, Crystal structure of $\text{Cu}_2\text{HgSnS}_4$, a synthetic analogue of the mineral velikite. *Crystallogr. Rep.* **1998**, *43*, 16–20 (*Transl. Kristallografiya* **1998**, *43*, 21–25).
- (59) Kaplunnik, L. N.; Pobedimskaya, E. A.; Belov, N. V. Crystal structure of velikite $\text{Cu}_{3.75}\text{Hg}_{1.75}\text{Sn}_2\text{S}_8$. *Kristallografiya* **1977**, *22*, 175–177.
- (60) Moodie, A. F.; Whitfield, H. J. Determination of the structure of $\text{Cu}_2\text{ZnGeS}_4$ polymorphs by lattice imaging and convergent-beam electron diffraction. *Acta Crystallogr. B* **1986**, *42*, 236–247.
- (61) Parasyuk, O. V.; Piskach, L. V.; Romanyuk, Y. E.; Olekseyuk, I. D.; Zaremba, V. I.; Pekhnyo, V. I. Phase relations in the quasi-binary $\text{Cu}_2\text{GeS}_3\text{–ZnS}$ and quasi-ternary $\text{Cu}_2\text{S–Zn(Cd)S–GeS}_2$ systems and crystal structure of $\text{Cu}_2\text{ZnGeS}_4$. *J. Alloys Compd.* **2005**, *397*, 85–94.
- (62) Doverspike, K.; Dwight, K.; Wold, A. Preparation and characterization of copper zinc germanium sulfide selenide ($\text{Cu}_2\text{ZnGeS}_{4-y}\text{Se}_y$). *Chem. Mater.* **1990**, *2*, 194–197.
- (63) Heinrich, C. P.; Day, T. W.; Zeier, W. G.; Snyder, G. J.; Tremel, W. Effect of isovalent substitution on the thermoelectric properties of the $\text{Cu}_2\text{ZnGeSe}_{4-x}\text{S}_x$ series of solid solutions. *J. Am. Chem. Soc.* **2014**, *136*, 442–448.
- (64) Schleich, D. M.; Wold, A. Optical and electrical properties of quaternary chalcogenides. *Mater. Res. Bull.* **1977**, *12*, 111–114.
- (65) Mangelis, P.; Aziz, A.; Silva, I. da; Grau-Crespo, R.; Vaqueiro, P.; Powell, A. V. Understanding the origin of disorder in kesterite-type chalcogenides $A_2\text{ZnBQ}_4$ ($A = \text{Cu}, \text{Ag}$; $B = \text{Sn}, \text{Ge}$; $Q = \text{S}, \text{Se}$): the influence of inter-layer interactions. *Phys. Chem. Chem. Phys.* **2019**, *21*, 19311–19317.
- (66) Rabi, I. I.; Zacharias, J. R.; Millman, S.; Kusch, P. A new method of measuring nuclear magnetic moment. *Phys. Rev.* **1938**, *53*, 318–318.
- (67) Bloch, F.; Hansen, W. W.; Packard, M. Physics Nobel price 1952. *Phys Rev* **1946**, *69*, 127.
- (68) Purcell, E. M.; Torrey, H. C.; Pound, R. V. Resonance absorption by nuclear magnetic moments in a solid. *Phys. Rev.* **1946**, *69*, 37.

- (69) Reif, B.; Ashbrook, S. E.; Emsley, L.; Hong, M. Solid-state NMR spectroscopy. *Nat. Rev. Methods Primer* **2021**, *1*, 1–23.
- (70) Wolf, P.; Valla, M.; Núñez-Zarur, F.; Comas-Vives, A.; Rossini, A. J.; Firth, C.; Kallas, H.; Lesage, A.; Emsley, L.; Copéret, C.; Hermans, I. Correlating synthetic methods, morphology, atomic-level structure, and catalytic activity of Sn- β catalysts. *ACS Catal.* **2016**, *6*, 4047–4063.
- (71) Grykałowska, A.; Nowak, B. High-resolution solid-state ^{119}Sn and ^{195}Pt NMR studies of MPtSn semiconductors ($M = \text{Ti, Zr, Hf, Th}$). *Solid State Nucl. Magn. Reson.* **2005**, *27*, 223–227.
- (72) Eckert, H. Spying with spins on messy materials: 60 years of glass structure elucidation by NMR spectroscopy. *Int. J. Appl. Glass Sci.* **2018**, *9*, 167–187.
- (73) Bhattacharya, A.; Qiu, Y.; Bernard, G. M.; Butler, S.; Mar, A.; Michaelis, V. K. Annealing induced structural evolution in feldspar dental glass-ceramics investigated by solid-state NMR spectroscopy. *J. Solid State Chem.* **2020**, *289*, 121501.
- (74) Karmakar, A.; Bhattacharya, A.; Sarkar, D.; M. Bernard, G.; Mar, A.; K. Michaelis, V. Influence of hidden halogen mobility on local structure of $\text{CsSn}(\text{Cl}_{1-x}\text{Br}_x)_3$ mixed-halide perovskites by solid-state NMR. *Chem. Sci.* **2021**, *12*, 3253–3263.
- (75) Rosales, B. A.; Men, L.; Cady, S. D.; Hanrahan, M. P.; Rossini, A. J.; Vela, J. Persistent dopants and phase Segregation in organolead mixed-halide perovskites. *Chem. Mater.* **2016**, *28*, 6848–6859.
- (76) Kalisvaart, W. P.; Chaudhary, M.; Bhattacharya, A.; Michaelis, V. K.; Buriak, J. M. Mixing, domains, and fast Li-ion dynamics in ternary Li–Sb–Bi battery anode alloys. *J. Phys. Chem. C* **2022**, *126*, 2394–2402.
- (77) Paris, M.; Larramona, G.; Bais, P.; Bourdais, S.; Lafond, A.; Choné, C.; Guillot-Deudon, C.; Delatouche, B.; Moisan, C.; Dennler, G. ^{119}Sn MAS NMR to assess the cationic disorder and the anionic distribution in sulfoselenide $\text{Cu}_2\text{ZnSn}(\text{S}_x\text{Se}_{1-x})_4$ compounds prepared from colloidal and ceramic routes. *J. Phys. Chem. C* **2015**, *119*, 26849–26857.
- (78) Lafond, A.; Guillot-Deudon, C.; Vidal, J.; Paris, M.; La, C.; Jobic, S. Substitution of Li for Cu in $\text{Cu}_2\text{ZnSnS}_4$: toward wide band gap absorbers with low cation disorder for thin film solar cells. *Inorg. Chem.* **2017**, *56*, 2712–2721.

- (79) Bhattacharya, A.; Tkachuk, D. G.; Mar, A.; Michaelis, V. K. Mere anarchy is loosed: structural disorder in $\text{Cu}_2\text{Zn}_{1-x}\text{Cd}_x\text{SnS}_4$. *Chem. Mater.* **2021**, *33*, 4709–4722.
- (80) Zeier, W. G.; Heinrich, C. P.; Day, T.; Panithipongwut, C.; Kieslich, G.; Brunklaus, G.; Snyder, G. J.; Tremel, W. Bond strength dependent superionic phase transformation in the solid solution series $\text{Cu}_2\text{ZnGeSe}_{4-x}\text{S}_x$. *J. Mater. Chem. A* **2014**, *2*, 1790–1794.
- (81) Hamdi, M.; Benamira, M. Crystallochemical characterizations, Raman spectroscopy and studies nuclear magnetic resonance (NMR) of $\text{Cu}_2\text{Zn}(\text{Sn},\text{Si})\text{S}_4$ compounds for photovoltaic applications. *J. Mater. Sci. Chem. Eng.* **2022**, *10*, 24-40
- (82) Duer, M. J. *Introduction to Solid-state NMR Spectroscopy*; Blackwell, 2004.
- (83) Harris, R. K. *Nuclear Magnetic Resonance Spectroscopy*; Longman, 1986.
- (84) Apperley, D. C.; Harris, R. K.; Hodgkinson, P. *Solid-state NMR: Basic Principles and Practice*; Momentum Press, 2012.
- (85) Harris, R. K.; Becker, E. D.; De Menezes, S. M. C.; Goodfellow, R.; Granger, P. NMR nomenclature. Nuclear spin properties and conventions for chemical shifts (IUPAC Recommendations 2001). *Pure Appl. Chem.* **2001**, *73*, 1795–1818.
- (86) Abragam, A. *The Principles of Nuclear Magnetism*; Oxford University Press, 1961.
- (87) Levitt, M. H. *Spin Dynamics: Basics of Nuclear Magnetic Resonance*; Wiley, 2013.
- (88) Dybowski, C. Zeeman interaction in nuclear magnetic resonance. In *Encyclopedia of Analytical Chemistry*; Wiley, 2006.
- (89) Mehring, M. *Principles of High Resolution NMR in Solids*; Springer-Verlag, 1983.
- (90) Anet, F. A. L.; O’Leary, D. J. *Concepts in Magn. Reson* **1991**, *3*, 193–214.
- (91) Herzfeld, J.; Berger, A. E. Sideband intensities in NMR spectra of samples spinning at the magic angle. *J. Chem. Phys.* **1980**, *73*, 6021–6030.
- (92) Eichele, K. WSolids1 Ver. 1.21. 3; University of Tübingen, 2015.
- (93) Ramsey, N. F. Magnetic shielding of nuclei in molecules. *Phys. Rev.* **1950**, *78*, 699–703.
- (94) Yesinowski, J. P. Solid-state NMR of inorganic semiconductors. In *Solid State NMR*; Chan, J. C. C., Ed.; Springer, 2012.
- (95) Harris, R. K.; Wasylishen, R. E.; Duer, M. J., Eds.; *NMR Crystallography*; Wiley, 2009.
- (96) Grant, D. M., Harris, R. K. Ed.; *Encyclopedia of NMR.*; Wiley, 1996.
- (97) Wasylishen, R. E.; Ashbrook, S. E.; Wimperis, S. *NMR of Quadrupolar Nuclei in Solid Materials*; Wiley, 2012.

- (98) Kentgens, A. P. M. A practical guide to solid-state NMR of half-integer quadrupolar nuclei with some applications to disordered systems. *Geoderma* **1997**, *80*, 271–306.
- (99) Müller, K.; Geppi, M. *Solid-state NMR: Principles, Methods, and Applications*; Wiley, 2021.
- (100) Ashbrook, S. E. Recent advances in solid-state NMR spectroscopy of quadrupolar nuclei. *Phys. Chem. Chem. Phys.* **2009**, *11*, 6892–6905.
- (101) Bryce, D. L.; Wasylishen, R. E. Quadrupolar nuclei in solids: influence of different interactions on spectra. In *NMR of Quadrupolar Nuclei in Solid Materials*; Wiley, 2011.
- (102) Andrew, E. R.; Bradbury, A.; Eades, R. G. Nuclear magnetic resonance spectra from a crystal rotated at high speed. *Nature* **1958**, *182*, 1659–1659.
- (103) Lowe, I. J. Free induction decays of rotating solids. *Phys. Rev. Lett.* **1959**, *2*, 285–287.
- (104) Hennel, J. W.; Klinowski, J. Magic-angle spinning: a historical perspective. *Top. Curr. Chem.* **2004**, *246*, 1–14
- (105) Wasylishen, R. E. *NMR Spectroscopy Techniques*; Marcel Dekker, 1987.
- (106) Damadian, R. Tumor Detection by nuclear magnetic resonance. *Science* **1971**, *171*, 1151–1153.

Chapter 2

- (1) Siebentritt, S.; Schorr, S. Kesterites – a challenging material for solar cells. *Prog. Photovolt. Res. Appl.* **2012**, *20*, 512–519.
- (2) Fan, F.-J.; Wu, L.; Yu, S.-H. Energetic I–III–VI₂ and I₂–II–IV–VI₄ nanocrystals: synthesis, photovoltaic and thermoelectric applications. *Energy Environ. Sci.* **2014**, *7*, 190–208.
- (3) Shin, B.; Gunawan, O.; Zhu, Y.; Bojarczuk, N. A.; Chey, S. J.; Guha, S. Thin film solar cell with 8.4% power conversion efficiency using an earth-abundant Cu₂ZnSnS₄ absorber. *Prog. Photovolt. Res. Appl.* **2013**, *21*, 72–76.
- (4) Chen, S.; Yang, J.-H.; Gong, X. G.; Walsh, A.; Wei, S.-H. Intrinsic point defects and complexes in the quaternary kesterite semiconductor Cu₂ZnSnS₄. *Phys. Rev. B* **2010**, *81*, 245204.
- (5) Larsen, J. K.; Scragg, J. J. S.; Ross, N.; Platzer-Björkman, C. Band tails and Cu–Zn disorder in Cu₂ZnSnS₄ solar cells. *ACS Appl. Energy Mater.* **2020**, *3*, 7520–7526.

- (6) Li, J.; Wang, D.; Li, X.; Zeng, Y.; Zhang, Y. Cation substitution in earth-abundant kesterite photovoltaic materials. *Adv. Sci.* **2018**, *5*, 1700744.
- (7) Yan, C.; Sun, K.; Huang, J.; Johnston, S.; Liu, F.; Veetil, B. P.; Sun, K.; Pu, A.; Zhou, F.; Stride, J. A.; Green, M. A.; Hao, X. Beyond 11% efficient sulfide kesterite $\text{Cu}_2\text{Zn}_x\text{Cd}_{1-x}\text{SnS}_4$ solar cell: effects of cadmium alloying. *ACS Energy Lett.* **2017**, *2*, 930–936.
- (8) Hall, S. R.; Szymański, J. T.; Stewart, J. M. kesterite, $\text{Cu}_2(\text{Zn,Fe})\text{SnS}_4$, and stannite, $\text{Cu}_2(\text{Fe,Zn})\text{SnS}_4$, structurally similar but distinct minerals. *Can. Mineral.* **1978**, *16*, 131–137.
- (9) Villars, P.; Cenzual, K. *Pearson's Crystal Data – Crystal Structure Database for Inorganic Compounds*, on DVD, release 2020/21; ASM International: Materials Park, OH, USA, 2020.
- (10) Schorr, S.; Hoebler, H.-J.; Tovar, M. A neutron diffraction study of the stannite-kesterite solid solution series. *Eur. J. Mineral.* **2007**, *19*, 65–73.
- (11) Ritscher, A.; Hoelzel, M.; Lerch, M. The order-disorder transition in $\text{Cu}_2\text{ZnSnS}_4$ – a neutron scattering investigation. *J. Solid State Chem.* **2016**, *238*, 68–73.
- (12) Xiao, Z.-Y.; Li, Y.-F.; Yao, B.; Deng, R.; Ding, Z.-H.; Wu, T.; Yang, G.; Li, C.-R.; Dong, Z.-Y.; Liu, L.; Zhang, L.-G.; Zhao, H.-F. Bandgap engineering of $\text{Cu}_2\text{Cd}_x\text{Zn}_{1-x}\text{SnS}_4$ alloy for photovoltaic applications: A complementary experimental and first-principles study. *J. Appl. Phys.* **2013**, *114*, 183506.
- (13) Pilvet, M.; Kauk-Kuusik, M.; Altosaar, M.; Grossberg, M.; Danilson, M.; Timmo, K.; Mere, A.; Mikli, V. Compositionally tunable structure and optical properties of $\text{Cu}_{1.85}(\text{Cd}_x\text{Zn}_{1-x})_{1.1}\text{SnS}_{4.1}$ ($0 \leq x \leq 1$) monograin powders. *Thin solid films* **2015**, *582*, 180–183.
- (14) Su, Z.; Tan, J. M. R.; Li, X.; Zeng, X.; Batabyal, S. K.; Wong, L. H. Cation substitution of solution-processed $\text{Cu}_2\text{ZnSnS}_4$ thin film solar cell with over 9% efficiency. *Adv. Energy Mater.* **2015**, *5*, 1500682.
- (15) Ibraheem, A. S.; Al-Douri, Y.; Hashim, U.; Prakash, D.; Verma, K. D.; Ameri, M. Fabrication, analysis and characterization of $\text{Cu}_2\text{Zn}_{1-x}\text{Cd}_x\text{SnS}_4$ quinary alloy nanostructures deposited on GaN. *J. Mater. Sci.* **2016**, *51*, 6876–6885.

- (16) Hadke, S.; Chen, W.; Tan, J. M. R.; Guc, M.; Izquierdo-Roca, V.; Rignanese, G.-M.; Hautier, G.; Wong, L. H. Effect of Cd on cation redistribution and order-disorder transition in $\text{Cu}_2(\text{Zn,Cd})\text{SnS}_4$. *J. Mater. Chem. A* **2019**, *7*, 26927–26933.
- (17) Heppke, E. M.; Küllmey, T.; Efthimiopoulous, I.; Acvi, F. D.; Appelt, O.; Paulus, B.; Lerch, M. Experimental and theoretical investigations on the composition-dependent structural phase transition in $\text{Cu}_2\text{Cd}_x\text{Zn}_{1-x}\text{SnS}_4$. *Mater. Res. Express* **2019**, *6*, 125525.
- (18) Zhang, Q.; Deng, H.; Chen, L.; Yu, L.; Tao, J.; Sun, L.; Yang, P.; Chu, J. Cation substitution induced structural transition, band gap engineering and grain growth of $\text{Cu}_2\text{Cd}_x\text{Zn}_{1-x}\text{SnS}_4$ thin films. *J. Alloys Compd.* **2017**, *695*, 482–488.
- (19) Choubrac, L.; Paris, M.; Lafond, A.; Guillot-Deudon, C.; Rocquefelte, X.; Jobic, S. Multinuclear (^{67}Zn , ^{119}Sn and ^{65}Cu) NMR spectroscopy – an ideal technique to probe the cationic ordering in $\text{Cu}_2\text{ZnSnS}_4$ photovoltaic materials. *Phys. Chem. Chem. Phys.* **2013**, *15*, 10722–10725.
- (20) Lafond, A.; Guillot-Deudon, C.; Vidal, J.; Paris, M.; La, C.; Jobic, S. Substitution of Li for Cu in $\text{Cu}_2\text{ZnSnS}_4$: toward wide band gap absorbers with low cation disorder for thin film solar cells. *Inorg. Chem.* **2017**, *56*, 2712–2721.
- (21) Paris, M.; Larramona, G.; Bais, P.; Bourdais, S.; Lafond, A.; Choné, C.; Guillot-Deudon, C.; Delatouche, B.; Moisan, C.; Dennler, G. ^{119}Sn MAS NMR to assess the cationic disorder and the anionic distribution in sulfoselenide $\text{Cu}_2\text{ZnSn}(\text{S}_x\text{Se}_{1-x})_4$ compounds prepared from colloidal and ceramic routes. *J. Phys. Chem. C* **2015**, *119*, 26849–26857.
- (22) Paris, M.; Choubrac, L.; Lafond, A.; Guillot-Deudon, C.; Jobic, S. Solid-state NMR and Raman spectroscopy to address the local structure of defects and the tricky issue of the Cu/Zn disorder in Cu-poor, Zn-rich CZTS materials. *Inorg. Chem.* **2014**, *53*, 8646–8653.
- (23) Choubrac, L.; Lafond, A.; Paris, M.; Guillot-Deudon, C.; Jobic, S. The stability domain of the selenide kesterite photovoltaic materials and NMR investigation of the Cu/Zn disorder in $\text{Cu}_2\text{ZnSnSe}_4$ (CZTSe). *Phys. Chem. Chem. Phys.* **2015**, *17*, 15088–15092.
- (24) Johnson, N.; Pogue, E.; Rockett, A. Multi-nuclear (^{119}Sn and ^{65}Cu) NMR and Raman spectroscopy to probe secondary phases in $\text{Cu}_2\text{ZnSnS}_4$. *2016 IEEE 43rd Photovoltaic Specialists Conference (PVSC)* **2016**, 3046–3050.

- (25) Rodríguez-Carvajal, J. Introduction to the program Fullprof: refinement of crystal and magnetic structures from powder and single crystal data. *Lab. Léon Brillouin CEA-CNRS Saclay Fr.* **2001**.
- (26) Le Bail, A. Whole powder pattern decomposition methods and applications: a retrospection. *Powder Diffr.* **2005**, *20*, 316–326.
- (27) Kubelka, P. Ein Beitrag Zur Optik Der Farbanstriche (Contribution to the optic of paint). *Z. Tech. Phys.* **1931**, *12*, 593–601.
- (28) Kortüm, G. *Reflectance Spectroscopy*. Springer, 1969.
- (29) Karmakar, A.; Bhattacharya, A.; Bernard, G. M.; Mar, A.; Michaelis, V. K. Revealing the local Sn and Pb arrangements in CsSn_xPb_{1-x}Br₃ perovskites with solid-state NMR spectroscopy. *ACS Mater. Lett.* **2021**, *3*, 261–267.
- (30) Gunther, W. R.; Michaelis, V. K.; Caporini, M. A.; Griffin, R. G.; Román-Leshkov, Y. Dynamic nuclear polarization NMR enables the analysis of Sn-beta zeolite prepared with natural abundance ¹¹⁹Sn precursors. *J. Am. Chem. Soc.* **2014**, *136*, 6219–6222.
- (31) Eichele, K.; Wasylishen, R. E. High-resolution ¹¹³Cd MAS NMR investigation of structure and bonding in cadmium thiocyanate coordination compounds. Distance dependence of cadmium-nitrogen indirect spin-spin coupling constants. *Inorg. Chem.* **1994**, *33*, 2766–2773.
- (32) Tang, J. A.; Ellis, B. D.; Warren, T. H.; Hanna, J. V.; Macdonald, C. L. B.; Schurko, R. W. Solid-state ⁶³Cu and ⁶⁵Cu NMR spectroscopy of inorganic and organometallic copper(I) complexes. *J. Am. Chem. Soc.* **2007**, *129*, 13049–13065.
- (33) Hibble, S. J.; Chippindale, A. M.; Marelli, E.; Kroeker, S.; Michaelis, V. K.; Greer, B. J.; Aguiar, P. M.; Bilbé, E. J.; Barney, E. R.; Hannon, A. C. Local and average structure in zinc cyanide: toward an understanding of the atomistic origin of negative thermal expansion. *J. Am. Chem. Soc.* **2013**, *135*, 16478–16489.
- (34) Eichele, K. WSolids1 Ver. 1.21. 3; University of Tübingen, 2015.
- (35) Clark, S. J.; Segall, M. D.; Pickard, C. J.; Hasnip, P. J.; Probert, M. I. J.; Refson, K.; Payne, M. C. First principles methods using CASTEP. *Z. Kristallogr.* **2005**, *220*, 567-570.
- (36) Perdew, J. P.; Burke, K.; Ernzerhof, M. Generalized gradient approximation made simple. *Phys. Rev. Lett.* **1996**, *77*, 3865–3868.

- (37) Yates, J. R.; Pickard, C. J.; Mauri, F. Calculation of NMR chemical shifts for extended systems using ultrasoft pseudopotentials. *Phys. Rev. B* **2007**, *76*, 024401.
- (38) Pickard, C. J.; Mauri, F. All-electron magnetic response with pseudopotentials: NMR chemical shifts. *Phys. Rev. B* **2001**, *63*, 245101.
- (39) Pickard, C. J.; Mauri, F.; Profeta, M. Accurate First Principles Prediction of ^{17}O NMR Parameters in SiO_2 : Assignment of the Zeolite Ferrierite Spectrum. *J. Am. Chem. Soc.* **2003**, *125*, 541–548.
- (40) Shannon, R. D. Revised effective ionic radii and systematic studies of interatomic distances in halides and chalcogenides. *Acta Crystallogr., Sect. A: Cryst. Phys., Diffr., Theor. Gen. Crystallogr.* **1976**, *32*, 751–767.
- (41) Phillips, J. C. Electronegativity and tetragonal distortions in $A^{\text{II}}B^{\text{IV}}C^{\text{V}}_2$ semiconductors. *J. Phys. Chem. Solids* **1974**, *35*, 1205–1209.
- (42) Harris, R. K.; Becker, E. D.; De Menezes, S. M. C.; Goodfellow, R.; Granger, P. NMR nomenclature. Nuclear spin properties and conventions for chemical shifts (IUPAC recommendations 2001). *Pure Appl. Chem.* **2001**, *73*, 1795–1818.
- (43) Ha, M.; Karmakar, A.; Bernard, G. M.; Basilio, E.; Krishnamurthy, A.; Askar, A. M.; Shankar, K.; Kroeker, S.; Michaelis, V. K. Phase evolution in methylammonium tin halide perovskites with variable temperature solid-state ^{119}Sn NMR spectroscopy. *J. Phys. Chem. C* **2020**, *124*, 15015–15027.
- (44) Kubicki, D. J.; Prochowicz, D.; Salager, E.; Rakhmatullin, A.; Grey, C. P.; Emsley, L.; Stranks, S. D. Local structure and dynamics in methylammonium, formamidinium, and cesium tin(II) mixed-halide perovskites from ^{119}Sn solid-state NMR. *J. Am. Chem. Soc.* **2020**, *142*, 7813–7826.
- (45) Karmakar, A.; Bhattacharya, A.; Sarkar, D.; Bernard, G. M.; Mar, A.; Michaelis, V. K. Influence of hidden halogen mobility on local structure of $\text{CsSn}(\text{Cl}_{1-x}\text{Br}_x)_3$ mixed-halide perovskites by solid-state NMR. *Chem. Sci.* **2021**, *12*, 3253–3263.
- (46) Karmakar, A.; Askar, A. M.; Bernard, G. M.; Terskikh, V. V.; Ha, M.; Patel, S.; Shankar, K.; Michaelis, V. K. Mechanochemical synthesis of methylammonium lead mixed-halide perovskites: unraveling the solid-solution behavior using solid-state NMR. *Chem. Mater.* **2018**, *30*, 2309–2321.
- (47) Mason, J. *Solid state Nucl. Magn. Reson.* **1993**, *2*, 285–288.

- (48) Herzfeld, J.; Berger, A. E. Sideband intensities in NMR spectra of samples spinning at the magic angle. *J. Chem. Phys.* **1980**, *73*, 6021–6030.
- (49) Robinson, K.; Gibbs, G. V.; Ribbe, P. H. Quadratic elongation: a quantitative measure of distortion in coordination polyhedra. *Science* **1971**, *172*, 567–570.
- (50) Michaelis, V. K.; Kroeker, S. ⁷³Ge solid-state NMR of germanium oxide materials: experimental and theoretical studies. *J Phys. Chem. C* **2010**, *114*, 21736–21744.
- (51) Choubrac, L.; Lafond, A.; Guillot-Deudon, C.; Moëlo, Y.; Jobic, S. Structure flexibility of the Cu₂ZnSnS₄ absorber in low-cost photovoltaic cells: from the stoichiometric to the copper-poor compounds. *Inorg. Chem.* **2012**, *51*, 3346–3348.
- (52) Rosmus, K. A.; Brant, J. A.; Wisneski, S. D.; Clark, D. J.; Kim, Y. S.; Jang, J. I.; Brunetta, C. D.; Zhang, J.-H.; Srnec, M. N.; Aitken, J. A. Optical nonlinearity in Cu₂CdSnS₄ and α/β -Cu₂ZnSiS₄: diamond-like semiconductors with high laser-damage thresholds. *Inorg. Chem.* **2014**, *53*, 7809–7811.
- (53) Kubicki, D. J.; Prochowicz, D.; Hofstetter, A.; Walder, B. J.; Emsley, L. ¹¹³Cd solid-state NMR at 21.1 T reveals the local structure and passivation mechanism of cadmium in hybrid and all-inorganic halide perovskites. *ACS Energy Lett.* **2020**, *5*, 2964–2971.
- (54) Dean, P. A. W. A ¹¹³Cd nuclear magnetic resonance study of some complexes of cadmium with phosphine oxides, sulfides, and selenides. *Can. J. Chem.* **1981**, *59*, 3221–3225.
- (55) Ratcliffe, C. I.; Yu, K.; Ripmeester, J. A.; Badruz Zaman, M.; Badarau, C.; Singh, S. Solid state NMR studies of photoluminescent cadmium chalcogenide nanoparticles. *Phys. Chem. Chem. Phys.* **2006**, *8*, 3510–3519.
- (56) Kuttathayil, A. V.; Handke, M.; Bergmann, J.; Lässig, D.; Lincke, J.; Haase, J.; Bertmer, M.; Krautscheid, H. ¹¹³Cd solid-state NMR for probing the coordination sphere in metal–organic frameworks. *Chem. Eur. J.* **2015**, *21*, 1118–1124.
- (57) Chen, Y.; Dorn, R. W.; Hanrahan, M. P.; Wei, L.; Blome-Fernandez, R.; Medina-Gonzalez, A. M.; Adamson, M. A. S.; Flintgruber, A. H.; Vela, J.; Rossini, A. J. Revealing the surface structure of CdSe nanocrystals by dynamic nuclear polarization-enhanced ⁷⁷Se and ¹¹³Cd solid-state NMR spectroscopy. *J. Am. Chem. Soc.* **2021**, *143*, 8747–8760.
- (58) Hanrahan, M. P.; Stein, J. L.; Park, N.; Cossairt, B. M.; Rossini, A. J. Elucidating the location of Cd²⁺ in post-synthetically treated InP quantum dots using dynamic nuclear

- polarization ^{31}P and ^{113}Cd solid-state NMR spectroscopy. *J. Phys. Chem. C* **2021**, *125*, 2956–2965.
- (59) Hanrahan, M. P.; Chen, Y.; Blome-Fernández, R.; Stein, J. L.; Pach, G. F.; Adamson, M. A. S.; Neale, N. R.; Cossairt, B. M.; Vela, J.; Rossini, A. J. Probing the surface structure of semiconductor nanoparticles by DNP SENS with dielectric support materials. *J. Am. Chem. Soc.* **2019**, *141*, 15532–15546.
- (60) Piveteau, L.; Dirin, D. N.; Gordon, C. P.; Walder, B. J.; Ong, T.-C.; Emsley, L.; Copéret, C.; Kovalenko, M. V. Colloidal-ALD-grown core/shell CdSe/CdS nanoplatelets as seen by DNP enhanced PASS-PIETA NMR spectroscopy. *Nano Lett.* **2020**, *20*, 3003–3018.
- (61) Larsen, F.H.; Lipton, A.S.; Jakobsen, H.J.; Nielsen, N.C.; Ellis, P.D. ^{67}Zn QCPMG solid-state NMR studies of zinc complexes as models of metalloproteins. *J. Am. Chem. Soc.* **1999**, *121*, 3783–3784.
- (62) Huang, Y., Sutrisno, A. Recent Advances in Solid-State ^{67}Zn NMR studies: from nanoparticles to biological systems. *Annu. Rep. NMR Spectrosc.* **2014**, *81*, 1–46.
- (63) Madsen, R. S. K.; Qiao, A.; Sen, J.; Hung, I.; Chen, K.; Gan, Z.; Sen, S.; Yue, Y. Ultrahigh-field ^{67}Zn NMR reveals short-range disorder in zeolitic imidazolate framework glasses. *Science* **2020**, *367*, 1473–1476.
- (64) Chen, S.; Gong, X. G.; Walsh, A.; Wei, S.-H. Crystal and electronic band structure of $\text{Cu}_2\text{ZnSnX}_4$ ($X = \text{S}$ and Se) photovoltaic absorbers: first-principles insights. *Appl. Phys. Lett.* **2009**, *94*, 041903.
- (65) Chen, S.; Gong, X. G.; Walsh, A. Wei, S.-H. Electronic structure and stability of quaternary chalcogenide semiconductors derived from cation cross-substitution of II-VI and I-III-VI₂ compounds. *Phys. Rev. B* **2009**, *79*, 165211.
- (66) Ramsey, N. F. Magnetic shielding of nuclei in molecules. *Phys. Rev.* **1950**, *78*, 699–703.
- (67) Yesinowski, J. P. Solid-state NMR of inorganic semiconductors. In *Solid State NMR*; Chan, J. C. C., Ed.; Springer, 2012.
- (68) Thiessen, A. N.; Ha, M.; Hooper, R. W.; Yu, H.; Oliynyk, A. O.; Veinot, J. G. C.; Michaelis, V. K. Silicon nanoparticles: are they crystalline from the core to the surface? *Chem. Mater.* **2019**, *31*, 678-688.

- (69) Cadars, S.; Smith, B. J.; Epping, J. D.; Acharya, S.; Belman, N.; Golan, Y.; Chmelka, B. F. Atomic positional versus electronic order in semiconducting ZnSe nanoparticles. *Phys. Rev. Lett.* **2009**, *103*, 136802.
- (70) Tomaselli, M.; Yarger, J. L.; Bruchez, M.; Havlin, R. H.; deGraw, D.; Pines, A.; Alivisatos, A. P. NMR study of InP quantum dots: surface structure and size effects. *J. Chem. Phys.* **1999**, *110*, 8861–8864.
- (71) Thayer, A. M.; Steigerwald, M. L.; Duncan, T. M.; Douglass, D. C. NMR study of semiconductor molecular clusters. *Phys. Rev. Lett.* **1988**, *60*, 2673–2676.
- (72) Bawendi, M. G.; Carroll, P. J.; Wilson, W. L.; Brus, L. E. Luminescence properties of CdSe quantum crystallites: resonance between interior and surface localized states. *J. Chem. Phys.* **1992**, *96*, 946–954.
- (73) Beshah, K.; Zamir, D.; Becla, P.; Wolff, P. A.; Griffin, R. G. Te and Cd nuclear-magnetic-resonance study of local structure and bonding in $\text{Cd}_{1-x}\text{Zn}_x\text{Te}$. *Phys. Rev. B* **1987**, *36*, 6420–6425.
- (74) Willig, A.; Sapoval, B.; Leibler, K.; Verie, C. Chemical shift of NMR in HgTe, CdTe and their alloys. *J. Phys. C: Solid State Phys.* **1976**, *9*, 1981–1989.

Chapter 3

- (1) Siebentritt, S.; Schorr, S. Kesterites – a challenging material for solar cells. *Prog. Photovoltaics* **2012**, *20*, 512-519.
- (2) Sun, K.; Yan, C.; Liu, F.; Huang, J.; Zhou, F.; Stride, J. A., Green M.; Hao, X. Over 9% efficient kesterite $\text{Cu}_2\text{ZnSnS}_4$ solar cell fabricated by using $\text{Zn}_{1-x}\text{Cd}_x\text{S}$ buffer layer. *Adv. Energy Mater.*, **2016**, *6*, 1600046.
- (3) Pal, K.; Singh, P.; Bhaduri A.; Thapa, K. B. Current challenges and future prospects for a highly efficient (> 20%) kesterite CZTS solar cell: a review. *Sol. Energy Mater. Sol. Cells*, **2019**, *196*, 138–156.
- (4) Shin, B.; Gunawan, O.; Zhu, Y.; Bojarczuk, N. A.; Chey, S. J.; Guha, S. Thin film solar cell with 8.4% power conversion efficiency using an earth-abundant $\text{Cu}_2\text{ZnSnS}_4$ absorber. *Prog. Photovoltaics* **2013**, *21*, 72–76.
- (5) Hasan, S.; Baral, K.; Li, N.; Ching, W.-Y. Structural and physical properties of 99 complex bulk chalcogenides crystals using first-principles calculations. *Sci. Rep.* **2021**, *11*, 9921.

- (6) Matyszczyk, G.; Zborecki, K. Application of artificial neural network and global optimization techniques for high throughput modeling of the crystal structure of stannites and kesterites. *J. Comput. Chem.* **2021**, *42*, 740–745.
- (7) Su, Z.; Tan, J. M. R.; Li, X.; Zeng, X.; Batabyal, S. K.; Wong, L. H. Cation substitution of solution-processed $\text{Cu}_2\text{ZnSnS}_4$ thin film solar cell with over 9% efficiency. *Adv. Energy Mater.*, **2015**, *5*, 1500682.
- (8) Yan, C.; Sun, K.; Huang, J.; Johnston, S.; Liu, F.; Veetil, B. P.; Sun, K.; Pu, A.; Zhou, F.; Stride, J. A.; Green, M. A.; Hao, X. Beyond 11% efficient sulfide kesterite. $\text{Cu}_2\text{Zn}_x\text{Cd}_{1-x}\text{SnS}_4$ solar cell: effects of cadmium alloying. *ACS Energy Lett.* **2017**, *2*, 930–936.
- (9) Hadke, S.; Chen, W.; Tan, J. M. R.; Guc, M.; Izquierdo-Roca, V.; Rignanese, G.-M.; Hautier, G.; Wong, L. H. Effect of Cd on cation redistribution and order-disorder transition in $\text{Cu}_2(\text{Zn,Cd})\text{SnS}_4$. *J. Mater. Chem. A* **2019**, *7*, 26927–26933.
- (10) Vu, T. V.; Lavrentyev, A. A.; Gabrelian, B. V.; Tong, H. D.; Tkach, V. A.; Parasyuk, O. V.; Khyzhun, O. Y. A theoretical and experimental study of the valence-band electronic structure and optical constants of quaternary copper mercury tin sulfide, $\text{Cu}_2\text{HgSnS}_4$, a potential material for optoelectronics and solar cells. *Opt. Mater.* **2019**, *96*, 109296.
- (11) Sarmadian, N.; Saniz, R.; Partoens, B.; Lamoen, D. First-principles study of the optoelectronic properties and photovoltaic absorber layer efficiency of Cu-based chalcogenides. *J. Appl. Phys.* **2016**, *120*, 085707.
- (12) Kukreti, S.; Gupta, G. K.; Dixit, A. Theoretical DFT studies of $\text{Cu}_2\text{HgSnS}_4$ absorber material and Al:ZnO/ZnO/CdS/ $\text{Cu}_2\text{HgSnS}_4$ / back contact heterojunction solar cell. *Sol. Energy* **2021**, *225*, 802–813.
- (13) Yu, K.; Carter, E. A. Elucidating structural disorder and the effects of Cu vacancies on the electronic properties of $\text{Cu}_2\text{ZnSnS}_4$. *Chem. Mater.* **2016**, *28*, 864–869.
- (14) Hahn, H.; Schulze, H. Über Ternäre Selenide Des Bariums. *Naturwissenschaften* **1965**, *52*, 426–426.
- (15) Schäfer, W.; Nitsche, R. Tetrahedral quaternary chalcogenides of the type $\text{Cu}_2\text{-II-IV-S}_4(\text{Se}_4)$. *Mater. Res. Bull.* **1974**, *9*, 645–654.
- (16) Schorr, S. The crystal structure of kesterite type compounds: a neutron and X-ray diffraction study. *Sol. Energy Mater. Sol. Cells* **2011**, *95*, 1482–1488.

- (17) Szymański, J. T. The crystal structure of černýite, $\text{Cu}_2\text{CdSnS}_4$, a cadmium analogue of stannite. *Can. Mineral.* **1978**, *16*, 147–151.
- (18) Rosmus, K. A.; Brant, J. A.; Wisneski, S. D.; Clark, D. J.; Kim, Y. S.; Jang, J. I.; Brunetta, C. D.; Zhang, J.-H.; Srnec, M. N.; Aitken, J. A. Optical nonlinearity in $\text{Cu}_2\text{CdSnS}_4$ and $\alpha/\beta\text{-Cu}_2\text{ZnSiS}_4$: diamond-like semiconductors with high laser-damage thresholds. *Inorg. Chem.* **2014**, *53*, 7809–7811.
- (19) Yu. K. Kabalov, T. L. Evstigneeva, E. M., Spiridonov, Crystal structure of $\text{Cu}_2\text{HgSnS}_4$, a synthetic analogue of the mineral velikite. *Crystallogr. Rep.* **1998**, *43*, 16–20 (*Transl. Kristallografiya* **1998**, *43*, 21–25).
- (20) Kaplunnik, L. N.; Pobedimskaya, E. A.; Belov, N. V. Crystal structure of velikite $\text{Cu}_{3.75}\text{Hg}_{1.75}\text{Sn}_2\text{S}_8$. *Kristallografiya* **1977**, *22*, 175–177.
- (21) Heppke, E. M.; Küllmey, T.; Efthimiopoulos, I.; Avci, F. D.; Appelt, O.; Paulus, B.; Lerch, M. Experimental and theoretical investigations on the composition-dependent structural phase transition in $\text{Cu}_2\text{Cd}_x\text{Zn}_{1-x}\text{SnS}_4$ thin films. *Mater. Res. Express* **2019**, *6*, 125525.
- (22) Lafond, A.; Guillot-Deudon, C.; Vidal, J.; Paris, M.; La, C.; Jovic, S. Substitution of Li for Cu in $\text{Cu}_2\text{ZnSnS}_4$: toward wide band gap absorbers with low cation disorder for thin film solar cells. *Inorg. Chem.* **2017**, *56*, 2712–2721.
- (23) Bhattacharya, A.; Tkachuk, D. G.; Mar, A.; Michaelis, V. K. Mere anarchy is loosed: structural disorder in $\text{Cu}_2\text{Cd}_x\text{Zn}_{1-x}\text{SnS}_4$. *Chem. Mater.* **2021**, *33*, 4709–4722.
- (24) Paris, M.; Larramona, G.; Bais, P.; Bourdais, S.; Lafond, A.; Choné, C.; Guillon-Deudon, C.; Delatouche, B.; Moisan, C.; Dennler, G. ^{119}Sn MAS NMR to assess the cationic disorder and the anionic distribution in sulfoselenide $\text{Cu}_2\text{ZnSn}(\text{S}_x\text{Se}_{1-x})_4$ compounds prepared from colloidal and ceramic routes. *J. Phys. Chem. C* **2015**, *119*, 26849–26857.
- (25) Shi, C.; Xi, X.; Hou, Z.; Liu, E.; Wang, W.; Chen, J.; Wu, G. Copper dynamics and structural transformation in noble metal chalcogenides CuAgS probed by ^{63}Cu NMR. *Solid State Ion.* **2017**, *300*, 182–186.
- (26) Hu, S.; Reimer, J. A.; Bell, A. T. ^{65}Cu NMR Spectroscopy of Cu-exchanged ZSM-5 catalysts. *J. Phys. Chem. B* **1997**, *101*, 1869–1871.
- (27) Reiser, S.; Brunklaus, G.; Hong, J. H.; Chan, J. C. C.; Eckert, H.; Pfitzner, A. $(\text{CuI})_3\text{P}_4\text{S}_4$: preparation, structural, and NMR spectroscopic characterization of a copper(I) halide adduct with $\beta\text{-P}_4\text{S}_4$. *Chem. Eur. J.* **2002**, *8*, 4228–4233.

- (28) Rodríguez-Carvajal, J. Introduction to the program Fullprof: refinement of crystal and magnetic structures from powder and single crystal data. Laboratoire Léon Brillouin (CEA-CNRS), Saclay, France, 2001
- (29) Kortüm, G. *Reflectance Spectroscopy*; Springer, 1969.
- (30) Massiot, D.; Fayon, F.; Capron, M.; King, I.; Le Calve, S.; Alonso, B.; Durand, O.; Bujoli, B.; Gan Z.; Hoatson G. Modeling one- and two- dimensional solid-state NMR spectra. *Magn. Reson. Chem.* **2002**, *40*, 70–76.
- (31) Tang, J. A.; Ellis, B. D.; Warren, T. H.; Hanna, J. V.; Macdonald, C. L. B.; Schurko, R. W. Solid-state ^{63}Cu and ^{65}Cu NMR spectroscopy of inorganic and organometallic copper(I) complexes. *J. Am. Chem. Soc.* **2007**, *129*, 13049-13065.
- (32) Gunther, W. R.; Michaelis, V. K.; Caporini, M. A.; Griffin, R. G.; Román-Leshkov, Y. Dynamic nuclear polarization NMR enables the analysis of Sn-beta zeolite prepared with natural abundance ^{119}Sn precursors. *J. Am. Chem. Soc.* **2014**, *136*, 6219–6222.
- (33) Taylor, R. E.; Bai, S.; Dybowski, C. A solid-state ^{199}Hg NMR study of mercury halides. *J. Mol. Struct.* **2011**, *987*, 193–198.
- (34) Mason, J. *Solid State Nucl. Magn. Res.* **1993**, *2*, 285–288.
- (35) Herzfeld, J.; Berger, A. E. Sideband intensities in NMR spectra of samples spinning at the magic angle. *J. Chem. Phys.* **1980**, *73*, 6021–6030.
- (36) Slichter, C. P. *Principles of Magnetic Resonance*; Springer, 1996.
- (37) Wasylishen, R. E.; Ashbrook, S. E.; Wimperis, S. *NMR of Quadrupolar Nuclei in Solid Materials*; Wiley, 2012.
- (38) Lucier, B. E. G.; Tang, J. A.; Schurko, R. W.; Bowmaker, G. A.; Healy, P. C.; Hanna, J. V. Solid-state ^{65}Cu and ^{31}P NMR spectroscopy of bis(triphenylphosphine) copper species. *J. Phys. Chem. C* **2010**, *114*, 7949–7962.
- (39) Marchetti, P. S.; Honkonen, R. S.; Ellis, P. D. Assignment of symmetry-related cadmium shielding tensors to lattice positions in cadmium acetate dihydrate. *J. Magn. Reson.* **1987**, *71*, 294–302.
- (40) Jiao, J.; Lee, M.-Y.; Barnes, C. E.; Hagaman, E. W. ^{119}Sn NMR Chemical shift tensors in anhydrous and hydrated $\text{Si}_8\text{O}_{20}(\text{SnMe}_3)_8$ crystals. *Magn. Reson. Chem.* **2008**, *46*, 690–692.
- (41) Sola, J.; Gonzalez-Duarte, P.; Sanz, J.; Casals, I.; Alsina, T.; Sobrados, I.; Alvarez-Larena, A.; Piniella, J. F.; Solans, X. Solid-state ^{113}Cd NMR studies of several cadmium-sulfur

- complexes. shielding tensor-structure correlations. *J. Am. Chem. Soc.* **1993**, *115*, 10018–10028.
- (42) Saitô, H.; Ando, I.; Ramamoorthy, A. Chemical shift tensor – the heart of NMR: insights into biological aspects of proteins. *Prog. Nucl. Magn. Reson. Spectrosc.* **2010**, *57*, 181–228.
- (43) Autschbach, J.; Zheng, S.; Schurko, R. W. Analysis of electric field gradient tensors at quadrupolar nuclei in common structural motifs. *Concepts Magn. Reson. Part A* **2010**, *36A*, 84–126.
- (44) NMRRamblingsKlausEichele. <http://anorganik.uni-tuebingen.de/klaus/nmr/index.php?p=conventions/csa/>
- (45) Clark, S. J.; Segall, M. D.; Pickard, C. J.; Hasnip, P. J.; Probert, M. I. J.; Refson, K.; Payne, M. C. First principles methods using CASTEP. *Z. Kristallgr.* **2005**, *220*, 567–570.
- (46) Perdew, J. P.; Burke K.; and Ernzerhof, M. Generalized gradient approximation made simple. *Phys. Rev. Lett.* **1996**, *77*, 3865–3868.
- (47) Pickard, C. J.; Mauri, F. All-electron magnetic response with pseudopotentials: NMR chemical shifts. *Phys. Rev. B* **2001**, *63*, 245101.
- (48) Yates, J. R.; Pickard, C. J.; Mauri, F. Calculation of NMR chemical shifts for extended systems using ultrasoft pseudopotentials. *Phys. Rev. B* **2007**, *76*, 024401.
- (49) Kresse, G.; Furthmüller, J. Efficient iterative schemes for ab initio total-energy calculations using a plane-wave basis set. *Phys. Rev. B* **1996**, *54*, 11169–11186
- (50) Kresse, G.; Joubert, D. From ultrasoft pseudopotentials to the projector augmented-wave method. *Phys. Rev. B* **1999**, *59*, 1758.
- (51) Blöchl, P. E. Projector augmented-wave method. *Phys. Rev. B* **1994**, *50*, 17953–17979.
- (52) Maintz, S.; Deringer, V. L.; Tchougréeff, A. L.; Dronskowski, R. LOBSTER: a tool to extract chemical bonding from plane-wave based DFT. *J. Comput. Chem.* **2016**, *37*, 1030–1035
- (53) Harris, R. K.; Becker, E. D.; de Menezes, S. M. C.; Goodfellow, R.; Granger, P. NMR nomenclature: Nuclear spin properties and conventions for chemical shifts (IUPAC recommendations 2001). *Pure Appl. Chem.* **2001**, *73*, 1795–1818.
- (54) Kubicki, D. J.; Prochowicz, D.; Salager, E.; Rakhmatullin, A.; Grey, C. P.; Emsley, L.; Stranks, S. D. Local structure and dynamics in methylammonium, formamidinium, and

- cesium tin(II) mixed-halide perovskites from ^{119}Sn solid-state NMR. *J. Am. Chem. Soc.* **2020**, *142*, 7813–7826.
- (55) Ha, M.; Karmakar, A.; Bernard, G. M.; Basilio, E.; Krishnamurthy, A.; Askar, A. M.; Shankar, K.; Kroeker, S.; Michaelis, V. K. Phase evolution in methylammonium tin halide perovskites with variable temperature solid-state ^{119}Sn NMR spectroscopy. *J. Phys. Chem. C* **2020**, *124*, 15015–15027.
- (56) Karmakar, A.; Bhattacharya, A.; Sarkar, D.; M. Bernard, G.; Mar, A.; Michaelis, V. K. Influence of hidden halogen mobility on local structure of $\text{CsSn}(\text{Cl}_{1-x}\text{Br}_x)_3$ mixed-halide perovskites by solid-state NMR. *Chem. Sci.* **2021**, *12*, 3253–3263.
- (57) Karmakar, A.; Bhattacharya, A.; Bernard, G. M.; Mar, A.; Michaelis, V. K. Revealing the local Sn and Pb arrangements in $\text{CsSn}_x\text{Pb}_{1-x}\text{Br}_3$ perovskites with solid-state NMR spectroscopy. *ACS Mater. Lett.* **2021**, *3*, 261–267.
- (58) Choubrac, L.; Lafond, A.; Guillot-Deudon, C.; Moëlo, Y.; Jobic, S. Structure flexibility of the $\text{Cu}_2\text{ZnSnS}_4$ absorber in low-cost photovoltaic cells: from the stoichiometric to the copper-poor compounds. *Inorg. Chem.* **2012**, *51*, 3346–3348.
- (59) Choubrac, L.; Paris, M.; Lafond, A.; Guillot-Deudon, C.; Rocquefelt, X.; Jobic, S. Multinuclear (^{67}Zn , ^{119}Sn and ^{65}Cu) NMR spectroscopy – an ideal technique to probe the cation ordering in $\text{Cu}_2\text{ZnSnS}_4$ photovoltaic materials. *Phys. Chem. Chem. Phys.* **2013**, *15*, 10722–10725.
- (60) Lipton, A. S.; Heck, R. W.; de Jong, W. A.; Gao, A. R.; Wu, X.; Roehrich, A.; Harbison, G. S.; Ellis, P. D. Low temperature ^{65}Cu NMR spectroscopy of the Cu^+ site in azurin. *J. Am. Chem. Soc.* **2009**, *131*, 13992–13999.
- (61) Wrackmeyer, B.; Contreras, R. ^{199}Hg NMR parameters. *Ann. Rep. NMR Spectrosc.* **1992**, *24*, 267–329.
- (62) Hung, I.; Rossini, A. J.; Schurko, R. W. Application of the Carr–Purcell Meiboom–Gill pulse sequence for the acquisition of solid-state NMR spectra of spin-1/2 nuclei. *J. Phys. Chem. A* **2004**, *108*, 7112–7120.
- (63) Gippius, A. A.; Antipov, E. V.; Hoffmann, W.; Lüders, K.; Buntkowsky, G. Low-frequency spin dynamics as probed by ^{63}Cu and ^{199}Hg NMR in $\text{HgBa}_2\text{CuO}_{4+\delta}$ superconductors with different oxygen content, *Phys. Rev. B*, **1999**, *59*, 654–660.

- (64) Peringer, Q P. ^{199}Hg Nuclear magnetic resonance studies of the mercury(II) halides. *Inorganica Chim. Acta* **1980**, *39*, 67–70.
- (65) Wu, G.; Wasylshen, R. E. Observation of ^{201}Hg NMR spectra for solid $\text{K}_2\text{Hg}(\text{CN})_4$. *Magn. Reson. Chem.* **1993**, *31*, 537–539.
- (66) Himmrich, M.; Haeuseler, H. Far infrared studies on stannite and wurtzstannite type compounds. *Spectrochim. Acta* **1991**, *47A*, 933–942.
- (67) Paier, J.; Asahi, R.; Nagoya A.; Kresse, G. $\text{Cu}_2\text{ZnSnS}_4$ as a potential photovoltaic material: A hybrid Hartree-Fock density functional theory study. *Phys. Rev. B* **2009**, *79*, 155126.
- (68) Seol, J.-S.; Lee, S.-Y.; Lee, J.-C.; Nam, H.-D.; Kim, K.-H. Electrical and optical properties of $\text{Cu}_2\text{ZnSnS}_4$ thin films prepared by rf magnetron sputtering process. *Sol. Energy Mater. Sol. Cells* **2003**, *75*, 155–162.
- (69) Scragg, J. J. S.; Larsen, J. K.; Kumar, M.; Persson, C.; Sandler, J.; Siebentritt, S.; Björkman, C. P. Cu–Zn Disorder and band gap fluctuations in $\text{Cu}_2\text{ZnSn}(\text{S},\text{Se})_4$: theoretical and experimental investigations. *Phys. Status Solidi B* **2016**, *253*, 247–254.
- (70) Matsushita, H.; Ichikawa, T.; Katsui, A. Structural, thermodynamical and optical properties of $\text{Cu}_2\text{-II-IV-VI}_4$ quaternary compounds. *J. Mater. Sci.* **2005**, *40*, 2003–2005.
- (71) Cui, Y.; Wang, G.; Pan, D. Synthesis and photoresponse of novel $\text{Cu}_2\text{CdSnS}_4$ semiconductor nanorods. *J. Mater. Chem.* **2012**, *22*, 12471–12473.
- (72) Guan, H.; Shi, Y.; Hou, H.; Wang, X.; Yu, F. Quaternary $\text{Cu}_2\text{CdSnS}_4$ nanoparticles synthesised by microwave irradiation method. *Micro Nano Lett.* **2014**, *9*, 251–252.

Chapter 4

- (1) Lee, T. D.; Ebong, A. U. A review of thin film solar cell technologies and challenges. *Renew. Sustain. Energy Rev.* **2017**, *70*, 1286–1297.
- (2) Kim, J. Y.; Lee, J.-W.; Jung, H. S.; Shin, H.; Park, N.-G. High-efficiency perovskite solar cells. *Chem. Rev.* **2020**, *120*, 7867–7918.
- (3) Jackson, P.; Hariskos, D.; Lotter, E.; Paetel, S.; Wuerz, R.; Menner, R.; Wischmann, W.; Powalla, M. New world record efficiency for $\text{Cu}(\text{In},\text{Ga})\text{Se}_2$ thin-film solar cells beyond 20%. *Prog. Photovolt. Res. Appl.* **2011**, *19*, 894–897.
- (4) Chirilă, A.; Reinhard, P.; Pianezzi, F.; Bloesch, P.; Uhl, A. R.; Fella, C.; Kranz, L.; Keller, D.; Gretener, C.; Hagendorfer, H.; Jaeger, D.; Erni, R.; Nishiwaki, S.; Buecheler, S.;

- Tiwari, A. N. Potassium-induced surface modification of Cu(In,Ga)Se₂ thin films for high-efficiency solar cells. *Nat. Mater.* **2013**, *12*, 1107–1111.
- (5) Berhe, T. A.; Su, W.-N.; Chen, C.-H.; Pan, C.-J.; Cheng, J.-H.; Chen, H.-M.; Tsai, M.-C.; Chen, L.-Y.; Aregahegn Dubale, A.; Hwang, B.-J. Organometal halide perovskite solar cells: degradation and stability. *Energy Environ. Sci.* **2016**, *9*, 323–356.
- (6) Li, J.; Cao, H.-L.; Jiao, W.-B.; Wang, Q.; Wei, M.; Cantone, I.; Lü, J.; Abate, A. Biological impact of lead from halide perovskites reveals the risk of introducing a safe threshold. *Nat. Commun.* **2020**, *11*, 310.
- (7) Sun, K.; Yan, C.; Liu, F.; Huang, J.; Zhou, F.; Stride, J. A.; Green, M.; Hao, X. Over 9% efficient kesterite Cu₂ZnSnS₄ solar cell fabricated by using Zn_{1-x}Cd_xS buffer layer. *Adv. Energy Mater.* **2016**, *6*, 1600046.
- (8) Pal, K.; Singh, P.; Bhaduri, A.; Thapa, K. B. Current challenges and future prospects for a highly efficient (>20%) kesterite CZTS solar cell: a review. *Sol. Energy Mater. Sol. Cells* **2019**, *196*, 138–156.
- (9) Shin, B.; Gunawan, O.; Zhu, Y.; Bojarczuk, N. A.; Chey, S. J.; Guha, S. Thin film solar cell with 8.4% power conversion efficiency using an earth-abundant Cu₂ZnSnS₄ absorber. *Prog. Photovolt. Res. Appl.* **2013**, *21*, 72–76.
- (10) Siebentritt, S.; Schorr, S. Kesterites – a challenging material for solar cells. *Prog. Photovolt. Res. Appl.* **2012**, *20*, 512–519.
- (11) Green, M.; Dunlop, E.; Hohl-Ebinger, J.; Yoshita, M.; Kopidakis, N.; Hao, X. Solar cell efficiency tables (version 57). *Prog. Photovolt. Res. Appl.* **2021**, *29*, 3–15.
- (12) National renewable energy laboratory (NREL). *Best research-cell efficiency chart*. <https://www.nrel.gov/pv/cell-efficiency.html>.
- (13) Xin, H.; Vorpahl, S. M.; Collord, A. D.; Braly, I. L.; Uhl, A. R.; Krueger, B. W.; Ginger, D. S.; Hillhouse, H. W. Lithium-doping inverts the nanoscale electric field at the grain boundaries in Cu₂ZnSn(S,Se)₄ and increases photovoltaic efficiency. *Phys. Chem. Chem. Phys.* **2015**, *17*, 23859–23866.
- (14) Gershon, T.; Sardashti, K.; Lee, Y. S.; Gunawan, O.; Singh, S.; Bishop, D.; Kummel, A. C.; Haight, R. Compositional effects in Ag₂ZnSnSe₄ thin films and photovoltaic devices. *Acta Mater.* **2017**, *126*, 383–388.

- (15) Yan, C.; Sun, K.; Huang, J.; Johnston, S.; Liu, F.; Veettil, B. P.; Sun, K.; Pu, A.; Zhou, F.; Stride, J. A.; Green, M. A.; Hao, X. Beyond 11% efficient sulfide kesterite $\text{Cu}_2\text{Zn}_x\text{Cd}_{1-x}\text{SnS}_4$ solar cell: effects of cadmium alloying. *ACS Energy Lett.* **2017**, *2*, 930–936.
- (16) Shin, D.; Zhu, T.; Huang, X.; Gunawan, O.; Blum, V.; Mitzi, D. B. Earth-abundant chalcogenide photovoltaic devices with over 5% efficiency based on a $\text{Cu}_2\text{BaSn}(\text{S},\text{Se})_4$ absorber. *Adv. Mater.* **2017**, *29*, 1606945.
- (17) Ghosh, A.; Chaudhary, D. K.; Biswas, A.; Thangavel, R.; Udayabhanu, G. Solution-processed Cu_2XSnS_4 ($X = \text{Fe}, \text{Co}, \text{Ni}$) photo-electrochemical and thin film solar cells on vertically grown ZnO nanorod arrays. *RSC Adv.* **2016**, *6*, 115204–115212.
- (18) Li, X.; Hou, Z.; Gao, S.; Zeng, Y.; Ao, J.; Zhou, Z.; Da, B.; Liu, W.; Sun, Y.; Zhang, Y. Efficient optimization of the performance of Mn^{2+} -doped kesterite solar cell: machine learning aided synthesis of high efficient $\text{Cu}_2(\text{Mn}, \text{Zn})\text{Sn}(\text{S},\text{Se})_4$ solar cells. *Sol. RRL* **2018**, *2*, 1800198.
- (19) Collord, A. D.; Hillhouse, H. W. Germanium alloyed kesterite solar cells with low voltage deficits. *Chem. Mater.* **2016**, *28*, 2067–2073.
- (20) Giraldo, S.; Neuschitzer, M.; Thersleff, T.; López-Marino, S.; Sánchez, Y.; Xie, H.; Colina, M.; Placidi, M.; Pistor, P.; Izquierdo-Roca, V. Large efficiency improvement in $\text{Cu}_2\text{ZnSnSe}_4$ solar cells by introducing a superficial Ge nanolayer. *Adv. Energy Mater.* **2015**, *5*, 1501070.
- (21) Kim, I.; Kim, K.; Oh, Y.; Woo, K.; Cao, G.; Jeong, S.; Moon, J. Bandgap-graded $\text{Cu}_2\text{Zn}(\text{Sn}_{1-x}\text{Ge}_x)\text{S}_4$ thin-film solar cells derived from metal chalcogenide complex ligand capped nanocrystals. *Chem. Mater.* **2014**, *26*, 3957–3965.
- (22) Hages, C. J.; Levenco, S.; Miskin, C. K.; Alsmeier, J. H.; Abou-Ras, D.; Wilks, R. G.; Bär, M.; Unold, T.; Agrawal, R. Improved performance of Ge-alloyed CZTGeSSe thin-film solar cells through control of elemental losses. *Prog. Photovolt. Res. Appl.* **2015**, *23*, 376–384.
- (23) Kim, S.; Kim, K. M.; Tampo, H.; Shibata, H.; Niki, S. Improvement of voltage deficit of Ge-incorporated kesterite solar cell with 12.3% conversion efficiency. *Appl. Phys. Express* **2016**, *9*, 102301.

- (24) Moodie, A. F.; Whitfield, H. J. Determination of the structure of $\text{Cu}_2\text{ZnGeS}_4$ polymorphs by lattice imaging and convergent-beam electron diffraction. *Acta Crystallogr. B* **1986**, *42*, 236–247.
- (25) Parasyuk, O. V.; Piskach, L. V.; Romanyuk, Y. E.; Olekseyuk, I. D.; Zaremba, V. I.; Pekhnyo, V. I. Phase relations in the quasi-binary $\text{Cu}_2\text{GeS}_3\text{--ZnS}$ and quasi-ternary $\text{Cu}_2\text{S--Zn(Cd)S--GeS}_2$ systems and crystal structure of $\text{Cu}_2\text{ZnGeS}_4$. *J. Alloys Compd.* **2005**, *397*, 85–94.
- (26) Doverspike, K.; Dwight, K.; Wold, A. Preparation and characterization of copper zinc germanium sulfide selenide ($\text{Cu}_2\text{ZnGeS}_{4-y}\text{Se}_y$). *Chem. Mater.* **1990**, *2*, 194–197.
- (27) Heinrich, C. P.; Day, T. W.; Zeier, W. G.; Snyder, G. J.; Tremel, W. Effect of isovalent substitution on the thermoelectric properties of the $\text{Cu}_2\text{ZnGeSe}_{4-x}\text{S}_x$ series of solid solutions. *J. Am. Chem. Soc.* **2014**, *136*, 442–448.
- (28) Schleich, D. M.; Wold, A. Optical and electrical properties of quaternary chalcogenides. *Mater. Res. Bull.* **1977**, *12*, 111–114.
- (29) Khadka, D. B.; Kim, J. Band gap engineering of alloyed $\text{Cu}_2\text{ZnGe}_x\text{Sn}_{1-x}\text{Q}_4$ ($Q = \text{S, Se}$) films for solar cell. *J. Phys. Chem. C* **2015**, *119*, 1706–1713.
- (30) Mangelis, P.; Aziz, A.; da Silva, I.; Grau-Crespo, R.; Vaqueiro, P.; Powell, A. V. Understanding the origin of disorder in kesterite-type chalcogenides $A_2\text{ZnBQ}_4$ ($A = \text{Cu, Ag}$; $B = \text{Sn, Ge}$; $Q = \text{S, Se}$): the influence of inter-layer interactions. *Phys. Chem. Chem. Phys.* **2019**, *21*, 19311–19317.
- (31) Lafond, A.; Guillot-Deudon, C.; Vidal, J.; Paris, M.; La, C.; Jobic, S. Substitution of Li for Cu in $\text{Cu}_2\text{ZnSnS}_4$: toward wide band gap absorbers with low cation disorder for thin film solar cells. *Inorg. Chem.* **2017**, *56*, 2712–2721.
- (32) Bhattacharya, A.; Tkachuk, D. G.; Mar, A.; Michaelis, V. K. Mere anarchy is loosed: structural disorder in $\text{Cu}_2\text{Zn}_{1-x}\text{Cd}_x\text{SnS}_4$. *Chem. Mater.* **2021**, *33*, 4709–4722.
- (33) Paris, M.; Larramona, G.; Bais, P.; Bourdais, S.; Lafond, A.; Choné, C.; Guillot-Deudon, C.; Delatouche, B.; Moisan, C.; Dennler, G. ^{119}Sn MAS NMR to assess the cationic disorder and the anionic distribution in sulfoselenide $\text{Cu}_2\text{ZnSn}(\text{S}_x\text{Se}_{1-x})_4$ compounds prepared from colloidal and ceramic routes. *J. Phys. Chem. C* **2015**, *119*, 26849–26857.

- (34) Shi, C.; Xi, X.; Hou, Z.; Liu, E.; Wang, W.; Chen, J.; Wu, G. Copper dynamics and structural transformation in noble metal chalcogenides CuAgS probed by ^{63}Cu NMR. *Solid State Ion.* **2017**, *300*, 182–186.
- (35) Zeier, W. G.; Heinrich, C. P.; Day, T.; Panithipongwut, C.; Kieslich, G.; Brunklaus, G.; Snyder, G. J.; Tremel, W. Bond strength dependent superionic phase transformation in the solid solution series $\text{Cu}_2\text{ZnGeSe}_{4-x}\text{S}_x$. *J. Mater. Chem. A* **2014**, *2*, 1790–1794.
- (36) Rodríguez-Carvajal, J. Introduction to the Program FULLPROF: Refinement of crystal and magnetic structures from powder and single crystal data. *Lab. Léon Brillouin CEA-CNRS Saclay Fr.* **2001**.
- (37) Kortüm, G. *Reflectance Spectroscopy*; Springer, 1969.
- (38) Rusanova, D.; Forsling, W.; Antzutkin, O. N.; Pike, K. J.; Dupree, R. Solid-State ^{31}P CP/MAS and Static ^{65}Cu NMR Characterization of polycrystalline copper(I) dialkyldithiophosphate clusters. *J. Magn. Reson.* **2006**, *179*, 140–145.
- (39) Gunther, W. R.; Michaelis, V. K.; Caporini, M. A.; Griffin, R. G.; Román-Leshkov, Y. Dynamic nuclear polarization NMR enables the analysis of Sn-beta zeolite prepared with natural abundance ^{119}Sn precursors. *J. Am. Chem. Soc.* **2014**, *136*, 6219–6222.
- (40) Wu, G. Zinc-67 nuclear magnetic resonance spectroscopy of solids. *Chem. Phys. Lett.* **1998**, *298*, 375–380.
- (41) Michaelis, V. K.; M. Aguiar, P.; V. Terskikh, V.; Kroeker, S. Germanium-73 NMR of amorphous and crystalline GeO_2 . *Chem. Commun.* **2009**, *31*, 4660–4662.
- (42) Massiot, D.; Fayon, F.; Capron, M.; King, I.; Le Calve S; Alonso B; Durand O.; Bujoli B. *Gan Z Hoatson G*. Modeling one- and two- dimensional solid-state NMR spectra, *Magn Reson Chem*, **2002**, *40*, 70–76.
- (43) Mason, J. *Solid State Nucl. Magn. Reson.* **1993**, *2*, 285–288.
- (44) Herzfeld, J.; Berger, A. E. Sideband intensities in NMR spectra of samples spinning at the magic angle. *J. Chem. Phys.* **1980**, *73*, 6021–6030.
- (45) Slichter, C. P. *Principles of Magnetic Resonance*; Springer, 1996.
- (46) Wasylishen, R. E.; Ashbrook, S. E.; Wimperis, S. *NMR of Quadrupolar Nuclei in Solid Materials*; Wiley, 2012.

- (47) Lucier, B. E. G.; Tang, J. A.; Schurko, R. W.; Bowmaker, G. A.; Healy, P. C.; Hanna, J. V. Solid-State ^{65}Cu and ^{31}P NMR spectroscopy of bis(triphenylphosphine) copper species. *J. Phys. Chem. C* **2010**, *114*, 7949–7962.
- (48) Taulelle, F. NMR of quadrupolar nuclei in the solid state. In *Multinuclear Magnetic Resonance in Liquids and Solids—Chemical Applications*; Springer, 1990.
- (49) MacKenzie, K. J. D.; Smith, M. E. *Multinuclear Solid-state NMR of Inorganic Materials*, 1st ed.; Pergamon, 2002.
- (50) Clark, S. J.; Segall, M. D.; Pickard, C. J.; Hasnip, P. J.; Probert, M. I. J.; Refson, K.; Payne, M. C. First principles methods using CASTEP. *Z. Kristallgr.* **2005**, *220*, 567–570.
- (51) Perdew, J. P.; Burke, K.; Ernzerhof, M. Generalized gradient approximation made simple. *Phys. Rev. Lett.* **1996**, *77*, 3865–3868.
- (52) Yates, J. R.; Pickard, C. J.; Mauri, F. Calculation of NMR chemical shifts for extended systems using ultrasoft pseudopotentials. *Phys. Rev. B* **2007**, *76*, 024401.
- (53) Kresse, G.; Furthmüller, J. Efficient iterative schemes for ab-Initio total-energy calculations using a plane-wave basis set. *Phys. Rev. B* **1996**, *54*, 11169–11186.
- (54) Kresse, G.; Joubert, D. From ultrasoft pseudopotentials to the projector augmented-wave method. *Phys. Rev. B* **1999**, *59*, 1758.
- (55) Blöchl, P. E. Projector augmented-wave method. *Phys. Rev. B* **1994**, *50*, 17953–17979.
- (56) Hohenberg, P.; Kohn, W. Inhomogeneous electron gas. *Phys. Rev.* **1964**, *136*, B864–B871.
- (57) Kohn, W.; Sham, L. J. Self-consistent equations including exchange and correlation effects. *Phys. Rev.* **1965**, *140*, A1133.
- (58) Tang, W.; Sanville, E.; Henkelman, G. A Grid-based bader analysis algorithm without lattice bias. *J. Phys. Condens. Matter* **2009**, *21*, 084204.
- (59) Müller, P. C.; Ertural, C.; Hempelmann, J.; Dronskowski, R. Crystal orbital bond index: covalent bond orders in solids. *J. Phys. Chem. C* **2021**, *125*, 7959–7970.
- (60) Deringer, V. L.; Tchougréeff, A. L.; Dronskowski, R. Crystal orbital hamilton population (COHP) analysis as projected from plane-wave basis sets. *J. Phys. Chem. A* **2011**, *115*, 5461–5466.
- (61) Grin, Y.; Savin, A.; Silvi, B. The ELF perspective of chemical bonding. In *The Chemical Bond: Fundamental Aspects of Chemical Bonding*; Wiley, 2014.

- (62) Maintz, S.; Deringer, V. L.; Tchougréeff, A. L.; Dronskowski, R. LOBSTER: a tool to extract chemical bonding from plane-wave based DFT. *J. Comput. Chem.* **2016**, *37*, 1030–1035.
- (63) Harris, R. K.; Becker, E. D.; De Menezes, S. M. C.; Goodfellow, R.; Granger, P. NMR nomenclature. Nuclear spin properties and conventions for chemical shifts (IUPAC recommendations 2001). *Pure Appl. Chem.* **2001**, *73*, 1795–1818.
- (64) Kubicki, D. J.; Prochowicz, D.; Salager, E.; Rakhmatullin, A.; Grey, C. P.; Emsley, L.; Stranks, S. D. Local structure and dynamics in methylammonium, formamidinium, and cesium tin(II) mixed-halide perovskites from ^{119}Sn solid-state NMR. *J. Am. Chem. Soc.* **2020**, *142*, 7813–7826.
- (65) Ha, M.; Karmakar, A.; Bernard, G. M.; Basilio, E.; Krishnamurthy, A.; Askar, A. M.; Shankar, K.; Kroeker, S.; Michaelis, V. K. Phase evolution in methylammonium tin halide perovskites with variable temperature solid-state ^{119}Sn NMR spectroscopy. *J. Phys. Chem. C* **2020**, *124*, 15015–15027.
- (66) Karmakar, A.; Bhattacharya, A.; Sarkar, D.; M. Bernard, G.; Mar, A.; K. Michaelis, V. Influence of hidden halogen mobility on local structure of $\text{CsSn}(\text{Cl}_{1-x}\text{Br}_x)_3$ mixed-halide perovskites by solid-state NMR. *Chem. Sci.* **2021**, *12*, 3253–3263.
- (67) Karmakar, A.; Bhattacharya, A.; Bernard, G. M.; Mar, A.; Michaelis, V. K. Revealing the local Sn and Pb arrangements in $\text{CsSn}_x\text{Pb}_{1-x}\text{Br}_3$ perovskites with solid-state NMR spectroscopy. *ACS Mater. Lett.* **2021**, *3*, 261–267.
- (68) Leroy, C.; Bryce, D. L. Recent advances in solid-state nuclear magnetic resonance spectroscopy of exotic nuclei. *Prog. Nucl. Magn. Reson. Spectrosc.* **2018**, *109*, 160–199.
- (69) Greer, B. J.; Michaelis, V. K.; Terskikh, V. V.; Kroeker, S. Reconnaissance of diverse structural and electronic environments in germanium halides by solid-state ^{73}Ge NMR and quantum chemical calculations. *Can. J. Chem.* **2011**, *89*, 1118–1129.
- (70) Michaelis, V. K.; Kroeker, S. ^{73}Ge Solid-State NMR of germanium oxide materials: experimental and theoretical studies. *J. Phys. Chem. C* **2010**, *114*, 21736–21744.
- (71) Hooper, R. W.; Ni, C.; Tkachuk, D. G.; He, Y.; Terskikh, V. V.; Veinot, J. G. C.; Michaelis, V. K. Exploring structural nuances in germanium halide perovskites using solid-state ^{73}Ge and ^{133}Cs NMR spectroscopy. *J. Phys. Chem. Lett.* **2022**, *13*, 1687–1696.

- (72) Kidd, R. G.; Spinney, H. G. Germanium-73 nuclear magnetic resonance spectra of germanium tetrahalides. *J. Am. Chem. Soc.* **1973**, *95*, 88–90.
- (73) Sutrisno, A.; A. Hanson, M.; A. Rupar, P.; V. Terskikh, V.; M. Baines, K.; Huang, Y. Exploring the limits of ^{73}Ge solid-state NMR spectroscopy at ultrahigh magnetic field. *Chem. Commun.* **2010**, *46*, 2817–2819.
- (74) Kaseman, D. C.; Sen, S. A review of the application of 2D isotropic-anisotropic correlation NMR spectroscopy in structural studies of chalcogenide glasses. *J. Non-Cryst. Solids* **2021**, *561*, 120500.
- (75) Sen, S.; Gan, Z. Chemical order around Ge atoms in binary germanium selenide glasses: results from ^{73}Ge solid-state NMR spectroscopy at 19.6 Tesla. *J. Non-Cryst. Solids* **2010**, *356*, 1519–1521.
- (76) Gonçalves, C.; Mereau, R.; Nazabal, V.; Boussard-Pledel, C.; Roiland, C.; Furet, E.; Deschamps, M.; Bureau, B.; Dussauze, M. Study of the $\text{Ge}_{20}\text{Te}_{80-x}\text{Se}_x$ glassy structures by combining solid state NMR, vibrational spectroscopies and DFT modelling. *J. Solid State Chem.* **2021**, *297*, 122062.
- (77) Choubrac, L.; Paris, M.; Lafond, A.; Guillot-Deudon, C.; Rocquefelte, X.; Jobic, S. Multinuclear (^{67}Zn , ^{119}Sn and ^{65}Cu) NMR spectroscopy – an ideal technique to probe the cationic ordering in $\text{Cu}_2\text{ZnSnS}_4$ photovoltaic materials. *Phys. Chem. Chem. Phys.* **2013**, *15*, 10722–10725.
- (78) Hibble, S. J.; Chippindale, A. M.; Marelli, E.; Kroeker, S.; Michaelis, V. K.; Greer, B. J.; Aguiar, P. M.; Bilbé, E. J.; Barney, E. R.; Hannon, A. C. Local and average structure in zinc cyanide: toward an understanding of the atomistic origin of negative thermal expansion. *J. Am. Chem. Soc.* **2013**, *135*, 16478–16489.
- (79) Huang, Y.; Sutrisno, A. Recent advances in solid-state ^{67}Zn NMR studies: from nanoparticles to biological systems. *Annu. Rep. NMR Spectrosc.*; Academic press, **2014**, *81*, 1–46.
- (80) Madsen, R. S. K.; Qiao, A.; Sen, J.; Hung, I.; Chen, K.; Gan, Z.; Sen, S.; Yue, Y. Ultrahigh-field ^{67}Zn NMR reveals short-range disorder in zeolitic imidazolate framework glasses. *Science* **2020**, *367*, 1473–1476.

- (81) Cadars, S.; Smith, B. J.; Epping, J. D.; Acharya, S.; Belman, N.; Golan, Y.; Chmelka, B. F. Atomic positional versus electronic order in semiconducting ZnSe nanoparticles. *Phys. Rev. Lett.* **2009**, *103*, 136802.
- (82) Tang, J. A.; Ellis, B. D.; Warren, T. H.; Hanna, J. V.; Macdonald, C. L. B.; Schurko, R. W. Solid-State ^{63}Cu and ^{65}Cu NMR spectroscopy of inorganic and organometallic copper(I) complexes. *J. Am. Chem. Soc.* **2007**, *129*, 13049–13065.
- (83) Reiser, S.; Brunklaus, G.; Hong, J. H.; Chan, J. C. C.; Eckert, H.; Pfitzner, A. $(\text{CuI})_3\text{P}_4\text{S}_4$: preparation, structural, and NMR spectroscopic characterization of a copper(I) halide adduct with $\beta\text{-P}_4\text{S}_4$. *Chem. – Eur. J.* **2002**, *8*, 4228–4233.
- (84) Hayashi, S.; Hayamizu, K. Effect of Spinning on chemical shifts in magic-angle-spinning nuclear magnetic resonance. *J. Chem. Phys.* **1990**, *92*, 2818–2827.
- (85) Garcia-Llamas, E.; Merino, J. M.; Serna, R.; Fontané, X.; Victorov, I. A.; Pérez-Rodríguez, A.; León, M.; Bodnar, I. V.; Izquierdo-Roca, V.; Caballero, R. Wide band-gap tuning $\text{Cu}_2\text{ZnSn}_{1-x}\text{Ge}_x\text{S}_4$ single crystals: optical and vibrational properties. *Sol. Energy Mater. Sol. Cells* **2016**, *158*, 147–153.
- (86) Mora-Herrera, D.; Pal, M.; Paraguay-Delgado, F. Facile solvothermal synthesis of $\text{Cu}_2\text{ZnSn}_{1-x}\text{Ge}_x\text{S}_4$ nanocrystals: effect of Ge content on optical and electrical properties. *Mater. Chem. Phys.* **2021**, *257*, 123764.
- (87) Kukreti, S.; Gupta, G. K.; Dixit, A. Theoretical DFT studies of $\text{Cu}_2\text{HgSnS}_4$ absorber material and $\text{Al:ZnO/ZnO/CdS/Cu}_2\text{HgSnS}_4/\text{back contact}$ heterojunction solar cell. *Sol. Energy* **2021**, *225*, 802–813.
- (88) Paier, J.; Asahi, R.; Nagoya, A.; Kresse, G. $\text{Cu}_2\text{ZnSnS}_4$ as a potential photovoltaic material: a hybrid hartree-fock density functional theory study. *Phys. Rev. B* **2009**, *79*, 115126.
- (89) Müller, P. C.; Ertural, C.; Hempelmann, J.; Dronskowski, R. Crystal orbital bond index: covalent bond orders in solids. *J. Phys. Chem. C* **2021**, *125*, 7959–7970.
- (90) Ramsey, N. F. Magnetic shielding of nuclei in molecules. *Phys. Rev.* **1950**, *78*, 699–703.
- (91) Yesinowski, J. P. Solid-state NMR of inorganic semiconductors. In *Solid State NMR*; Chan, J. C. C., Ed.; Springer, 2012.

Chapter 5

- (1) Chen, K. A practical review of NMR lineshapes for spin-1/2 and quadrupolar nuclei in disordered materials. *Int. J. Mol. Sci.* **2020**, *21*, 5666.
- (2) Bhattacharya, A.; Tkachuk, D. G.; Mar, A.; Michaelis, V. K. Mere anarchy is loosed: structural disorder in $\text{Cu}_2\text{Zn}_{1-x}\text{Cd}_x\text{SnS}_4$. *Chem. Mater.* **2021**, *33*, 4709–4722.
- (3) Pinto, A. H.; Shin, S. W.; Isaac, E.; Knutson, T. R.; Aydil, E. S.; Penn, R. L. Controlling $\text{Cu}_2\text{ZnSnS}_4$ (CZTS) phase in microwave solvothermal synthesis. *J. Mater. Chem. A* **2017**, *5*, 23179–23189.
- (4) Fan, C. M.; Regulacio, M. D.; Ye, C.; Lim, S. H.; Lua, S. K.; Xu, Q.-H.; Dong, Z.; Xu, A.-W.; Han, M.-Y. Colloidal nanocrystals of orthorhombic $\text{Cu}_2\text{ZnGeS}_4$: phase-controlled synthesis, formation mechanism and photocatalytic behaviour. *Nanoscale* **2015**, *7*, 3247–3253.
- (5) Rosmus, K. A.; Aitken, J. A. $\text{Cu}_2\text{ZnSiS}_4$. *Acta Crystallogr., Sect. E* **2011**, *67*, i28.
- (6) Rosmus, K. A.; Brunetta, C. D.; Srnec, M. N.; Karuppanan, B.; Aitken, J. A. Synchrotron X-ray powder diffraction and electronic band structure of α - and β - $\text{Cu}_2\text{ZnSiS}_4$. *Z. Für Anorg. Allg. Chem.* **2012**, *638*, 2578–2584.
- (7) Nakamura, S.; Maeda, T.; Wada, T. Phase stability and electronic structure of In free photovoltaic materials: $\text{Cu}_2\text{ZnSiSe}_4$, $\text{Cu}_2\text{ZnGeSe}_4$, and $\text{Cu}_2\text{ZnSnSe}_4$. *Jpn. J. Appl. Phys.* **2010**, *49*, 121203.
- (8) Zhang, X.; Rao, D.; Lu, R.; Deng, K.; Chen, D. First-principles study on electronic and optical properties of $\text{Cu}_2\text{ZnSiVI}_4$ (VI = S, Se, and Te) quaternary semiconductors. *AIP Adv.* **2015**, *5*, 057111.
- (9) Haeuseler, H.; Ohrendorf, F. W.; Himmrich, M. Z. Zur Kenntnis quaternärer Telluride $\text{Cu}_2\text{MM}'\text{Te}_4$ mit Tetraederstrukturen/Quaternary Tellurides $\text{Cu}_2\text{MM}'\text{Te}_4$ with Tetrahedral Structures *Naturforsch. B.* **1991**, *46*, 1049–1052.

Appendix 1: Supplementary data for Chapter 1

Introduction: Chalcogenide photovoltaic materials and solid-state NMR spectroscopy

Table A1.1. Effect of cation substitutions on PCE in $\text{Cu}_2\text{ZnSnS}_4$.

Compound	PCE (%)	Comment
$\text{Cu}_2\text{Zn}_{0.6}\text{Cd}_{0.4}\text{SnS}_4$	9.2 (Su et al.) 11.5 (Yan et al.)	Su et al. used sol-gel synthesis method, whereas Yan et al. used a chemical bath deposition method to synthesize.
$\text{Cu}_2\text{HgSnS}_4$	11.6 to >17	Reported using simulations. Based on design and optimization, efficiency can vary.
$\text{Cu}_2\text{ZnSn}_{0.5}\text{Ge}_{0.5}\text{S}_4$	6.3	1.5% increment in PCE from pristine $\text{Cu}_2\text{ZnSnS}_4$. Nanoparticles were synthesized by hot-injection.
$\text{Cu}_2\text{ZnSn}_{0.7}\text{Ge}_{0.3}\text{S}_x\text{Se}_{4-x}$	9.4	Devices were fabricated using nanocrystal ink synthesized by hot-injection method.
$\text{Cu}_2\text{ZnSn}_{0.96}\text{Ge}_{0.04}\text{S}_4$	10.1	Incorporated Ge through evaporation of 10 nm thick Ge layer.
$\text{Cu}_2\text{Zn}(\text{Sn}_{0.78}\text{Ge}_{0.22})\text{Se}_4$	12.3	Thin film was synthesized by co-evaporation.

Appendix 2: Supplementary data for Chapter 2

Mere anarchy is loosed: structural disorder in $\text{Cu}_2\text{Zn}_{1-x}\text{Cd}_x\text{SnS}_4$

Table A2.1. EDX analyses (mol. %) for $\text{Cu}_2\text{Zn}_{1-x}\text{Cd}_x\text{SnS}_4$. ^a

Nominal composition	x	Cu	Zn	Cd	Sn	S
$\text{Cu}_2\text{ZnSnS}_4$	0	26 (25)	11 12	0 0	13 13	51 50)
$\text{Cu}_2\text{Zn}_{0.95}\text{Cd}_{0.05}\text{SnS}_4$	0.05	23 (25)	11 12	1 1	13 13	52 50)
$\text{Cu}_2\text{Zn}_{0.9}\text{Cd}_{0.1}\text{SnS}_4$	0.1	24 (25)	10 11	2 1	13 13	52 50)
$\text{Cu}_2\text{Zn}_{0.8}\text{Cd}_{0.2}\text{SnS}_4$	0.2	26 (25)	11 10	3 2	13 13	49 50)
$\text{Cu}_2\text{Zn}_{0.7}\text{Cd}_{0.3}\text{SnS}_4$	0.3	23 (25)	8 9	4 4	13 13	53 50)
$\text{Cu}_2\text{Zn}_{0.6}\text{Cd}_{0.4}\text{SnS}_4$	0.4	23 (25)	7 7	5 5	13 13	51 50)
$\text{Cu}_2\text{Zn}_{0.4}\text{Cd}_{0.6}\text{SnS}_4$	0.6	23 (25)	6 5	7 7	13 13	52 50)
$\text{Cu}_2\text{Zn}_{0.2}\text{Cd}_{0.8}\text{SnS}_4$	0.8	23 (25)	3 3	10 10	13 13	52 50)
$\text{Cu}_2\text{CdSnS}_4$	1.0	24 (25)	0 0	13 12	13 13	51 50)

^a Experimental composition shown in first line; expected composition shown in the second line.

Table A2.2. Cell parameters for $\text{Cu}_2\text{Zn}_{1-x}\text{Cd}_x\text{SnS}_4$. ^a

Compound	x	Space group	a (Å)	c (Å)	V (Å ³)	η ($c/2a$ ratio)
$\text{Cu}_2\text{ZnSnS}_4$	0	$I\bar{4}$	5.4103(3)	10.8441(4)	317.42(3)	1.002
$\text{Cu}_2\text{Zn}_{0.95}\text{Cd}_{0.05}\text{SnS}_4$	0.05	$I\bar{4}$	5.4179(3)	10.8609(6)	318.81(3)	1.002
$\text{Cu}_2\text{Zn}_{0.9}\text{Cd}_{0.1}\text{SnS}_4$	0.1	$I\bar{4}$	5.4193(3)	10.8648(6)	319.09(3)	1.002
$\text{Cu}_2\text{Zn}_{0.8}\text{Cd}_{0.2}\text{SnS}_4$	0.2	$I\bar{4}$	5.4337(3)	10.8854(4)	321.40(3)	1.002
$\text{Cu}_2\text{Zn}_{0.7}\text{Cd}_{0.3}\text{SnS}_4$	0.3	$I\bar{4}$	5.4458(3)	10.9111(5)	323.59(3)	1.002
$\text{Cu}_2\text{Zn}_{0.6}\text{Cd}_{0.4}\text{SnS}_4$	0.4	$I\bar{4}2m$	5.4652(2)	10.8477(6)	324.00(3)	0.992
$\text{Cu}_2\text{Zn}_{0.4}\text{Cd}_{0.6}\text{SnS}_4$	0.6	$I\bar{4}2m$	5.5050(2)	10.8615(6)	329.16(3)	0.986
$\text{Cu}_2\text{Zn}_{0.2}\text{Cd}_{0.8}\text{SnS}_4$	0.8	$I\bar{4}2m$	5.5381(4)	10.8350(9)	332.32(4)	0.978
$\text{Cu}_2\text{CdSnS}_4$	1.0	$I\bar{4}2m$	5.5829(5)	10.8245(10)	337.39(5)	0.969

^a Refined from powder XRD patterns. Standard uncertainties are shown in parentheses.

Table A2.3. Isotropic ^{119}Sn chemical shifts (ppm) for $L^{(n)}$ resonances with environments $[\text{Cu}_8\text{Zn}_{4-n}\text{Cd}_n]$ in $\text{Cu}_2\text{Zn}_{1-x}\text{Cd}_x\text{SnS}_4$.

Compound	$L^{(0)}$	$L^{(1)}$	$L^{(2)}$	$L^{(3)}$	$L^{(4)}$	average
$\text{Cu}_2\text{ZnSnS}_4$	-120.9					-120.9
$\text{Cu}_2\text{Zn}_{0.95}\text{Cd}_{0.05}\text{SnS}_4$	-121.7	-111.4				-121.6
$\text{Cu}_2\text{Zn}_{0.9}\text{Cd}_{0.1}\text{SnS}_4$	-122.3	-111.9	-102.9			-122.1
$\text{Cu}_2\text{Zn}_{0.8}\text{Cd}_{0.2}\text{SnS}_4$	-123.1	-112.7	-103.6	-91.9		-118.5
$\text{Cu}_2\text{Zn}_{0.6}\text{Cd}_{0.4}\text{SnS}_4$						-117.2
$\text{Cu}_2\text{Zn}_{0.4}\text{Cd}_{0.6}\text{SnS}_4$						-97.9
$\text{Cu}_2\text{Zn}_{0.2}\text{Cd}_{0.8}\text{SnS}_4$		-112.2	-98.9	-91.5	-82.7	-88.4
$\text{Cu}_2\text{CdSnS}_4$					-81.9	-81.9

^a Determined from deconvolution of ^{119}Sn MAS NMR spectra (9.4 T), with uncertainties of ± 0.5 ppm. For $\text{Cu}_2\text{Zn}_{0.6}\text{Cd}_{0.4}\text{SnS}_4$ and $\text{Cu}_2\text{Zn}_{0.4}\text{Cd}_{0.6}\text{SnS}_4$, the individual peaks are unresolved.

Table A2.4. Linewidths (FWHM in Hz) for $L^{(n)}$ resonances with environments $[\text{Cu}_8\text{Zn}_{4-n}\text{Cd}_n]$ in ^{119}Sn NMR spectra for $\text{Cu}_2\text{Zn}_{1-x}\text{Cd}_x\text{SnS}_4$. ^a

Compound	$L^{(0)}$	$L^{(1)}$	$L^{(2)}$	$L^{(3)}$	$L^{(4)}$	Cumulative FWHM
$\text{Cu}_2\text{ZnSnS}_4$	790					790
$\text{Cu}_2\text{Zn}_{0.95}\text{Cd}_{0.05}\text{SnS}_4$	874	803				1677
$\text{Cu}_2\text{Zn}_{0.9}\text{Cd}_{0.1}\text{SnS}_4$	1006	855	862			2723
$\text{Cu}_2\text{Zn}_{0.8}\text{Cd}_{0.2}\text{SnS}_4$	1513	991	1184	503		4191
$\text{Cu}_2\text{Zn}_{0.6}\text{Cd}_{0.4}\text{SnS}_4$						5100
$\text{Cu}_2\text{Zn}_{0.4}\text{Cd}_{0.6}\text{SnS}_4$						3630
$\text{Cu}_2\text{Zn}_{0.2}\text{Cd}_{0.8}\text{SnS}_4$		1116	1594	982	1237	4929
$\text{Cu}_2\text{CdSnS}_4$					823	823

^a Uncertainties in FWHM are ± 50 Hz. For $\text{Cu}_2\text{Zn}_{0.6}\text{Cd}_{0.4}\text{SnS}_4$ and $\text{Cu}_2\text{Zn}_{0.4}\text{Cd}_{0.6}\text{SnS}_4$, the individual peaks are unresolved.

Table A2.5. Relative areas for $L^{(n)}$ resonances with environments $[\text{Cu}_8\text{Zn}_{4-n}\text{Cd}_n]$ in ^{119}Sn NMR spectra for $\text{Cu}_2\text{Zn}_{1-x}\text{Cd}_x\text{SnS}_4$. ^a

Compound		$L^{(0)}$	$L^{(1)}$	$L^{(2)}$	$L^{(3)}$	$L^{(4)}$
$\text{Cu}_2\text{Zn}_{0.95}\text{Cd}_{0.05}\text{SnS}_4$	experimental	0.841	0.159	0	0	0
	binomial	0.815	0.171	0.014	0.000	0.000
$\text{Cu}_2\text{Zn}_{0.9}\text{Cd}_{0.1}\text{SnS}_4$	experimental	0.737	0.216	0.046	0	0
	binomial	0.656	0.292	0.049	0.004	0.000
$\text{Cu}_2\text{Zn}_{0.8}\text{Cd}_{0.2}\text{SnS}_4$	experimental	0.586	0.241	0.158	0.0140	0
	binomial	0.410	0.410	0.154	0.026	0.002
$\text{Cu}_2\text{Zn}_{0.2}\text{Cd}_{0.8}\text{SnS}_4$	experimental	0	0.023	0.275	0.211	0.490
	binomial	0.002	0.026	0.154	0.410	0.410

^a The theoretical areas are based on a binomial distribution of Zn and Cd atoms disordered over four sites. Uncertainties are ± 0.04 for relative areas.

Table A2.6. Isotropic chemical shifts, linewidths (FWHM), and relative areas for resonances assigned to $I\bar{4}$ and $I\bar{4}2m$ structures in ^{113}Cd MAS NMR spectra for $\text{Cu}_2\text{Zn}_{1-x}\text{Cd}_x\text{SnS}_4$.^a

Compound	$I\bar{4}$			$I\bar{4}2m$		
	δ_{iso} (ppm)	FWHM (Hz)	Area (%)	δ_{iso} (ppm)	FWHM (Hz)	Area (%)
$\text{Cu}_2\text{Zn}_{0.8}\text{Cd}_{0.2}\text{SnS}_4$	723.7	1220	100.0			
$\text{Cu}_2\text{Zn}_{0.7}\text{Cd}_{0.3}\text{SnS}_4$	720.1	1907	69.6	679.7	2472	30.4
$\text{Cu}_2\text{Zn}_{0.6}\text{Cd}_{0.4}\text{SnS}_4$	718.5	3330	19.5	673.9	1760	80.5
$\text{Cu}_2\text{Zn}_{0.4}\text{Cd}_{0.6}\text{SnS}_4$				661.4	3250	100.0
$\text{Cu}_2\text{Zn}_{0.2}\text{Cd}_{0.8}\text{SnS}_4$				651.9	2775	100.0
$\text{Cu}_2\text{CdSnS}_4$				639.6	435	100.0

^a Uncertainties are ± 0.5 ppm for peak positions, ± 50 Hz for linewidths, and $\pm 3\%$ for relative areas.

Table A2.7. Isotropic chemical shifts (ppm) and centers of gravity (ppm) in ^{63}Cu MAS NMR spectra for $\text{Cu}_2\text{Zn}_{1-x}\text{Cd}_x\text{SnS}_4$.^a

Compound	δ_{iso}	Center of gravity, δ_{cgs}
$\text{Cu}_2\text{ZnSnS}_4$	787 (2a site), 807 (2c site)	748 (2a site), 792 (2c site)
$\text{Cu}_2\text{Zn}_{0.8}\text{Cd}_{0.2}\text{SnS}_4$		726 (2a site), 785 (2c site)
$\text{Cu}_2\text{Zn}_{0.6}\text{Cd}_{0.4}\text{SnS}_4$		771 (4d site)
$\text{Cu}_2\text{Zn}_{0.4}\text{Cd}_{0.6}\text{SnS}_4$		766 (4d site)
$\text{Cu}_2\text{Zn}_{0.2}\text{Cd}_{0.8}\text{SnS}_4$		759 (4d site)
$\text{Cu}_2\text{CdSnS}_4$	762 (4d site)	752 (4d site)

^a Isotropic chemical shifts were determined for the end-members from non-spinning ^{63}Cu NMR spectra, and centers of gravity were determined for all members from Gaussian fitting of ^{63}Cu MAS NMR spectra. Uncertainties are ± 3 ppm for chemical shifts and ± 1 ppm for centers of gravity.

Table A2.8. Comparison of experimental and DFT-computed NMR parameters for $\text{Cu}_2\text{ZnSnS}_4$ and $\text{Cu}_2\text{CdSnS}_4$.

Parameter	$\text{Cu}_2\text{ZnSnS}_4$		$\text{Cu}_2\text{CdSnS}_4$	
	Experimental	Computed	Experimental	Computed
^{119}Sn parameters				
Ω (ppm)	32	55	115	112
κ	-0.4	-1	+0.9	+1
^{113}Cd parameters				
Ω (ppm)			54	45
κ			+0.8	+1
^{63}Cu parameters				
Ω (ppm)	271 (2a), 114 (2c)	366 (2a), 295 (2c)	310	292
κ	+1 (2a), -1 (2c)	+1 (2a), -1 (2c)	-1	-1
C_Q (MHz)	6.7 (2a), 1.7 (2c)	7.8 (2a), 5.1 (2c)	0.8	4.7
η_Q	0 (2a), 0 (2c)	0 (2a), 0 (2c)	0	0

Table A2.9. DFT-computed ^{63}Cu and ^{113}Cd NMR parameters for various site distributions of Cu, Zn, and Cd atoms in $\text{Cu}_2\text{ZnSnS}_4$ and $\text{Cu}_2\text{CdSnS}_4$.

Model	occupancy			$\delta_{\text{Cu}}, \delta_{\text{Cd}}$ and δ_{Zn} (ppm)			C_Q for Cu and Zn (MHz)		
	$2a$	$2c$	$2d$	$2a$	$2c$	$2d$	$2a$	$2c$	$2d$
Space group $I\bar{4}$									
(1) $\text{Cu}_2\text{ZnSnS}_4$	Cu	Cu	Zn	789	804	357	7.8	5.1	2.5
(2) $\text{Cu}_2\text{ZnSnS}_4$	Cu	Zn	Cu	823	466	783	7.7	4.1	3.1
(3) $\text{Cu}_2\text{ZnSnS}_4$	Zn	Cu	Cu	—	874	864	—	10.1	7.9
(4) $\text{Cu}_2\text{CdSnS}_4$	Cu	Cu	Cd	758	800	1131	9.1	6.2	—
(5) $\text{Cu}_2\text{CdSnS}_4$	Cu	Cd	Cu	760	1132	797	9.1	—	4.2
(6) $\text{Cu}_2\text{CdSnS}_4$	Cd	Cu	Cu	1079	843	852	—	7.5	9.7
Space group $I\bar{4}2m$									
(7) $\text{Cu}_2\text{CdSnS}_4$	Cd	Cu		1086	839		—	4.7	

Table A2.10. Site distributions in substitution models for $\text{Cu}_2\text{Zn}_{0.8}\text{Cd}_{0.2}\text{SnS}_4$ in space group $I\bar{4}$.

Model	$2a$	$2c$	$2d$
(8) $\text{Cu}_2\text{Zn}_{0.8}\text{Cd}_{0.2}\text{SnS}_4$	0.8 Cu / 0.2 Cd	1.0 Cu	0.2 Cu / 0.8 Zn
(9) $\text{Cu}_2\text{Zn}_{0.8}\text{Cd}_{0.2}\text{SnS}_4$	1.0 Cu	0.8 Cu / 0.2 Cd	0.2 Cu / 0.8 Zn
(10) $\text{Cu}_2\text{Zn}_{0.8}\text{Cd}_{0.2}\text{SnS}_4$	1.0 Cu	1.0 Cu	0.8 Zn / 0.2 Cd

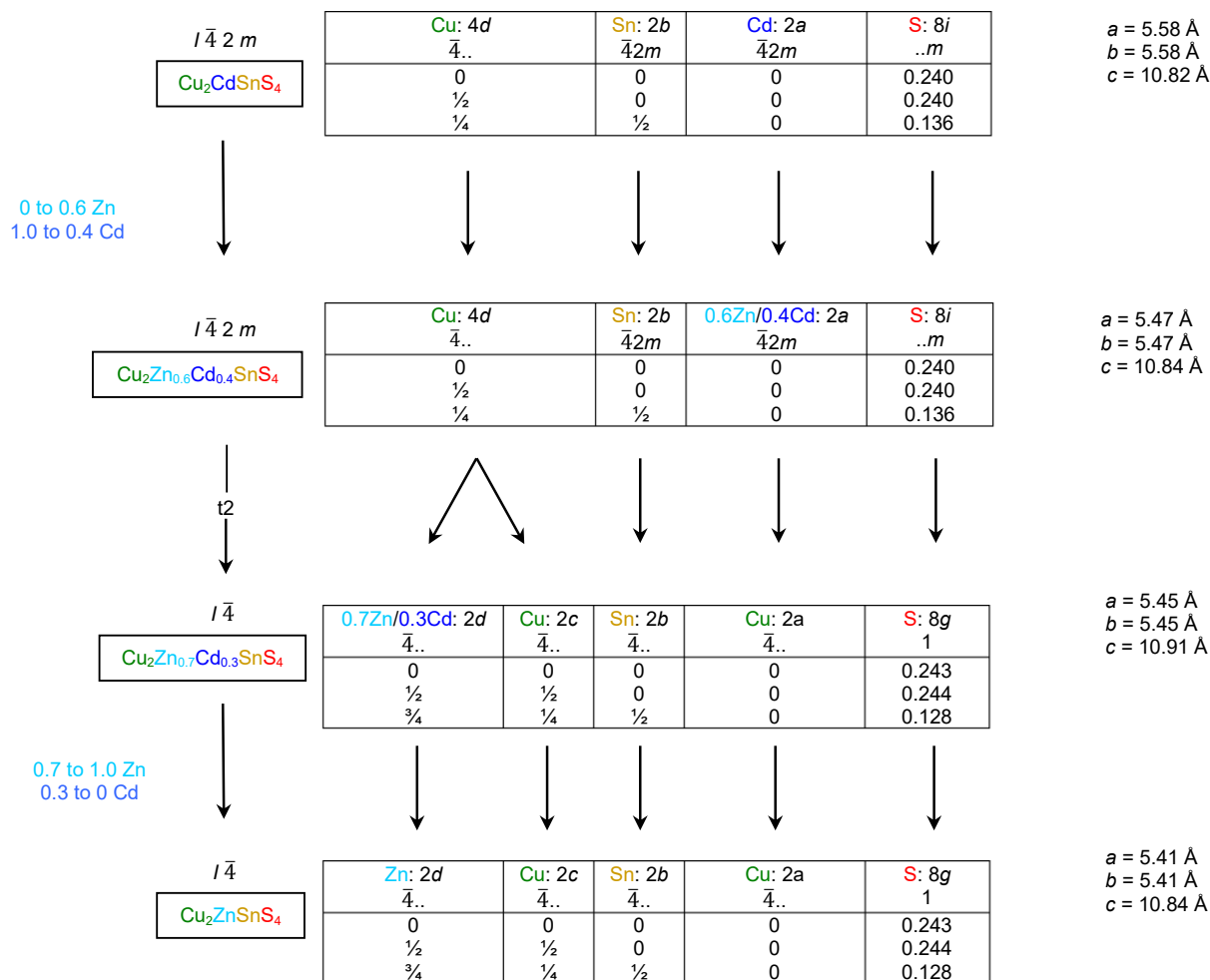


Figure A2.1. Group-subgroup relationships in $\text{Cu}_2\text{Zn}_{1-x}\text{Cd}_x\text{SnS}_4$. Cell parameters were taken as refined from powder XRD patterns obtained in the present work. Coordinates for the S atoms were taken from previous reports for $\text{Cu}_2\text{ZnSnS}_4$ (Choubrac, L.; Lafond, A.; Guillon-Deudon, C.; Moëlo, Y.; Jobic, S.; *Inorg. Chem.* **2012**, *51*, 3346–3348) and $\text{Cu}_2\text{CdSnS}_4$ (Rosmus, K.A.; Brant J.A.; Wisneski, S.D.; Clark, D.J.; Kim, Y.S.; Jang, J.I.; Brunetta, C.D.; Zhang, J.-H.; Srnc, M.N.; Aitken, J.A. *Inorg. Chem.* **2014**, *53*, 7809–7811); these coordinates were then assumed for solid solution members with the $I\bar{4}$ and $I\bar{4}2m$ structures, respectively.

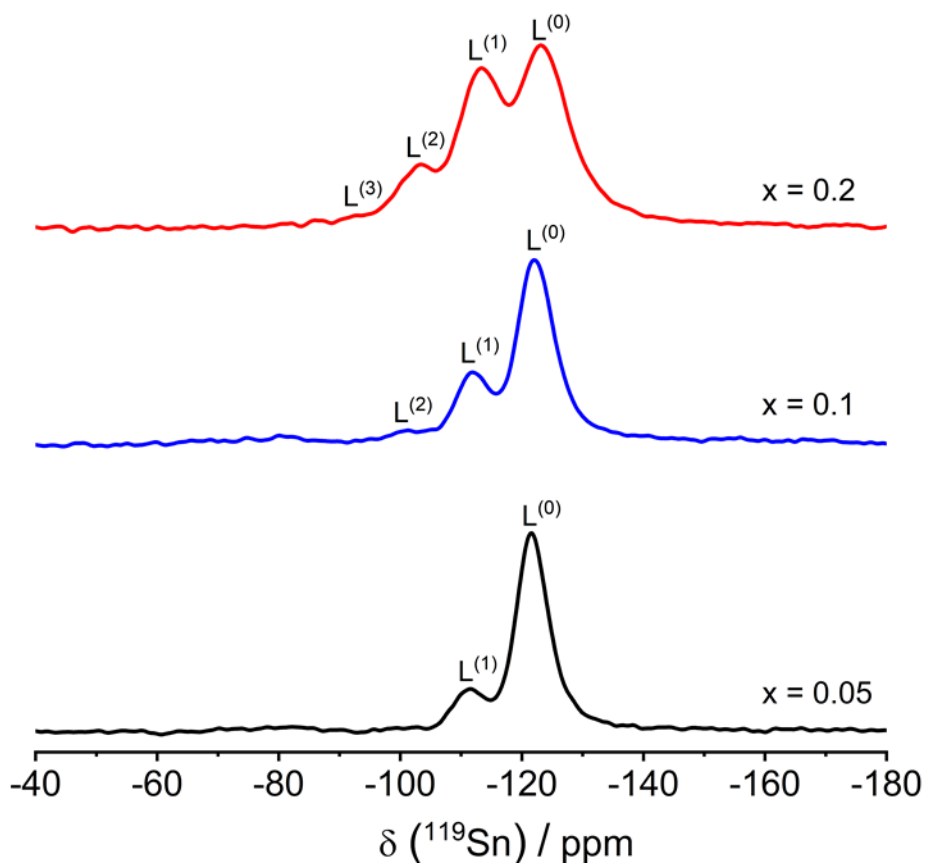


Figure A2.2. ^{119}Sn MAS NMR spectra ($B_0 = 9.4$ T) for lightly substituted Cd members of $\text{Cu}_2\text{Zn}_{1-x}\text{Cd}_x\text{SnS}_4$ ($x = 0.05$ – 0.2).

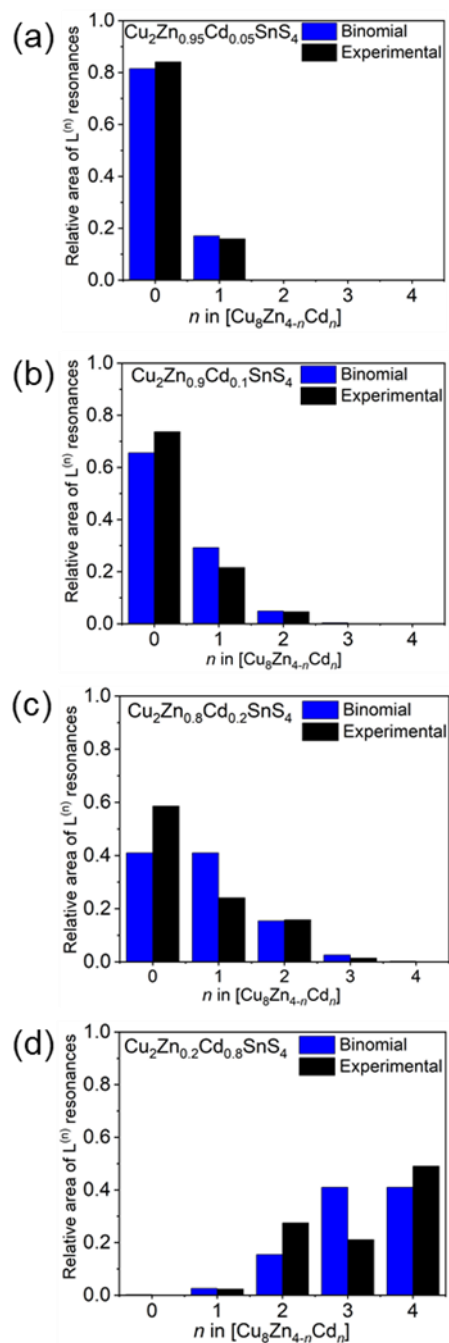


Figure A2.3. Relative areas for $L^{(n)}$ resonances with environments $[\text{Cu}_8\text{Zn}_{4-n}\text{Cd}_n]$ around Sn atoms, obtained from ^{119}Sn NMR spectra for $\text{Cu}_2\text{Zn}_{1-x}\text{Cd}_x\text{SnS}_4$ ($x = 0.05, 0.1, 0.2, 0.8$) and compared with model assuming binomial distribution of Zn and Cd atoms over four sites. Uncertainties are ± 0.04 for relative areas.

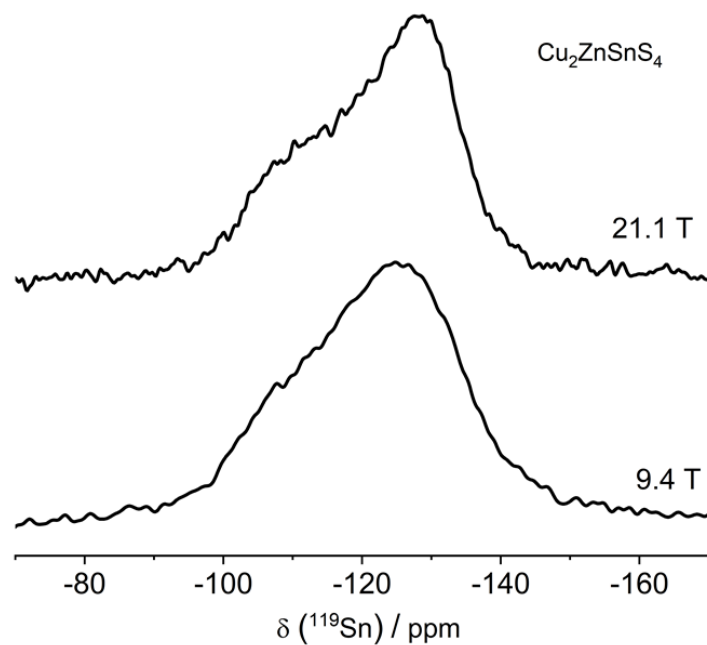


Figure A2.4. Non-spinning ^{119}Sn NMR spectra for $\text{Cu}_2\text{ZnSnS}_4$ acquired at $B_0 = 9.4$ and 21.1 T.

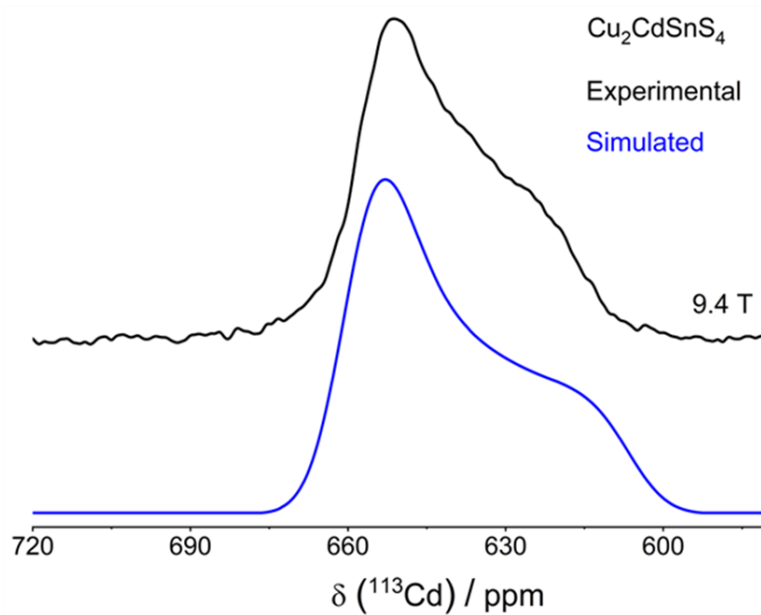


Figure A2.5. Experimental (black) and simulated (blue) non-spinning ^{113}Cd NMR spectrum for $\text{Cu}_2\text{CdSnS}_4$ ($B_0 = 9.4$ T, $\delta_{\text{iso}} = -639$ ppm, $\Omega = 54 \pm 5$ ppm, $\kappa = 0.8 \pm 0.1$).

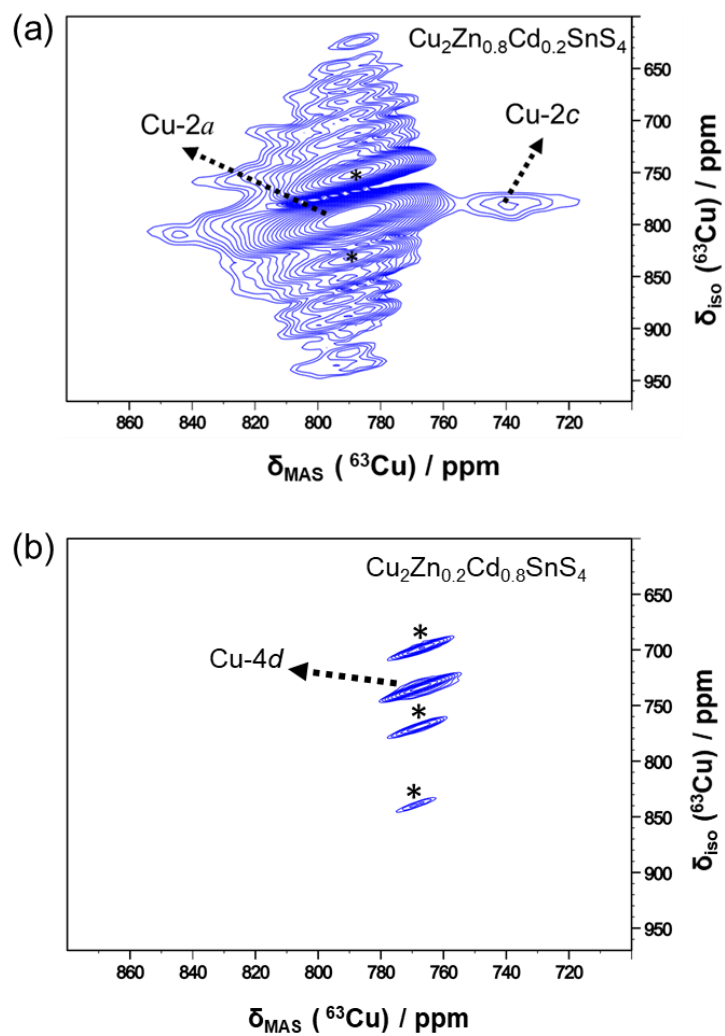


Figure A2.6. Triple quantum (3Q) MAS NMR spectra ($B_0 = 21.1$ T; $\omega_r/2\pi = 31.25$ kHz) for $\text{Cu}_2\text{Zn}_{0.8}\text{Cd}_{0.2}\text{SnS}_4$ and $\text{Cu}_2\text{Zn}_{0.2}\text{Cd}_{0.8}\text{SnS}_4$. The asterisks (*) indicate spinning sidebands.

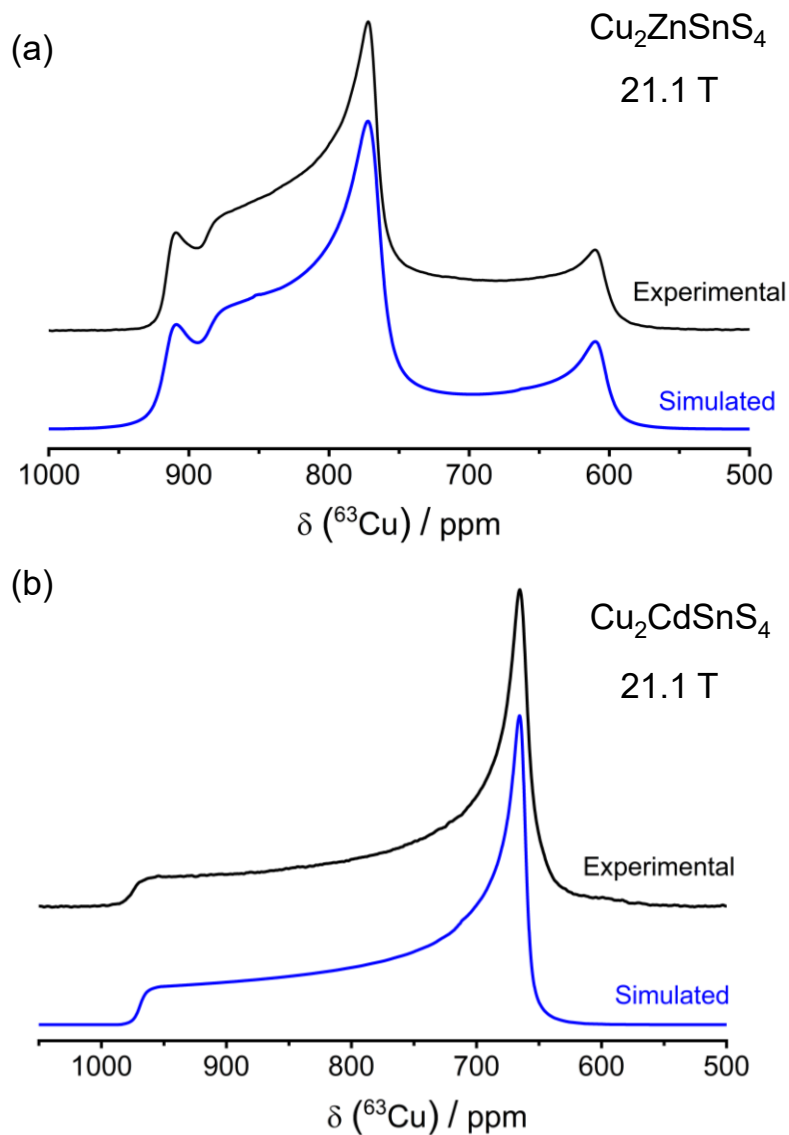


Figure A2.7. Experimental and simulated non-spinning ^{63}Cu NMR spectra ($B_0 = 21.1$ T) for (a) $\text{Cu}_2\text{ZnSnS}_4$ ($\delta_{\text{iso}} = 787 \pm 2$ ppm, $\Omega = 271 \pm 10$ ppm, $\kappa = 1 \pm 0.1$, $C_Q = 6.7 \pm 0.2$ MHz, $\eta_Q = 0 \pm 0.1$ for $2a$ site; $\delta_{\text{iso}} = 807 \pm 2$ ppm, $\Omega = 114 \pm 10$ ppm, $\kappa = -1 \pm 0.1$, $C_Q = 1.7 \pm 0.2$ MHz, $\eta_Q = 0 \pm 0.1$ for $2c$ site) and (b) $\text{Cu}_2\text{CdSnS}_4$ ($\delta_{\text{iso}} = 762 \pm 2$ ppm, $\Omega = 310 \pm 10$ ppm, $\kappa = -1 \pm 0.1$, $C_Q = 0.8 \pm 0.2$ MHz, $\eta_Q = 0 \pm 0.1$ for $4d$ site).

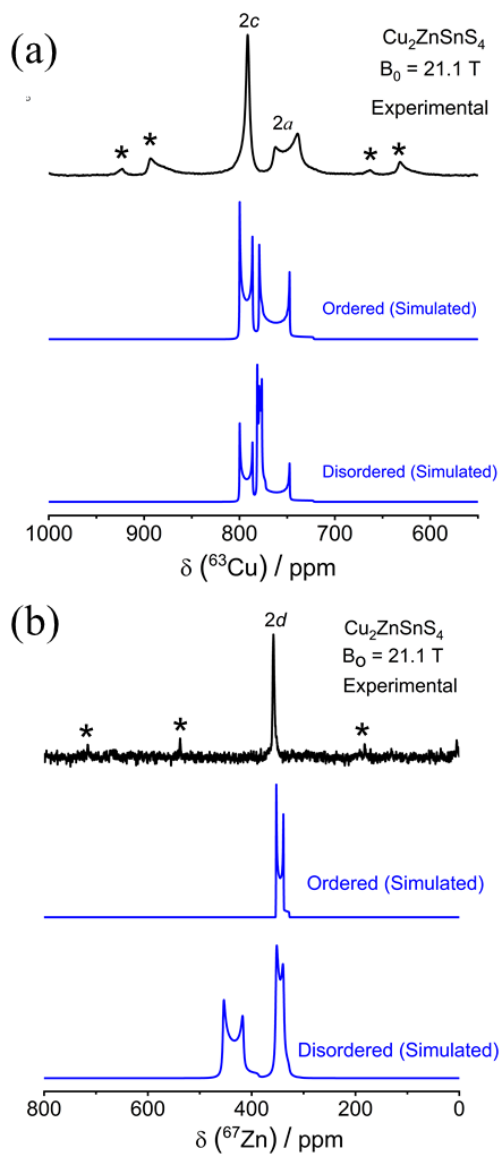


Figure A2.8. Comparison of experimental NMR spectra ($B_0 = 21.1$ T) of (a) ^{63}Cu and (b) ^{67}Zn with spectra simulated using DFT computed parameters for $\text{Cu}_2\text{ZnSnS}_4$ (see Table A2.9). The asterisks (*) indicate spinning sidebands. Ordered simulation assumes Cu occupies $2a$ and $2c$, and Zn occupies $2d$; Disordered simulation assumes Cu occupies $2a$, $2c$, and $2d$, and Zn occupies $2d$ and $2c$.

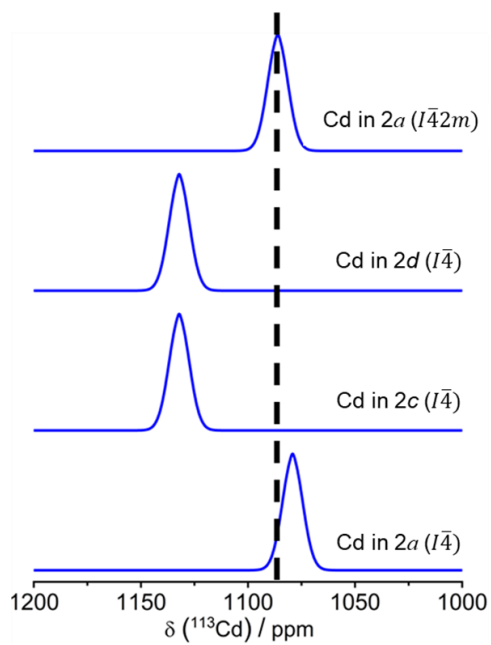


Figure A2.9. DFT-computed ^{113}Cd NMR isotropic chemical shifts following in models of $\text{Cu}_2\text{CdSnS}_4$ with Cd atoms placed in different sites (see Table A2.9).

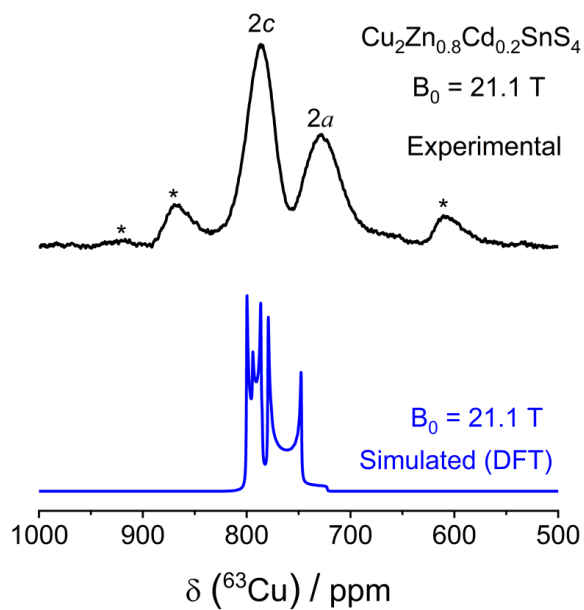


Figure A2.10. DFT-computed ^{63}Cu NMR parameters of Cu chemical environments in models of $\text{Cu}_2\text{ZnSnS}_4$ with Cu atoms placed in different sites (see Table A2.9 and Table A2.10), compared with the experimental spectrum of $\text{Cu}_2\text{Zn}_{0.8}\text{Cd}_{0.2}\text{SnS}_4$. The asterisks (*) indicate spinning sidebands.

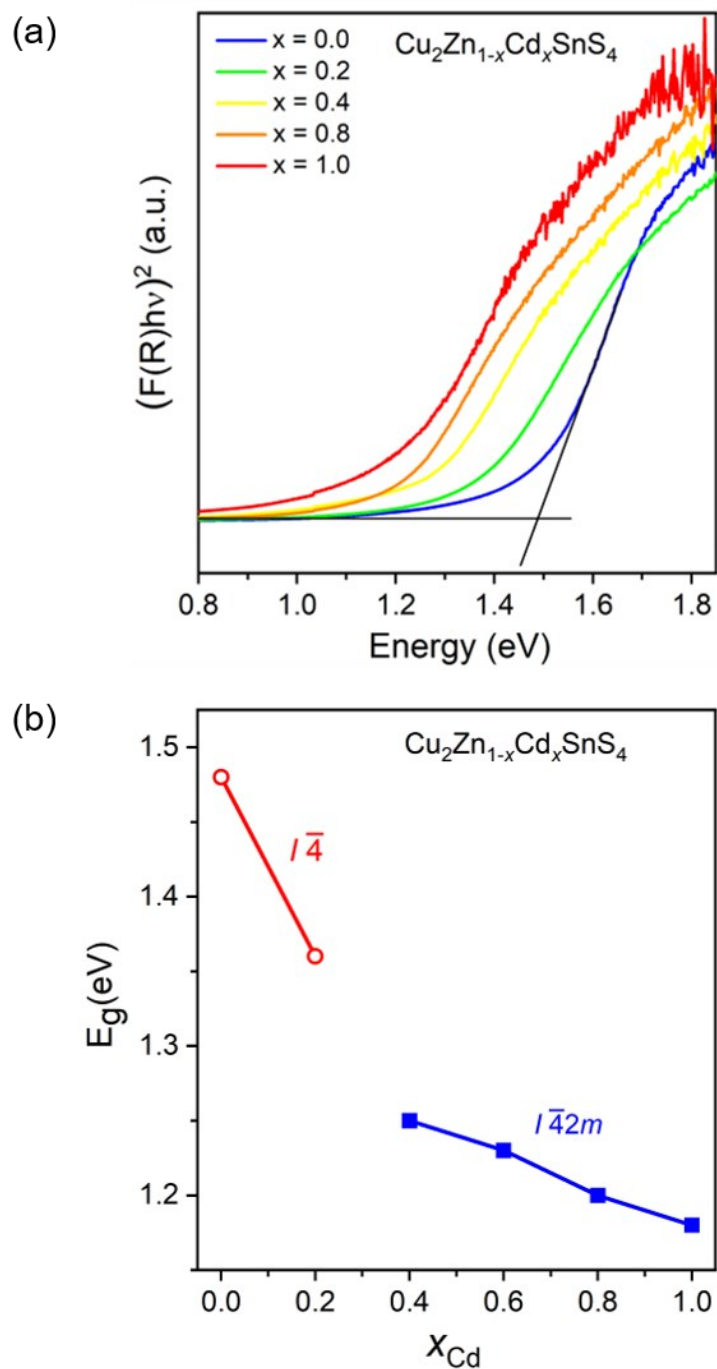


Figure A2.11. (a) Optical absorption spectra for $\text{Cu}_2\text{Zn}_{1-x}\text{Cd}_x\text{SnS}_4$. The optical band gaps were determined by extrapolation of the absorption edge, as illustrated for one sample. (b) Dependence of band gap on Cd content in $\text{Cu}_2\text{Zn}_{1-x}\text{Cd}_x\text{SnS}_4$.

Appendix 3: Supplementary data for Chapter 3

Mercurial possibilities: determining site distributions in $\text{Cu}_2\text{HgSnS}_4$ using $^{63/65}\text{Cu}$, ^{119}Sn , and ^{199}Hg solid-state NMR spectroscopy

Table A3.1. EDX analyses (mol%) for Cu_2MSnS_4 ($M = \text{Zn, Cd, Hg}$).

	$\text{Cu}_2\text{ZnSnS}_4$	$\text{Cu}_2\text{CdSnS}_4$	$\text{Cu}_2\text{HgSnS}_4$	expected
Cu	24	24	25	25
<i>M</i>	12	13	11	12
Sn	13	12	11	13
S	51	51	53	50

Table A3.2. Tetragonal cell parameters for Cu_2MSnS_4 ($M = \text{Zn, Cd, Hg}$).^a

	a (Å)	c (Å)	$c/2a$ ratio	V (Å ³)	Reference
$\text{Cu}_2\text{ZnSnS}_4$	5.436	10.85	0.998	320.6	Hahn ¹ 1965
	5.4356(1)	10.8352(2)	0.997	320.13(1)	This work
$\text{Cu}_2\text{CdSnS}_4$	5.582	10.86	0.973	338.4	Hahn ¹ 1965
	5.5920(1)	10.8399(2)	0.969	338.97(1)	Rosmus ² 2014
	5.583	10.824	0.969	337.4	Olekseyuk ³ 2019
	5.5829(5)	10.8245(10)	0.969	337.39(5)	Bhattacharya ⁴ 2021
	5.5930(1)	10.8441(2)	0.969	339.22(1)	This work
$\text{Cu}_2\text{HgSnS}_4$	5.566	10.88	0.977	337.1	Hahn ¹ 1965
	5.542(3)	10.908(7)	0.984	335.0(2)	Kaplunnik ⁵ 1977
	5.555	10.911	0.982	336.7	Gruzdev ⁶ 1988
	5.577(1)	10.898(2)	0.977	339.0(1)	Himmrich ⁷ 1991
	5.5749(6)	10.882(1)	0.976	338.21(4)	Kabalov ⁸ 1998
	5.580(2)	10.895(3)	0.976	339.2(2)	Vu ⁹ 2019
	5.5819(1)	10.8925(2)	0.976	339.38(1)	This work

^a Standard uncertainties, where reported, are shown in parentheses. The list for $\text{Cu}_2\text{ZnSnS}_4$ is not comprehensive, because there are hundreds of previous reports of this compound.

References

- Hahn, H.; Schulze, H. Über Ternäre Selenide Des Bariums. *Naturwissenschaften* **1965**, *52*, 426–426.
- Rosmus, K. A.; Brant, J. A.; Wisneski, S. D.; Clark, D. J.; Kim, Y. S.; Jang, J. I.; Brunetta, C. D.; Zhang, J.-H.; Srnec, M. N.; Aitken, J. A. Optical nonlinearity in $\text{Cu}_2\text{CdSnS}_4$ and $\alpha/\beta\text{-Cu}_2\text{ZnSiS}_4$: Diamond-like semiconductors with high laser-damage thresholds. *Inorg. Chem.* **2014**, *53*, 7809–7811.
- Olekseyuk, I.; Marushko, L.; Ivashchenko, B. I.; Piskach, L.; Parasyuk, O. Phase Equilibria between the quaternary semiconductors $A_2B^{II}C^IVX_4$ ($A^I - \text{Cu}$; $B^{II} - \text{Zn, Cd}$; $C^{IV} - \text{Si, Ge, Sn, X} - \text{S, Se}$). *Chem. Met. Alloys*, **2019**, *12*, 51–60.
- Bhattacharya, A.; Tkachuk, D. G.; Mar, A.; Michaelis, V. M. Mere anarchy is loosed: Structural disorder in $\text{Cu}_2\text{Cd}_x\text{Zn}_{1-x}\text{SnS}_4$. *Chem. Mater.* **2021**, *33*, 4709–4722.
- Kaplunnik, L. N.; Pobedimskaya, E. A.; Belov, N. V. Crystal structure of velikite $\text{Cu}_{3.75}\text{Hg}_{1.75}\text{Sn}_2\text{S}_8$. *Kristallografiya* **1977**, *22*, 175–177.
- Gruzdev, V. S.; Volgin, V. Yu.; Spiridonov, E. M.; Kaplunnik, L. N.; Pobedimskaya, E. A.; Chvileva, T. N.; Chernitsova, N. M. Velikite, $\text{Cu}_2\text{HgSnS}_4$ – a mercury member of the stannite group. *Dokl. Akad. Nauk SSSR*, **1988**, *300*, 432–435.
- Himmrich, M.; Haeuselner, H. Far infrared studies on stannite and wurtzstannite type compounds. *Spectrochim. Acta* **1991**, *47A*, 933–942.
- Kabalov, Yu. K.; Evstigneeva, T. L.; Spiridonov, E. M. Crystal structure of $\text{Cu}_2\text{HgSnS}_4$, a synthetic analogue of the mineral velikite. *Crystallogr. Rep.* **1998**, *43*, 16–20 (*Transl. Kristallografiya* **1998**, *43*, 21–25).
- Vu, T. V.; Lavrentyev, A. A.; Gabrelian, B. V.; Tong, H. D.; Tkach, V. A.; Parasyuk, O. V.; Khyzhun, O. Y. A theoretical and experimental study of the valence-band electronic structure and optical constants of quaternary copper mercury tin sulfide, $\text{Cu}_2\text{HgSnS}_4$, a potential material for optoelectronics and solar cells. *Opt. Mater.* **2019**, *96*, 109296.

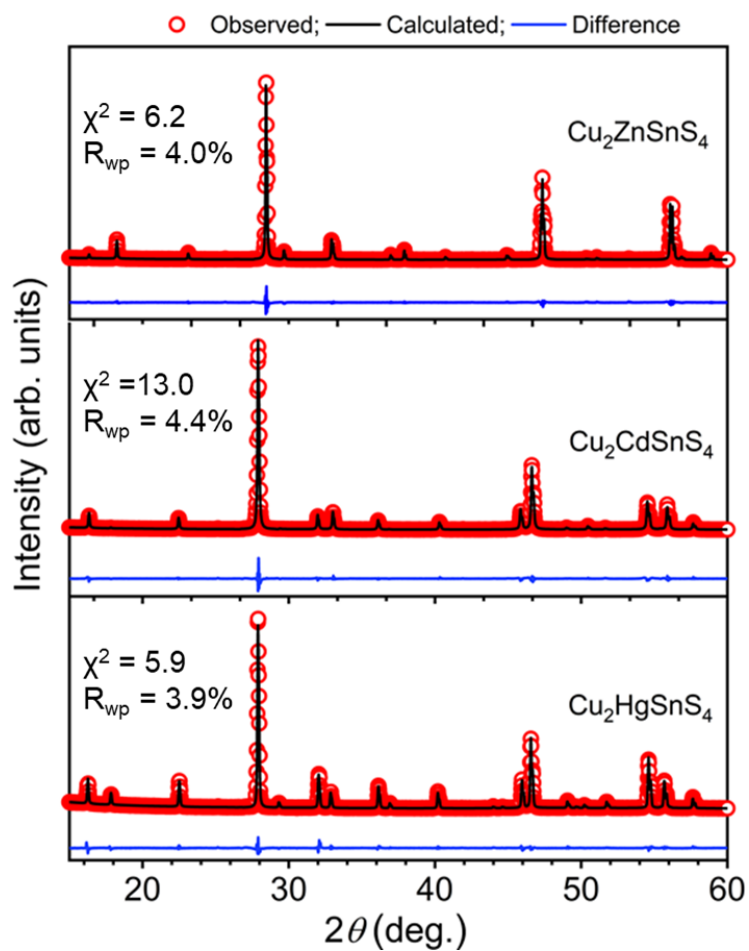


Figure A3.1. The Le Bail fittings of powder XRD patterns for $\text{Cu}_2\text{ZnSnS}_4$, $\text{Cu}_2\text{CdSnS}_4$, and $\text{Cu}_2\text{HgSnS}_4$.

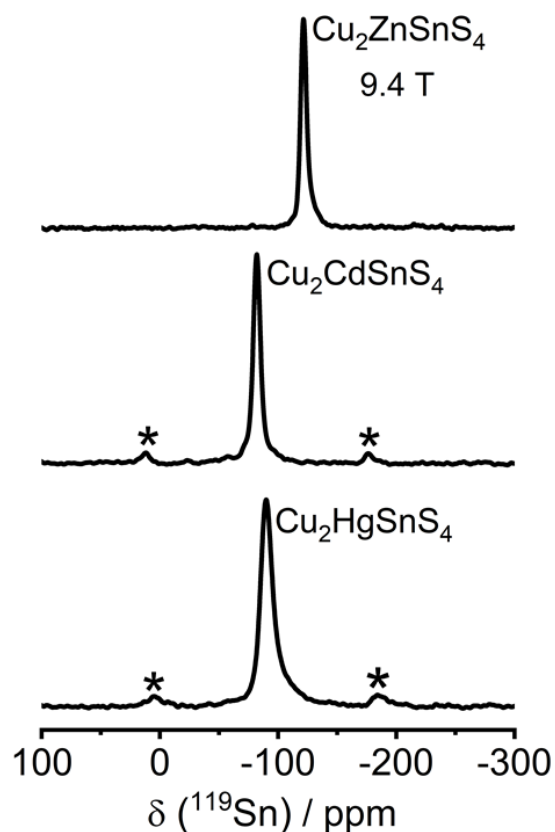


Figure A3.2. Experimental ^{119}Sn MAS NMR spectra for $\text{Cu}_2\text{ZnSnS}_4$, $\text{Cu}_2\text{CdSnS}_4$, and $\text{Cu}_2\text{HgSnS}_4$. The asterisks (*) mark spinning sidebands due to a small CSA.

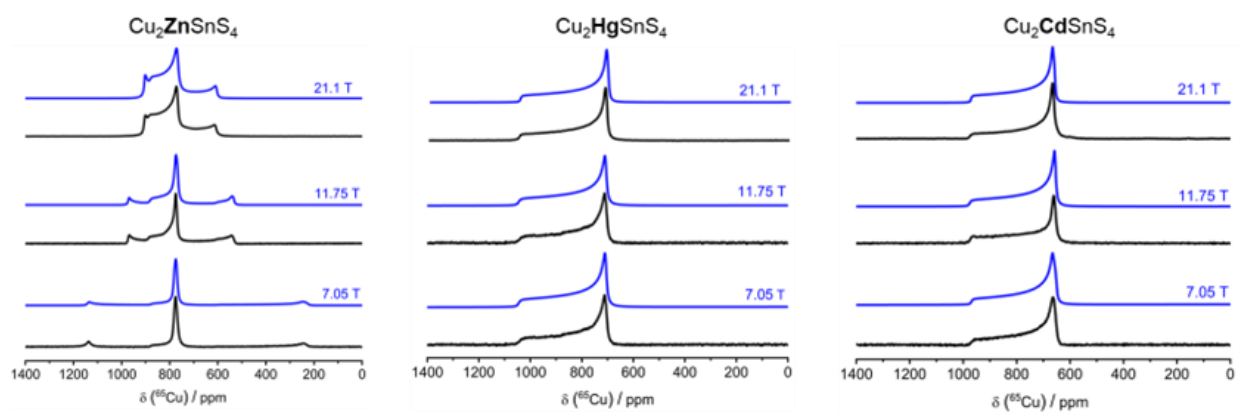


Figure A3.3. Experimental (black, ppm scale) and spectral simulations (blue) for non-spinning ^{65}Cu NMR spectra at 7.05, 11.75 and 21.1 T for $\text{Cu}_2\text{ZnSnS}_4$, $\text{Cu}_2\text{HgSnS}_4$, and $\text{Cu}_2\text{CdSnS}_4$. The NMR spectral simulations were performed using the Dmfit software.

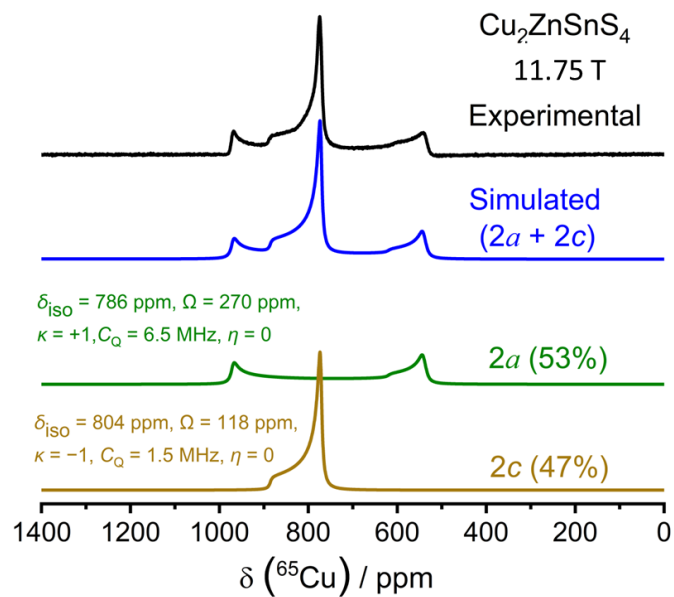


Figure A3.4. Deconvolution of the non-spinning ⁶⁵Cu NMR spectrum for Cu₂ZnSnS₄.

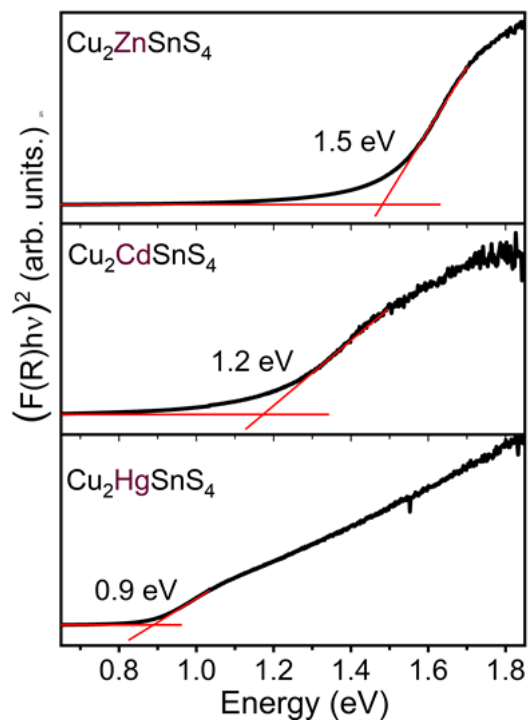


Figure A3.5. Optical diffuse reflectance spectra for Cu₂ZnSnS₄, Cu₂CdSnS₄, and Cu₂HgSnS₄, with fittings made on the assumption of direct band gaps.

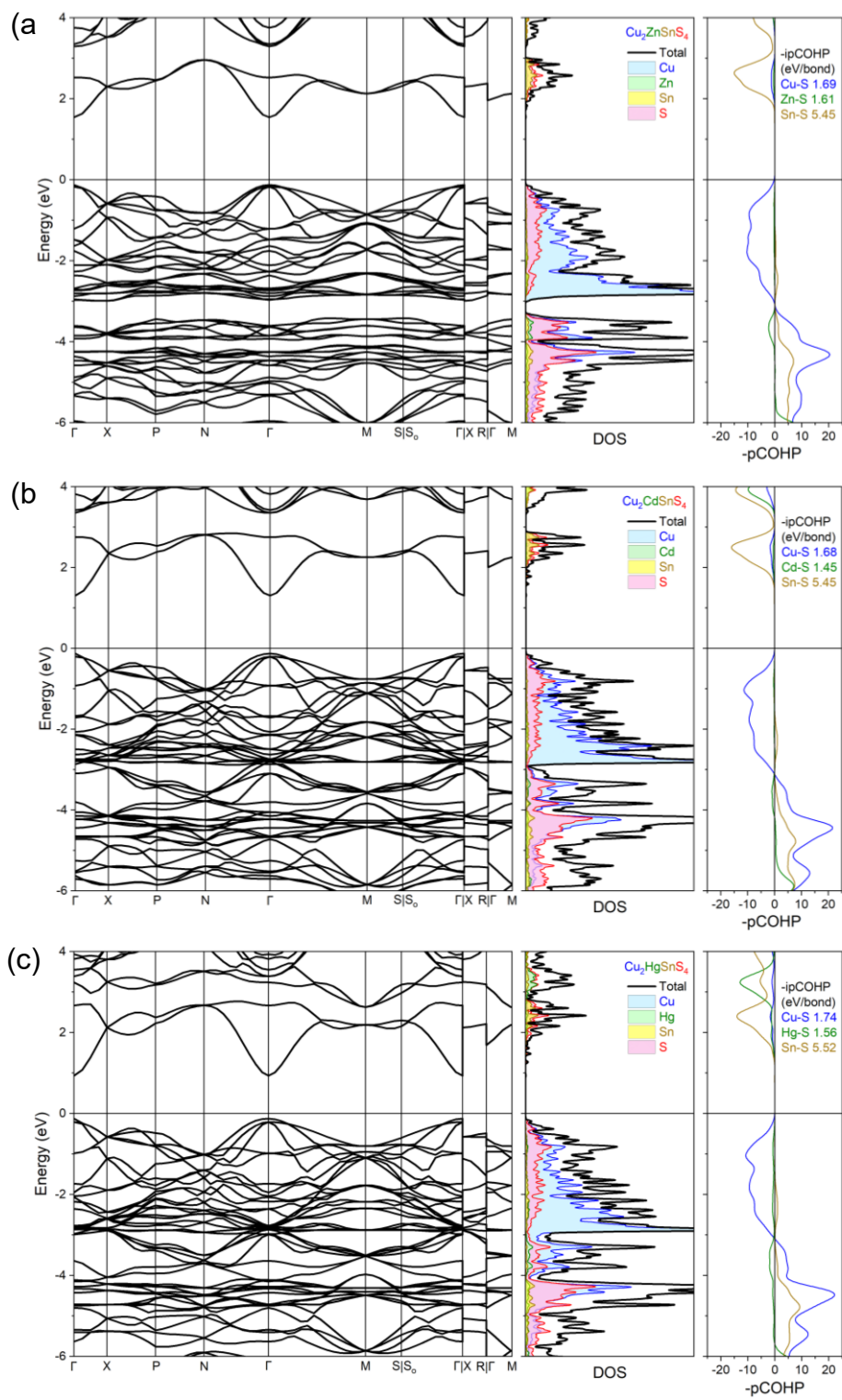


Figure A3.6. Electronic band structure, DOS, and $-p\text{COHP}$ curves for $\text{Cu}_2\text{ZnSnS}_4$, $\text{Cu}_2\text{CdSnS}_4$, and $\text{Cu}_2\text{HgSnS}_4$ compounds.

Appendix 4: Supplementary data for Chapter 4

Influence of Ge substitution on the structure and optoelectronic properties of $\text{Cu}_2\text{ZnSn}_{1-x}\text{Ge}_x\text{S}_4$ photovoltaic materials

Table A4.1. Experimental conditions for acquisition of NMR spectra.

	^{119}Sn	^{73}Ge	^{67}Zn	^{65}Cu
spinning conditions	non-spinning	non-spinning		non-spinning
B_0 (T)	7.05	21.1		7.05, 11.75, 21.1
pulse sequence	Hahn echo	one-pulse		quadrupolar echo
$\pi/2$ pulse (μs)	4	4	3	1
$\gamma B_1/2\pi$ (kHz)	62.5	62.5	83.3	125
τ (μs)	30	—		50
recycle delay (s)	50–100	5	5	2
co-added transients	1024–2048	8192	15360	1024–8048
	^{119}Sn	^{73}Ge	^{67}Zn	^{63}Cu
spinning conditions	MAS ($\omega_r/2\pi = 14$ kHz)	MAS ($\omega_r/2\pi = 5$ kHz)	MAS ($\omega_r/2\pi = 5$ kHz)	MAS ($\omega_r/2\pi = 62.5$ kHz)
B_0 (T)	7.05	21.1	21.1	21.1
pulse sequence	rotor-synchronized Hahn echo	one-pulse	one-pulse	rotor-synchronized quadrupolar echo
$\pi/2$ pulse (μs)	4	4	3	1
$\gamma B_1/2\pi$ (kHz)	62.5	62.5	83.3	125
τ (μs)	71.4	—	—	16
recycle delay (s)	50–150	2–5	2–5	2
co-added transients	1024–5120	1024–16384	32768	3072–4096

Table A4.2. EDX analyses (mol%) for $\text{Cu}_2\text{ZnSn}_{1-x}\text{Ge}_x\text{S}_4$ ($x = 0.0$ to 1.0).

Nominal composition	x	Cu	Zn	Sn	Ge	S
$\text{Cu}_2\text{ZnSnS}_4$	0	26 (25)	11 12	13 13	0 0	51 50)
$\text{Cu}_2\text{ZnSn}_{0.95}\text{Ge}_{0.05}\text{S}_4$	0.05	23 (25)	11 12	13 12	1 1	52 50)
$\text{Cu}_2\text{ZnSn}_{0.8}\text{Ge}_{0.2}\text{S}_4$	0.2	24 (25)	10 12	11 10	2 3	53 50)
$\text{Cu}_2\text{ZnSn}_{0.6}\text{Ge}_{0.4}\text{S}_4$	0.4	24 (25)	12 12	8 8	5 5	51 50)
$\text{Cu}_2\text{ZnSn}_{0.4}\text{Ge}_{0.6}\text{S}_4$	0.6	25 (25)	13 12	5 5	7 8	50 50)
$\text{Cu}_2\text{ZnSn}_{0.2}\text{Ge}_{0.8}\text{S}_4$	0.8	24 (25)	12 12	3 3	10 10	51 50)
$\text{Cu}_2\text{ZnGeS}_4$	1.0	25 (25)	12 12	0 0	12 13	51 50)

Table A4.3. Cell parameters and tetragonal distortion coefficient values as a function of x for the $\text{Cu}_2\text{ZnSn}_{1-x}\text{Ge}_x\text{S}_4$ series.

Compound	x	a (Å)	c (Å)	V (Å ³)	$(c/2a)$ ratio	E_g
$\text{Cu}_2\text{ZnSnS}_4$	0	5.4356(3)	10.8354(1)	320.14	0.997	1.49
$\text{Cu}_2\text{ZnSn}_{0.95}\text{Ge}_{0.05}\text{S}_4$	0.05	5.4294(1)	10.8239(1)	319.08	0.997	-
$\text{Cu}_2\text{ZnSn}_{0.8}\text{Ge}_{0.2}\text{S}_4$	0.2	5.4167(1)	10.7758(1)	316.17	0.995	1.59
$\text{Cu}_2\text{ZnSn}_{0.6}\text{Ge}_{0.4}\text{S}_4$	0.4	5.3987(2)	10.7128(5)	312.23(2)	0.992	1.71
$\text{Cu}_2\text{ZnSn}_{0.4}\text{Ge}_{0.6}\text{S}_4$	0.6	5.3754(1)	10.6414(3)	307.48(1)	0.989	1.78
$\text{Cu}_2\text{ZnSn}_{0.2}\text{Ge}_{0.8}\text{S}_4$	0.8	5.3641(1)	10.5855(1)	304.58	0.987	1.92
$\text{Cu}_2\text{ZnGeS}_4$	1.0	5.3449(1)	10.5137(1)	300.35	0.983	1.97

Table A4.4. Isotropic chemical shift, centre of gravity shift, and linewidth (FWHM in Hz) for the ^{119}Sn and ^{73}Ge MAS NMR in $\text{Cu}_2\text{ZnSn}_{1-x}\text{Ge}_x\text{S}_4$.

Compound	^{119}Sn		^{73}Ge	
	δ_{iso} (ppm)	FWHM (Hz)	δ_{cgs} (ppm)	FWHM (Hz)
$\text{Cu}_2\text{ZnSnS}_4$	121.5	795	—	—
$\text{Cu}_2\text{ZnSn}_{0.95}\text{Ge}_{0.05}\text{S}_4$	-119.8	919	21.2	280
$\text{Cu}_2\text{ZnSn}_{0.8}\text{Ge}_{0.2}\text{S}_4$	-118.1	1252	21.6	195
$\text{Cu}_2\text{ZnSn}_{0.6}\text{Ge}_{0.4}\text{S}_4$	-112.1	1080	23.4	488
$\text{Cu}_2\text{ZnSn}_{0.4}\text{Ge}_{0.6}\text{S}_4$	-111.4	2254	23.1	236
$\text{Cu}_2\text{ZnSn}_{0.2}\text{Ge}_{0.8}\text{S}_4$	-103.2	1199	26.3	151
$\text{Cu}_2\text{ZnGeS}_4$	—	—	28.5	95

Table A4.5. Comparison between computed (DFT- GIPAW) and experimentally determined NMR parameters.

	Cu ₂ ZnSnS ₄		Cu ₂ ZnGeS ₄		
	Experimental	DFT	Experimental	DFT (<i>I</i> $\bar{4}$)	DFT (<i>I</i> $\bar{4}2m$)
¹¹⁹Sn parameters					
Ω (ppm, ± 5)	32	39	—	—	—
κ (± 0.05)	-0.4	-1	—	—	—
⁷³Ge parameters					
Ω (ppm)	—	— ^a	14	26	39
κ	—	— ^a	-1	-1	+1
C_Q (MHz, ± 0.1)	—	—	0.3	0.3	1.8
η (± 0.1)	—	—	0.0	0	0
⁶⁷Zn parameters					
Ω (ppm, ± 5)	29	34	— ^a	15	17
κ (± 0.05)	-0.5	-1	— ^a	+1	-1
C_Q (MHz, ± 0.2)	0.9	1.8	2.8	5.1	7.4
η (± 0.1)	0	0	0.2	0	0
⁶⁵Cu parameters					
Ω (ppm, ± 5)	272 (<i>2a</i>)	284 (<i>2a</i>)	150 (<i>2a</i>)	176 (<i>2a</i>)	185
	117 (<i>2c</i>)	136 (<i>2c</i>)	83 (<i>2c</i>)	190 (<i>2c</i>)	
κ (± 0.05)	+1 (<i>2a</i>)	+1 (<i>2a</i>)	-1 (<i>2a</i>)	+1 (<i>2a</i>)	-1
	-1 (<i>2c</i>)	-1 (<i>2c</i>)	-1 (<i>2c</i>)	-1 (<i>2c</i>)	
C_Q (MHz, ± 0.1)	6.5 (<i>2a</i>)	7.1 (<i>2a</i>)	15.2 (<i>2a</i>)	15.5 (<i>2a</i>)	8.2
	1.5 (<i>2c</i>)	3.6 (<i>2c</i>)	4.3 (<i>2c</i>)	4.2 (<i>2c</i>)	
η (± 0.1)	0 (<i>2a</i>)	0 (<i>2a</i>)	0 (<i>2a</i>)	0 (<i>2a</i>)	0
	0 (<i>2c</i>)	0 (<i>2c</i>)	0 (<i>2c</i>)	0 (<i>2c</i>)	

^a Ω and κ do not improve the fitting noticeably.

Table A4.6. Atomic positions and bond angles for Cu₂ZnSnS₄ and Cu₂ZnGeS₄ were obtained from Rietveld refinement.

Atom	Wyckoff position	<i>x</i>	<i>y</i>	<i>z</i>	Angle A(°)	Angle B(°)
Cu ₂ ZnSnS ₄ (<i>I</i> $\bar{4}$)						
Cu1	2 <i>a</i>	0	0	0	109.9(2)	108.5(2)
Cu2	2 <i>c</i>	0	0.5	0.25	109.2(2)	110.1(2)
Zn	2 <i>d</i>	0	0.5	0.75		
Sn	2 <i>b</i>	0	0	0.5		
S	8 <i>g</i>	0.2469(4)	0.2524(4)	0.1274(3)		
Cu ₂ ZnGeS ₄ (<i>I</i> $\bar{4}$)						
Cu1	2 <i>a</i>	0	0	0	108.1(11)	112.3(10)
Cu2	2 <i>c</i>	0	0.5	0.25	110.8(10)	108.8(7)
Zn	2 <i>d</i>	0	0.5	0.75		
Sn	2 <i>b</i>	0	0	0.5		
S	8 <i>g</i>	0.2601(14)	0.244(4)	0.1217(1)		
Cu ₂ ZnGeS ₄ (<i>I</i> $\bar{4}$ 2 <i>m</i>)						
Cu	2 <i>a</i>	0	0.5	0.25	109.1(4)	110.3(3)
Zn	4 <i>d</i>	0	0	0		
Ge	2 <i>b</i>	0	0	0.5		
S	8 <i>g</i>	0.2616(9)	0.2616(2)	0.1247(7)		

Note: Occupancy for the Cu, Zn Sn, Ge, and S sites was fixed to 1. Angles A and B have multiplicity of 4 and 2, respectively.

Table A4.7. Isotropic chemical shifts [L(0) and L(4)] and centre of gravity shifts [L(0)] of ^{67}Zn MAS NMR for $\text{Cu}_2\text{ZnSn}_{1-x}\text{Ge}_x\text{S}_4$.

Compound	δ_{iso} (ppm)	δ_{cgs} [ppm, L(0)]
$\text{Cu}_2\text{ZnSnS}_4$	361 [L(0)]	359
$\text{Cu}_2\text{ZnSn}_{0.95}\text{Ge}_{0.05}\text{S}_4$		361
$\text{Cu}_2\text{ZnSn}_{0.8}\text{Ge}_{0.2}\text{S}_4$		368
$\text{Cu}_2\text{ZnSn}_{0.6}\text{Ge}_{0.4}\text{S}_4$		382
$\text{Cu}_2\text{ZnSn}_{0.4}\text{Ge}_{0.6}\text{S}_4$		378
$\text{Cu}_2\text{ZnSn}_{0.2}\text{Ge}_{0.8}\text{S}_4$		367
$\text{Cu}_2\text{ZnGeS}_4$	358 [L(0)]	343

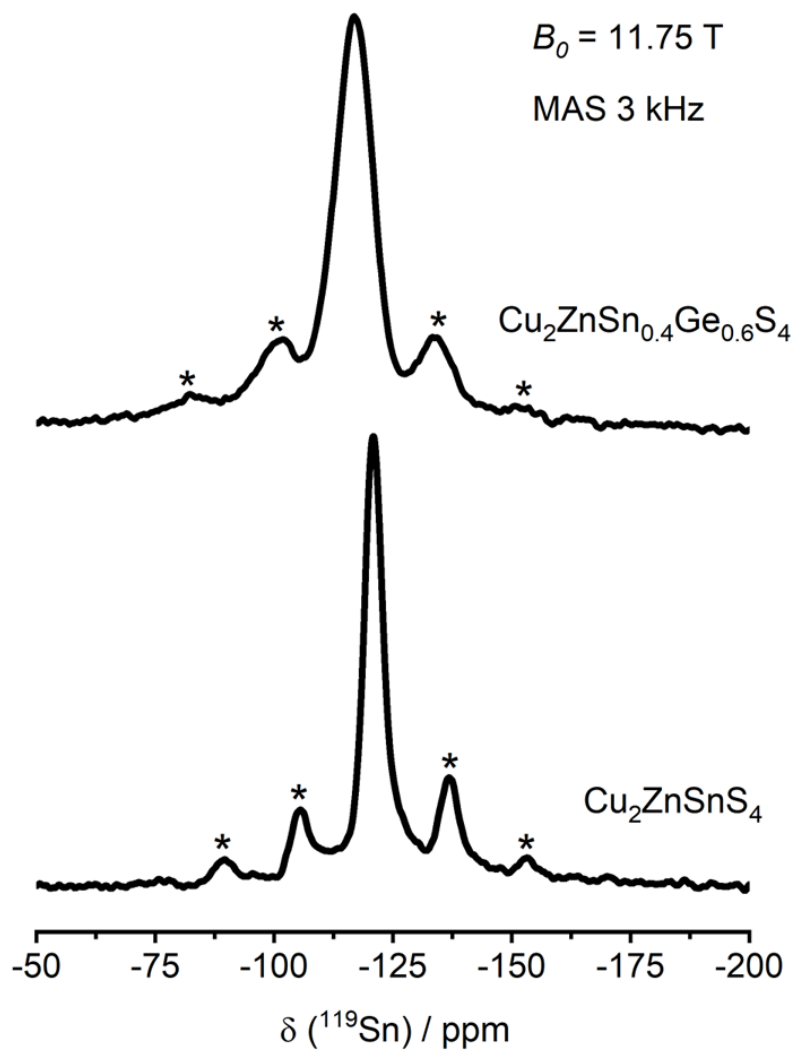


Figure A4.1. Comparison of slow MAS ($\omega_r/2\pi = 3$ kHz) data of $\text{Cu}_2\text{ZnSnS}_4$ and $\text{Cu}_2\text{ZnGeS}_4$ at 11.75 T.

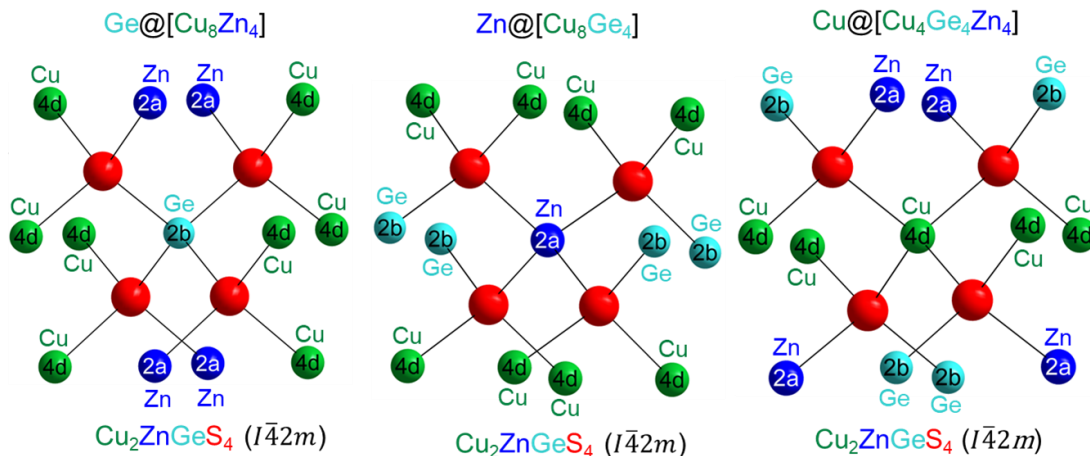


Figure A4.2. Local structure around Ge, Zn, and Cu for $\text{Cu}_2\text{ZnGeS}_4$ in $I\bar{4}2m$ structure.

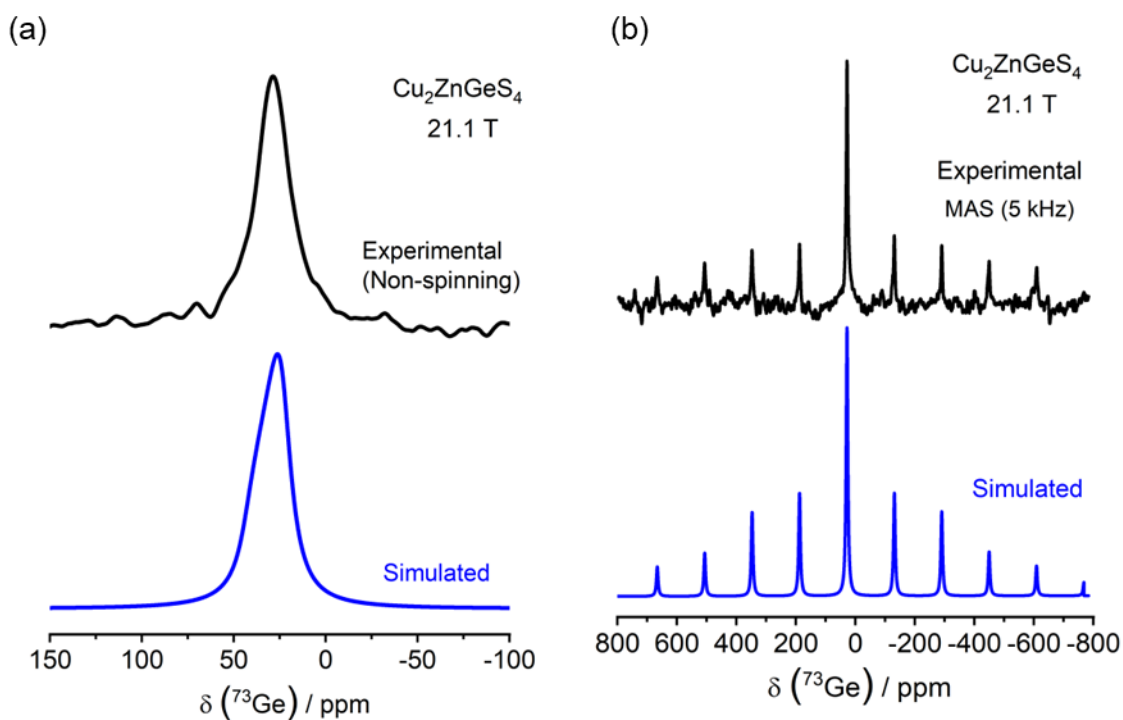


Figure A4.3. Experimental (black) non-spinning (a) and ^{73}Ge MAS ($\omega_r/2\pi = 5$ kHz) NMR spectra for $\text{Cu}_2\text{ZnGeS}_4$ ($\delta_{\text{iso}} = 28.5$ ppm, $C_Q = 0.3$ MHz, $\eta = 0$) at 21.1 T. The experimental NMR simulations (blue) were performed using the Dmfit software.

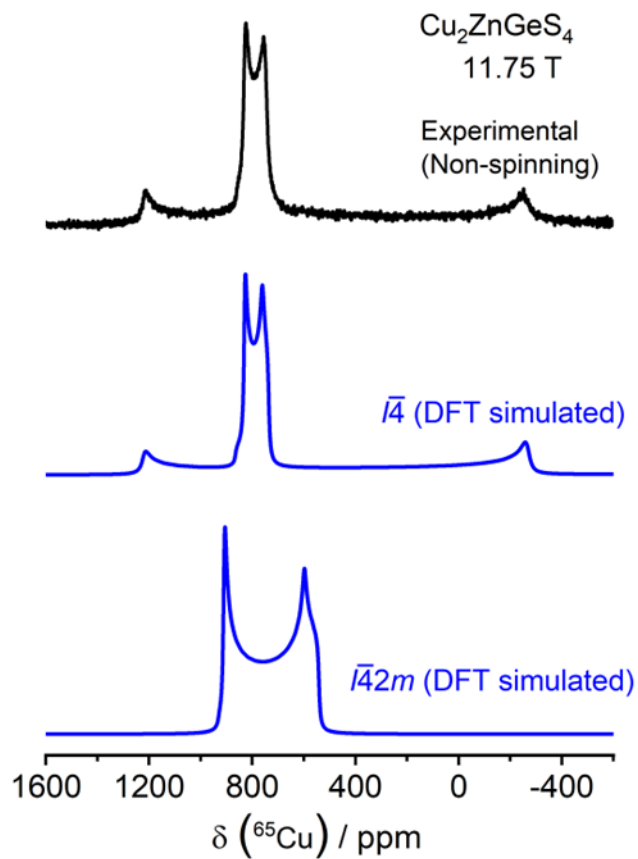


Figure A4.4. Experimental (black) and DFT (blue) predicted ^{65}Cu non-spinning NMR spectra for $\text{Cu}_2\text{ZnGeS}_4$. The parameters for the DFT predicted spectra are listed in Table A4.5.

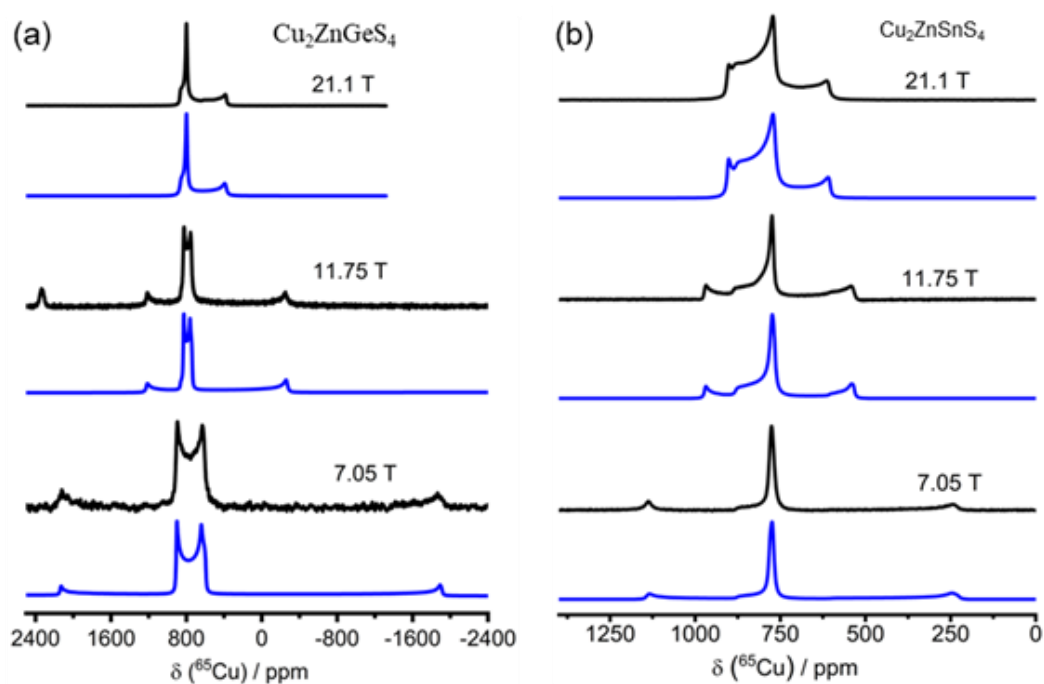


Figure A4.5. Experimental (black traces) and simulated (blue traces) non-spinning ^{65}Cu NMR spectra ($B_0 = 7.05, 11.75$ and 21.1 T) for (a) $\text{Cu}_2\text{ZnSnS}_4$ ($\delta_{\text{iso}} = 785$ ppm, $\Omega = 272$ ppm, $\kappa = +1$, $C_Q = 6.5$ MHz, $\eta = 0$ for $2a$ site; $\delta_{\text{iso}} = 805$ ppm, $\Omega = 117$ ppm, $\kappa = -1$, $C_Q = 1.5$ MHz, $\eta = 0$ for $2c$ site) and (b) $\text{Cu}_2\text{ZnGeS}_4$ ($\delta_{\text{iso}} = 705$ ppm, $\Omega = 150$ ppm, $\kappa = -1$, $C_Q = 15.2$ MHz, $\eta = 0$ for $2a$ site; $\delta_{\text{iso}} = 812$ ppm, $\Omega = 83$ ppm, $\kappa = -1$, $C_Q = 4.3$ MHz, $\eta = 0$ for $2c$ site). The experimental NMR simulations (blue) were performed using the Dmfit software.

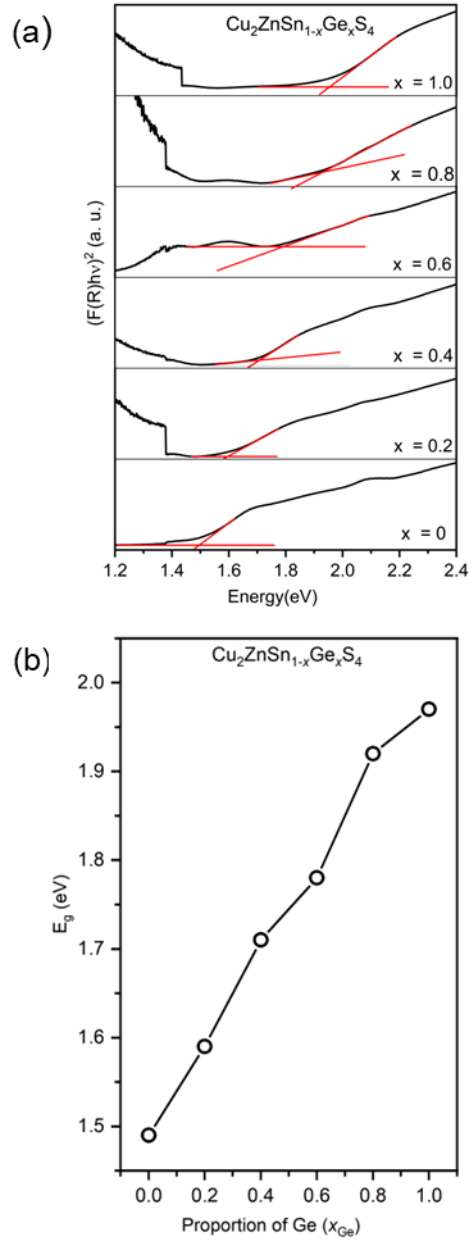


Figure A4.6. (a) Determination of the optical band gap using Tauc plot from UV-vis spectroscopy and (b) variation of the band gaps with the mole fraction of Ge in $\text{Cu}_2\text{ZnSn}_{1-x}\text{Ge}_x\text{SnS}_4$.

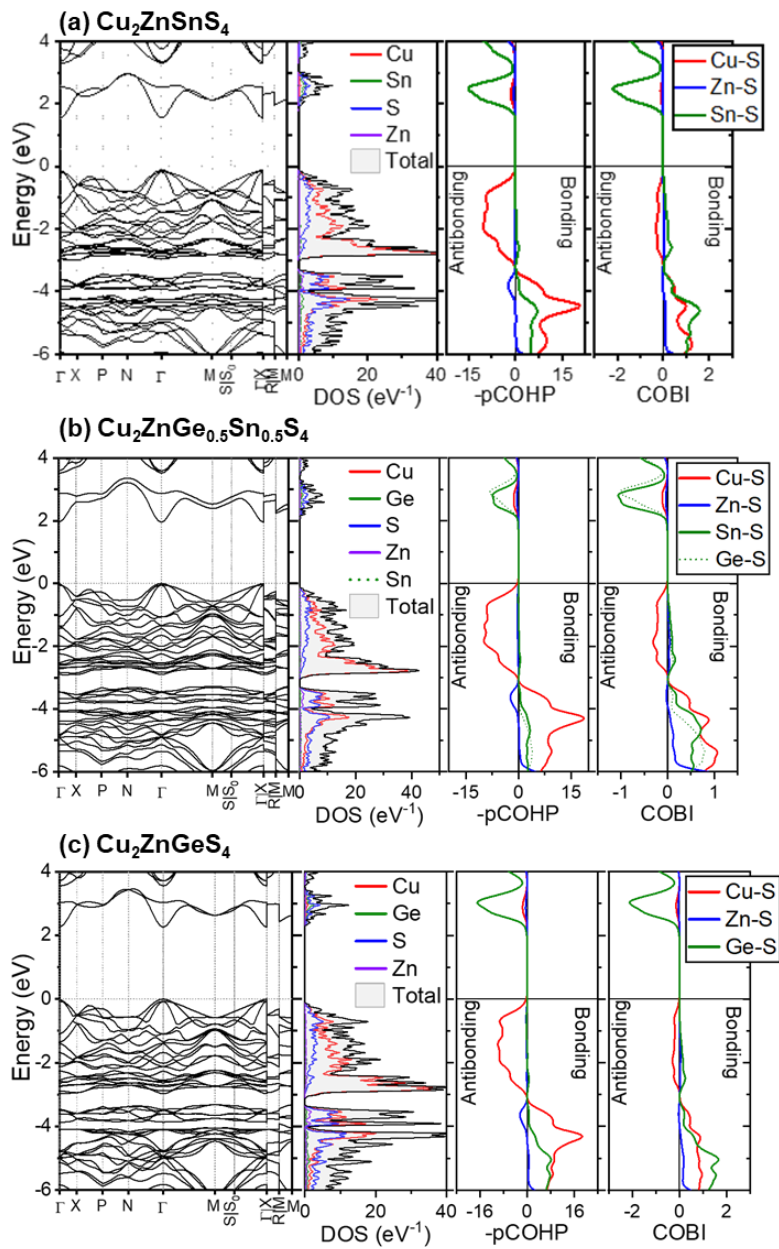


Figure A4.7. HSE06 band structure, density of states, and crystal orbital Hamiltonian population, and crystal orbital curves of (a) $\text{Cu}_2\text{ZnSnS}_4$, (b) $\text{Cu}_2\text{ZnGe}_{0.5}\text{Sn}_{0.5}\text{S}_4$, and (c) $\text{Cu}_2\text{ZnGeS}_4$. Positive values correspond to bonding interactions while negative values signify antibonding interactions.